

Trinity College Dublin
Coláiste na Tríonóide, Baile Átha Cliath
The University of Dublin

INVESTIGATION OF FOUNDATION DAMPING FOR MONOPILE-SUPPORTED OFFSHORE WIND TURBINES

Mohammed Barzan Mohammed

Submitted in fulfilment of the requirements for the degree of

Doctor of Philosophy

Department of Civil, Structural and Environmental Engineering

School of Engineering

Trinity College Dublin, the University of Dublin

2025

Supervisor: Dr. David Igoe

Declaration

I declare that this thesis has not been submitted as an exercise for a degree at this or any other university and it is entirely my own work.

I agree to deposit this thesis in the University's open access institutional repository or allow the library to do so on my behalf, subject to Irish Copyright Legislation and Trinity College Library conditions of use and acknowledgement.

I consent to the examiner retaining a copy of the thesis beyond the examining period, should they so wish

Signed: 

Date: 03/01/2025

Dedicated to:

My parents and my sister

Acknowledgements

First and foremost, I would like to thank my supervisor, Prof. David Igoe, for his unwavering support, guidance, and mentorship throughout the project. I also would like to my thanks to the Sustainable Energy Authority of Ireland (SEAI) for funding this project Furthermore, I would like to thank my internal and external examiners, Dr. Luke Prendergast and Dr. Breiffni Fitzgerald, for their valuable comments and recommendations, which greatly helped improve the quality of this work.

Secondly, I would like to thank the technical staff of the Civil, Structural, and environmental department for supporting me during the laboratory work. In particular, I would like to thank Joseph O'Connell for the numerous times he fixed the triaxial apparatus, and Robert Fitzpatrick for helping me with the triaxial tests in the early days of the research.

Thirdly, I would like to thank my fellow PhD students who shared this journey with me. Special thanks goes to my colleagues in the Pearse street office (Sathwik Kasyap, Alejandro Criado, and Louis-Marin Lapastoure) for the many times they helped me to stay sane and for the frequent visits to O'Neills.

Lastly, I would like to express my gratitude to my parents, sister, aunts, and grandmothers for their encouragement throughout the research. I am especially thankful to my mother and father for their emotional support, without which the completion of this work would not have been possible.

ABSTRACT

Modern offshore wind turbines (OWTs) are characterized by their large, slender structures, with natural frequencies often lying in close proximity to the frequencies of environmental and mechanical loads, thereby significantly increasing the likelihood of resonance. As a result, it becomes crucial to evaluate the contributions of energy dissipation from various sources, as the overall damping ratio plays a key role in governing the dynamic amplification of the OWT response during resonance. One source of damping that is often overlooked is the contribution of the foundation to attenuate the dynamic response of OWTs through the nonlinear hysteretic behaviour of the surrounding soil. Therefore, the aim of this study is to evaluate the contribution of foundation damping for monopile-supported OWTs through finite element analyses adopting soil constitutive models calibrated with laboratory triaxial tests. To provide a comprehensive understanding of foundation damping, finite element simulations are conducted to investigate its variation with different monopile dimensions and soil relative densities. The study offers new insights into foundation damping, offering a deeper understanding of soil-structure interaction for OWTs and enabling the design of more efficient monopiles that extend the fatigue life-time of the support structure.

To reasonably represent soil behaviour in the finite element analyses, the parameters of the HSsmall and SANISAND-MS constitutive models were calibrated using the results of an extensive campaign of monotonic and cyclic triaxial tests conducted on Blessington sand. The experiments were performed under varying mean effective stresses and relative densities to examine their influence on both monotonic and dynamic soil behaviour. In addition to informing the calibration of the constitutive models, the results of the cyclic triaxial tests were curve-fitted with hyperbolic functions, allowing the use of these functions to derive representative damping and shear modulus reduction curves for cohesionless materials when laboratory data is unavailable in the early stages of design.

A comprehensive set of finite element analyses is conducted to assess the variation of foundation damping for monopiles of different dimensions installed in various soil relative densities. Dynamic free vibration simulations are performed to evaluate the foundation damping ratio, while cyclic (pseudo-dynamic) simulations are carried out to determine the foundation damping factors at the mudline level and along the monopile depth. The importance of the damping factors determined in this study is that they can be used in integrated wind turbine numerical analyses, enabling foundation damping effects to be incorporated.

Table of Contents

INTRODUCTION **22**

1.1 Background 22

1. 2 Characteristics of OWT Design Loads 26

1.3 Current Design Practice and Limitations 28

1.4 Research Aims and Objectives 29

1.5 Thesis outline 30

LITERATURE REVIEW **32**

2.1 Introduction 32

2.2 Cyclic soil behaviour 32

2.2.1 Dependency of soil deformation on shear strain *32*

2.2.2 Stress-strain hysteresis loops *34*

2.2.3 Cyclic thresholds *36*

2.2.4 Factors affecting G/G_0 and damping ratio curves *38*

2.3 Monotonic behaviour of soil 43

2.3.1 Shear strength *44*

2.3.2 Critical state and steady state *46*

2.3.3 State parameter (Ψ) *47*

2.3.4 Characteristic and phase transformation lines *48*

2.4 Soil constitutive modelling 50

2.5 HSsmall model 52

2.6 SANISAND-MS model 53

2.7 General behaviour of monopiles 53

2.8 Monopile load-deformation response 55

2.9 Geotechnical modelling 58

2.9.1 Continuum 3D FE approach *58*

2.9.2 Winkler approach *59*

2.9.3 Macro-element approach *61*

2.10 Foundation damping 63

2.11 Foundation damping studies 67

2.11.1 Field studies *67*

2.11.2 Laboratory studies *69*

2.11.3 Numerical modelling studies *73*

2.12 Research gap 77

2.13 Conclusions 78

MATERIALS AND EXPERIMENTAL METHODS **80**

3.1 Introduction 80
3.2 Tested materials 81
3.3 Triaxial apparatus 83
3.3.1 Axial actuator unit *84*
3.3.2 Triaxial cell *85*
3.3.3 Internal load cell *85*
3.3.4 Data acquisition and control unit *86*
3.3.5 Cell and back pressure controllers *86*
3.3.6 Pore water pressure transducer *87*
3.3.7 Local LVDTs *87*
3.4 Bender element testing system 89
3.5 Triaxial test procedure 91
3.5.1 Sample preparation *91*
3.5.2 Attaching the local LVDTs *96*
3.5.3 Saturation *96*
3.5.4 Consolidation *97*
3.5.5 Shearing *98*
3.6 Calculations of stresses, strains, and dynamic parameters 98
3.6.1 Axial strain *98*
3.6.2 Volumetric strain *99*
3.6.3 Shear strain *99*
3.6.4 Deviatoric stress *101*
3.6.5 Mean effective stress *101*
3.6.6 Damping ratio and secant shear modulus *102*
3.7 Conclusions 103

LABORATORY TESTS 104

4.1 Introduction 104
4.2 Undrained cyclic tests 105
4.2.1 Effects of mean effective stress and relative density *106*
4.2.2 Comparison between Blessington and Kilmuckridge *111*
4.2.3 Effect of number of cycles (N) *113*
4.3 Bender element tests 115
4.4 Drained triaxial tests 117
4.4.1 Effects of mean effective stress and relative density *118*
4.4.2 Comparison between drained and undrained *121*
4.4.3 Effect of number of cycles (N) *124*
4.5 Fitting empirical functions 125
4.5.1 Normalised shear modulus reduction *126*
4.5.2 Damping ratio *129*

4.6 MONOTONIC BEHAVIOUR 130
4.6.1 Peak angle of shearing resistance (φ_p) *131*
4.6.2 Critical state parameters *135*
4.6.3 Characteristic line *136*
4.7 SUMMARY 138

CONSTITUTIVE MODEL CALIBRATION 141

5.1 INTRODUCTION 141
5.2 HSSMALL MODEL CALIBRATION 141
5.2.1 HSsmall model parameters *142*
5.2.2 c, φ, ψ, and K_0^{NC} Parameters *142*
5.2.3 E_{50}^{ref}, E_{oed}^{ref}, E_{ur}^{ref}, m, and v_{ur} Parameters *144*
5.2.4 G_0^{ref} and $\gamma_{0.7}$ Parameters *150*
5.3 SANISAND-MS MODEL CALIBRATION 154
5.3.1 e_0, λ_c, ξ, M_c, and c parameters *156*
5.3.2 G, v, and m parameters* *157*
5.3.3 n^b and n^d parameters *158*
5.3.4 h_0, c_h, and A_0 parameters *158*
5.3.5 e_{ini}, e_{min}, e_{max} parameters *159*
5.3.6 μ_0, ζ, and β parameters *161*
5.3.7 Alternative set of parameters *164*
5.3.8 Issue related to SANISAND-MS model *165*
5.3.9 Selected SANISAND-MS parameters *167*
5.4 SUMMARY 168

3D FINITE ELEMENT MODELLING 169

6.1 INTRODUCTION 169
6.2 3D FE NUMERICAL MODELS 170
6.3 RADIATION DAMPING 176
6.4 FREE-DECAY ANALYSES 177
6.4.1 HSsmall simulations *181*
6.4.2 SANISAND-MS simulations *185*
6.4.3 Comparison between HSsmall and SANISAND-MS results *187*
6.5 CYCLIC PUSH-OVER SIMULATIONS 190
6.5.1 Mudline hysteretic foundation damping ratios *192*
6.5.2 Distributed hysteretic foundation damping ratios *208*
6.6 SUMMARY 219

CONCLUSIONS 221

REFERENCES 225

APPENDIX A **244**

APPENDIX B **245**

List of Figures

Figure 1.1: Current and projected onshore and offshore wind turbine installations in Europe (Wind Europe, 2024) 22
Figure 1.2: Size evolution of OWTs (IEA, 2019) 23
Figure 1.3: Types of foundations used is OWTs: mono-pile (a), monopod (skirted caisson) (b), jacket structure (c), tripod (d) and floating wind turbine with anchors (e) (Kaynia, 2019). 24
Figure 1.4: Main components of a typical OWT 25
Figure 1.5: Types of loads applied to OWTs with their typical wave forms (Nikitas et al., 2016). 26
Figure 1.6: Environmental and operational loading frequency spectrum (Bhattacharya et al., 2013) 27
Figure 1.7: Campbell diagram (Damgaard et al., 2014) 27
Figure 2.1: Variation of soil properties with different strain levels (Ishihara, 1996) 33
Figure 2.2: Stress-strain hysteresis loop 34
Figure 2.3: Shear modulus and damping ratio with shear strain increase 35
Figure 2.4: Relation between damping ratio and G/G_0 (Ishihara, 1996) 36
Figure 2.5: G/G_0 and damping ratio curves with different zones of cyclic shear strain amplitude (modified after Vucetic, 1994) 37
Figure 2.6: Three zones of soil behaviour characterisation (Kallioglou et al., 2008) 38
Figure 2.7: damping ratio curves of very dense silica sand (Blaker and Andersen, 2019) 41
Figure 2.8: Summary of qualitative descriptions of soil behaviour under cyclic loading (Rascol, 2009) 42
Figure 2.9: The effect of OCR on the variation of (a) shear modulus, (b) normalised shear modulus, and (c) material damping ratio with shearing strain amplitude (modified after Darendeli, 2001) . 43
Figure 2.10: Soil monotonic behaviour: (a) stress-strain curve, (b) failure envelopes (Mitchell and Soga, 2005) 45
Figure 2.11: Critical state lines of sand and clay: (a) Weald clay, (b) Toyoura sand (Mitchell and Soga, 2005) 46
Figure 2.12: CSL of sand and clay in the compressibility plane: (a) CSL of Weald clay on the e-ln(p') plane, (b) CSL of Toyoura sand on the e-log(p') plane (Mitchell and Soga, 2005) 47
Figure 2.13: Definition of the state parameter, Ψ (modified after White, 2020) 48
Figure 2.14: Influence of Ψ on: (a) peak friction angle and (b) Maximum dilation rate (Been and Jefferies, 1985) 48
Figure 2.15: Definition of the phase transformation line (Lade and Ibsen, 1997) 49
Figure 2.16: Hysteretic stress-strain loops 52
Figure 2.17: SANISAND-MS surfaces: (a) Triaxial stress space, (b) deviatoric stress ratio plane (SANISAND-MS manual, 202 53
Figure 2.18: Flexible versus rigid pile behaviour (Augustesen et al., 2009) 54

Figure 2.19: K_r versus L_p/D_p for full scale monopiles used for UK OWFs (Modified after Abadie, 2015) 54
Figure 2.20: Monopile response under monotonic and cyclic loading (modified after Richards, 2019) 57
Figure 2.21: (a) Vertical cut through the soil, along the loading direction, (b) Sketch of soil domains (Cuéllar et al., 2009) 57
Figure 2.22: Monopile soil-structure interaction methods (modified after Abadie, 2015) 58
Figure 2.23: Schematic of the Winkler approach 60
Figure 2.24: PISA design model: (a) idealisation of the soil reaction components acting on the pile; (b) 1D finite-element implementation of the model (modified after Burd et al., 2020b) 60
Figure 2.25: Macro-element modelling approach 61
Figure 2.26: Comparison between the macro-element model and Cowden pile field test (Page et al., 2018) 62
Figure 2.27: Foundation damping ratio calculation from load-deformation hysteretic loop at the mudline 64
Figure 2.28: Distributed foundation damping ratio calculation along monopile depth 65
Figure 2.29: Free-decay response at the RNA level 66
Figure 2.30: Degradation of ξ_θ with N (modified after Abadie, 2015) 71
Figure 2.31: Distributed ξ_y profile with embedment depth (modified after Jindal et al., 2024) 72
Figure 2.32: Moment time histories with and without foundation damping (modified after Carswell et al., 2015) 74
Figure 2.33: ζ_f versus mudline displacement (modified after Panagoulias et al., 2023) 76
Figure 2.34: ζ_f versus mudline displacement (modified after Ryan et al., 2025) 77

Figure 3.1: Particle size distribution curves of Blessington and Kilmuckridge sands 81
Figure 3.2: Triaxial apparatus testing system 83
Figure 3.3: Balanced ram configuration 84
Figure 3.4: Triaxial cell 85
Figure 3.5: GDS submersible load cell 86
Figure 3.6: ADVDCS V2 control unit 86
Figure 3.7: Schematic of a GDS Standard Level Controller 87
Figure 3.8: Pore pressure transducer 87
Figure 3.9: (a) Radial LVDT and (b) Axial LVDTs 89
Figure 3.10: Bender element testing system 90
Figure 3.11: GDS transmitter and receiver bender elements 91
Figure 3.12: Sample preparation: (a) securing the membrane to the base pedestal, (b) setting up the split mould and securing the membrane on the split mould, (c) Compacting the soil, (d) Placing the top cap, (e) removing the split mould 95

Figure 3.13: LVDTs secured on the sample 96
Figure 3.14: Behaviour of LVDTs at small cyclic deviatoric stress 100
Figure 3.15: Behaviour of LVDTs at large cyclic deviatoric stress 100
Figure 3.16: Typical hysteretic stress-strain loop 102
Figure 4.1: typical strain ranges for laboratory tests and structures (Atkinson & Sallfors,1991). 105
Figure 4.2: (a) Shear modulus reduction and (b) damping ratio of Blessington sand with $D_r \approx 30\%$ 107
Figure 4.3: (a) Shear modulus reduction and (b) damping ratio of Blessington sand with $D_r \approx 60\%$ 107
Figure 4.4: (a) Shear modulus reduction and (b) damping ratio of Blessington sand with $D_r \approx 80\%$ 107
Figure 4.5: (a) Shear modulus reduction and (b) damping ratio of Blessington sand with $D_r \approx 90\%$ 108
Figure 4.6: (a) Shear modulus reduction and (b) damping ratio of Kilmuckridge sand with $D_r \approx 60\%$ 108
Figure 4.7: (a) Shear modulus reduction and (b) damping ratio of Kilmuckridge sand with $D_r \approx 90\%$ 108
Figure 4.8: (a) Shear modulus reduction and (b) damping ratio of Blessington sand tested at p_0'=50 kPa 109
Figure 4.9: (a) Shear modulus reduction and (b) damping ratio of Blessington sand tested at p_0'=150 kPa 109
Figure 4.10: (a) Shear modulus reduction and (b) damping ratio of Blessington sand tested at p_0'=300 kPa 109
Figure 4.11: (a) Shear modulus reduction and (b) damping ratio of Kilmuckridge sand tested at p_0'=150 kPa 110
Figure 4.12: (a) Shear modulus reduction and (b) damping ratio of Kilmuckridge sand tested at p_0'=300 kPa 110
Figure 4.13: (a) stress-strain loops for small strain levels, (b) stress-strain loops for large strain levels 111
Figure 4.14: (a) Shear modulus reduction and (b) damping ratio for p_0'=50 kPa and $D_r \approx 60\%$. 112
Figure 4.15: (a) Shear modulus reduction and (b) damping ratio for p_0'=150 kPa and $D_r \approx 60\%$ 112
Figure 4.16: (a) Shear modulus reduction and (b) damping ratio for p_0'=300 kPa and $D_r \approx 60\%$ 112
Figure 4.17: (a) Shear modulus reduction and (b) damping ratio for p_0'=150 kPa and $D_r \approx 90\%$ 113
Figure 4.18: (a) Shear modulus reduction and (b) damping ratio for p_0'=300 kPa and $D_r \approx 90\%$ 113
Figure 4.19: (a) Shear modulus reduction and (b) damping ratio for BCU(30)150 at N = 1, 5, 10, 20, 30, and 40 114
Figure 4.20: (a) Shear modulus reduction and (b) damping ratio for BCU(60)150a at N = 1, 5, 10, 20, 30, and 40 114

Figure 4.21: (a) Shear modulus reduction and (b) damping ratio for BCU(90)150 at N = 1, 5, 10, 20, 30, and 40 114
Figure 4.22: Determination of travel time from signal recordings 116
Figure 4.23: Maximum shear modulus G_0 versus mean effective stress p' 116
Figure 4.24: (a) Shear modulus reduction and (b) damping ratio of Blessington sand with $D_r \approx 60\%$ 120
Figure 4.25: (a) Shear modulus reduction and (b) damping ratio of Blessington sand tested at p_0'=50 kPa 120
Figure 4.26: (a) Shear modulus reduction and (b) damping ratio of Blessington sand tested at p_0'=150 kPa 120
Figure 4.27: (a) Shear modulus reduction and (b) damping ratio of Blessington sand tested at p_0'=300 kPa 121
Figure 4.28: Effect of p_0' on G/G_0-γ_c curves: (a) fitting of G-γ_c curves; (b) G/G_0-γ_c curves for D_r = 60% 121
Figure 4.29: Effect of D_r on G/G_0-γ_c curves: (a) fitting of G-γ_c curves; (b) G/G_0-γ_c curves for p_0' = 300 kPa 121
Figure 4.30: Drained and undrained damping ratio comparison (p_0'= 50 kPa) 123
Figure 4.31: Drained and undrained damping ratio comparison (p_0'= 150 kPa) 123
Figure 4.32: Drained and undrained damping ratio comparison (p_0'= 300 kPa) 123
Figure 4.33: Influence of N on the damping ratio of soil (horizontal axis in logarithmic scale).. 125
Figure 4.34: Influence of N on the damping ratio of soil (horizontal axis in linear scale) 125
Figure 4.35: Curve fitting of the undrained tests: (a) α and (b) γ_r 127
Figure 4.36: Curve fitting of the drained tests: (a) α and (b) γ_r 128
Figure 4.37: Comparison between laboratory results and the fittings with Equation 4.4 128
Figure 4.38: Comparing the results of the empirical function (Equation 4.8) and triaxial results 130
Figure 4.39: φ_m versus axial strain for samples reconstituted at $D_r \approx 60\%$ 133
Figure 4.40: Volumetric strain versus axial strain for samples reconstituted at $D_r \approx 60\%$ 133
Figure 4.41: φ_m versus axial strain for samples reconstituted at $D_r \approx 30\%$ 134
Figure 4.42: Volumetric strain versus axial strain for samples reconstituted at $D_r \approx 30\%$ 134
Figure 4.43: φ_p versus p_0' for all the monotonic tests 134
Figure 4.44: Identification of CSL for Blessington sand 136
Figure 4.45: φ_{cl} versus p_o' for all the monotonic tests at $D_r \approx 60\%$ and $D_r \approx 90\%$ 137
Figure 5.1: Angle of internal friction (φ) versus initial mean effective stress (p_0') for D_r = 60% 143
Figure 5.2: E_{50} versus normalised effective confining stress (σ_3'/ P_{ref}) for $D_r \approx 30\%$ 144
Figure 5.3: E_{50} versus normalised effective confining stress (σ_3'/ P_{ref}) for $D_r \approx 60\%$ 145
Figure 5.4: Comparing monotonic q-ε_q curves between triaxial simulation and laboratory results for $D_r \approx 30\%$ 148

Figure 5.5: Comparing monotonic q-ε_a curves between triaxial simulations and laboratory results for $D_r \approx 30\%$ 148
Figure 5.6: Comparing monotonic q-ε_q curves between triaxial simulation and laboratory results for $D_r \approx 60\%$ 149
Figure 5.7: Comparing monotonic q-ε_a curves between triaxial simulations and laboratory results for $D_r \approx 60\%$ 149
Figure 5.8: HSsmall and laboratory derived damping ratio curves 152
Figure 5.9: HSsmall and laboratory derived normalised shear modulus reduction curves 152
Figure 5.10: Comparison between damping from HSsmall relations and triaxial simulations 154
Figure 5.11: Critical state line (CSL) for Blessington sand 157
Figure 5.12: Comparing monotonic q-ε_q curves between triaxial simulation and laboratory results for $D_r \approx 30\%$ 159
Figure 5.13: Comparing monotonic q-ε_a curves between triaxial simulations and laboratory results for $D_r \approx 30\%$ 160
Figure 5.14: Comparing monotonic q-ε_q curves between triaxial simulation and laboratory results for $D_r \approx 60\%$ 160
Figure 5.15: Comparing monotonic q-ε_a curves between triaxial simulations and laboratory results for $D_r \approx 60\%$ 161
Figure 5.16: the q-p' stress paths for BCD(30)100L and BCD(60)200L tests 162
Figure 5.17: Axial strain accumulation from laboratory and triaxial simulations for BCD(30)100L 163
Figure 5.18: Axial strain accumulation from laboratory and triaxial simulations for BCD(60)200L 163
Figure 5.19: D-γ curves obtained from SANISAND-MS and laboratory derived curve fit 164
Figure 5.20: Monotonic simulation results obtained using PS1 and PS2 parameters 165
Figure 5.21: Damping ratio curves obtained using PS1 and PS2 parameters 165
Figure 5.22: Damping ratio (D) against number of cycles (N) 166
Figure 5.23: Comparing the stress-strain response of laboratory experiment and SANISAND-MS simulation 167
Figure 6.1: 3D FE numerical model 171
Figure 6.2: Comparison between the monotonic simulation of SANISAND-MS and HSsmall 172
Figure 6.3: Stiff plate connecting the foundation and the structure 174
Figure 6.4: Lateral displacement time history at the RNA level 177
Figure 6.5: Numerical control parameters 178
Figure 6.6: Lateral displacement of the tower at the RNA level 179
Figure 6.7: Time history of the lateral displacement of the foundation at the mudline level 180
Figure 6.8: Free vibration simulations of the tower at RNA level 181

Figure 6.9: Effect of embedment depth on ζ_f for soil profile with D_r = 30%: (a) D_p = 10 m; (b) D_p = 12 m 181
Figure 6.10: Effect of embedment depth on ζ_f for soil profile with D_r = 60%: (a) D_p = 10 m; (b) D_p = 12 m 182
Figure 6.11: Effect of D_p on ζ_f: (a) D_r = 30%; (b) D_r = 60% 182
Figure 6.12: Effect of D_r on ζ_f: (a) MP10-30; (b) MP10-50 183
Figure 6.13: Effect of D_r on ζ_f: (a) MP12-36; (b) MP12-60 183
Figure 6.14: Effect of embedment depth on ζ_f for soil profile with D_r = 30%: (a) D_p = 10 m; (b) D_p = 12 m 185
Figure 6.15: Effect of embedment depth on ζ_f for soil profile with D_r = 60%: (a) D_p = 10 m; (b) D_p = 12 m 185
Figure 6.16: Effect of D_p on ζ_f: (a) D_r = 30%; (b) D_r = 60% 186
Figure 6.17: Effect of D_r on ζ_f: (a) MP10-30; (b) MP10-50 187
Figure 6.18: Effect of D_r on ζ_f: (a) MP12-36; (b) MP12-60 187
Figure 6.19: Comparison of ζ_f versus y_g/D_p using HSsmall and SANISAND-MS models (D_r=30% and D_p=10m) 188
Figure 6.20: Comparison of ζ_f versus y_g/D_p using HSsmall and SANISAND-MS models (D_r=30% and D_p=12m) 188
Figure 6.21: Comparison of ζ_f versus y_g/D_p using HSsmall and SANISAND-MS models (D_r=60% and D_p=10m) 189
Figure 6.22: Comparison of ζ_f versus y_g/D_p using HSsmall and SANISAND-MS models (D_r=60% and D_p=12m) 189
Figure 6.23: Cyclic push-over simulations: (a) Loading; (b) Unloading; (c) Reloading 191
Figure 6.24: Numerical control parameters for the cyclic push-over analyses 191
Figure 6.25: Representative load-deformation hysteresis loop at the mudline 192
Figure 6.26: Effect of L_p on (a) ξ_y versus y_g/D_p, and (b) ξ_θ versus θ_g, for the monopiles with D_p =10 m and soil D_r = 30% 193
Figure 6.27: Effect of L_p on (a) ξ_y versus y_g/D_p, and (b) ξ_θ versus θ_g, for the monopiles with D_p =12 m and soil D_r = 30% 194
Figure 6.28: Effect of L_p on (a) ξ_y versus y_g/D_p, and (b) ξ_θ versus θ_g, for the monopiles with D_p =10 m and soil D_r = 60% 194
Figure 6.29: Effect of L_p on (a) ξ_y versus y_g/D_p, and (b) ξ_θ versus θ_g, for the monopiles with D_p =12 m and soil D_r = 60% 194
Figure 6.30: Effect of D_p on (a) ξ_y versus y_g/D_p, and (b) ξ_θ versus θ_g, for the soil profile with D_r = 30% 196
Figure 6.31: Effect of D_p on (a) ξ_y versus y_g/D_p, and (b) ξ_θ versus θ_g, for the soil profile with D_r = 60% 196
Figure 6.32: Foundation stiffness for D_r = 30%: (1) k_y versus y_g/D_p; (2) k_θ versus θ_g 197

Figure 6.33: Foundation stiffness for D_r = 60%: (1) k_y versus y_g/D_p; (2) k_θ versus θ_g 198
Figure 6.34: Free-decay simulation at the RNA level 199
Figure 6.35: ζ_f derived from 1D FE analyses (30% relative density) 199
Figure 6.36: ζ_f derived from 1D FE analyses (60% relative density) 199
Figure 6.37: Effect of relative density on MP10-40: (1) ξ_y versus y_g/D_p; (2) ξ_θ versus θ_g 200
Figure 6.38: Effect of relative density on MP12-48: (1) ξ_y versus y_g/D_p; (2) ξ_θ versus θ_g 201
Figure 6.39: Effect of load eccentricity on: (a) ξ_y versus y_g/D_p; (2) ξ_θ versus θ_g 201
Figure 6.40: Comparison of ζ_f obtained from 1D FE and 3D FE (MP10-30) 204
Figure 6.41: Comparison of ζ_f obtained from 1D FE and 3D FE (MP10-40) 204
Figure 6.42: Comparison of ζ_f obtained from 1D FE and 3D FE (MP10-50) 204
Figure 6.43: Effect of L_p on (a) ξ_y versus y_g/D_p, and (b) ξ_θ versus θ_g, for D_p =10 m and soil D_r = 30% 205
Figure 6.44: Effect of L_p on (a) ξ_y versus y_g/D_p, and (b) ξ_θ versus θ_g, for D_p =12 m and soil D_r = 30% 206
Figure 6.45: Effect of L_p on (a) ξ_y versus y_g/D_p, and (b) ξ_θ versus θ_g, for D_p =10 m and soil D_r = 60% 206
Figure 6.46: Effect of L_p on (a) ξ_y versus y_g/D_p, and (b) ξ_θ versus θ_g, for D_p =12 m and soil D_r = 60% 206
Figure 6.47: Effect of monopile diameter (D_p) on: (a) ξ_y versus y_g/D_p; (b) ξ_θ versus θ_g 207
Figure 6.48: Effect of relative density on MP10-40: (1) ξ_y versus y_g/D_p; (2) ξ_θ versus θ_g 207
Figure 6.49: p-y and m-θ loops along the monopile length 208
Figure 6.50: PISA design model: (a) components of soil reactions; (b) 1D FE implementation 209
Figure 6.51: Coordinates of the monopile model 210
Figure 6.52: Pile element section 211
Figure 6.53: Soil reaction-deformation loops near the mudline: (a) p-y; (b) m-θ 212
Figure 6.54: Soil reaction-deformation loops near the point of rotation: (a) p-y, (b) m-θ 213
Figure 6.55: Soil reaction-deformation loops near the monopile tip: (a) p-y, (b) m-θ 213
Figure 6.56: Distributed foundation damping ratios with depth: (a) ξ_y; (b) ξ_θ 214
Figure 6.57: Foundation damping ratios with depth for monopiles MP10-30 and MP10-50: (a) ξ_y; (b) ξ_θ 215
Figure 6.58: deformation profiles with depth for monopiles MP10-30 and MP10-50: (a) y/D_p; (b) θ 215
Figure 6.59: Effect of L_p on a pile section 5.5 m below the mudline: (a) ξ_y-y/D_p; (b) ξ_θ-θ 216
Figure 6.60: Effect of L_p on a pile section 12.5 m below the mudline: (a) ξ_y-y/D_p; (b) ξ_θ-θ 216
Figure 6.61: Effect of D_p on the profiles of: (a) ξ_θ with depth; (b) θ with depth 217
Figure 6.62: Effect of D_p on a pile section 5.5 m below the mudline: (a) ξ_y-y/D_p; (b) ξ_θ-θ 218
Figure 6.63: Effect of D_p on a pile section 12.5 m below the mudline: (a) ξ_y-y/D_p; (b) ξ_θ-θ 218

List of Tables

Table 3.1: Grain size characteristics of Blessington and Kilmuckridge sands 82
Table 4.1. Database of undrained cyclic tests 106
Table 4.2: Parameters of equation 4.2 fitted with Blessington G_0 data 116
Table 4.3: Database for drained cyclic tests 117
Table 4.4: Correlated parameters of Equation 4.8 130
Table 4.5: Summary of Blessington monotonic tests 131
Table 4.6: CSL parameters in the *e-p'* space for Blessington sand 136
Table 5.1: HSsmall mode parameters 142
Table 5.2: HSsmall model parameter for 30% relative density 153
Table 5.3: HSsmall model parameter for 60% relative density 153
Table 5.4: SANISAND-MS model parameter 155
Table 5.5: SANISAND04 (Dafalias and Manzari, 2004) parameter values summarised by Kowalczyk (2020) 156
Table 5.6: Values of parameter set 1 (PS1) 167
Table 6.1: Monopile dimensions 176

NOMENCLATURE

L_p	Embedment depth of pile
D_p	Diameter of pile
f_1	First natural bending mode
f	Loading frequency
K_r	Relative pile stiffness
E_p	Young's modulus of the pile
I_p	Second moment of area of pile
E_s	Young's modulus of the soil material
N	Number of cycles
p	Lateral soil reaction
y	Lateral displacement
m	Distributed moment soil reaction
Hb	Base shear
Mb	Base moment
G_0	initial or maximum shear modulus
G	Secant shear modulus
γ	Shear strain
D	Damping ratio
W_D	Dissipated energy
W_s	Elastic stored energy
D_{min}	Minimum damping ratio
γ_{tl}	Linear threshold shear strain
γ_{tv}	Volumetric threshold shear strain
p'	Mean effective stress
p_{atm}	Atmospheric pressure
P_{ref}	Reference confining pressure
C_u	Coefficient of uniformity
C_c	Coefficient of curvature
γ_{td}	Cyclic degradation threshold shear strain
γ_{tp}	Pore water pressure threshold shear strain
q	Deviatoric stress
PI	Plasticity index
d_{50}	Mean particle size

p_o'	Initial mean effective stress
τ	Shear stress
τ_f	Shear stress at failure
σ_n'	Effective normal stress on the failure plane
φ	Angle of shearing resistance
φ_p	Peak angle of shearing resistance
φ_c	Critical angle of shearing resistance
φ_r	Residual angle of shearing resistance
e	Void ratio
e_{min}	Minimum void ratio
e_{max}	Maximum void ratio
e_c	Critical void ratio
Γ	Critical void ratio at p' = 1 kPa
λ	The slope of the critical state line (CSL)
e_0	Critical void ratio at p' = 0 kPa
Ψ	State parameter
$\Delta\varepsilon_v$	Volumetric strain increment
$\Delta\varepsilon_a$	Axial strain increment
η_{cl}	Characteristic line stress ratio
φ_{cl}	Characteristic line friction angle
φ_{pl}	Phase transformation line friction angle
$\gamma_{0.7}$	Shear strain corresponding G/G_0 = 0.722
G_s	Specific gravity
U_n	Percent undercompaction factor
U_{ni}	Percent undercompaction factor of the bottom-most layer
U_{nt}	Percent undercompaction factor of the top-most layer
$\Delta\sigma_3$	Change in cell pressure
Δu	Change in pore water pressure
B	Value used to check saturation
ε_a	Axial strain
ΔL	Change in length
ε_v	Volumetric strain
ΔV	Change in volume
V	Volume of sample
ε_r	Radial strain
ν	Poisson's ratio
A_c	Corrected area of soil sample

A_0	Original area of soil sample
E_m	Young's modulus of the membrane
t_m	Thickness of the membrane
D_c	Diameter of the sample after consolidation
σ_1'	Major principal or vertical effective stress
σ_3'	Minor principal or horizontal effective stress
σ_{cell}	Cell pressure
u	Pore water pressure measured by the pore pressure transducer
p_0'	Initial mean effective stress
D_r	Relative density
e_i	Initial void ratio of sample after consolidation
V_s	Shear wave velocity
ρ	Bulk density of soil
p_{ref}	Reference pressure
φ_m	Mobilized angle of friction
G_0^{ref}	Shear modulus at reference pressure
ψ	Dilatancy angle
E_{50}^{ref}	Secant stiffness in standard drained triaxial test
E_{oed}^{ref}	Tangent stiffness for primary oedometer loading
E_{ur}^{ref}	Unloading / reloading stiffness
m	Power for stress-level dependency of stiffness
v_{ur}	Poisson's ratio for unloading-reloading
K_0	Coefficient of lateral earth pressure
K_0^{NC}	Coefficient of lateral earth pressure (Normally consolidated)
σ_{v0}'	Initial vertical effective stress
ε_q	Deviatoric strain
G_t	Tangent shear modulus
R_{inter}	Interface strength reduction factor
γ'	Effective unit weight
$M_c^b{}_{max}$	Maximum bounding stress ratio in triaxial compression
λ_c	Slope of the CSL in the compressibility plane
ξ	Critical state line constant
M_c	Stress ratio at critical state in triaxial compression
G^*	Shear modulus coefficient
n^b	Bounding parameter
n^d	Dilatancy surface parameter
h_0	Hardening parameter

c_h	Hardening parameter
A_0	Dilatancy parameter
μ_0	Memory surface parameter
ζ	Memory surface parameter
β	Memory surface parameter
M^b	Bounding stress ratio
M^d	Dilatancy stress ratio
q_{cyc}	Cyclic deviatoric stress
q_{av}	Average deviatoric stress
p_{av}'	Average mean effective stress
η_{av}	Average stress ratio
η_{cyc}	Cyclic stress ratio
t	Pile wall thickness
c'_{ref}	Effective cohesion
I	Second moment of area
m_w	Hydrodynamic added water mass
ρ_w	Density of water
ζ_f	Foundation damping ratio
δ	Logarithmic-decrement ratio
θ	Rotation
D_y	Translational hysteretic damping factor
D_θ	Rotational hysteretic damping factor
K_y	Translational secant stiffness
K_θ	Rotational secant stiffness
ω	Angular frequency of the applied load
ω_n	Angular natural frequency
ζ	Critical damping ratio
c_y	Translational damping coefficient
c_θ	Rotational damping coefficient

Chapter 1

Introduction

1.1 Background

The negative impacts of burning fossil fuels for the purpose of power generation, primarily through the emission of greenhouse gases, have caused severe disruptions in weather patterns and increased environmental pollution. These effects have led to significant human and economic losses, threatening the sustainability of future generations. As a result, several international schemes and treaties, such as the 2015 Paris Agreement, were signed in order to mitigate climate change through financial and technological cooperation and promoting the reliance on renewable energy. The European Commission has also laid down ambitious plans to increase the share of renewable energy consumption to a target level of at least 42.5% (aiming to 45%) by 2030 to reduce the net greenhouse gas emissions by 55%, and to ultimately become carbon neutral by the year of 2050. To achieve these targets, the EU is substantially relying on wind energy, which as of 2023 has a total power capacity of 220 GW, meeting around 19% of the total electricity demand, and is expected to rise steadily to 393 GW by the year of 2030 (Wind Europe, 2024). To meet the 2030 targets, the EU requires to install 33 GW a year on average. The annual trend of installed (Onshore and Offshore) wind turbines and the outlook for the period of 2024-2030 is shown in Figure 1.1.

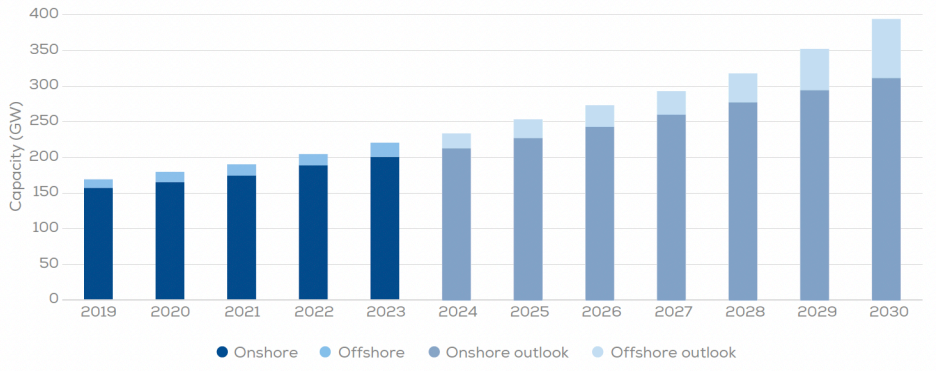


Figure 1.1: Current and projected onshore and offshore wind turbine installations in Europe (Wind Europe, 2024)

Wind turbines installed offshore provide a more effective and steady supply of energy compared to those of onshore, as wind generally blows at higher speeds and consistency at the sea, and they do not suffer from social acceptance and land use issues which constrain the installation of wind turbines in terms of size and number. These advantages make offshore wind a key renewable energy

resource to overcome climate change and global warming, and securing the electricity demand in Europe (IEA, 2019). According to the statistics from the year 2023 (Wind Europe, 2024), a record capacity of 3.8 GW of offshore wind turbines (OWTs) were installed in Europe, which made up around 21% of the total 18.3 GW wind turbine capacity. The highest share of OWTs were installed in the Netherlands (1.9 GW) followed by the UK (833 MW), France (360 MW), Denmark (344 MW), Germany (329 MW) and Norway (35 MW). Moreover, it is anticipated that the proportion of OWTs is likely to further increase in the coming years such that a third of all wind turbines will be installed offshore between the years of 2024-2030. This is reflected by the increase of Final Investment Decisions (FIDs), which reached a record of €30 billions, and the improved commitment of many EU governments on permitting volumes of new wind farms (Wind Europe, 2024). Globally, 10.8 GW of OWTs were added to the grid in 2023, making it the second highest year on record in the offshore wind history, and increasing the total capacity to 75.2 GW (GWEC, 2024). As a result, GWEC expects that an additional 410 GW will be installed by 2033. Furthermore, as the worldwide investments for OWTs are steadily growing, it is expected that by 2040 the offshore wind market will turn to a $1 trillion industry (IEA, 2019).

However, the primary limitation hindering the growth of OWTs is the substantial cost associated with their fabrication, installation, and the extensive maintenance required due to the harsh marine environment. The cost-effectiveness of OWTs has improved through creating efficient supply chains and building large size wind turbines (IEA, 2019). OWTs generally perform better than onshore wind turbines since their larger swept areas capture more wind and hence produce more power. The size evolution of OWTs is shown in Figure 1.2.

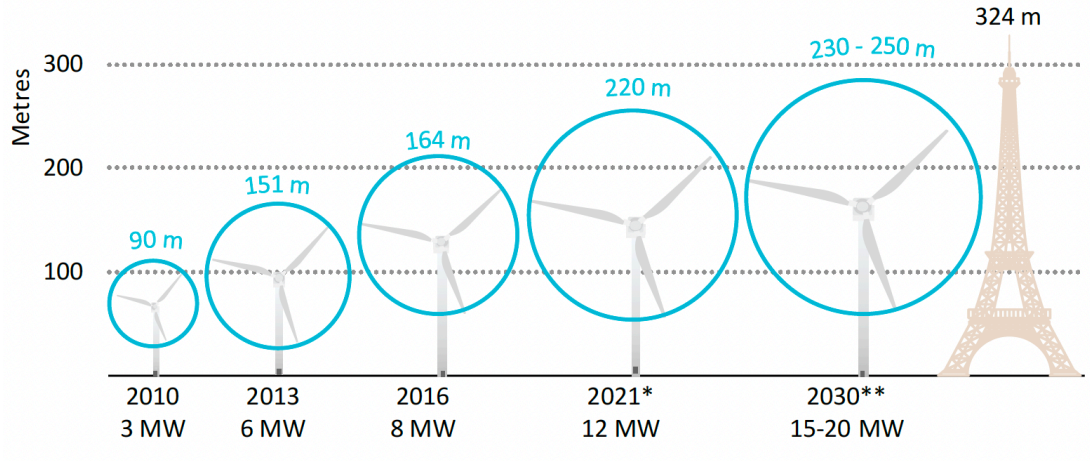


Figure 1.2: Size evolution of OWTs (IEA, 2019)

Further reductions to the cost of OWTs can be obtained through improving the technology and optimising the design of the support structure and the foundation. The foundation makes up roughly 30% of the overall OWT cost (Malekjafarian et al., 2021). As a result, understanding the mechanism of the foundation behaviour could be regarded as an integral component in improving the cost-effectiveness of OWTs such that they are competitive with onshore wind turbines. There are

multiple types of foundations that are used such as monopiles, suction caissons, jacket structures, tripods, and anchors (shown in Figure 1.3) which are selected according to the water depth and other site conditions. Monopiles, which are characterised as hollow steel cylinders, are the most preferred option in Europe with almost 80% of OWTs resting on them because of their simplicity and ease of fabrication (IEA, 2019). The diameters of monopiles are considerably larger than the diameters of conventional piles used in oil and gas industry, and thus are characterised as rigid structures with low slenderness ratios (L_p/D_p), where L_p is the embedment depth of the pile and D_p is the diameter of the pile. This difference in behaviour questions the validity of applying traditional design approaches for monopiles. Optimising the monopile design could allow cutting down the costs through saving between 10-25% of the steel tonnage and enable using monopiles for deeper water depths (Kallehave et al., 2015). It is expected that large size monopiles with diameters of about 10 m could be installed in water depths as deep as 60 m (Kallehave et al., 2015). Relying on monopiles for deeper water depths is more cost-effective than using other foundation options since this brings about the benefits of the already well-existing supply chain in steel fabrication, transportation, and installation with impact driving. Furthermore, monopiles provide great potential of feasibility in streamlining and maturing the supply chains to suit many site conditions (Kallehave et al., 2015). Current monopiles have diameters in the range 5-10 m, slenderness ratios between 2-6 (Burd et al., 2020b), and wall thickness 40-150 mm (Anandavijayan et al., 2018). This thesis is primarily focusing on monopiles due to its current and future prevalence as a foundation option for OWTs.

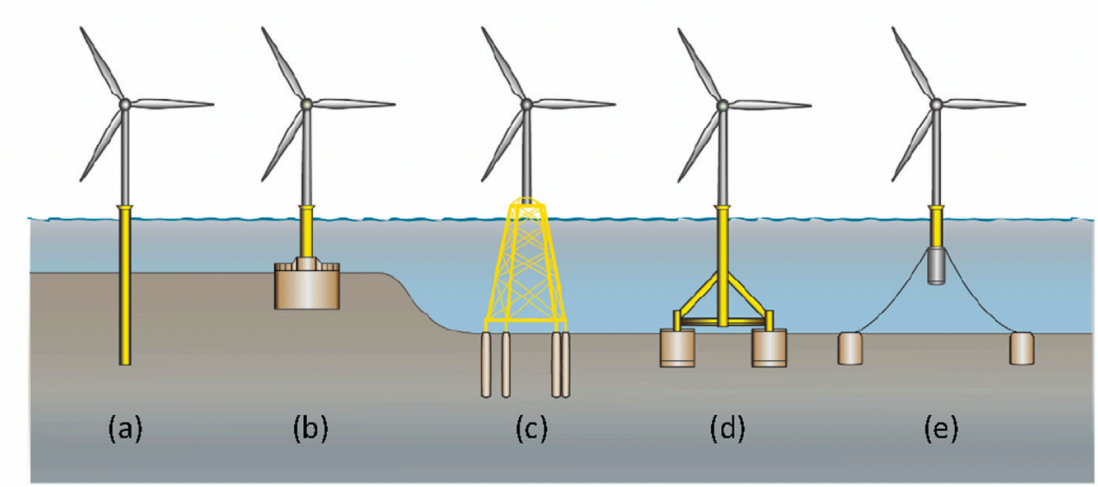


Figure 1.3: Types of foundations used is OWTs: mono-pile (a), monopod (skirted caisson) (b), jacket structure (c), tripod (d) and floating wind turbine with anchors (e) (Kaynia, 2019).

The main components of a typical OWT are shown in Figure 1.4. These include the tower; the substructure, which comprises the transition piece and the portion of the monopile above the mudline; the foundation, which is the portion of the monopile embedded in the seabed; and the rotor nacelle assembly (RNA), which consists of the nacelle, hub, and blades. The support structure refers to the entire structure supporting the RNA, including the tower, substructure, and foundation. The

transition piece is used to correct any vertical misalignment of the monopile during driving and to establish the connection between the tower and the monopile. A fixed connection is achieved by grouting the annular space between the transition piece and the monopile, while the tower is connected to the transition piece using bolted flange connections. The RNA mainly consists of the nacelle, which houses the main shaft, drivetrain, and generator and is responsible for converting rotational mechanical energy into electrical energy, and the hub, which is connected to the blades and transmits their rotation to the main shaft inside the nacelle.

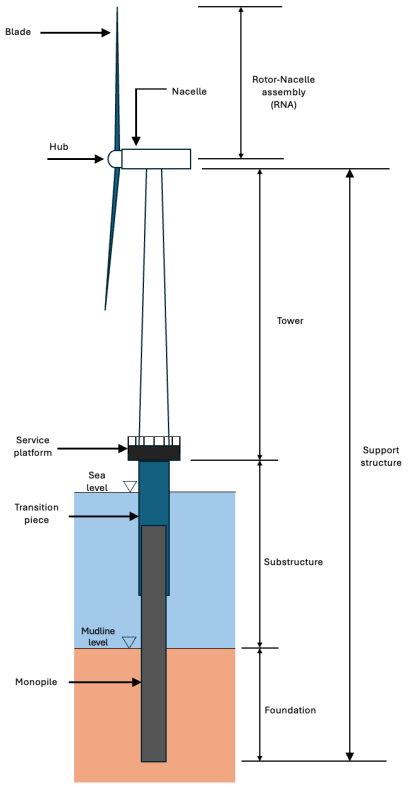


Figure 1.4: Main components of a typical OWT

OWTs are often characterised as dynamically sensitive structures that are highly susceptible to resonance and dynamic amplification when the environmental and operational loads are in close vicinity to the fundamental natural frequency of the overall system. The interaction between the monopile and the surrounding soil affect the dynamic behaviour of the OWT to a large extent. The stiffness of the foundation, which influence the natural frequencies, is governed by the geometry of the monopile and the characteristics of the supporting ground. In addition, the foundation contributes to energy dissipation through hysteretic soil damping and radiation damping. Foundation damping, which plays an important role in attenuating the vibrations and extending the fatigue lifetime of OWTs, is the least understood source of energy dissipation and it is poorly accounted for in monopile design (Abadie, 2015; Carswell et al., 2022; Germanischer Lloyd, 2005; Malekjafarian et al., 2021; Versteijlen et al., 2011). Estimating soil damping is important for slender structures whose fundamental natural frequencies are close to the loading frequency (Andersen, 2015).

1. 2 Characteristics of OWT Design Loads

The foundations of OWTs are subjected to static vertical loads as a result of the self-weight of the turbines and their support structure, along with lateral loads and bending moments due to environmental and operational loads as shown in Figure 1.5. The contribution of the vertical load is relatively small when compared to the substantial impact caused by environmental loads of wind and waves during extreme storm events. Thus, the conditions under which OWTs operate are significantly different than those of oil and gas structures and require design efforts to mainly target the resistance of the foundation to horizontal loads and bending moments at the mudline level.

The environmental loads predominantly consist of wind, waves and currents. Wind is composed of a mean velocity component and a fluctuating velocity component that is often referred to as turbulence. The distribution of turbulence with frequency is represented by a power spectral density. The most common power spectral density that is applied in practice is Kaimal spectrum. Waves are generated by wind action and typically have a frequency range between 0.05-0.50 Hz. Extreme waves, however, occur within the frequency range of 0.08-0.14 Hz (Damgaard, 2014). The kinematic of water particle movement is described with multiple wave theories such as linear Airy wave theory, and the applied wave force is often calculated with Morrison's equation which consist of a drag and an inertial component. The resultant lateral force due to wind and waves usually acts within an eccentricity ratio of 2-25 times the diameter of the monopile (Klinkvort and Hededal, 2013). The operational loads are comprised of 1P loading which is generated as a result of mass and aerodynamic imbalance at the rotor level, and (2P/3P) loading which is caused by the blade shadowing effect. (2P/3P) loading is two or three times the frequency of 1P loading depending on whether the turbine is made of two or three blades. The frequency of 1P load is not constant and varies with the revolution speed of the rotor. The analysis of OWTs is normally implemented using software packages such as HAWC or FAST to simulate the combined loading effects of aerodynamic, hydrodynamic and operational loads to calculate the resulting horizontal forces and bending moments.

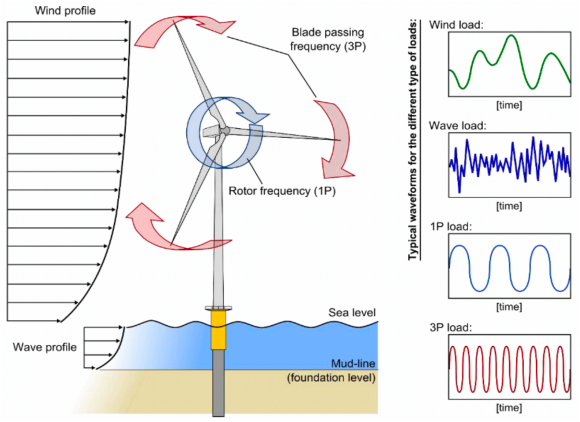


Figure 1.5: Types of loads applied to OWTs with their typical wave forms (Nikitas et al., 2016).

There are three theoretical design options in order to avoid resonance (see Figure 1.6). The first option is referred to as soft-soft design which requires the foundation to be dimensioned such that the first natural bending mode f_1 is below 1P frequency. However, such a design option is not practically feasible and will result in a very flexible structure. The second option is to design the foundation such that f_1 falls above 3P frequency, however, this design option will require large quantities of materials and hence is economically not viable. The third option is the one utilised in the offshore industry which is achieved through dimensioning the foundation and the tower such that f_1 is between the frequencies associated with 1P and 3P loading. As a result, accurate estimation of the foundation stiffness is necessary to avoid resonance and satisfy fatigue and serviceability requirements. Since modern wind turbines operate at variable rotational speeds which consequently cause the 1P and 3P frequencies to change, the OWT must designed such that its lowest eigenfrequency does not fall within operational range of 1P and 3P (see Figure 1.7).

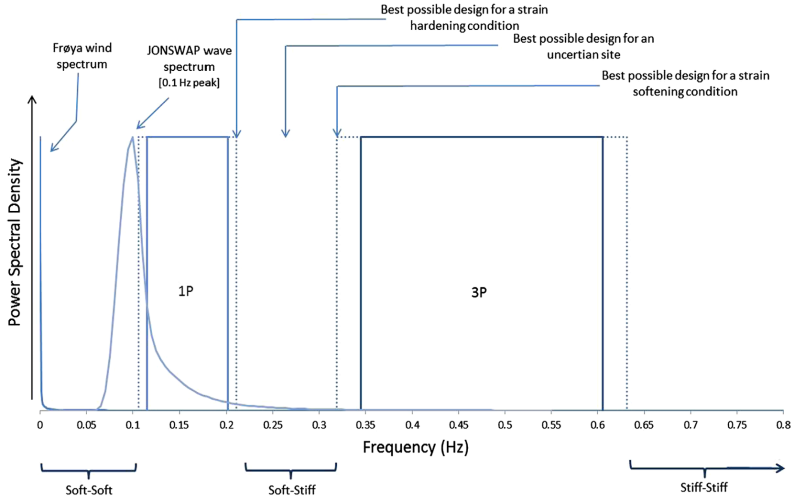


Figure 1.6: Environmental and operational loading frequency spectrum (Bhattacharya et al., 2013)

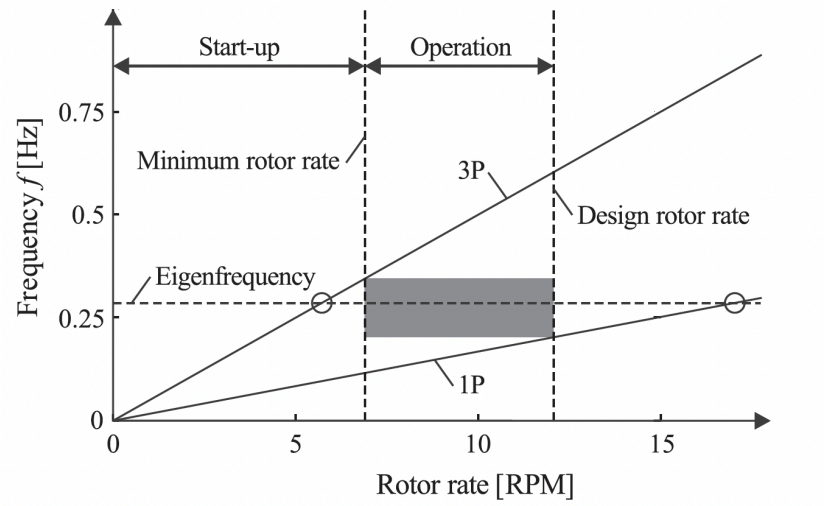


Figure 1.7: Campbell diagram (Damgaard et al., 2014)

1.3 Current Design Practice and Limitations

The design of monopiles is conducted to ensure that three main limit states are satisfied:

(i) **Ultimate Limit State (ULS):** This refers to the maximum load a monopile can endure during an extreme storm event, determined by either displacement or rotation criteria. Failure is typically assumed when the mudline displacement reaches 0.1 times the monopile diameter (Alderlieste et al., 2011; Burd et al., 2020b). Alternatively, if mudline rotation is used as the failure criterion, Beuckelaers (2017) defined the ultimate limit state as the load corresponding to a mudline rotation of 2°, whereas Leblanc et al. (2010) considered ULS to be reached at a mudline rotation of 4°.

(ii) **Serviceability Limit State (SLS):** This limit state is satisfied when the mudline rotation of the monopile is below 0.5° as set by DNV (2014) standard. The tolerance limit during installation is 0.25° leaving the maximum allowable permanents rotation to 0.25° during the design life of the OWT.

(iii) **Fatigue Limit State (FLS):** This limit state is satisfied when the natural frequency of the first mode of vibration does not coincide with the frequencies of the external loads. FLS prevents the development of large stresses during resonance which can lead to progressive failure with time.

The response of monopiles is analysed by modelling the interaction between the pile and the surrounding soil using the Winkler approach. The soil reactions along the monopile depth are represented by a series of independent spring elements, which are connected to discretized beam elements that capture the monopile behaviour. The Winkler approach in offshore pile design standards such as DNV (2014) and API (2010) is commonly known as the p-y approach where p is the lateral reaction of the soil spring and y is the lateral movement of the pile at a particular depth. The p-y approach for both sand and clay was developed based on limited field tests on relatively small-diameter flexible piles, primarily designed for structures in the oil and gas industry The current API p-y formulation for clay is based on the back analysis carried out by Matlock (1970) on field tests that were conducted in the mid 1950s. Whereas, the API p-y formulation for sand is based on the results of the field tests by Cox et al. (1974) that were conducted on piles with diameters of around 0.60 m and slenderness ratio (L_p/D_p) of about 30. The equations for sand were derived by Reese et al. (1974) and later modified by O'neill and Murchison (1984). The p-y approach employs one-dimensional (1D) finite element (FE) analyses to determine the deformations and internal forces along the pile length. The limitations of using API p-y curves for modelling the behaviour of monopiles supporting OWTs are largely acknowledged within the wind energy sector, and its applicability has been questioned by many researchers (e.g., Abadie, 2015; Achmus et al., 2009; Byrne et al., 2015b; Doherty and Gavin, 2012; Kallehave et al., 2012; Kallehave et al., 2015; LeBlanc et al., 2010; Lombardi et al., 2013; Page et al., 2016; Wichtmann et al., 2008). Mainly, the API p-y formulations fail to capture the rigid behaviour of monopiles and

were calibrated for a small number of load cycles. Furthermore, while the API p-y curves can be formulated to incorporate Masing rules, enabling the p-y curves to exhibit nonlinear hysteretic force-deformation loops, in practice, the API p-y curves are typically implemented as nonlinear elastic curves. As a result, unloading and reloading follow the same path, with no hysteretic energy dissipation.

These limitations along with ambitious goals to further reduce the cost of OWTs have brought about significant creative efforts and collaborative schemes among academics and research institutes to improve and to develop new design philosophies and methods that are capable of understanding the complex interaction between OWTs and the supporting ground. One such collaboration was the PISA (Pile Soil Analysis) project which included large scale field tests supported by laboratory soil element experiments that provided input into state-of-the-art numerical modelling software packages. The output from the research was obtaining a new rigorous design methodology that permitted the reaction curves to be based on laboratory experiments and numerical modelling. However, the PISA project mainly focused on understanding the monotonic behaviour, and thus the knowledge gaps and uncertainties related to cyclic soil behaviour and foundation damping are still far from being realised. Current research efforts are aimed towards implementing further complex soil constitutive models with parameters that are obtained from advanced laboratory dynamics tests such as triaxial, hollow cylinder and simple shear tests. The next chapter will provide the different methods that are developed to take soil-monopile interaction into account.

1.4 Research Aims and Objectives

The primary aim of this research is to investigate hysteretic foundation damping for monopile-supported OWTs using three-dimensional (3D) finite element (FE) numerical models that incorporate the nonlinear hysteretic behaviour of soil. The influence of the radiation component of foundation damping, which is frequency dependent and stems from the propagation of elastic waves away from the monopile, is insignificant for the dominant response frequencies of OWTs, which are generally below 1Hz (Malekjafarian et al., 2021). As a result, its contribution is excluded from this study. The second component of foundation damping, which is referred to as hysteretic foundation damping, is generated due to the movement of the monopile against the surrounding soil and hence causing nonlinear hysteretic behaviour in the soil domain. Hysteretic damping at the soil element level occurs due to the friction between the individual soil grains and the formation of nonlinear hysteretic stress-strain loops during cyclic loading. Thus, the global energy dissipated through hysteretic foundation damping results from the integration of the hysteretic damping contributions of all soil elements resisting the movement of the monopile (Malekjafarian et al., 2021, Zhang et al., 2021). The soil continuum supporting the monopile plays a critical role in attenuating stresses and deformations in the support structure of OWTs, thereby extending their fatigue design lifetime. Consequently, this study focuses on evaluating foundation damping through

3D FE analyses, utilizing appropriate constitutive models to simulate the nonlinear behaviour of soil, with the model parameters calibrated based on laboratory experiments. To understand foundation damping in greater detail, a series of 3D FE analyses are performed to investigate how foundation damping varies with changes in monopile dimensions and soil relative densities. To achieve the aim of this research, the following objectives are outlined:

(i) Perform cyclic and monotonic triaxial tests:

- Conduct cyclic and monotonic tests to calibrate the parameters of the constitutive models.
- Obtain a database of soil damping ratios and shear modulus reduction, and evaluate how these dynamic parameters vary with relative density, mean effective stress, drainage conditions, and the number of cycles.
- Perform cyclic on tests two types of sand to assess whether the dynamic parameters, particularly the damping ratio, differ significantly between them.
- Perform monotonic triaxial tests on Blessington sand to determine the peak friction angles at various mean effective stresses and relative densities, and to obtain the critical state parameters.

(ii) Calibration of constitutive models:

- Calibrate the parameters of hardening soil with small strain stiffness (HSsmall) and Simple ANIsotropic SAND (SANISAND-MS) constitutive models using the triaxial test results.
- Discuss the procedure for calibrating each parameter.
- Identify the inherent limitations of both models through comparing triaxial simulation results with experimental results.

(iii) Perform extensive 3D FE analyses

- Build 3D FE models using the Plaxis 3D software for different monopile dimensions and soil relative densities.
- Run dynamic analyses to obtain the foundation damping ratios and investigate the effects of monopile embedment depth, diameter, slenderness ratio, and relative density.
- Run cyclic (pseudo-dynamic) analyses to obtain the foundation damping factors at the mudline and the distributed foundation damping factors along the monopile depth.

1.5 Thesis outline

This thesis consists of seven chapters. The structure of the thesis is outlined below:

- **Chapter 1 (Introduction)** provides an overview of the offshore wind industry, highlighting its significance and projected growth in the coming years. It also discusses the benefits of optimising the design of monopile foundations to reduce the overall cost of OWTs. Additionally, the chapter introduces the loads and limit states that must be satisfied in the design process. Finally, it outlines the aims and key objectives of this study.

- **Chapter 2 (Literature Review)** gives an overview of the global behaviour of monopiles and the behaviour of soil observed in laboratory tests. This chapter provides details regarding the different cyclic phenomena exhibited by monopiles and reviews various modelling strategies for considering soil-monopile interaction. Furthermore, it introduces the key findings derived from field monitoring studies in terms of the back-calculated foundation damping ratio values. Finally, the chapter discusses the cyclic and monotonic behaviour of soil and introduces the different theories of plasticity used to simulate the behaviour of soil in 3D FE analyses.
- **Chapter 3 (Methodology)** details the components of the cyclic triaxial apparatus and outlines the procedure for reconstituting the samples and conducting the experiments.
- **Chapter 4 (Laboratory results)** initially presents the cyclic test results and aims to evaluate the variation of soil damping ratio and shear modulus reduction under the effects of different factors. Furthermore, the chapter proposes empirical functions for damping ratio and normalised shear modulus reduction, and evaluates the parameters of the empirical functions through fitting them to the laboratory results using nonlinear regression analysis. It also presents the monotonic test results of Blessington sand, focusing on determining the peak friction angles and critical state parameters.
- **Chapter 5 (Constitutive model calibration)** discusses the procedure for calibrating the parameters of the HSsmall and SANISAND-MS models and compares triaxial simulation results with those derived from the experiments. Additionally, the chapter addresses some of the inherent limitations of the models.
- **Chapter 6 (3D Finite element modelling)** discusses the procedure for constructing the 3D FE models and presents the results of free-decay simulations and cyclic (pseudo-dynamic) simulations. The free-decay analyses provide the foundation damping ratio, while the cyclic (pseudo-dynamic) simulations yield the foundation damping factors at the mudline and their distribution along the monopile depth. Comparisons are made for monopiles of different dimensions and installed in soils with varying relative densities to investigate how foundation damping varies with monopile dimensions and ground conditions.
- **Chapter 7 (Conclusions)** gives a summary and conclusions of this research, with the limitations and suggestions for future work.

Chapter 2

Literature Review

2.1 Introduction

Since this research focuses on characterising soil behaviour at the element level and integrating its response into the global behaviour of the monopile, the literature review is broadly divided into two parts. The first part addresses the cyclic and monotonic behaviour of soil, along with relevant constitutive modelling approaches, while the second examines key aspects of monopile behaviour, reviews foundation damping studies, and identifies the existing research gap. The discussion of soil behaviour begins with cyclic loading, highlighting the hysteretic stress-strain response, key dynamic parameters such as shear modulus and damping ratio, and the factors that influence them. Monotonic behaviour is then explored in terms of shear strength evolution with strain, as well as the characteristic states that define strength and the volumetric response of soil. Given that this research involves calibrating constitutive models to capture element-level soil behaviour in 3D FE analyses, a brief overview of relevant plasticity theory families is included. However, the main focus is on two models that are used in the numerical simulations. Namely, the hardening soil model with small strain stiffness (HSsmall), and the bounding surface SANISAND-MS model. The critical state framework is discussed in detail when discussing the monotonic behaviour of soil since the critical state framework forms the backbone of the SANISAND-MS model. The key aspects of monopile behaviour and current analysis methods are examined to provide the reader with an understanding of monopile foundations and soil-structure interaction. The chapter concludes by reviewing relevant studies on the main focus of this research, namely foundation damping, and by identifying the research gap addressed in this study.

2.2 Cyclic soil behaviour

2.2.1 Dependency of soil deformation on shear strain

The behaviour of soil heavily depends on the magnitude of the imposed shear strains. Soil behaviour can be elastic, elasto-plastic, or at failure according to the shear strain ranges illustrated in Figure 2.1. For very small shear strains, for example below 10^{-5}, soil behaviour can be described as linear elastic, and deformations are recoverable upon stress removal. In the intermediate shear strain range, between 10^{-4} and 10^{-2}, the soil response becomes elasto-plastic. Within this range, stiffness is non-linear, and stress reversals produce irrecoverable deformations. Large shear strains that are

greater than 10^{-2}, generate deformations that are associated with failure and bearing capacity problems. For each strain range, different phenomena are observed, and various in-situ and laboratory test methods are used to study the governing parameters (shown in Figure 2.1).

For shear strain levels in the intermediate range, approximately below 10^{-3}, the stress-strain response is elasto-plastic and forms non-linear hysteresis loops. The stiffness of soil tends to decrease with increasing shear strain, and rate-independent energy dissipation occurs due to the hysteretic nature of soils (Ishihara, 1996). The energy dissipation of soils is represented with the damping ratio parameter which is introduced in the following section. The intermediate strain range below 10^{-3} is large enough to produce non-linear hysteretic response but is small enough such that the stiffness and hysteretic damping remain constant with continuous load cycles. This non-linear cycle-independent behaviour is referred to as *non-degraded hysteresis type* (Ishihara, 1996). The stiffness and hysteretic damping parameters calculated from nearly closed hysteresis loops, are the key parameters for describing the soil behaviour for shear strains in the medium range.

As the cyclic shear strains exceed approximately 10^{-3}, the dilatant tendency of granular materials becomes prominent, manifesting as either contraction or dilation during drained shearing and pore water pressure generation during undrained shearing. The tendency of soil to dilate does not appear for very small strain levels. The dilatancy effect brings about progressive changes in the shape of the hysteresis loops, leading to variations in the stiffness and hysteretic damping parameters over the duration of the cyclic event. This cyclic-dependent behaviour is termed *degraded hysteresis type* (Ishihara, 1996). The degradation or growth of stiffness during cyclic loading can be mainly attributed to the dilative tendency of soils.

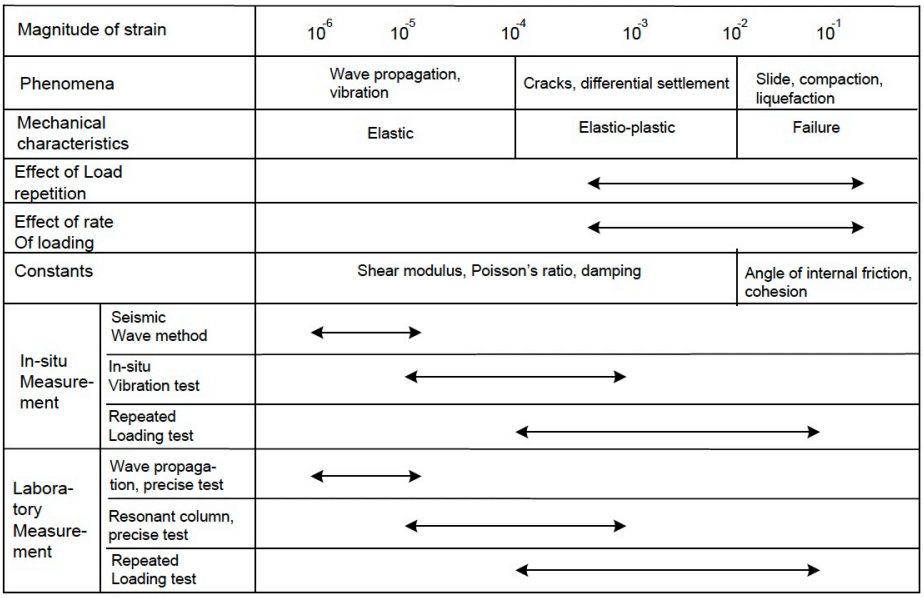


Figure 2.1: Variation of soil properties with different strain levels (Ishihara, 1996)

2.2.2 Stress-strain hysteresis loops

The cyclic non-linear behaviour of soil is complex and depends on both inherent parameters related to the soil itself and external parameters associated with the nature of the imposed cyclic loads. However, the stress-strain behaviour, at least for small and medium strains, exhibits closed hysteresis loops which define the shear modulus and damping ratio parameters of soil (shown in Figure 2.2). The idealised hysteretic stress-strain loop in Figure 2.2 is shown in terms of shear stress (τ) and shear strain (γ). When the soil is subjected to very small shear strains, the response is linear, and the corresponding tangent shear modulus is referred to as the *initial* or *maximum shear modulus* (G_0 or G_{max}). However, as the strain level increases, the stiffness reduces due to the breakage of the initial inter-particle contacts. This stress-strain response associated with a monotonic decrease of stiffness with strain is termed the *skeleton* or *backbone curve* as depicted in Figure 2.2. The earliest attempt to characterise the cyclic behaviour of materials was through the rules suggested by Masing (1926). Based on Masing rules, the behaviour of a soil element during a complete load cycle shows unloading and reloading curves in the hysteresis loop that conform to the same shape as the backbone curve but are stretched by a factor of two. The key strength of adopting Masing rules, is that the dynamic behaviour of soil can be yielded directly from the backbone curve. The original two rules introduced by Masing (1926) are as follows:

(i) The tangent shear modulus after load reversal is equal to G_0 of the initial backbone curve.
(ii) The shape of the unloading and reloading curves is identical to initial backbone curve, scaled by a factor of two.

For irregular cyclic loads, Masing rules are extended by two additional rules:

(iii) The unloading and reloading curves follow the initial backbone curve when the pervious maximum shear stress is exceeded.
(iv) If an unloading or a reloading curve intersects a curve from a previous cycle, it should follow the path of that previous curve.

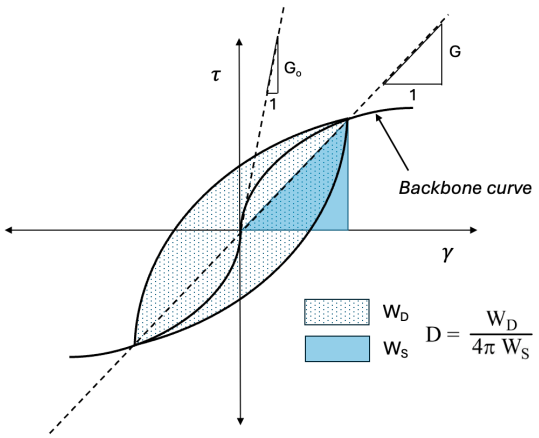


Figure 2.2: Stress-strain hysteresis loop

The shear stiffness of soil can be represented with either the tangent or the secant shear modulus. However, for applications related to soil dynamics, the stiffness reduction is mostly represented by the secant shear modulus, denoted simply as G in Figure 2.2, and is equal to the slope of the line that connects the points of maximum and minimum stresses for a full load cycle. The secant shear modulus G is normalised with maximum shear modulus G_0 to illustrate the reduction of shear stiffness with the cyclic shear strain (G/G_0-γ_c). The damping ratio (D) of soil for a particular cyclic shear strain is calculated according to the following equation:

$$D = \frac{W_D}{4\pi W_S} \tag{2.1}$$

where W_D is the amount of the dissipated energy per cycle and is equal to the area of the enclosed hysteretic stress-strain loop. W_s is the elastic stored energy and is equal to the area of the triangle shown in Figure 2.2. The dissipation of energy within the soil mass can be attributed mainly to the friction between the soil particles, the non-linear behaviour of soil, and strain rate (viscous) effects (Zhang et al., 2005). The relationship between damping ratio D and the cyclic shear strain (γ_c) is denoted as D-γ_c. The evolution of damping ratio (D) and normalised shear modulus (G/G_0) with γ_c is presented in Figure 2.3. As γ_c increases, G/G_0 decreases due to the reduction of the secant shear modulus (G), while the damping ratio (D) increases as the area of the stress-strain hysteresis loop expands, indicating greater dissipation of plastic energy.

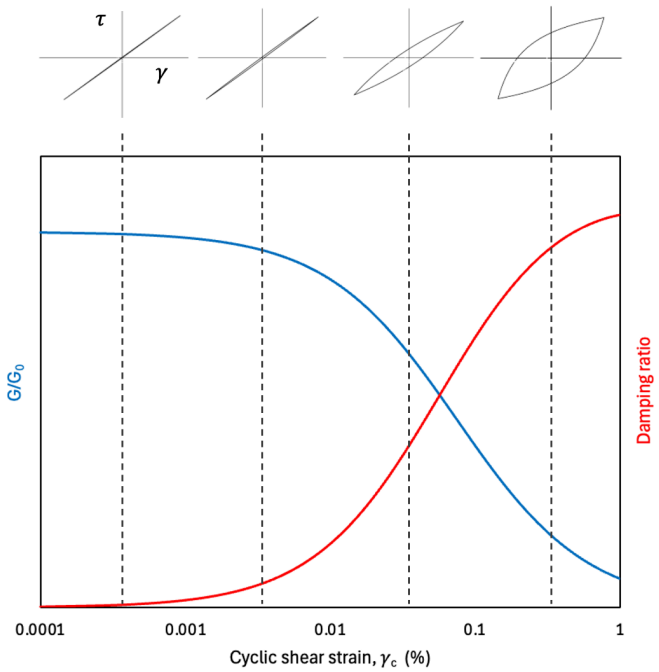


Figure 2.3: Shear modulus and damping ratio with shear strain increase

It is noteworthy to highlight that from a mathematical point of view, the soil mass does not dissipate any energy for very small cyclic shear strains, since the behaviour is linear and the area enclosed by the stress-strain response is zero. However, experimental studies have shown that even within the linear elastic range, a small amount of constant damping occurs due to inter-particle friction and

viscosity (Darendeli, 2003; Zhang et al., 2005; Ciancimino, 2021). The damping ratio in the linear elastic strain region is denoted as D_{min}. Damping due to viscosity and friction between grains is significant only at very small strains. At strains beyond the elastic range, damping becomes predominantly hysteretic, governed by the progressively developing plastic shear strains.

According to Masing rules, the damping ratio is directly related to the normalised shear modulus reduction G/G_0. Using the Hardin and Drnevich (1972b) hyperbolic expression, Ishihara (1996) applied Masing rules to derive an analytical equation between the damping ratio and G/G_0. To evaluate whether Masing rules provide a reasonable relationship between damping and G/G_0, Ishihara compared the analytical expression against the range of damping ratios obtained from previously published laboratory tests (shown in Figure 2.4). The comparison shows that while the calculated damping ratio is closely within the range of test data during small shear strains (i.e., when G/G_0 is large), it deviates from the experimental range when G/G_0 becomes low due to large cyclic shear strains. As a result, it can be concluded that modelling the cyclic response with Masing rules may not reflect the actual shape of hysteretic stress-strain loops and can lead to overestimation of soil damping. This is especially true when the effect of dilation becomes prominent, causing significant volumetric and mean effective stress changes, such that the hysteretic stress-strain response bears little resemblance to the initial backbone curve.

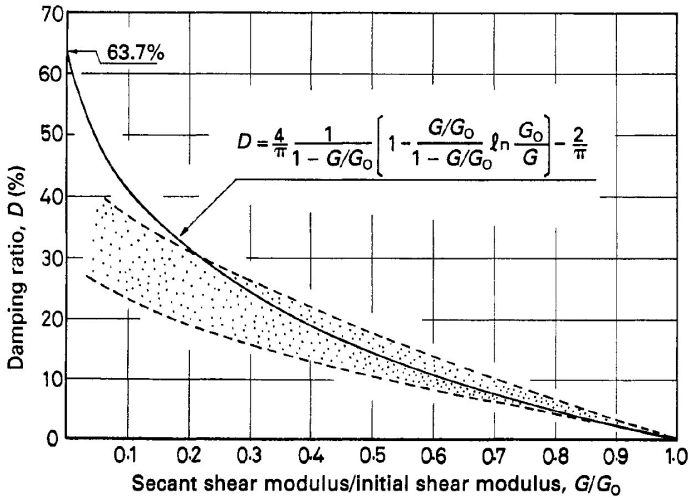


Figure 2.4: Relation between damping ratio and G/G_0 (Ishihara, 1996)

2.2.3 Cyclic thresholds

Various attempts have been made in the literature to define accurate criteria for classifying cyclic soil behaviour. The concept of cyclic threshold shear strains was initially introduced by Dobry et al., (1982) to define the domains of different soil behaviour. Vucetic (1994) defined two cyclic threshold shear strains that divides the G/G_0-γ_c and D-γ_c curves into three main domains (i.e., very small strains, small strains, and medium to large strains) as shown in Figure 2.5. The threshold that defines the transition from very small to small strains is referred to as the linear threshold shear strain (γ_{tl}), which defines the upper bound of linear elastic soil behaviour. The value of γ_{tl} is

determined as the cyclic shear strain corresponding to G/G_0 = 0.99. The transition between small strains and medium to large strains is represented with the volumetric threshold shear strain (γ_{tv}). Between γ_{tl} and γ_{tv}, the hysteretic stress-strain response is nonlinear but shows no permanent microstructural changes. However, cyclic shear strains exceeding γ_{tv} lead to gradual changes in soil microstructure. These changes are reflected by the development of residual cyclic pore water pressures under undrained conditions and permanent volumetric changes in drained conditions. The value of the volumetric threshold strain γ_{tv} is generally one order of magnitude higher than that of the elastic threshold strains γ_{tl} (Mitchell and Soga, 2005). At γ_{tv} strain level, the ratio G/G_0 reduces to approximately 60%- 85% (Ishihara, 1996). The range of cyclic threshold shear strains for granular materials increase with the mean effective stress. Oztoprak and Bolton, (2013) derived a linear empirical equation (Equation 2.2) for describing the increase of γ_{tl} as a function of the mean effective stress (for mean effective stresses between 70 kPa and 600 kPa).

$$\gamma_{tl}(\%) = (8\ x\ 10^{-5})\left(\frac{p'}{p_{atm}}\right) + 6\ x\ 10^{-4} \tag{2.2}$$

here p' is the mean effective stress and p_{atm} is the atmospheric pressure. In addition to p', Menq, (2003) found that particle size distribution influences the cyclic threshold limits, with the γ_{tl} reducing as the coefficient of uniformity (C_u) increases. Further cyclic threshold shear strains have been introduced in the literature to provide a more detailed description of soil behaviour. For example, Mortezaie and Vucetic (2016) defined the cyclic degradation threshold shear strain (γ_{td}) as the amplitude below which no stiffness degradation occurs, and the pore water pressure threshold shear strain (γ_{tp}) as the amplitude below which no residual excess pore water pressure is generated.

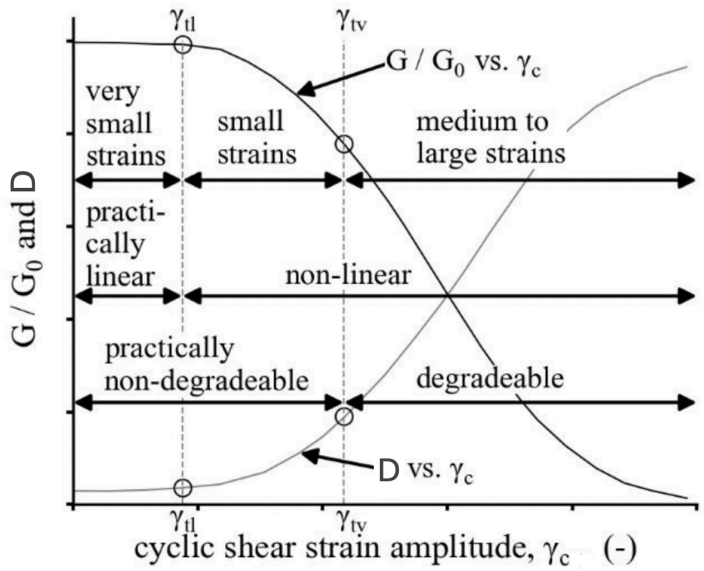


Figure 2.5: G/G_0 and damping ratio curves with different zones of cyclic shear strain amplitude (modified after Vucetic, 1994)

Alternatively, the different phases of soil behaviour can be defined by yield surfaces in the mean effective stress-deviatoric stress space (p'-q). Jardine (1992) suggested that the transition from

linear elastic to fully plastic soil behaviour can be described using three yield surfaces, denoted as Y_1, Y_2, and Y_3 (as shown in Figure 2.6). Within Zone 1, the behaviour is linear elastic, as the soil particles do not slide relative to each other, and the shear stiffness is at its maximum ($G = G_0$). The boundary of the linear elastic behaviour is represented with the Y_1 yield surface. The elastic threshold shear strain, γ_{tl}, is the strain limit corresponding to Y_1. Once the stresses exceed Y1 but remain within Zone 2, the response is no longer linear, and the stiffness begins to decrease while the damping ratio increases. The behaviour in Zone 2 is hysteretic, but the stress-strain loops tend to close as a result of cyclic loading without developing residual pore water pressures or permanent plastic strains. The shear strain corresponding to the outer boundary of the nonlinear elastic Zone 2 (Y_2 surface) is the volumetric threshold strain γ_{tv}. Once the stress path exceeds Y_2 (i.e., the shear strain exceeds γ_{tv}) and enters Zone 3, the behaviour becomes inelastic, characterized by significant stiffness degradation, increased damping, and residual pore water pressure build-up. Classifying different soil behaviours in the *p'-q* stress space as shown in Figure 2.6, is particularly useful for developing constitutive soil models.

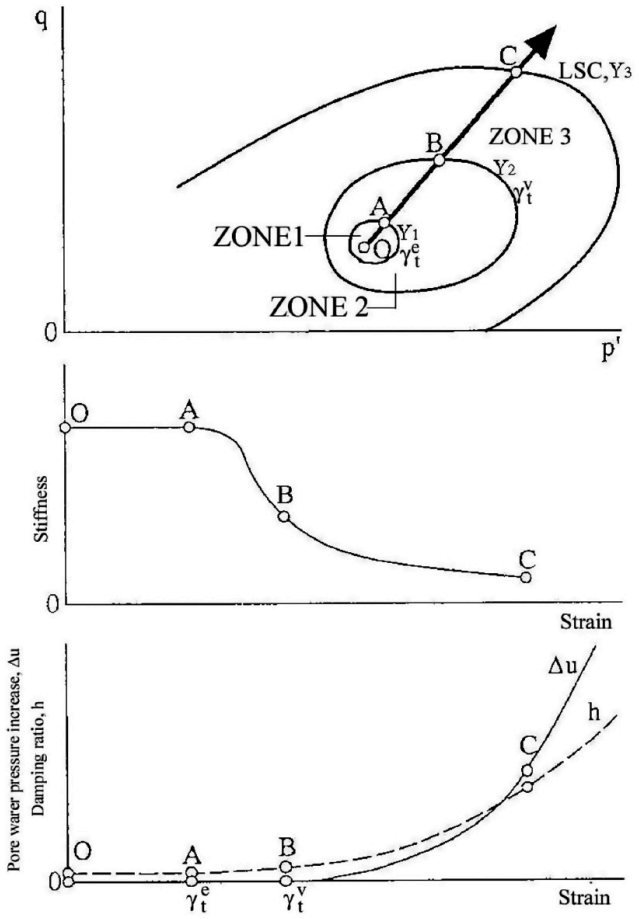


Figure 2.6: Three zones of soil behaviour characterisation (Kallioglou et al., 2008)

2.2.4 Factors affecting G/G_0 and damping ratio curves

The dynamic behaviour of soil is governed by various parameters, which were extensively investigated in many research studies (e.g., Seed and Idriss, 1970; Hardin and Drnevich, 1972a;

Kokusho, 1980; Vucetic and Dobry, 1991; Ishibashi and Zhang, 1993; Rollins et al., 1998; Darendeli, 2001; Menq, 2003; Wichtmann and Triantafyllidis, 2013). This section discusses the effects of the following factors:

(i) Mean effective stress (*p'*)
(ii) Plasticity Index (*PI*)
(iii) Void ratio
(iv) Loading frequency (*f*)
(v) Number of cycles (*N*)
(vi) Over-consolidation ratio (OCR)
(vii) Grain size distribution

The main parameters that affect G/G_0 and damping ratio curves are the mean effective stress (*p'*) and plasticity index (*PI*). For granular soils, grain characteristics in terms of the mean particle size (d_{50}) and coefficient of uniformity (C_u) are of significant importance. Other less important parameters include the degree of saturation and sample preparation method.

2.2.4.1 Mean effective stress (*p'*)

The stiffness and damping characteristics of coarse grained soils, such as sands, are heavily influenced by the mean effective stress (*p'*). Key studies examining the dynamic behaviour of coarse grained materials (e.g., Kokusho, 1980; Darendeli, 2001; Menq, 2003; Wichtmann and Triantafyllidis, 2013) observed that for the same cyclic shear strain level, G/G_0 increases and the damping ratio decreases as higher *p'* values are applied. The effect of *p'* is significant for soils with low plasticity index *PI* values, but the influence of *p'* becomes lower for soils with high *PI* (Lanzo et al., 1997).

2.2.4.2 Plasticity index (*PI*)

Soils with higher plasticity tend to exhibit greater G/G_0 values compared to soils with a lower plasticity index (*PI*) at the same cyclic shear strain level. The effect of *PI* on soil damping ratio is slightly more complex. For small cyclic shear strains in the elastic range, D_{min} increases as *PI* becomes higher, however, for larger cyclic shear strains in the medium and large strain range, damping ratios decrease with increasing *PI* (Stokoe et al., 1995, Vucetic et al., 1998). Vucetic and Dobry (1991) provided representative G/G_0 and damping ratio curves for different values of *PI*.

2.2.4.3 Void ratio

The void ratio or relative density affects the shear stiffness of soil. However, the normalised shear modulus reduction G/G_0 and damping ratio curves are nearly independent of the void ratio (Kokusho, 1980; Wichtmann and Triantafyllidis, 2013). Darendeli (2001) classified the effect of void ratio on the variation of G/G_0-γ_c and D-γ_c as a secondary or a less important parameter.

2.2.4.4 Loading frequency (*f*)

The effect of *f* on G/G_0 and damping ratio curves is inconsistent and varies depending on the soil type. The stress-strain rate dependency of soil has led to discrepancies in the literature regarding the effect of *f* on the dynamic behaviour of soil. High plasticity cohesive soils typically exhibit greater strain rate sensitivity compared to coarse-grained, cohesionless soils. From resonant column and torsional shear tests, Darendeli (2001) found that *f* marginally affects G/G_0-γ_c, while the damping ratio tends to increase as *f* exceeds 1 Hz. As *f* increases, the D-γ_c curves shift higher due to the increase of D_{min}, which is viscous in nature and is dependent of the applied *f*. The effect of *f* is also dependent on the moisture content. Based on cyclic torsional shear tests, Menq (2003) found that damping increases with *f* when the soil is wet and is almost independent of *f* when the soil is dry. Similarly, Lo Presti et al. (1997) also found that *f* has no influence on the shear stiffness and damping ratio of dry sands. Wichtmann (2005) examined the effect of frequency on the cyclic behaviour of fully saturated sand through drained cyclic triaxial tests and found that for frequencies between 0.05 Hz and 2.0 Hz, the cyclic behaviour of the soil is not governed by the applied frequency. Given that the frequency of the stresses subjected to the soil as result of the dynamic response of OWTs due environmental loads of wind and waves are generally lower than 1 Hz, the effect of frequency on the soil behaviour can be ignored.

2.2.4.5 Number of cycles (*N*)

The number of load cycles (*N*) can affect both the damping ratio and shear modulus degradation of soil, primarily due to alterations in soil fabric and the progressive accumulation of excess pore water pressure under continued cyclic loading. Moreover, the influence of *N* is dependent on the amplitude of the applied cyclic shear strains. For cyclic shear strains below γ_{tv}, no significant changes occur in the soil microstructure, and the shape of the hysteretic stress-strain loops remains unchanged. Consequently, the stiffness and damping parameters do not vary with *N*. However, as the cyclic shear strain exceeds γ_{tv}, *N* could play an important role in influencing the cyclic behaviour. Darendeli (2001) investigated the effect of *N* on damping ratio and shear modulus reduction for cohesive soil samples using a combined resonant column and torsional shear apparatus. Darendeli found that for the same cyclic shear strain, the G/G_0 reduced as *N* increased. However, Darendeli also noted that the variation in G/G_0 with *N* is soil-dependent, and for intact stiff cohesive soils, the influence of *N* on G/G_0 was negligible. In terms of damping ratio, Darendeli (2001) found that with increasing *N*, the damping ratio of soil decreased, with the majority of the reduction occurring in the first 10 cycles. Furthermore, Darendeli noted that *N* has a greater influence on the damping ratio than on the G/G_0. This finding is consistent with the observations of Lo Presti et al. (1997), who found that G/G_0 showed no variations with *N* after 10 cycles, while the effect of *N* on the damping ratio (*D*) continued even after hundreds of cycles. Lo Presti et al. (1997) also compared the effect of *N* on sands and clays, and found that variations in damping ratio and shear modulus with increasing cycles are more pronounced in sandy soils than in clays.

Blaker and Andersen (2019) investigated the undrained dynamic behaviour of very dense silica sand under a large number of cycles using cyclic simple shear and triaxial tests. They observed that the damping ratio, at the same cyclic shear strain, decreases significantly with increasing *N*. The authors provided cyclic contour diagrams of damping ratio for *N* values of 1, 10, and 25 as shown in Figure 2.7. Based on the damping ratio contour diagrams presented in Figure 2.7, Blaker and Andersen (2019) stated that damping ratio curves proposed in the literature (e.g., Seed and Idriss, 1970; Darendeli, 2001) tend to overestimate the damping ratio with *N*, which could have significant implications for the fatigue analysis of offshore structures.

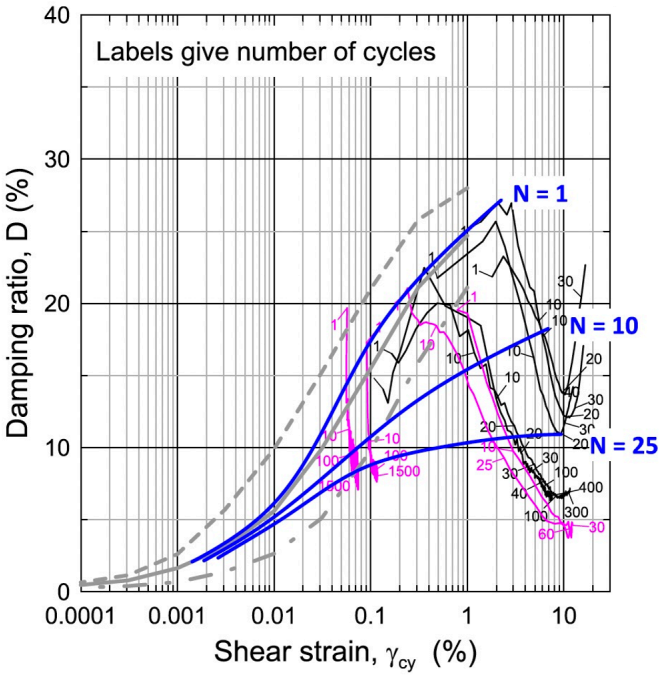


Figure 2.7: damping ratio curves of very dense silica sand (Blaker and Andersen, 2019)

Since soil fabric evolves under cyclic loading, potentially leading to variations in the stress-strain loop shapes, Rascol (2009) introduced various concepts of qualitative cyclic soil behaviour, summarised in Figure 2.8 and defined as follows:

(i) Adaptation: The cyclic soil behaviour transitions to a nearly linear elastic stress-strain response after a few load cycles, with nonlinear hysteretic behaviour effectively diminishing. However, in practice, soil behaviour rarely becomes fully linear; even under very small cyclic loads, it continues to exhibit nonlinear hysteretic stress-strain loops, though the loop sizes may become extremely small. Another term coined to describe adaptation in the literature is elastic shakedown.

(ii) Accommodation: The cyclic soil behaviour shows plastic strain accumulation before the response stabilises and forms completely closed hysteretic stress strain loops. After further cycling, the shape and the size of loops remain unchanged. Accommodation is also referred to as plastic shakedown in the literature.

(iii) Ratcheting: This qualitative soil behaviour concept describes the case in which the soil continuously accumulating plastic strains. Failure does not necessarily occur but the structure could exceed its serviceability limits.

(iv) Softening: During cyclic loading, the secant stiffness of the soil may soften or degrade with continued cycling. This behaviour typically occurs under undrained loading conditions, where excess pore water pressure progressively accumulates.

(v) Hardening: This behaviour is usually associated with cyclic loading under drained conditions where the soil arrives at a denser state and thereby exhibit a higher secant stiffness.

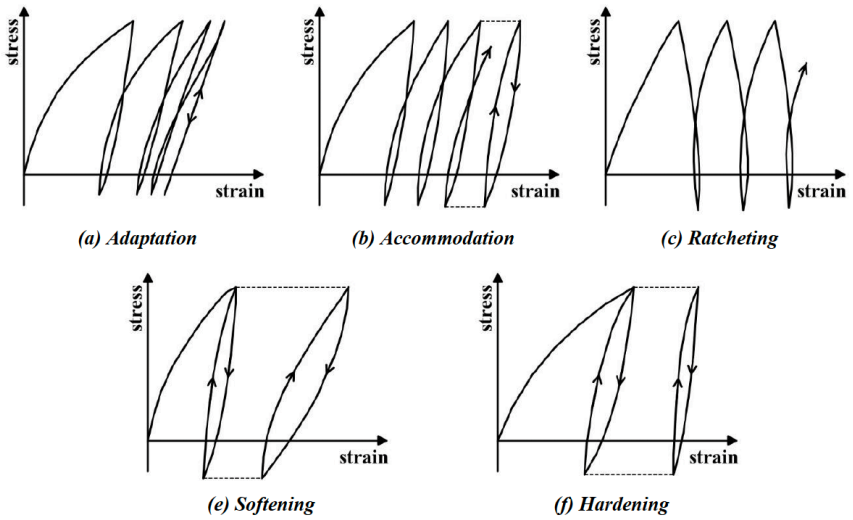


Figure 2.8: Summary of qualitative descriptions of soil behaviour under cyclic loading (Rascol, 2009)

2.2.4.6 Overconsolidation ratio (OCR)

The effect of OCR on the damping ratio and shear modulus mainly depends on the soil type, with a greater influence on the dynamic behaviour of clay soils compared to sandy soils. Darendeli (2001) investigated the effect of OCR by comparing the dynamic behaviour of a cohesive soil sample tested under OCR values of 1 and 4. Darendeli found that while the shear modulus of the soil increases and D_{min} decreases with increasing OCR, the G/G_0-γ_c and D-γ_c curves are only slightly influenced by OCR, with these curves overlapping for OCR values of 1 and 4, as shown in Figure 2.9. Harding and Drnevich (1972a) investigated the influence of various parameters based on previously published data. They categorised the parameters affecting dynamic soil response into three groups: *very important, less important,* and *relatively unimportant*. The authors classified the effect of the OCR as *relatively unimportant* for G/G_0 and *less important* for D. Furthermore, Abdellaziz et al. (2023) studied the effect of OCR on the damping ratio curves of sensitive eastern Canadian clays. Soil samples were subjected to approximately the same initial mean effective stress (p_0') and tested under various OCR values. The authors concluded that their observations were consistent with those of Harding and Drnevich (1972a), as the damping ratio curves fell within a narrow band and did not show notable scatter with variations in OCR.

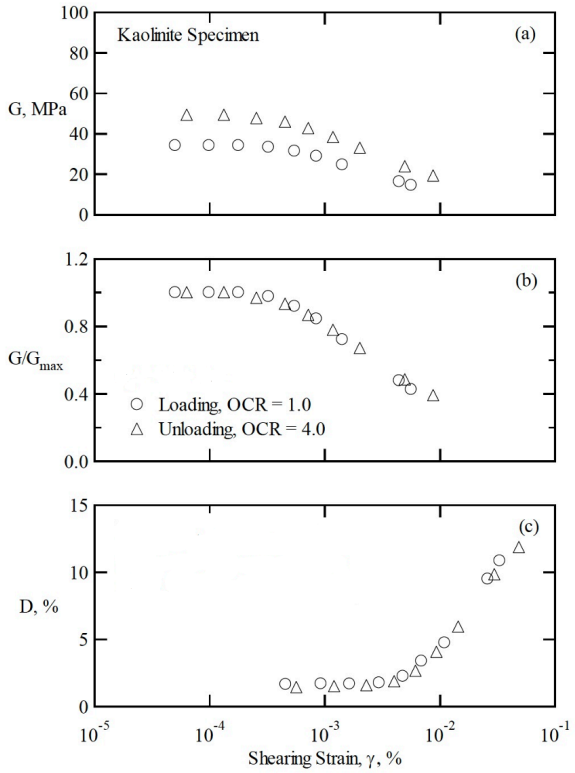


Figure 2.9: The effect of OCR on the variation of (a) shear modulus, (b) normalised shear modulus, and (c) material damping ratio with shearing strain amplitude (modified after Darendeli, 2001)

2.2.4.7 Grain size distribution

The effect of grain size distribution (or particle size distribution) is discussed in terms of mean particle size (d_{50}) and uniformity coefficient (C_u). Menq (2003) conducted resonant column tests on various gravelly and sandy soils to examine the influence of grain size characteristics (d_{50} and C_u) on G/G_0-γ_c and D-γ_c curves. The resonant column tests revealed that soil nonlinearity is strongly influenced by C_u, with the G/G_0 decreasing and damping ratio increasing at a given cyclic shear strain as C_u becomes higher. In contrast, while D_{min} decreases and G_0 increases with an increase in d_{50}, the normalised G/G_0-γ_c and D-γ_c curves show little dependence on d_{50}. Further studies were carried out to examine the effects of grain size distribution, such as Wichtmann and Triantafyllidis (2013), who conducted approximately 280 resonant column tests on 27 clean quartz sand samples with specially mixed grain size distribution curves. The resonant column test results confirmed the findings of Menq (2003) regarding the negligible effect of d_{50} on the G/G_0-γ_c and D-γ_c curves. Furthermore, Wichtmann and Triantafyllidis (2013) found that, at a given cyclic shear strain, the ratio G/G_0 decreases with increasing C_u , which is consistent with the findings of Menq (2003). However, while Menq (2003) observed that damping increases with C_u, Wichtmann and Triantafyllidis (2013) reported that the influence of C_u on D-γ_c curves is insignificant.

2.3 Monotonic behaviour of soil

The monotonic behaviour of soil is characterised in terms of the critical state framework, which describes the relation between shear strength and the volume of the soil as it is sheared to failure.

The behaviour of the soil varies according to the applied effective stresses and its initial state of compactness. However, it is important to highlight that, although the critical state framework is formulated in terms of effective stresses and void ratio (i.e., volume), soil behaviour is far more complex. For example, in granular soils, two specimens of the same soil, reconstituted to identical void ratios and subjected to the same effective stresses, may behave differently due to variations in the arrangement of soil grains (also defined as fabric). The soil fabric depends on the method used to prepare the specimens. Furthermore, for fine-grained cohesive soils, the stress-strain response is highly dependent on the strain rate, which is generally not captured within the critical state framework. However, the main aim of this section is to provide a brief description of the shear strength and volumetric behaviour of soil in relation to effective stresses and void ratio, based on the critical state theory, as it forms the basis of numerous recent advanced constitutive models. Additionally, concepts associated with the critical state, such as steady state, state parameter, phase transformation, and characteristic lines, are also described due to their significance in advanced soil constitutive modelling.

2.3.1 Shear strength

Since soil materials are generally particulate in nature, soil strength is often described in terms of shear stress (τ), which arises from the frictional resistance between soil particles during sliding. The shear strength of soil is most commonly described using the Mohr-Coulomb failure criterion, which states:

$$\tau_f = c' + \sigma_n' \tan(\varphi) \tag{2.3}$$

where τ_f is the shear stress at failure, c' is a cohesion intercept, σ_n' is the effective normal stress on the failure plane, and φ is the angle of shearing resistance. For uncemented soil materials that are purely frictional, c' is equal to zero, and the shear strength is only a function of σ_n' and φ. As shearing continues at a constant σ_n', the shear strength and the corresponding φ vary. Figure 2.10a illustrates a representative monotonic stress-strain response of soil, showing that a given soil can exhibit three distinct shear strengths: peak shear strength, critical state shear strength, and residual shear strength. The failure envelopes corresponding to these shear strength states are defined by the peak (φ_p), critical (φ_c), and residual (φ_r) friction angles, as shown in Figure 2.10b. The peak friction angle (φ_p) corresponding to the peak shear strength arises from the combined effects of internal rolling, sliding, and the degree of interlocking between the soil grains. The degree of interlocking depends on the dilatancy (i.e., volume change tendency) of soil, which is influenced by the applied σ_n' and the packing of the soil grains (i.e., void ratio). Interlocking causes volume expansion (dilation) in a densely packed soil as it undergoes shearing. The peak shear strength failure envelope shown in Figure 2.10b is curved because, as σ_n' increases, the normal contact forces between soil grains also increase, suppressing dilation and causing grain crushing allowing slipping between the soil grains to occur with less resistance. As σ_n' increases further, the peak shear strength failure

envelope, represented by φ_p, converges with the critical state shear strength failure envelope, represented by φ_c. The critical state failure envelope represents the condition in which the soil undergoes continued shearing with a constant void ratio, along with constant effective normal and shear stresses. The critical state condition occurs when the interlocking effect between soil particles diminishes, and the soil structure is fully destroyed. The critical state failure envelope is generally regarded as a unique line that is independent of the initial packing of the soil, the effective confining stresses, and its loading stress history. Furthermore, while sample preparation influences the initial structure of the soil, which in turn affects its stiffness and peak shear strength, the critical state envelope remains unchanged with different sample preparation methods. This has been observed in studies by Ishihara (1993) and Sadrekarimi and Olson (2012), as once a soil reaches the critical state, its initial fabric is permanently destroyed. Although the critical state is defined as the ultimate state of a soil, the shear strength of some soils can further decrease below the critical shear strength, eventually reaching the residual strength failure envelope defined by φ_r. This occurs when fine-grained soils with plate-like particles are subjected to very large deformations, causing the soil particles to reorient and align along the failure plane. However, this failure envelope is mainly a feature of clay soils with platy grains, and for most sandy soil with rounded or sub-rounded grains, the critical and residual failure envelopes are identical.

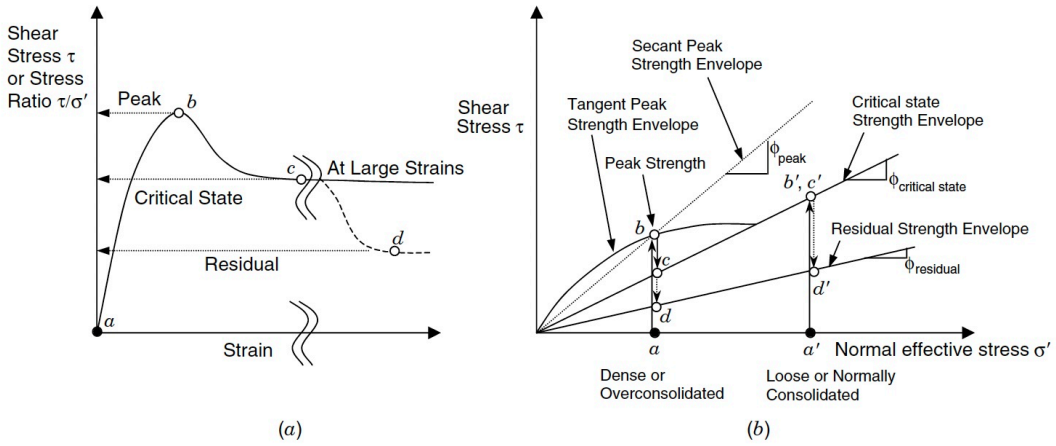


Figure 2.10: Soil monotonic behaviour: (a) stress-strain curve, (b) failure envelopes (Mitchell and Soga, 2005)

The typical monotonic behaviour of dense sands (or overconsolidated clays) is illustrated in Figure 2.10, which show the shear stress (τ) increasing from the initial stage (point a) to the peak shear strength failure envelope (point b), before softening to the critical state failure envelope (point c). Further shearing of platy clay materials reduces τ to the residual failure envelope (point d). In contrast, the typical monotonic behaviour of loose sands (or normally consolidated clays), as shown in Figure 2.10, exhibits that unlike the behaviour of dense sands (or overconsolidated clays), the shear stress (τ) at the peak and critical state failure envelopes are identical (points b' and c').

2.3.2 Critical state and steady state

As mentioned in the previous section, the critical state of soil is the unique ultimate state where the soil undergoes continued shearing while stresses and void ratio remain constant. For both sand and clay materials, the critical state in the triaxial mean effective stress-deviatoric stress plane (p'-q) forms a straight line, as shown in Figure 2.11. The critical state line (CSL) shown in Figure 2.11a is based on drained triaxial compression tests conducted by Roscoe et al. (1958) on normally consolidated and overconsolidated Weald clay. While the CSL shown Figure 2.11b is based on the results of undrained triaxial compression tests conducted by Verdugo and Ishihara (1996) on Toyoura sand.

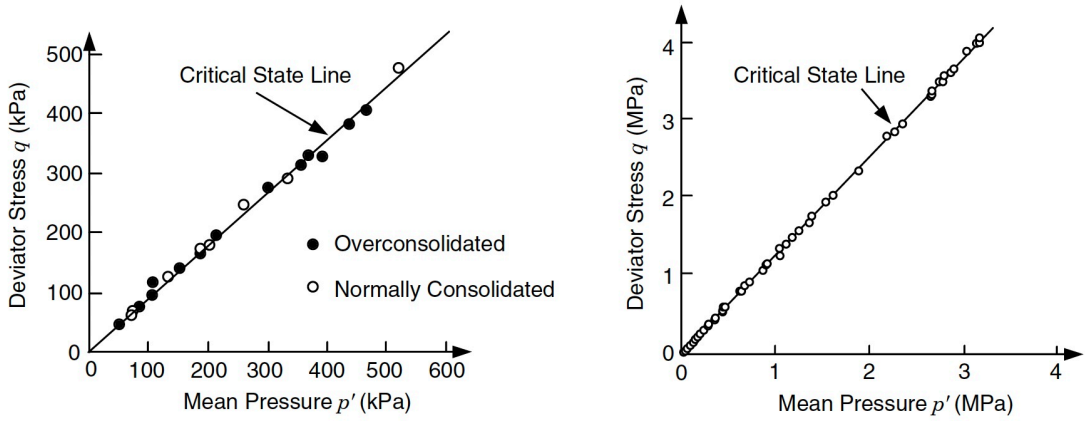


Figure 2.11: Critical state lines of sand and clay: (a) Weald clay, (b) Toyoura sand (Mitchell and Soga, 2005)

The CSL also forms a unique line in the compressibility plane, which is a plot of void ratio versus the mean effective stress (e-p'). The compressibility plane is typically plotted on a logarithmic axis of the mean effective stress (p'), either as e-ln(p') or e-log(p'). The critical state lines for Weald clay and Toyoura sand are shown in Figure 2.12. The CSL of Weald clay in the e-ln(p') plane is generally linear, as shown in Figure 2.12a, and hence the critical void ratio (e_c) as a function of p' can be represented with the following expression proposed by Schofield and Wroth (1968):

$$e_c = \Gamma - \lambda ln\,(p') \tag{2.4}$$

where Γ is the critical void ratio at p' = 1 kPa, λ is the slope of the CSL. Although the CSL is linear for clays, for a representative sand material such as Toyoura sand, the CSL in the e-log(p') plane is nonlinear as shown in Figure 2.12b. Due to the nonlinearity of the CSL for sands, Equation 2.4 does not adequately capture the relationship between e_c and p', which is better represented by the following power law proposed by Li et al. (1999):

$$e_c = e_0 - \lambda(\frac{p'}{p_{atm}})^{\xi} \tag{2.5}$$

where e_0 is the critical void ratio at p' = 0 kPa, p_{atm} is the atmospheric pressure, and λ and ξ are curve fitting parameters. Constitutive models that capture the critical state behaviour of sands, such

as SANISAND-MS, use Equation 2.5 and require the values of the intrinsic curve fitting parameters ($e_{0,}$ λ, and ξ) as inputs.

Another state similar to the critical state, which describes the behaviour of soil based on its volume and applied stresses, is the steady state. Poulos (1981) defined the steady state as "*the state in which the mass is continuously deforming at constant volume, constant normal effective stress, constant shear stress, and constant velocity*". This definition of steady state is very similar to that of the critical state, in that both describe an ultimate state where the soil behaviour remains unchanged in terms of volume (i.e., void ratio) and stresses, and hence there has been much debate in the literature about whether the two states are equivalent. The main difference between the two states is that: the critical state line on the *e-p'* plane of a given soil is located based on drained strain-controlled tests, whereas the location of the steady state line is determined from undrained stress-controlled tests (White, 2020). The difference between the critical state and steady state has been examined by various studies (e.g., Sladen et al., 1985; Been et al., 1991; Chu, 1995), which concluded that, for all practical purposes, the critical state and the steady state are identical.

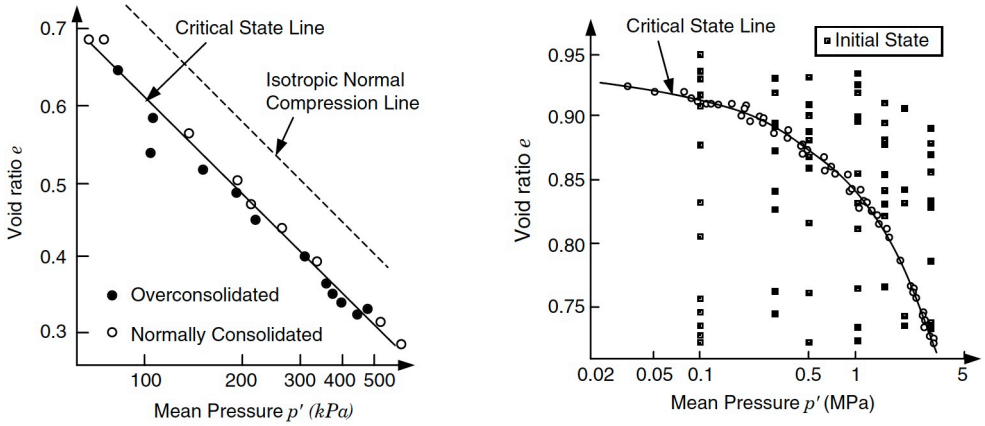


Figure 2.12: CSL of sand and clay in the compressibility plane: (a) CSL of Weald clay on the e-ln(p') plane, (b) CSL of Toyoura sand on the e-log(p') plane (Mitchell and Soga, 2005)

2.3.3 State parameter (Ψ)

The state parameter (Ψ) was proposed by Been and Jefferies (1985) to qualitatively predict soil behaviour according to its void ratio (e) and the applied mean effective stress (p') with reference to the CSL location in the compressibility plane. The definition of Ψ is shown in Figure 2.13, and is determined as follows:

$$\Psi = e - e_c \tag{2.6}$$

where Ψ is the difference between the current void (e) and the corresponding critical state void ratio (e_c) at the same p' value. According to the state parameter concept, a given soil reconstituted to different void ratios (e) and subjected to different p' values will exhibit similar peak friction angles (φ_p) and volume change tendencies if their state parameter values (Ψ) are the same. Furthermore,

the sign of Ψ indicates whether the soil behaviour is dilative or contractive. As illustrated in Figure 2.13, when Ψ is negative, the soil is dilative (dense of critical) and expands in volume when sheared to the CSL, whereas when Ψ is positive, the soil is contractive (loose of critical) and the volume decreases when sheared to the CSL.

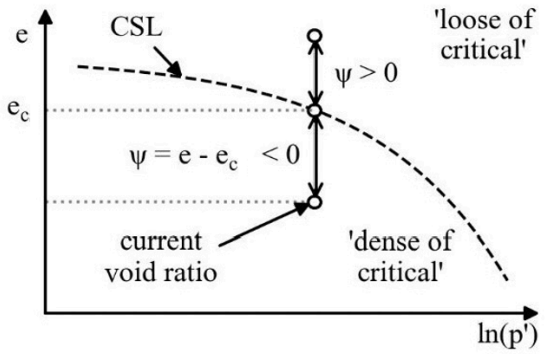


Figure 2.13: Definition of the state parameter, Ψ (modified after White, 2020)

The magnitude of Ψ governs the peak friction angle (φ_p) and the maximum dilation rate, which is defined as follows:

$$\text{Dilation rate} = \frac{\Delta\varepsilon_v}{\Delta\varepsilon_a} \tag{2.7}$$

where $\Delta\varepsilon_v$ is the volumetric strain increment, and $\Delta\varepsilon_a$ is the axial strain increment. As Ψ becomes more negative, the values of φ_p and the maximum dilation rate increase, as shown in Figure 2.14a and Figure 2.14b, respectively. The state parameter (Ψ) has been incorporated into several modern constitutive soil models, including SANISAND-MS, as it offers a robust framework for predicting soil behaviour based on its distance to the CSL. Additionally, it allows the model parameters for a given soil to remain independent of initial density and stress conditions.

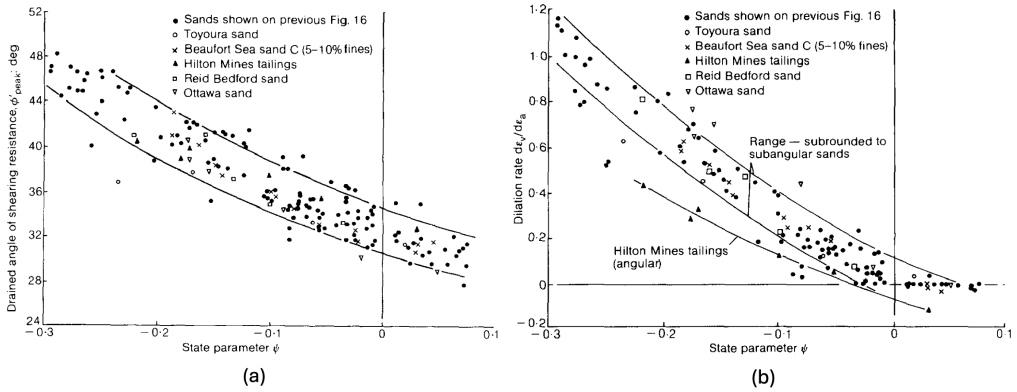


Figure 2.14: Influence of Ψ on: (a) peak friction angle and (b) Maximum dilation rate (Been and Jefferies, 1985)

2.3.4 Characteristic and phase transformation lines

The characteristic and phase transformation lines are two transient states which describe the transition of soil behaviour from compaction to dilation. The characteristic line, initially defined by

Luong (1980), is the stress ratio (q/p') at which the soil volume ceases to decrease and begins to expand. The characteristic line stress ratio (η_{cl}) is determined from drained triaxial tests and corresponds to the stress ratio at which $\Delta\varepsilon_v \approx 0$. The characteristic line friction angle corresponding to η_{cl} is commonly denoted as φ_{cl}.

The phase transformation state is similar to the characteristic state as it also marks the point where the dilatancy behaviour of soil changes. However, this state is identified from triaxial tests conducted under undrained conditions, where the suppression of drainage results in changes in pore water pressure rather than changes in the soil volume. The phase transformation line, defined by Ishihara et al. (1975), represents the stress ratio (q/p') at the point where the minimum p' occurs due to the generation of positive excess pore water pressure, before the direction of q/p' changes as p' increases due to the development of negative excess pore pressure. The definition of the phase transformation line and its corresponding angle of friction (φ_{pl}) are illustrated in Figure 2.15.

Due to the similar definitions of the characteristic line and phase transformation line, various studies have examined whether they are equivalent. Chu (1995) stated that since volume change tendency in drained conditions is interrelated to pore pressure generation in undrained conditions, the characteristic state and the phase transformation state are identical. Lade and Ibsen (1997) compared the two states and investigated their variation under the effects of relative density and effective confining stress, using triaxial test results from previous studies on different types of sands. The authors found that while the φ_{cl} and φ_{pl} values are nearly identical for Sacramento River sand, the φ_{cl} values for Lund No. 0 sand and Fuji River sand are higher than their corresponding φ_{pl} values. Furthermore, White (2020) compared between the two states mathematically and concluded that the definition of two states are not equivalent. Lade and Ibsen (1997) reported that while the friction angles φ_{cl} and φ_{pl} are not influenced by relative density, they increase with increasing the applied effective confining stress.

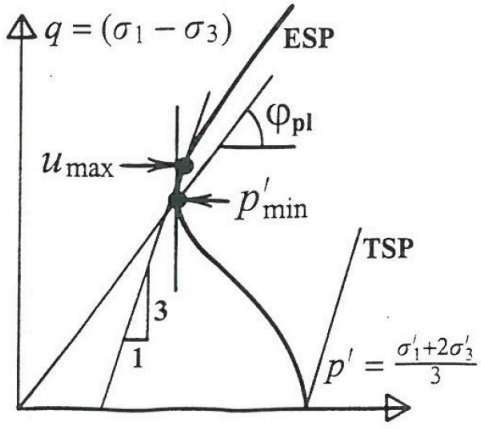


Figure 2.15: Definition of the phase transformation line (Lade and Ibsen, 1997)

2.4 Soil constitutive modelling

Constitutive models are mathematical relationships between stresses and strains that enable soil behaviour to be simulated through numerical modelling techniques, such as finite element or finite difference analyses, to represent soil behaviour in various geotechnical structures and soil-structure interaction problems. The complexity of constitutive models varies depending on their ability to capture multiple aspects of soil behaviour and simulate soil responses under different loading scenarios. For simple problems, such as determining the bearing capacity of a foundation, soil behaviour can be adequately represented using a simple linear elastic perfectly plastic Mohr-Coulomb model. However, for detailed analyses involving complex aspects of soil behaviour, such as stress-strain nonlinearity, cyclic strain accumulation, pore pressure generation, and liquefaction, more advanced constitutive models based on different theories of plasticity are required. This section provides a brief overview of the key theories of plasticity that underpin many constitutive models developed for simulating soil response. For a comprehensive review of the characteristics and capabilities of different constitutive models, the reader is referred to Lade (2005). The main plasticity theories are as follows:

(i) Elastoplasticity:
   - Single yield surface
   - Multisurface plasticity

(ii) Hypoplasticity

(iii) Hyperplasticity

- **Elastoplasticity:** Elasto-plastic constitutive models were developed to overcome the shortcomings of the linear elastic perfectly plastic Mohr-Coulomb model by allowing the yield surfaces to expand or contract (isotropic hardening) and to translate in stress space (kinematic hardening). The first elasto-plastic constitutive model was the Cam-Clay model developed by Schofield and Wroth (1968) for soft soils based on the critical state framework. The Cam-Clay consists of a single yield surface that expands and contracts, simulating the hardening and softening behaviour of soil, while the behaviour of the soil is linear elastic when the stresses are within the yield surface. Since the model is developed based on the critical state framework, it forms the foundation for many critical state constitutive models used for sands and clays. However, the main drawback of the Cam-Clay model is its large elastic strain domain, which contradicts the nonlinear behaviour of soil even at small strains, as the truly recoverable elastic domain lies at strains below approximately 0.001% (Jardine, 1992). Furthermore, due to its single yield surface, the model does not provide a smooth transition from elastic to plastic soil behaviour. The linear elastic behaviour within the yield surface also makes the Cam-Clay model unsuitable for cyclic loading, as it cannot form hysteretic stress-strain loops. To address these limitations, several models have been developed to account for the nonlinearity of soil behaviour within the yield surface. One such model is the hardening soil model with small strain stiffness (HSsmall) which was developed by Benz

(2007). The model consists of a single isotropic hardening yield surface and incorporates strain-dependent elastic functions, allowing for soil nonlinearity and a reduction in secant shear stiffness while the soil remains within the yield surface. Although the HSsmall model is primarily used for monotonic loading applications, Sheil and McCabe (2016) employed it in 3D finite element (FE) modelling to predict the cyclic behaviour of a monopile foundation and found that it produced reasonable results.

Another concept within the theory of elastoplasticity is multisurface plasticity. Models developed using the multisurface plasticity concept are categorised into nested surface models and bounding surface models. The concept of using multiple nested yield surfaces to represent the variation in stiffness with deformation was first proposed by Mróz (1967). Nested surface models consist of several kinematic hardening yield surfaces that translate in stress space, each with a given stiffness once activated. The first application of this concept to simulate the behaviour of cohesionless soils was by Prevost (1985), and it was later implemented in the FE code LAGAMINE by Cerfontaine (2014) to model the behaviour of suction caissons installed in sands. Nested surface models are particularly useful for simulating the cyclic behaviour of soil, as they allow hysteretic stress-strain loops to form.

In addition to nested surface models, several soil models were developed based on the concept of bounding surface plasticity, initially proposed by Dafalias and Popov (1975).The theory of bounding (or two-surface) plasticity consists of an inner yield surface and an outer bounding surface. A key feature of this theory is that the stiffness depends on the distance between the current stress and the corresponding image stress on the bounding surface, which reduces as this distance decreases. Manzari and Dafalias (1997) developed a model based on the critical state framework and couples the state parameter (Ψ) concept with the bounding surface plasticity theory. Several versions enhancing the capabilities of this model were introduced (e.g., Dafalias and Manzari 2004; Loukidis and Salgado, 2009; Taborda et al., 2014) which collectively form the “SANISAND” (Simple ANIsotropic SAND) model family. A recent addition to the SANISAND family is the SANISAND-MS model, developed by Liu (2020), which incorporates a memory surface to track the loading history and account for cyclic strain accumulation.

- **Hypoplasticity:** Unlike elastoplasticity theory, which separates strain into elastic and plastic components, hypoplasticity assumes that material behaviour is inelastic from the beginning and does not differentiate between elastic and plastic strains. One notable model is the hypoplastic model with intergranular strain (Niemunis and Herle, 1997) which is suitable for simulating the cyclic behaviour of cohesionless soils.

- **Hyperplasticity:** The main aim of the hyperplasticity theory is developing models that obey the law of thermodynamics. The theory was initially developed by Ziegler (1977) and it mainly involves describing the material behaviour through deriving two scalar functions: an energy function and a

dissipation function. An extensive description of hyperplasticity theory can be found in Houlsby and Puzrin (2006).2.5 HSsmall model

2.5 HSsmall model

The HSsmall model was developed by Benz (2007) as an extension of the isotropic hardening model (HS) to incorporate the capability of capturing the shear stiffness decay of soil in the range of small to medium strains. The reduction of the normalised secant shear modulus (G/G_0) with shear strain (γ) is represented by a modified form of the Hardin and Drnevich (1972b) hyperbolic function, proposed by Santos and Correia (2001). The modified hyperbolic function is expressed as follows:

$$\frac{G}{G_0} = \frac{1}{1+a\left|\frac{\gamma}{\gamma_{0.7}}\right|} \tag{2.8}$$

where $\gamma_{0.7}$ is the shear strain corresponding G/G_0 = 0.722, and the coefficient a is fixed at 0.385. Santos and Correia (2001) found that Equation 2.10 fits well with the results of previously published shear modulus reduction curves. The HSsmall overlay model is a strain history dependent, multiaxial extension of the modified hyperbolic function (Equation 2.8), which represents the stiffness decay of a soil element subjected to three-dimensional loading. Benz (2007) introduced the following scalar valued shear strain (γ_{hist}), which is equivalent to γ in Equation 2.8:

$$\gamma_{\text{hist}} = \sqrt{3}\frac{\|\mathbf{H}\Delta\underline{e}\|}{\|\Delta\underline{e}\|} \tag{2.9}$$

where $\Delta\underline{e}$ is the actual deviatoric strain increment, **H** is a symmetric tensor that represents the deviatoric strain history of the material. To detect strain reversals, the HSsmall model independently examines all three principal deviatoric strain directions. When a strain reversal is identified, the tensor **H** is either partially or fully reset before the strain increment $\Delta\underline{e}$ is added. Within the yield surface, the HSsmall behaviour is nonlinear elastic and forms hysteretic stress-strain loops during load reversal (shown in Figure 2.16), in accordance with Masing rules, which were discussed in Section 2.2.2. The HSsmall model is relatively simple and consists of only a handful of parameters. The parameters and their calibrations are presented in detail in Chapter 5.

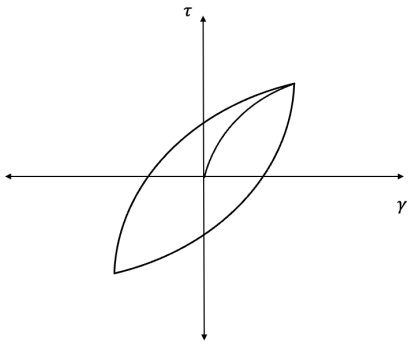


Figure 2.16: Hysteretic stress-strain loops

2.6 SANISAND-MS model

The SANISAND-MS model is the most recent addition to the SANISAND model family and was developed by Liu (2020). The SANISAND-MS model features five surfaces: the inner yield surface (YS), the critical state surface (CS), bounding surface (BS), the dilatancy surface (DS), and the newly added memory surface (MS). The memory surface replaces the fabric dilatancy tensor in the SANISAND04 model (Dafalias and Manzari, 2004) and is added to track the loading history and allow the behaviour of the soil to evolve during cyclic loading. The SANISAND-MS surfaces are shown in the triaxial stress space (*q-p'*) in Figure 2.17a and in the deviatoric stress ratio plane in Figure 2.17b. The hardening mechanism of the MS is a mixed isotropic-kinematic type, as the surface both translates in stress space and evolves in size, while the YS undergoes only kinematic hardening. The sizes of the bounding (BS) and dilatancy (DS) surfaces represent the peak and phase transformation stress ratios and they evolve based on the state parameter (Ψ). When Ψ is equal to zero, both BS and DS surfaces coincide with the critical state surface (CS). Furthermore, the stiffness and dilation rate in the model depend on the distances between the current stress and its corresponding images on the BS and DS surfaces, respectively. Details regarding the model parameters and their evaluated values are thoroughly discussed in Chapter 5.

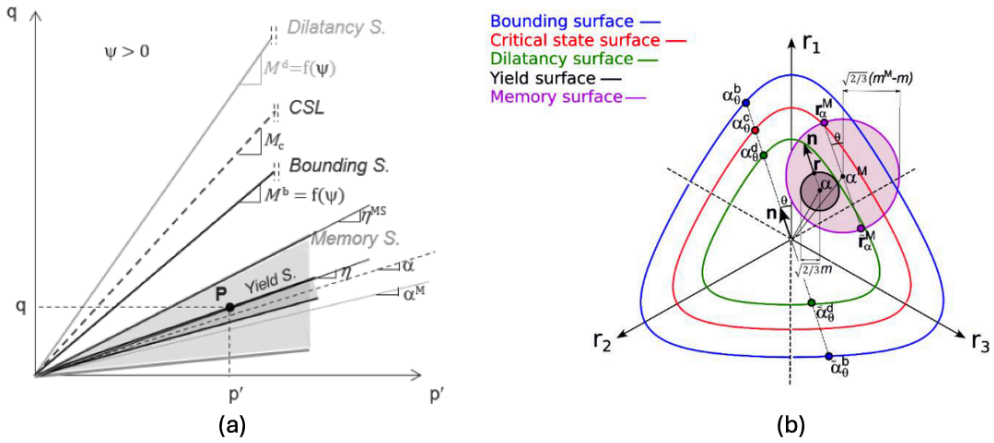


Figure 2.17: SANISAND-MS surfaces: (a) Triaxial stress space, (b) deviatoric stress ratio plane (SANISAND-MS manual, 202

2.7 General behaviour of monopiles

The key feature that differentiates monopiles from conventional piles is the small L_p/D_p ratio that causes monopiles to rotate and behave rigidly as they deform. The different behaviour of flexible (slender or long) and rigid (short) piles during loading is shown in Figure 2.18. Rigid piles rotate with little or no bending around a point that is referred to as the point of rotation. The direction of the passive soil resistance changes below the point of rotation. The tip movement of rigid piles (known as toe-kick) generates a shear force and a moment that increases the ultimate capacity of the pile. Furthermore, the rotation of the monopile generates shear tractions around the monopile shaft resulting in distributed moments along the monopile depth.

A pile with a given diameter, thickness, and ground conditions becomes more flexible as its embedment depth increases. Eventually, the pile reaches a point where further increase in the embedment depth does not influence the pile head response. This embedment depth is the critical pile length, which marks the transition into fully flexible pile behaviour, as defined by Poulos and Hull (1989). The relative pile stiffness (K_r) was proposed by Poulos and Hull (1989) for defining piles as either rigid or flexible for homogenous linear elastic ground conditions:

$$K_r = \frac{E_p I_p}{E_s L_p^4} \begin{cases} > 0.208 & Rigid\ pile\ behaviour \\ < 0.0025 & Slender\ pile\ behaviour \end{cases} \quad (2.10)$$

where E_p is the Young's modulus of the pile, I_p is the second moment of area, and E_s is the Young's modulus of the soil material. The behaviour of the pile, for the same ground conditions, could change depending on the load level which affects the soil stiffness. Finite element simulations by Zhang and Andersen (2019), showed that the gradual reduction of soil stiffness with increasing strain levels, caused the pile response transition from flexible/semi-rigid to rigid behaviour. Abadie (2015) compiled a database of K_r values for various offshore wind farms (OWFs) in the UK for piles resting on sand and clay (shown in Figure 2.19). The piles that were used for the development of the API p-y methods for sand and clay were also included for comparison. Furthermore, Abadie (2015) incorporated the expected K_r values for piles that will support OWTs in the future. The dashed lines in Figure 2.19 classify the response of piles based on the criteria that were proposed by Poulos and Hull (1989).

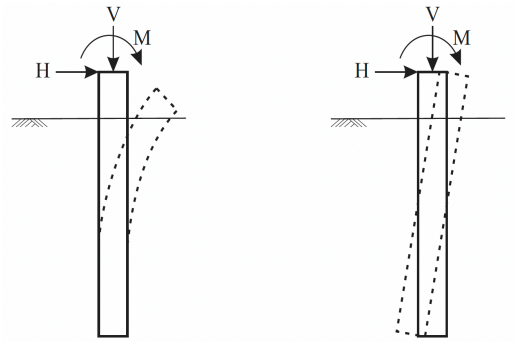


Figure 2.18: Flexible versus rigid pile behaviour (Augustesen et al., 2009)

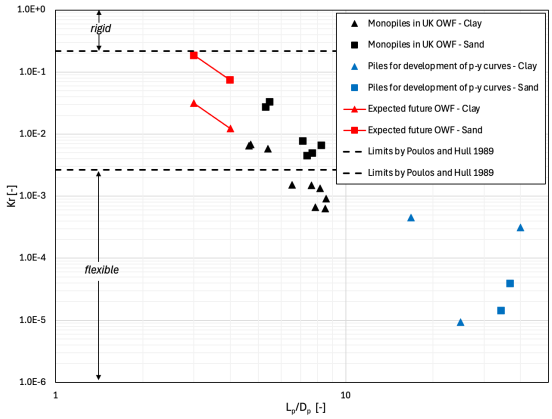


Figure 2.19: K_r versus L_p/D_p for full scale monopiles used for UK OWFs (Modified after Abadie, 2015)

Even though the stiffness of soil is non-uniform, Abadie (2015) used the initial young's modulus of the soil at the pile tip to generate the database in Figure 2.19. The compiled database shows that the behaviour of monopiles for OWTs falls within the intermediate zone and lies far away from the pile tests that were implemented to develop the traditional p-y methods for oil and gas structures. Furthermore, the behaviour of future monopiles for large size OWTs is expected to become even more rigid, and likely to reach the limit that designates full rigid behaviour. Given that the behaviour of piles depends on both the L_p/D_p ratio and the pile stiffness, Peralta (2010) claimed that the behaviour of fully rigid piles relies on the L_p/D_p ratio, whereas the response of fully flexible piles is mainly governed by the bending stiffness.

2.8 Monopile load-deformation response

The behaviour of monopiles in terms of their load-deformation response must be well understood to optimise their design against the loads that are subjected during the operational lifetime of OWTs. The two parameters that are of main concern for engineers are the stiffness and the ultimate load carrying capacity, which are heavily dependent on the surrounding soil characteristics. The monopile behaviour is characterised as non-linear with the stiffness gradually reducing as the soil strength is mobilised to failure. The ultimate capacity of the monopile is used in ULS design to determine whether the monopile is capable of withstanding the maximum loads of wind and waves during extreme storm events. The initial stiffness of the monopile, which is almost linear for very small load levels, is used for estimating the natural frequencies and the corresponding mode shapes of the overall OWT structure. The load-deformation response for monotonic and cyclic loading is shown in Figure 2.20. The response of the monopile at the ground (or the mudline) level is represented by either the horizontal force-displacement (H-y_g) or moment-rotation (M-θ_g) curves. The monotonic response refers to the case where the load increases gradually without changing its direction. The load-deformation curve as a result of monotonic loading is known as the *backbone curve*. Obtaining the backbone curves is critical in design and forms the basis for modelling the cyclic response in conventional and new design approaches. The cyclic loading causes the monopile to form hysteretic load-deformation loops, which are responsible for energy dissipation in the foundation-soil system and attenuation of structural vibrations. The hysteretic foundation damping, which is due to the non-linearity of the monopile-soil stiffness, is crucial to incorporate in fatigue design. Geotechnical analysis of monopile behaviour for cyclic loading aims to investigate three main phenomena:

(i) **Deformation accumulation (Ratcheting):** The effect of ratcheting (or cyclic deformation accumulation) is of significant importance for design engineers to ensure that serviceability limits are satisfied. The rate of accumulation is dependent on the nature of the cyclic loads (the cyclic amplitude, the mean load component, and load direction), stiffness and strength characteristics of the soil. This phenomenon has been studied extensively in physical modelling tests. For example,

experimental studies by Cuéllar et al. (2009), Leblanc et al. (2010), Peralta and Achmus (2010), Klinkvort (2012), Abadie (2015), and Richards (2019) aimed to capture the ratcheting of piles in sand under fully drained conditions with different cyclic amplitudes and mean load levels. The authors used the laboratory test results to derive empirical formulas by fitting the test data in either logarithmic or power laws.

(ii) **Evolution of foundation hysteretic loops:** The determination of the shape and size of the load-deformation hysteretic loops plays an important role in the dynamic response of OWTs. Hysteretic foundation damping increases with load level since the plastic deformations of the soil around the monopile become higher. Furthermore, hysteretic foundation damping changes with number of load cycles N. This can be seen in Figure 2.20b, which shows that the hysteretic loops become narrower as N increases as a result of soil densification (i.e. soil becoming stiffer). Evaluating hysteretic foundation damping is extremely challenging, as the stress-strain response of the soil elements in the vicinity of the pile must be reproduced accurately. The evolution of the hysteretic response with N has been investigated in various research studies (e.g., Abadie, 2015; Beuckelaers, 2017; Richards, 2019). Abadie (2015) and Richards (2019) conducted 1g laboratory experiments to study the variation of the hysteretic load-deformation response, while Beuckelaers (2017) analysed the cyclic field test results of the PISA project to investigate the effect of N on the hysteretic response of monopiles.

(iii) **Foundation stiffness:** The stiffness of the foundation which is a function of the monopile dimensions and the soil stiffness, governs the resonance frequency f_1 of the OWT structure,. As the soil mobilisation furthers its stiffness degradation accelerates thereby reducing the stiffness of the monopile backbone curve. Likewise, with hysteretic foundation damping and deformation accumulation, the stiffness varies with N. The evolution of stiffness should be addressed in the design process to ensure that f_1 remains well outside the frequency ranges of the different loads acting on the foundation. For granular soils, various researchers demonstrated that the secant stiffness increases with N (Leblanc et al., 2010; Klinkvort, 2012; Abadie, 2015; Richards, 2019). However, Lombardi et al. (2013) conducted 1g physical model tests for a scaled wind turbine model installed in kaolin clay, and found that as N increases, the natural frequency f_1 reduces indicating that the stiffness of the monopile softens with N. As a result, the evolution of the foundation stiffness is dependent on the nature of the soil supporting the monopile.

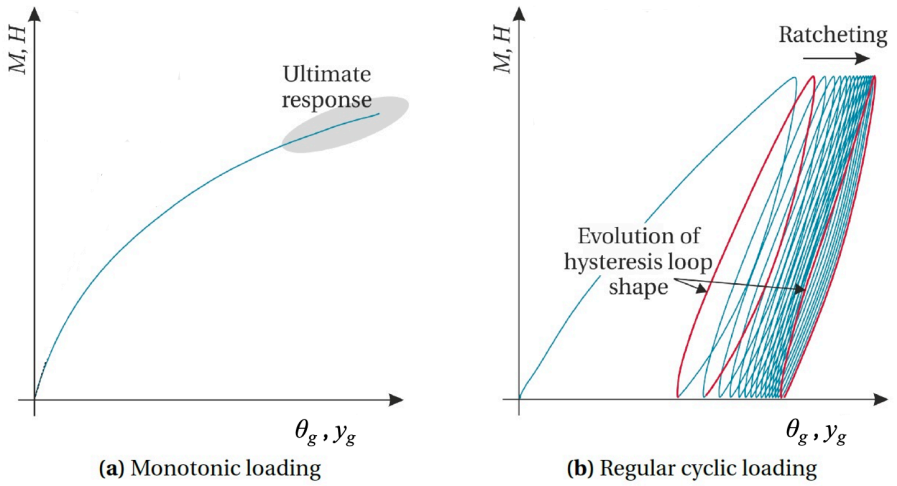


Figure 2.20: Monopile response under monotonic and cyclic loading (modified after Richards, 2019)

Although these cyclic aspects are often addressed separately in design, they are all interrelated and are governed by the behaviour of the soil. The mechanism of the grain migration during long-term two-way asymmetric cyclic loading was investigated through laboratory 1g pile tests on saturated sand by Cuéllar et al. (2009). The results showed that the soil undergoes convective granular flow and local densification near the pile as a result of particle rearrangement. Cuéllar et al. (2009) also showed that the grain migration resulted in the formation of two domains in the soil continuum: a convected and a static soil domain (see Figure 2.21). The local densification near the pile is deduced from the formation of a conical subsidence zone. The coupled mechanisms of convective flow and local densification control the evolution of ratcheting, secant stiffness, and the hysteretic pile response (Richards, 2019). Although local densification may imply that the f_1 of the OWT would increase, (Bakri, 2021) discussed that the associated local subsidence increases the free length of the structure and hence lead to f_1 reduction.

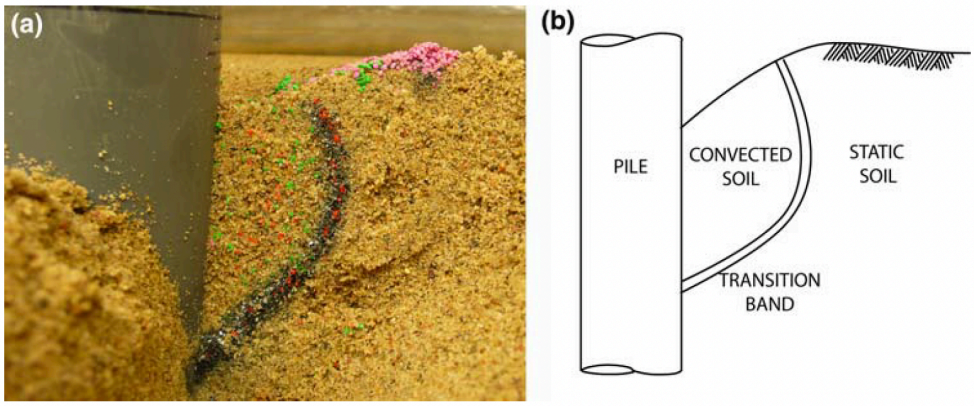


Figure 2.21: (a) Vertical cut through the soil, along the loading direction, (b) Sketch of soil domains (Cuéllar et al., 2009)

2.9 Geotechnical modelling

The soil-structure interaction for piles in terms of monotonic and cyclic loading is taken into account with various modelling approaches. These approaches (shown in Figure 2.22) differ from each other based on the desired level of accuracy, and are summarised as follows:

(1) Continuum 3D FE approach
(2) Winkler approach
(3) Macro-element approach

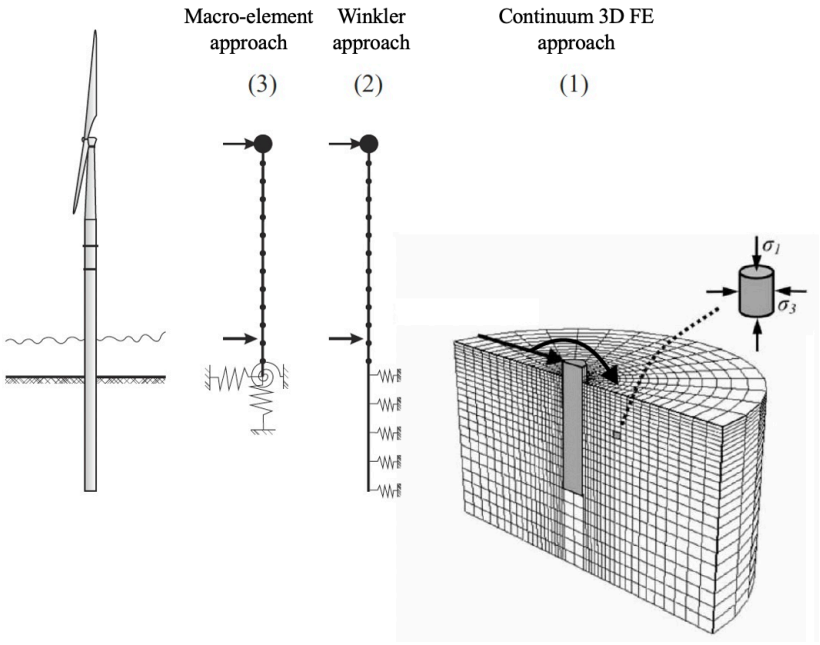


Figure 2.22: Monopile soil-structure interaction methods (modified after Abadie, 2015)

2.9.1 Continuum 3D FE approach

This methodology involves building a 3D FE model that incorporates the entire soil domain and the monopile. Particular advantage of this approach is that it allows for visualization of the stresses and strains throughout the soil volume, while obtaining the deformations and internal forces along the monopile. The accuracy of this method is highly dependent on using an appropriate constitutive model, with the input parameters carefully selected based on laboratory or field data. This method is one of the highly accurate approaches, as it can be used to analyse sites with complex soil stratigraphies. Furthermore, the 3D FE analysis can be coupled with field pile test data to examine the validity of the input parameters for simulating different pile geometries, and to extract the soil reaction curves required for 1D FE analysis. This was the framework of the PISA project for developing the monotonic design methods for sands and clays. However, the extended computational time and the difficulty in obtaining accurate input parameters are the primary limitations that restrict the use of 3D FE modelling as the standard analysis method for OWTs.

In the context of monopile design, soil constitutive models can be divided into implicit and explicit models. An implicit model simulates the stress-strain response of the soil during each cycle and is very useful for short-term load applications. Examples of implicit soil models are the HSsmall model, the hypoplastic model with intergranular strain (Niemunis and Herle, 1997), Severn-Trent sand model (Gajo and Wood, 1999), the ISA (intergranular strain anisotropy) model (Fuentes and Triantafyllidis, 2015), the SANISAND04 model (Dafalias and Manzari, 2004), and the newly enhanced SANISAND-MS model (Liu, 2020) which has a memory surface to account for fabric effects during cyclic loading. A database of the parameters for the hypoplastic model with intergranular strain, the Severn-Trent model, and the SANISAND04 model for different sands can be found in Kowalczyk (2020). Implicit constitutive models offer the capability to study the effects of soil hysteretic behaviour on the overall dynamics of OWT structures (mainly damping and natural frequency). However, implicit constitutive models are often restricted to short-term cyclic loading since they become prone to accumulating numerical errors with large number of load cycles (Achmus et al., 2009). On the other hand, explicit constitutive models approach cyclic loading similarly to a creep problem by using cycle number instead of time. They are employed to determine the accumulation of deformation for long-term cyclic loading without simulating stress-strain soil hysteresis for each cycle. An example of an explicit constitutive model is the HCA (High Cyclic Accumulation) model which was developed by Niemunis et al. (2005) for the strain accumulation of sand. Murphy et al. (2018) compared the results of 3D FE analyses with field tests conducted on piles with diameters of 0.245 m and 0.510 m installed in sand. Their 3D FE analysis results showed very good agreement with the field test data, highlighting the capability of 3D FE modelling to accurately capture the behaviour of piles in the field.

2.9.2 Winkler approach

The pile-soil interaction along the embedded depth is captured with a series of independent springs representing the soil reaction, and discretised beam elements to account for the pile behaviour (shown in Figure 2.23). The soil reaction at a specific depth is a function only of the local beam element deformation. The analyses of piles using the Winkler approach is usually implemented in 1D FE models. The Winkler approach is also generally known as the *p-y* method, in which *p* is the lateral soil reaction and *y* is the lateral displacement of the pile section. This method is considered less accurate than the 3D FE due to its inability to capture the interaction between the different soil layers and obtaining the stresses and strains in the soil domain. However, the Winkler approach provides a satisfactory compromise between accuracy and computational time and is often used as the main design tool for OWTs. The Winkler approach is utilised in the API (2010) design method for analysing the behaviour of piles using soil reactions for sand and clay to incorporate the local resistance of soil against the lateral pile movement. The soil reaction for sand is modelled using the hyperbolic equation recommended by O'Neill and Murchison (1983), while the lateral resistance of clay is represented by the equation proposed by Matlock (1970).

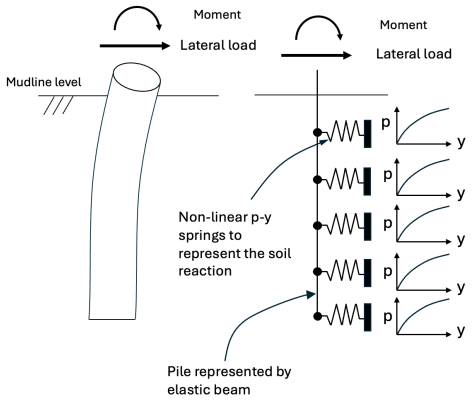


Figure 2.23: Schematic of the Winkler approach

The inherent limitations of the API p-y framework gave rise to numerous research efforts to improve the understanding of rigid monopile behaviour. One of the most recent research initiatives is the PISA project, coordinated by DONG Energy and managed by the Academic Work Group (AWG), led by the University of Oxford in collaboration with Imperial College London (ICL) and University College Dublin. The objective of the PISA project was to develop a new design framework for laterally loaded monopiles, addressing the limitations of the conventional API p-y design approach (Byrne et al., 2015a). The project involved extensive pile field studies, and state-of-the-art soil element laboratory tests to provide the inputs for numerical FE modelling. The majority of the field tests were conducted to provide a new design framework for monopiles subjected to monotonic loading. The main contribution of the PISA project is incorporating additional soil reaction components to the lateral *p* resistance, which become important for capturing the rigid monopile deformation mechanism. The additional soil reactions are the distributed moment *m*, developed due the shear tractions induced at the soil-pile interface, the base shear *Hb* and the base moment *Mb* generated at the pile tip. Figure 2.24 shows the soil reactions incorporated in a 1D FE model to analyse the behaviour against the load applied at the pile head.

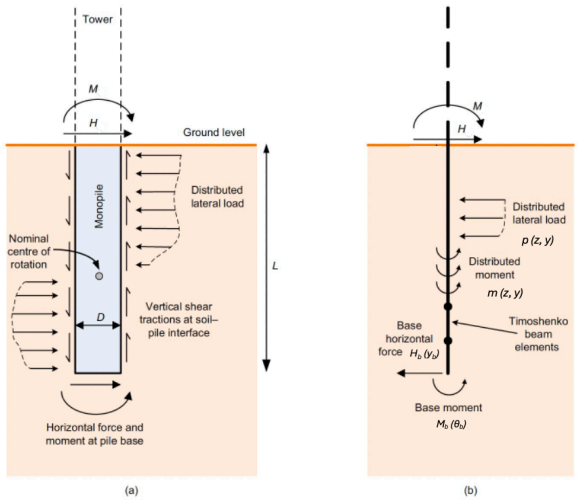


Figure 2.24: PISA design model: (a) idealisation of the soil reaction components acting on the pile; (b) 1D finite-element implementation of the model (modified after Burd et al., 2020b)

The PISA framework for cyclic loading was implemented by Beuckelaers (2017) in 1D FE analyses, using the Hyperplastic Accelerated Ratcheting Model (HARM) to replicate the hysteretic response and deformation accumulation of soil. The HARM model is framed within the hyperplasticity framework presented by Houlsby and Puzrin (2007) and was initially developed by Abadie (2015) for the analysis of monopiles as a macro-element model. Beuckelaers (2017) improved the HARM model by integrating a gapping element and incorporating rate effects through adding dashpots to the soil reaction curves. The 1D FE simulations using the HARM model showed good results in comparison with PISA field tests for both sand and clay. However, calibrating the input parameters could be challenging and further studies are required to demonstrate its predictive capability. Ryan et al. (2023) implemented a fully integrated numerical analysis framework that couples an aeroelastic OWT model with a 1D Winkler model which simulates the hysteretic soil behaviour according to the multisurface plasticity method. The authors showed that including the hysteretic response reduces the forces generated at the mudline.

2.9.3 Macro-element approach

This approach condenses the entire soil-monopile interaction at a single point which is usually located at the mudline (Figure 2.25). The macro-element approach is regarded as the least accurate method, but it is computationally fast and can be easily integrated into aeroelastic numerical analysis tools. The global soil-pile interaction is often represented with a stiffness matrix which consists of the lateral stiffness, the rotational stiffness, and a cross coupling stiffness. The stiffness terms can be calibrated using 3D FE analysis, effectively combining the accuracy of the 3D FE method with the low computational effort of macro-element modelling. Soil hysteretic damping can be integrated using equivalent viscous dashpots, which is a simple approach adopted by some research studies (Damgaard, 2014; Carswell et al., 2015; Li et al., 2020).

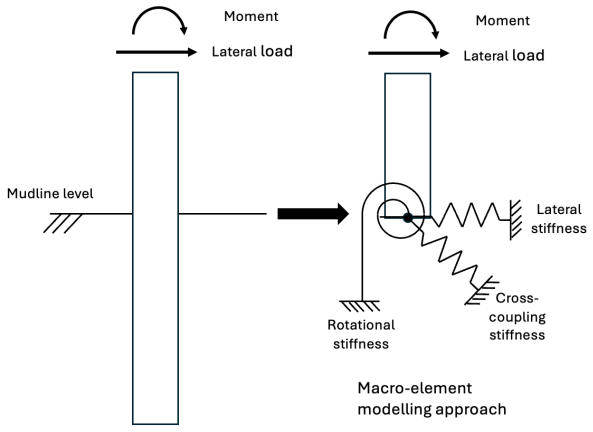


Figure 2.25: Macro-element modelling approach

The accuracy and capabilities of the macro-element method can be enhanced when the constitutive load-deformation relations are formulated using different plasticity frameworks, allowing for the capture of global foundation non-linearity and hysteretic response. Two of the main implicit macro-

element models that are specifically developed for monopiles are the HARM model (Abadie, 2015), and the multi-surface kinematic hardening model developed by Page et al. (2018). The HARM model formulated by Abadie (2015), is based on the framework of hyperplasticity and was designed based on the insights obtained from 1g physical modelling of monopiles in dry sand subjected to cyclic loads of up to 100,000 cycles. The key concept of the model is to capture the deformation accumulation and the variation of the size and shape of the hysteretic loops. The HARM model combines the concept of multisurface kinematic hardening which allows the hysteretic loops to obey the Masing rules (Masing, 1926), with a ratcheting element which governs the deformation accumulation and the evolution of the hysteretic behaviour. The model displays pure kinematic hardening during two-way symmetrical loads and is shows ratcheting for non-zero mean loads. The model demonstrates the capability to simulate the mitigation of ratcheting rate, the stiffness increase, and the hysteretic damping decrease as a result of the loops becoming narrower. The HARM model is robust, but the ratcheting element is not straightforward and could be difficult to calibrate.

Page et al. (2018) developed a multisurface kinematic hardening model that is similar to the HARM model but without ratcheting and is formulated using the framework of elastoplasticity. The model generates load-deformation loops that conform to Masing rules, enabling the cyclic behaviour to be described by the mudline monotonic backbone curves. The yield surfaces are elliptical in shape and are described with kinematic hardening, allowing the surfaces to remain the same size and shape. The flow rule is associated, causing the vectors of the plastic deformation increments to be normal to the yield surfaces. The associated flow rule greatly simplifies the model implementation but could be inconvenient for monopiles installed in purely frictional materials. The calibration is fairly straightforward and can be easily informed from 3D FE analyses. Page et al. (2018) showed that the model performs well when compared against the pile field tests of PISA in Cowden clay as shown in Figure 2.26. However, the limitation of the model, apart from its inability to simulate ratcheting, is that it follows Masing rules which overestimates the hysteretic damping for large deformations as discussed by Kaynia and Andersen (2015).

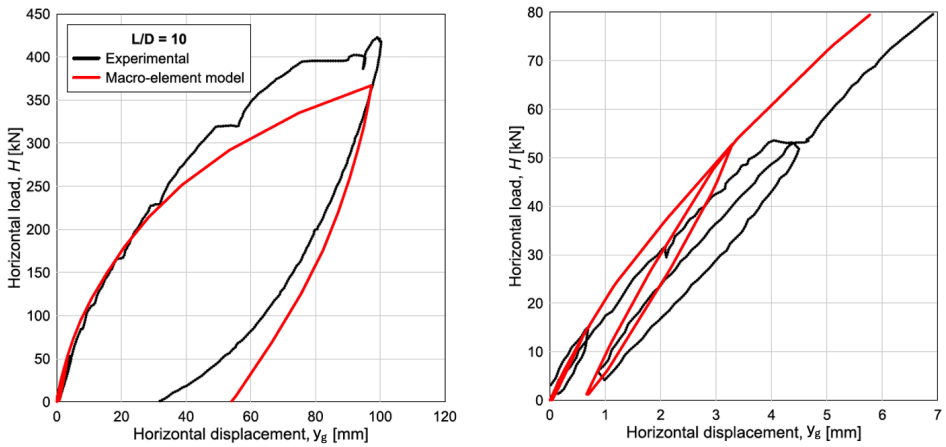


Figure 2.26: Comparison between the macro-element model and Cowden pile field test (Page et al., 2018)

Aasen et al. (2017) conducted fully integrated time-domain simulations to evaluate the predicted accumulated fatigue damage of OWTs using different foundation models. The results indicated that the macro-element model developed by Page et al. (2018) predicted the least accumulated fatigue damage, owing to its ability to exhibit hysteretic damping.

2.10 Foundation damping

OWTs are often characterised as dynamically sensitive structures, as their designed fundamental natural frequencies typically lie within a narrow band, making them prone to resonance. This susceptibility can negatively affect fatigue resistance and reduce the overall design lifespan of the structure. As result, determining the overall damping from different sources is crucial, since damping governs the dynamic amplification of the structural response during resonance. The main sources that contribute to the overall damping of OWT structures consist of aerodynamic damping, hydrodynamic damping, structural damping, tower oscillation dampers, and foundation (or soil) damping (Malekjafarian et al., 2021). Of these sources, foundation damping has the largest contribution for turbines in parked conditions and for the response in the side-side (SS) direction, and has the second highest contribution, after aerodynamic damping, for turbines in operational conditions and for the response in the for-aft (FA) direction (Germanischer Lloyd, 2005). Although design standards such as DNV (2014) recommend that foundation damping should be considered in the design, there are no standardised methods for estimating its contribution or incorporating it into the design process. This is due to the complexity of foundation damping and the difficulty in estimating its effect on the structural behaviour of OWTs (Carswell et al., 2022). The foundations of OWT structures dissipate dynamic energy primarily through two mechanisms: (1) radiation damping and (2) hysteretic soil damping. However, as was discussed in the previous chapter, the influence of radiation damping is generally negligible for the response frequencies experienced by OWTs. Thus, the main energy dissipation mechanism for monopile foundations of OWTs is through the hysteretic behaviour of the supporting soil. When the monopile is subjected to cyclic loads, the behaviour of the surrounding soil elements becomes nonlinear, forming hysteretic stress-strain loops that result in the dissipation of plastic energy. The damping produced by a soil element is often represented with the damping ratio parameter (D), which is defined as the ratio of the dissipated energy during a cycle to the elastic stored energy (see Equation 2.1).

The damping ratio (D) characterising the internal energy dissipated by the soil, is mathematically equivalent to the critical damping ratio (ξ) of a single degree of freedom (SDOF) Kelvin-Voigt (KV) model subjected to harmonic motion at its natural frequency. The KV SDOF system consists of a mass attached to a spring and a viscous dashpot. The relationship between the equivalent damping ratio (D) and the critical damping ratio (ξ) of an SDOF KV model is as follows:

$$D = \frac{\omega}{\omega_n}\xi \tag{2.11}$$

where ω is the angular frequency of the applied load and ω_n is the angular natural frequency of the SDOF system.

For a combined system such as monopiles, which involve interaction between the foundation and the surrounding soil, the hysteretic damping ratio is calculated by dividing the energy dissipated by the soil by the elastic energy stored in the soil-foundation system. This combined hysteretic damping ratio is referred to as the hysteretic foundation damping ratio (ξ_f), and is calculated according to the following equation:

$$\xi_f = \frac{1}{4\pi} \frac{W_{D,soil}}{W_{S,(soil+foundation)}} \tag{2.12}$$

where $W_{D,soil}$ is the dissipated energy by the soil continuum surrounding the monopile, and $W_{S,(soil+foundation)}$ is the elastic energy stored by the combined soil-foundation system. The hysteretic foundation damping ratio (ξ_f) can be calculated based on 3D FE analyses using constitutive models that are calibrated to represent the behaviour of soil. Using 3D FE modelling, the hysteretic foundation damping ratio (ξ_f) can be determined from cyclic push-over analyses, which involve applying unload-reload cycles to the foundation. ξ_f is calculated using Equation 2.12, according to the resulting hysteretic load-deformation loops generated at the mudline level of the monopile, as illustrated in Figure 2.27.

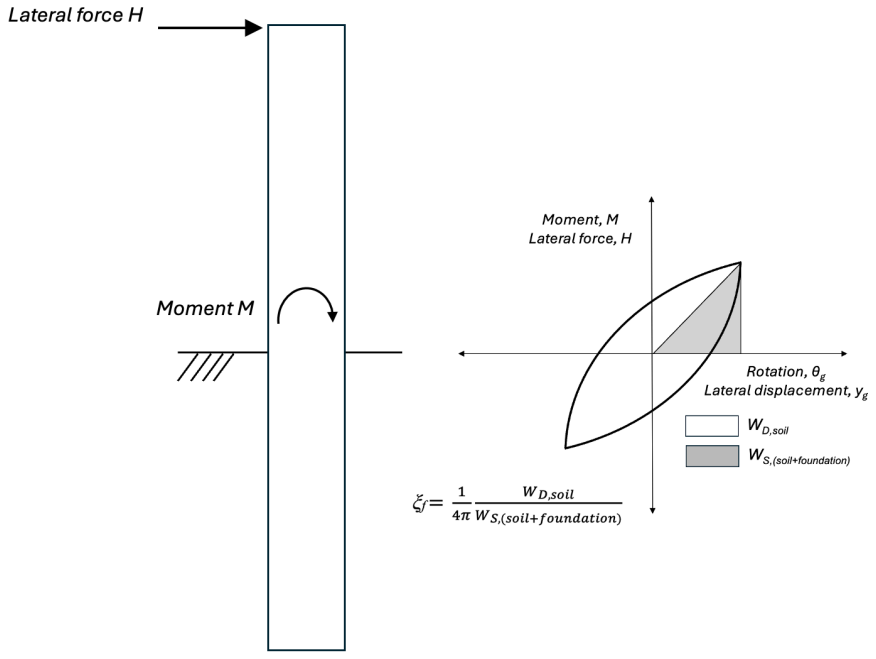


Figure 2.27: Foundation damping ratio calculation from load-deformation hysteretic loop at the mudline

Given that the load-deformation behaviour of monopiles at the mudline level is often represented by the horizontal force-displacement (H-y_g) and moment-rotation (M-θ_g) relationships, the foundation damping ratio (ξ_f) can be decomposed into a lateral foundation damping ratio (ξ_y) and a rotational foundation damping ratio (ξ_θ). Furthermore, since soil-monopile interaction can be modelled in terms of distributed soil reactions, foundation damping ratios (ξ_y and ξ_θ) can also be

evaluated along the monopile depth based on the hysteretic *p-y* and *m-θ* loops as illustrated in Figure 2.28. Determining the foundation damping ratios, either at the mudline or distributed along the monopile depth, allows incorporating the effect of soil damping in dynamic time-domain numerical analyses by converting these damping ratios into equivalent viscous dashpots. The damping of the soil surrounding the monopile governs the foundation damping, and hence determining the soil damping ratios from element-level tests (e.g., triaxial or resonant column tests) provides an accurate basis for incorporating foundation damping into fully integrated numerical models of OWTs, which include the entire structure and the monopile foundation.

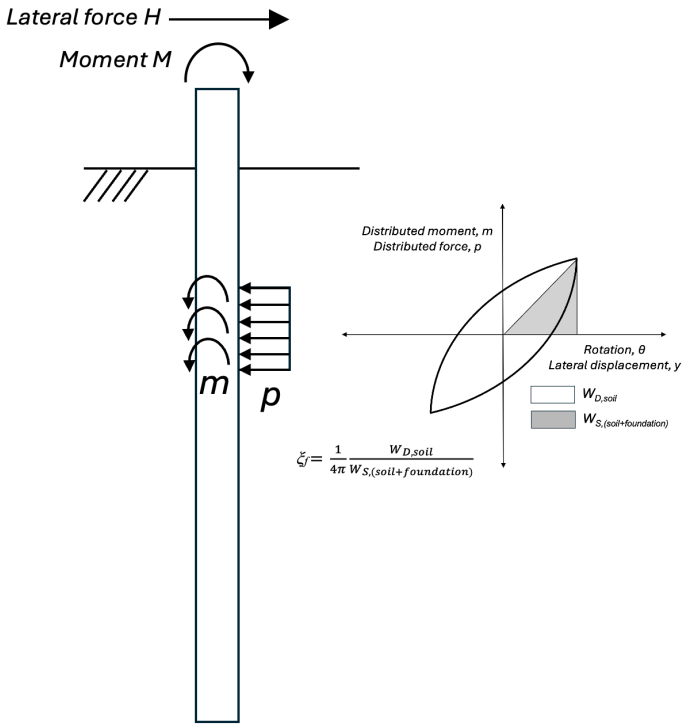


Figure 2.28: Distributed foundation damping ratio calculation along monopile depth

The effect of soil damping on an entire structure such as OWTs, which consists of the interaction between the soil-foundation system and the tower, can be assessed from a global point of view. This is important, as it enables the determination of the global damping ratio of the OWT structure due to the plastic energy dissipated by the soil continuum through the foundation. In this research, this damping ratio is referred to as the global foundation damping ratio (ζ_f). For a given mode of vibration (i), ζ_f can be calculated as follows:

$$\zeta_{f,i} = \frac{1}{4\pi} \frac{W_{D,soil,i}}{W_{S,(soil+foundation+tower),i}} \tag{2.13}$$

where $W_{D,soil,i}$ is the dissipated energy by the soil for i_{th} vibration mode, and $W_{S,(soil+foundation+tower),i}$ is the elastic stored energy by the overall soil-foundation-tower system for the same mode. Although OWTs exhibit multiple modes of vibration, the dynamic response predominantly occurs near the first natural frequency (ω_1), since the amplification of the structural response is greatest at ω_1 and the natural frequencies of the higher modes typically lie outside the frequency range of the applied

loads (Seidel, 2014). As a result, ζ_f in this thesis refers to only the global foundation damping ratio associated with the first mode of vibration. ζ_f can be determined from numerical 3D FE analyses by performing cyclic push-over simulations to compute $W_{D,soil,}$ and $W_{S,(soil+foundation+tower)}$ and using Equation 2.13 to evaluate the value of ζ_f. However, ζ_f is most commonly determined by the logarithmic decrement approach which involves analysing the behaviour of OWTs during free-decay when the response in terms of displacements or accelerations attenuate with time. This is typically achieved in the field either by applying a pulse load to the OWT or by conducting rotor-stop tests, both of which induce a free-decay response. The global foundation damping ratios (ζ_f) obtained from field monitoring studies are covered in the next section. ζ_f can also be estimated from numerical 1D or 3D FE analyses by accurately accounting for the stiffness and mass properties of the various components making up the OWT. For example, beam elements may be used instead of plate elements to model the tower, and the RNA can be represented as a lumped point mass, omitting the detailed modelling of the blades and internal components of the nacelle and hub. To simulate the free-decay response of OWTs, the structure is initially displaced by applying a monotonic load. The load is then removed, and time-domain simulations are performed, during which the structure experiences inertia effects and undergoes free vibration. The response of an OWT at the RNA level in terms of horizontal displacement versus time during free-decay is shown in Figure 2.29. Based on the logarithmic decrement method, the logarithmic decrement ratio (δ) is computed from the free-decay response as follows:

$$\delta = \frac{1}{n} \cdot ln\left(\frac{A_0}{A_n}\right) \tag{2.14}$$

where A_0 and A_n are two successive amplitudes (as shown in Figure 2.29) and n is the number of cycles apart. The relationship between the global foundation damping ratio (ζ_f) and δ is as follows:

$$\zeta_f = \frac{1}{\sqrt{1+\left(\frac{2\pi}{\delta}\right)^2}} \tag{2.15}$$

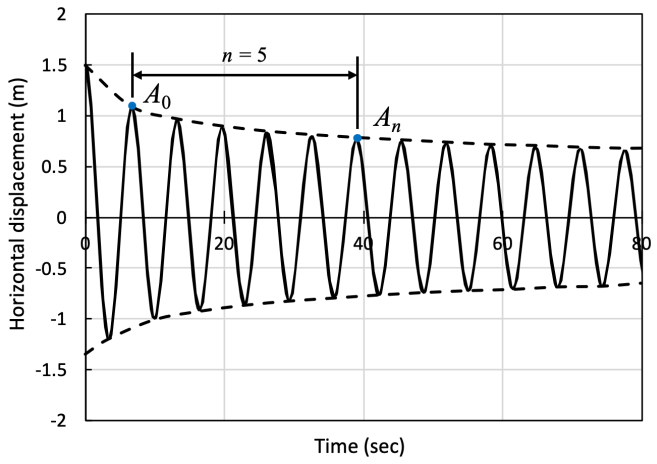


Figure 2.29: Free-decay response at the RNA level

This section has presented the various damping ratio terms that are central to this study and will be discussed in greater detail in the subsequent chapters of the thesis. Given the similarity in

terminology, which may cause confusion, the following provides a summary of the distinct damping ratio terms used:

(1) Soil damping ratio (D): This is the local soil damping ratio which can be determined from the hysteretic stress-strain loops displayed by the soil during element scale tests such as the cyclic triaxial or simple shear tests.

(2) Hysteretic foundation damping ratio (ξ_f): This represents the damping ratio of the soil-foundation system and is derived from hysteretic load-deformation loops. In this study, ξ_f is decomposed into a lateral foundation damping ratio (ξ_y) and a rotational foundation damping ratio (ξ_θ), which are determined from horizontal force-displacement and moment-rotation loops, respectively. Since soil-foundation interaction can be modelled either using a macro-element approach, in which the interaction between the monopile and surrounding soil is concentrated at a single point at the mudline, or using distributed soil reactions along the monopile depth, the hysteretic foundation damping ratios (ξ_y and ξ_θ) can be evaluated either at the mudline or distributed along the monopile length.

(3) Global foundation damping ratio (ζ_f): This term denotes the damping ratio associated with the overall soil-foundation-tower interaction, resulting from hysteretic energy dissipation in the soil continuum surrounding the monopile. ζ_f differs from the hysteretic foundation damping ratio (ξ_f) in that it also includes the contribution of the elastic energy stored in the tower. Since the first mode of vibration is the most critical for the dynamic response of OWTs, ζ_f in this study is primarily discussed with respect to vibration at ω_1.

The hysteretic foundation damping ratios (ξ_y and ξ_θ), whether determined from the load-deformation loops at the mudline or from soil reactions along the monopile depth, can also be referred to as local hysteretic foundation damping ratios. This term helps distinguish them from the global foundation damping ratio (ζ_f), which characterises the damping of the entire OWT structure due to energy dissipated in the soil domain and the total elastic energy stored in the soil-foundation-tower system.

2.11 Foundation damping studies

This section addresses the main studies that were carried out to investigate foundation damping and is divided into field studies, laboratory studies, and numerical modelling studies.

2.11.1 Field studies

Field studies often involve relying on installed strain gauges and accelerometers to measure the dynamic characteristics of the system and how they vary throughout the operational lifetime. Over the past decade, numerous efforts have been made to characterize various forms of damping, including ζ_f, through field monitoring of OWTs in operational and parked conditions. Many of these campaigns have relied heavily on rotor-stop tests, which minimise the influence of aerodynamic damping and enable back-calculating ζ_f by subtracting the contributions of other damping sources

from the total damping ratio of the OWT. During rotor-stop tests, the blades are pitched into a feathered position and the rotor is shut down, which reduces aerodynamic excitations, allowing the OWT to freely vibrate and its dynamic response gradually decays over time (e.g., Damgaard et al., 2012; Damgaard et al., 2013a; Damgaard et al., 2013b; Tarp-Johansen et al., 2009; Versteijlen et al., 2011). The damping ratio from rotor stop tests is determined by logarithmic decrement approach which involves using Equation 2.15 to determine δ from successive points of maxima of the free-decay response. The basic assumption of this approach is that the structure experiences only one fundamental mode of vibration and the OWT acts as a single degree of freedom system. Another technique that is also frequently used is measuring modal damping parameters from ambient vibrations of wind and waves through implementing operational modal analysis (OMA) (e.g., Devriendt et al., 2013; Koukoura et al., 2015; Shirzadeh et al., 2013; Weijtjens et al., 2014). The advantage of Operational Modal Analysis (OMA) lies in its ability to determine modal parameters without requiring prior knowledge of the frequency content of the applied loads, which is why it is also known as output-only analysis. Furthermore, OMA is used when the turbine is in operation, thus, natural frequencies and modal damping ratios correspond to actual boundary conditions.

For a wind turbine in the North Sea, Damgaard et al. (2012) carried out several rotor-stop tests and measured the for-aft (FA) and side-side SS accelerations at the RNA level. The average measured total damping ratio was 2.31% and the back-calculated ζ_f was equal to 0.58%. Furthermore, Damgaard et al. (2013a) analysed modal parameters from over 1500 rotor stop tests across four offshore wind parks between 2006 and 2011. The measured total damping ratios ranged from 2.3% to 2.5%, with the lowest recorded value being 1.43%. Using this lowest measured ratio (1.43%), the back-calculated ζ_f was approximately 1%, assuming contributions from steel, aerodynamic, and hydrodynamic damping were 0.19%, 0.12%, and 0.12%, respectively. Damgaard et al. (2013b) evaluated the dynamic properties for 30 OWTs located in the North Sea based on monitoring the accelerations at the RNA level of more than 650 free vibration tests. The back calculated global foundation damping ratios (ζ_f) varied in the range 0.8%-1.27%.

Based on ambient vibration measurements and overspeed stop tests conducted on 3MW wind turbines at the Belwind wind farm near the Belgian coast, Devriendt et al. (2012) concluded that the additional damping (excluding aerodynamic damping) for offshore wind turbines ranges from 0.8% to 1.2%. These values are in agreement with Shirzadeh et al (2013), who showed that the additional damping ratio from ambient vibrations falls within 1.05%-1.27%. Versteijlen et al. (2011) conducted twelve rotor stop tests on an OWT at the Burbo Bank wind farm. The results indicated a global modal damping ratio of 3% for the OWT, with a localized modal damping of 1.5% at the rotor level. The authors concluded that the 1.5% difference between the two modes can be attributed to the contribution of ζ_f. Based on field monitoring tests involving various methods (e.g., rotor-stop, ambient excitation, and over-speed tests), the back-calculated ζ_f generally falls within the range of 0.25-1.5% (Carswell et al., 2015).

Another form of field studies is testing small scale piles to investigate their monotonic and cyclic load-deformation behaviour and to develop analysis methods that can be used to estimate monopile behaviour under various loading scenarios. These studies focus on evaluating the load-deformation behaviour up to failure under monotonic loading, as well as examining the variation in hysteretic response and the accumulation of deformations during cyclic loading. One such study is the PISA field testing project, which involved testing piles instrumented with fibre-optic strain gauges, inclinometers, and displacement transducers in order to obtain the displacement and rotation profiles along the length of the piles and to derive the soil reaction curves (Burd et al., 2020a). Three different pile diameters (D_p) were selected for the tests: the small piles had a diameter of 0.273 m, while the medium and large piles had diameters of 0.762 m and 2.0 m, respectively. The embedment depths (L_p) were selected such that the slenderness ratios (L_p/D_p) ranged between 3 and 10, falling within the typical range observed for monopiles supporting OWTs in the field. Although the PISA project primarily focused on monotonic tests, a limited number of cyclic tests were also conducted to investigate ratcheting, as well as the variation in pile stiffness and hysteretic response with the N. The results of the cyclic tests were analysed by Beuckelaers (2017) as part of the development of his generalised Winkler foundation model.

Beuckelaers (2017) analysed the cyclic test data to examine the variation of the lateral hysteretic foundation damping ratio (ξ_y) and the rotational hysteretic foundation damping ratio (ξ_θ) separately. The results showed that both ξ_y and ξ_θ increase with cyclic load amplitude, which can be attributed to the increasing nonlinearity of the soil around the piles. Furthermore, the results showed that the loading rate (or frequency) has a minimal impact on the hysteretic response. With respect to the number of cycles (N), the results were analysed in terms of ξ_θ, which showed that ξ_θ marginally decreases with increasing N for both the clayey soil at the Cowden site and the sandy soil at Dunkirk. However, due to the limited number of large-scale cyclic tests and the scatter observed in sensor readings, it was challenging to derive an empirical formula to characterise the variation of the hysteretic foundation damping ratios with N.

2.11.2 Laboratory studies

Several research studies have investigated the behaviour of monopiles using small-scale laboratory tests. These experiments are highly cost-effective compared to full-scale field testing and enable the examination of monopile behaviour under various soil conditions and complex loading scenarios. Laboratory tests can be conducted under normal gravity conditions (1g) or under artificially increased gravity levels (Ng) using a centrifuge, in order to replicate the stresses imposed on the soil in the field. However, because centrifuge testing is costly and requires extensive sample preparation and post-processing, the majority of laboratory studies have been conducted under 1g conditions. Laboratory studies can also be referred to as physical modelling studies. One of the earliest physical modelling studies was conducted by Lombardi et al. (2013) to investigate the variation in natural frequency and damping ratio of a scaled wind turbine model supported by a

monopile foundation embedded in kaolin clay and subjected to cyclic lateral loading for up to 172,000 cycles. The physical model had a scale of 1:100 and replicated the 3 MW Vestas V90 wind turbine. Environmental loads were applied to the scaled model using an electro-dynamic actuator, and accelerations and displacements at the pile head and top of the pile were measured using accelerometers and linear variable differential transformers (LVDTs). The pile was installed using controlled jacking, and the excess pore water pressure generated during installation was allowed to dissipate prior to the initiation of the dynamic tests. Dynamic tests were subsequently conducted by applying loads of varying amplitudes over different numbers of cycles (N). Following the completion of a dynamic test for a given N, the load applied by the actuator was removed, and the damping ratio and natural frequency of the scaled OWT model were determined from a free vibration test induced by a hammer impulse. The main finding of the study conducted by Lombardi et al. (2013) is that the damping ratio of OWTs installed in soft clay increases with the number of loading cycles. This behaviour is likely attributed to the softening of the soil surrounding the monopile, caused by the accumulation of excess pore water pressure.

Abadie (2015) conducted physical model tests on monopiles subjected to high-cycle loading to characterise the evolution of their hysteretic load-deformation behaviour. The experiments focused on the three key aspects of monopile cyclic behaviour: ratcheting, and the variation of hysteretic foundation damping and stiffness as loading continues. The main aspect that differentiates this physical model study from previous laboratory investigations is its effort to relate the shape of hysteretic loops under one-way and two-way cyclic loading to the underlying yielding mechanisms, specifically, whether the response resembles pure kinematic hardening or combined kinematic-isotropic hardening. Understanding the underlying yielding mechanism is essential for developing constitutive models of foundations that can accurately capture the nonlinear hysteretic response of monopiles. To replicate the field behaviour of monopiles supporting OWTs in laboratory-scale physical models, appropriate scaling laws were applied to ensure that the governing mechanisms are reliably represented. Abadie (2015) adopted the scaling framework proposed by Leblanc et al. (2010), which defines a set of dimensionless parameters to represent the actual physical parameters. The physical model experiments were conducted on piles installed in dry sand in order to reproduce the behaviour of soil under drained conditions. Under two-way cyclic loading, Abadie (2015) found that the response of the hysteretic moment-rotation loops adheres to some extent the extended Masing rules (discussed in section 2.2.2) and can be captured with the kinematic hardening mechanism. However, under one-way or non-zero-mean cyclic loading, the physical modelling results indicated that the foundation behaviour can no longer be accurately captured using pure kinematic hardening, as the monopile exhibited ratcheting, leading to deviations of the unloading-reloading loops from the extended Masing rules. Furthermore, the cyclic tests revealed that as N increases, the monopile response becomes progressively stiffer due to soil densification, and the resulting load-deformation loops become tighter, indicating reduced plastic energy dissipation.

Based on the physical model tests performed by Abadie (2015), the degradation of the rotational foundation damping ratio (ξ_θ), computed from the moment-rotation loops at the mudline, with increasing N is shown in Figure 2.30.

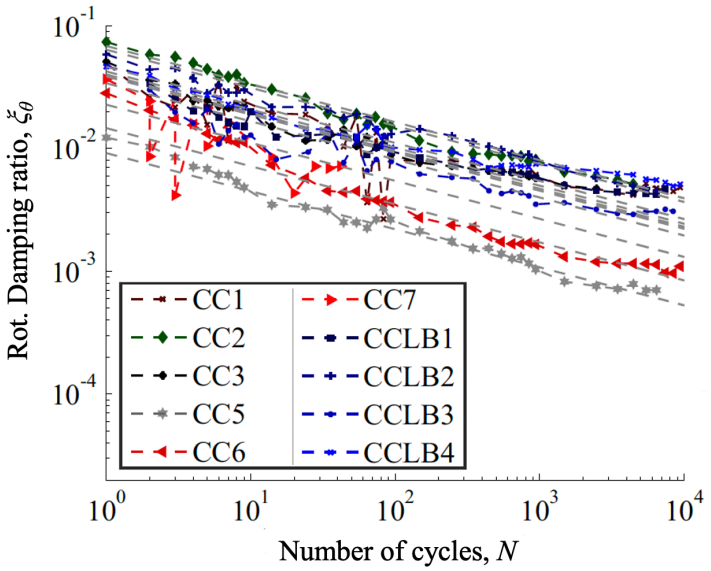


Figure 2.30: Degradation of ξ_θ with N (modified after Abadie, 2015)

Richards (2019) carried out a physical modelling study on monopiles to validate the findings of Abadie (2015) and other prior experimental studies, and to investigate the hysteretic response of monopiles installed in both dense and loose sand subjected to multidirectional cyclic loading. Richards (2019) confirmed the observation made by Abadie (2015) that monopile behaviour under two-way cyclic loading with a small number of cycles closely follows the extended Masing rules, but deviates from them under high-cycle or non-zero mean cyclic loading. Furthermore, Richards (2019) confirmed the trend observed in Figure 2.30, where the rotational foundation damping ratio (ξ_θ) reduces with the number of cycles (N). Richards (2019) also noted that the monopile dissipated more plastic energy under multidirectional cyclic loading than under unidirectional loading. This observation could be attributed to the monopile disturbing a larger volume of soil during multidirectional loading than during unidirectional loading.

Physical model tests on small-scale monopiles installed in dry sand were conducted by Jindal et al. (2024) to investigate the effects of slenderness ratio, cyclic load amplitude, loading frequency, and number of cycles (N) on the distributed lateral foundation damping (ξ_y) along the monopile embedment depth. The experiments were conducted for slenderness ratios (L_p/D_p) ranging from 3.75 to 7.5, with loading frequencies between 0.1 Hz and 5 Hz, and up to 50,000 loading cycles. The main finding from this physical modelling study is that the distributed ξ_y profile along the monopile embedment depth (Figure 2.31) is non-uniform and exhibits a nonlinear distribution, with a distinct maximum at one depth and a minimum at another. Jindal et al. (2024) observed that the maximum value of ξ_y occurs near the depth where the soil reaction is greatest, while the minimum ξ_y corresponds to the depth near the point of rotation, where the pile experiences the least soil

reaction. According to the locations of the maximum and minimum ξ_y, the distributed ξ_y profile can be divided into three segments as shown in Figure 2.31. By analysing the distributed damping profiles for various piles under different loading amplitudes, Jindal et al. (2024) observed that the positions of maximum and minimum ξ_y shift upward or downward depending on the slenderness ratio (L_p/D_p) and the magnitude of the cyclic load. The results showed that as L_p/D_p decreases and the magnitude of the cyclic load increases, the depths at which maximum and minimum ξ_y occur shift downward. With regard to loading frequency, Jindal et al. (2024) found that for frequencies between 0.1 Hz and 5 Hz, the distributed ξ_y profile exhibited minimal variation, indicating that the effect of loading frequency can be considered insignificant. Furthermore, although the experimental results showed that the distributed ξ_y decreases with the number of cycles (N), this effect is most pronounced up to around 100 cycles and becomes negligible beyond 10,000 cycles. Jindal et al. (2024) attributed the reduction in damping with increasing N to the stiffening of the soil around the monopile as it becomes denser, confirming the observations noted by Abadie (2015), and Richards (2019).

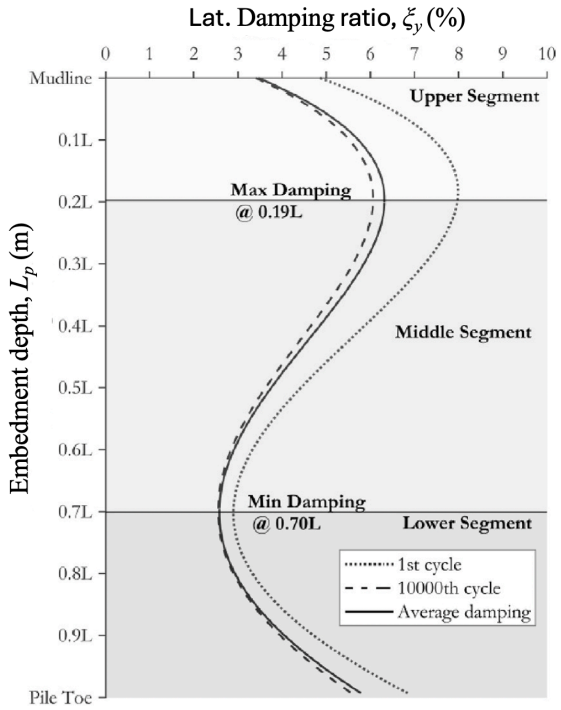


Figure 2.31: Distributed ξ_y profile with embedment depth (modified after Jindal et al., 2024)

Centrifuge model tests at 50g were conducted by Takahashi et al. (2022) to reproduce the behaviour of monopiles in the field subjected to loading frequencies ranging from 0.002 Hz to 0.4 Hz. Unlike the aforementioned 1g physical studies, the centrifuge tests were conducted on saturated dense sand to examine the effect of excess pore water pressure development on the variation of the hysteretic response and the degradation of monopile resistance. The centrifuge modelling was performed for monopiles with slenderness ratios of 3.75, 5, and 8, embedded in dense sand reconstituted using the air pluviation method to a relative density of 80%. Based on the analysis of the force-displacement

and moment-rotation hysteretic loops at the mudline level, Takahashi et al. (2022) observed that the hysteretic foundation damping ratios (ξ_y and ξ_θ) decreased with the number of cycles initially, before quickly stabilising and reaching a steady state. Furthermore, based on the analysis of the hysteretic damping ratios from tests conducted at different slenderness ratios, Takahashi et al. (2022) observed that the hysteretic damping decreases for the same normalised displacement (y_g/D_p) at the mudline level as the slenderness ratio increases. Takahashi et al. (2022) justified this observation by arguing that a monopile with a lower slenderness ratio causes greater plastic deformation in the soil around the deeper portion of the pile than a monopile with a higher slenderness ratio, even though both experience the same normalised displacement (y_g/D_p) at the mudline level. A monopile with a lower slenderness ratio tends to undergo rigid-body rotation, thereby inducing greater soil plasticity, whereas a monopile with a higher slenderness ratio bends below the ground surface and induces significantly less plastic deformation near its tip.

2.11.3 Numerical modelling studies

Foundation damping and its influence on the overall dynamic behaviour of OWTs can be investigated through numerical analyses, which provide valuable insights into expected damping values under various ground conditions and monopile configurations. A key advantage of numerical modelling is its ability to explicitly represent monopile-soil interaction, enabling the damping contribution of the foundation to be isolated from other sources of energy dissipation. According to the literature, hysteretic foundation damping is incorporated into the dynamic analysis of OWTs using various modelling approaches, primarily through 3D and 1D FE models. The damping arising from soil-monopile interaction is typically captured either by applying viscous damping or by using incremental constitutive models that allow for nonlinear foundation stiffness, thereby reproducing hysteretic load-deformation behaviour under cyclic loading.

Damgaard et al. (2013b) conducted 1D FE analyses to determine the global foundation damping ratios (ζ_f) for a 3 MW OWT, incorporating soil-structure interaction through the Winkler foundation model. The distributed soil reactions along the depth of the monopile were represented using the API p-y curves. Static load simulations, based on wind speeds prior to rotor-stop tests, were used to displace the monopile. The resulting soil reactions were transformed into idealised hysteretic load-displacement loops, which were subsequently converted into equivalent viscous dashpots distributed along the pile depth. By integrating the equivalent viscous dashpots into the 1D FE computational model, the computed ζ_f values varied in the range of 0.8-1.27%. Similarly, Carswell et al. (2015) performed numerical analyses using a two-dimensional (2D) FE model incorporating foundation damping to determine ζ_f for a 5 MW OWT, based on the logarithmic decrement approach. The numerical models excluded hydrodynamic and aerodynamic damping, allowing the study to focus primarily on the contribution of foundation damping. However, instead of representing the soil-monopile interaction using the Winkler approach, foundation damping was incorporated via a macro-element approach with a lumped rotational viscous dashpot placed at the

mudline level. Furthermore, the rotational viscous damping coefficient was determined based on the total dissipated energy in the soil continuum surrounding the monopile calculated from static 3D FE analyses. From the analysis of the free-decay response of the 2D FE model, ζ_f fell within the range of 0.17-0.28%. Carswell et al. (2015) also studied the impact of including foundation on the moment at the at the mudline level during an extreme storm event. Figure 2.32 compares the moment time histories from two analyses: one incorporating foundation damping via a rotational viscous dashpot, and the other excluding foundation damping. The results show that foundation damping leads to reduced moments at the mudline level. Carswell et al. (2015) found that including foundation damping resulted in a 7-9% reduction of the maximum mudline moment during an extreme storm event.

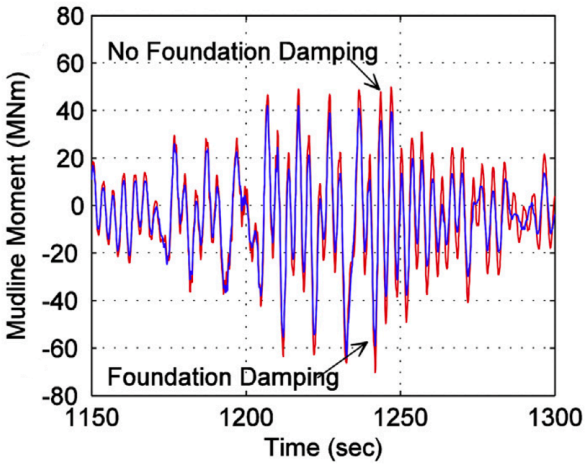


Figure 2.32: Moment time histories with and without foundation damping (modified after Carswell et al., 2015)

Malekjafarian et al. (2019) conducted a 3D FE analysis study to evaluate ζ_f using the logarithmic decrement approach for a 10 MW OWT, modelled with the commercial software Plaxis 3D. The soil surrounding the monopile was modelled using 10-node tetrahedral volume elements. The portion of the monopile below the mudline was represented with plate elements, while the section above the mudline and the tower were modelled using beam elements. To simulate the free vibration response of the OWT, a static load was initially applied at the RNA level to generate deformation corresponding to the first mode shape, followed by releasing the load to allow the structure to freely vibrate under dynamic analysis. The numerical analyses excluded all damping sources except hysteretic soil damping; therefore, the decay of the response of the OWT structure during free vibration is primarily attributed to foundation damping. Malekjafarian et al. (2019) determined ζ_f for each cycle during the free vibration response and found that, as the amplitudes decayed, ζ_f decreased from about 1.11% to 0.41%.

To promote the utilisation of advanced 3D FE simulation tools in the analysis of modern OWTs supported on large-diameter monopiles, Kementzetzidis et al. (2019) conducted a comprehensive 3D FE modelling study. The study examined the influence of environmental load intensity, as well

as ground conditions such as relative density and permeability, on the dynamic behaviour of the soil-monopile-OWT system. Additionally, it focused on the development of excess pore water pressure and its effects on the global damping ratio and the evolution of the fundamental natural frequency of the OWT during dynamic simulations. The analyses were conducted for an 8 MW OWT using the OpenSees simulation platform, with the advanced SANISAND04 constitutive model adopted to simulate the cyclic behaviour of sand. The SANISAND04 model was chosen due to its capability to simulate the behaviour of sand for different relative densities using a single set of parameters. Simulations were carried out for relative densities of 40%, 60%, and 80%, under three environmental loading conditions: two storm scenarios with average wind speeds of 47 m/s and 24 m/s, and one mild loading case. After each loading event, the lateral loads were removed to allow the structure to undergo free vibration, from which the global foundation damping ratios (ζ_f) were calculated. From the free-decay simulations, the ζ_f values ranged between 0.76% and 7.7% for the 8 MW OWT supported on a monopile foundation with diameter of 8 m and embedded 27 m into the ground. The analysis results showed that ζ_f values were higher under more extreme loading scenarios and for the ground condition with the lowest relative density (40%), which can be attributed to the increased nonlinearity of the soil surrounding the monopile. Although the ζ_f values obtained in this study were notably higher than those reported in field monitoring investigations, Kementzetzidis et al. (2019) noted that the simulations conducted under mild loading produced ζ_f values consistent with those observed in the field. The main conclusion from the numerical modelling study conducted by Kementzetzidis et al. (2019) is that excess pore water pressure generation has a significant impact on the dynamic behaviour of OWTs, primarily due to the increased nonlinearity it induces in the soil domain.

Carswell et al. (2022) conducted a numerical study using a methodology similar to that of Carswell et al. (2015) to investigate the effect of foundation damping on cyclic moment demand under power production, emergency shutdown, and parked design conditions. The simulations were carried out for a 5 MW OWT, and foundation damping was incorporated using a rotational viscous dashpot calibrated through iterative 3D FE analyses. Results from dynamic time-domain analyses showed that foundation damping can significantly reduce cyclic moment demand by approximately 30% during power production, 25–33% during emergency shutdown, and 2–3% under parked conditions. As a result, Carswell et al. (2022) emphasised that incorporating foundation damping in numerical analyses can reduce costs by minimising steel usage and improve the accuracy of fatigue design assessments of OWTs.

Panagoulias et al. (2023) carried out 3D FE simulations to investigate the hysteretic foundation damping using the logarithmic decrement approach, adopting the HSsmall constitutive model to represent the behaviour of the soil for an actual offshore wind farm in the North Sea. The HSsmall parameters were obtained from correlations with CPT data, and calibration against monotonic and cyclic laboratory element tests. The procedure used to simulate the free-decay response follows that

of Malekjafarian et al. (2019), in which the OWT is displaced by applying a lateral load at the RNA level, followed by removing the load and initiating dynamic simulations. The global foundation damping ratios (ζ_f) obtained from the free vibration simulations by Panagoulias et al. (2023) are plotted in Figure 2.33 as a function of lateral monopile displacement at the mudline.

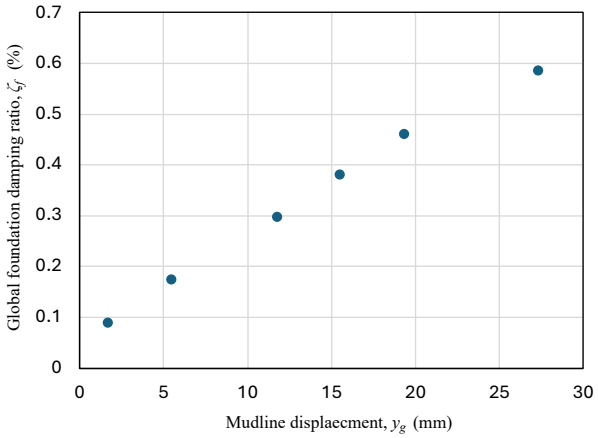


Figure 2.33: ζ_f versus mudline displacement (modified after Panagoulias et al., 2023)

Vo (2022) conducted an extensive 3D FE modelling study to develop empirical correlations between monopile deformations at the mudline and the global foundation damping ratio (ζ_f). The Plaxis 3D software package was used to perform free-decay simulations for a 3.6 MW OWT installed in sand. To reproduce the hysteretic behaviour of soil in the 3D FE analyses, Vo (2022) adopted the HSsmall constitutive model and determined the values of the parameters based on the commonly used empirical formulas in the literature. To generate correlations between monopile deformations and ζ_f, a series of simulations was conducted to investigate the effects of monopile dimensions, specifically monopile diameter and embedment depth. Vo (2022) performed logarithmic decrement analyses for monopiles with diameters between 4.0 m and 5.0 m and embedment depths varying from 19.2 m to 38 m. The main observation from the numerical analyses was that, for monopiles of varying dimensions subjected to the same lateral displacements and rotations at the mudline, ζ_f increased as the embedment depth and monopile diameter decreased. Furthermore, Vo (2022) found that the influence of embedment depth (L_p) on ζ_f depends on its proximity to the critical pile length, which is the depth beyond which further increases in embedment have no significant effect on the pile head response. The analyses showed that as L_p approaches the critical length, its influence on ζ_f gradually diminishes, and once L_p exceeds the critical length, its effect on ζ_f becomes negligible.

Ryan et al. (2025) conducted a numerical study to estimate the global foundation damping ratio (ζ_f) for the reference IEA 15 MW wind turbine (Gaertner et al., 2020), using the Winkler-based 1D modelling approach with the PISA rule-based soil reaction curves for cohesive soils. The cyclic load-deformation behaviour of each soil reaction curve is modelled using kinematic hardening based on the parallel Iwan model, assuming Masing-type hysteresis. In contrast to previous studies that estimated ζ_f from free-decay simulations, Ryan et al. (2025) performed two-cycle analyses to

calculate the total energy dissipated by the soil ($W_{D,soil}$) from load-deformation loops along the monopile, and the total elastic energy stored in the OWT system ($W_{S,soil+foundation+tower}$), using these values in Equation 2.13 to compute ζ_f. The variation of ζ_f with the lateral displacement at the mudline is shown in Figure 2.34.

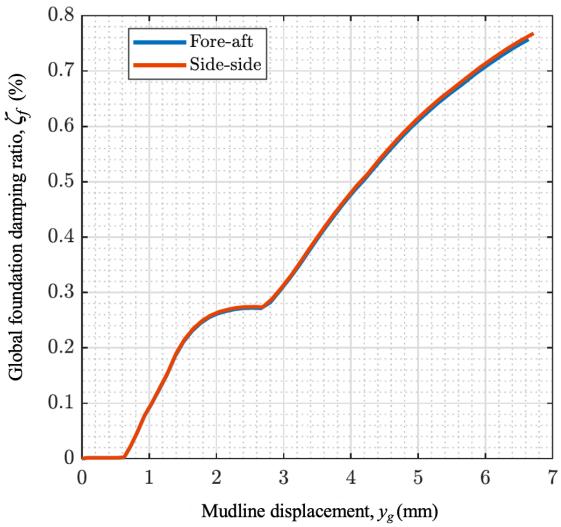


Figure 2.34: ζ_f versus mudline displacement (modified after Ryan et al., 2025)

2.12 Research gap

The primary research gap identified in the reviewed studies is the limited investigation into how foundation damping varies with key monopile design parameters, including monopile diameter (Dp), embedment depth (L_p), and slenderness ratio (L_p/D_p), as well as with varying ground conditions, represented by relative density (D_r). Although these factors have been examined to some extent in previous physical and numerical modelling studies, a comprehensive understanding of their influence on foundation damping remains lacking, particularly for large OWTs with capacities of 15 MW or more, which may require monopiles exceeding 10 m in diameter. This research aims to address that gap through 3D FE analyses, incorporating advanced soil constitutive models capable of capturing cyclic soil nonlinearity. The foundation damping parameters investigated in this research are:

(1) Hysteretic foundation damping ratios (ξ_y and ξ_θ): derived from force-displacement and moment-rotation loops at the mudline and from distributed reactions along the monopile depth.
(2) Global foundation damping ratio (ζ_f): Derived from free-decay simulations and is the damping ratio of entire OWT system due the energy dissipated by the hysteretic behaviour of the soil surrounding the monopile.

Investigating foundation damping at different levels, both globally for the entire OWT system and locally from load and deformation loops at the mudline and along the monopile depth, provides a more complete understanding of how monopile geometry and ground conditions influence dynamic soil-structure interaction in OWTs.

2.13 Conclusions

Understanding the soil-structure interaction in monopile-supported OWTs is a complex topic, as the behaviour of the monopile, which influences the dynamic characteristics of the OWT structure, is heavily dependent on the surrounding soil dynamic and monotonic response . Consequently, this chapter began by introducing the dynamic behaviour of soil and its key parameters, namely the secant shear modulus and the hysteretic damping ratio, followed by outlining and discussing the various factors that affect these parameters. The monotonic behaviour of soil was also examined, focusing on shear strength envelopes and key reference states, including the critical state, the steady state, and the phase transformation and characteristic lines. Understanding the critical state is especially important, as it forms the theoretical basis for many advanced constitutive soil models developed in recent years.

Given that the objective of this research is to implement 3D FE analyses to investigate foundation damping, a brief overview of the plasticity theories commonly used in constitutive modelling was also presented. The chapter then proceeded to review the various approaches commonly used to analyse the soil-structure interaction of OWTs and to introduce the different foundation damping parameters. Since this research focuses on foundation damping, the relevant literature was reviewed across field testing, laboratory testing, and numerical modelling studies. The chapter concluded by identifying the main research gap, which concerns the influence of monopile dimensions and ground conditions, particularly relative density, on foundation damping parameters.

Although foundation damping has been addressed in numerous studies, particularly through the development of models that capture soil hysteresis and provide methods for estimating foundation damping, a comprehensive understanding of how it varies with monopile dimensions and ground conditions is still lacking. The literature reviewed in this chapter indicates that the effect of monopile geometry has received only limited attention. For example, the physical modelling studies by Jindal et al. (2024) and Takahashi et al. (2022) examined the influence of slenderness ratio and noted some initial observations. However, further detailed investigation is needed, particularly through numerical modelling, which avoids the limitations inherent in physical testing such as scaling effects and instrumentation constraints that can introduce inaccuracies.

In addition, while Vo (2022) studied the effects of monopile diameter and embedment depth, the constitutive model was calibrated using empirical formulas rather than through rigorous calibration based on laboratory element tests. Moreover, the analyses conducted by Vo (2022) focused solely on the global foundation damping ratio (ζ_f). For a more complete understanding of foundation damping, it is also necessary to examine the local hysteretic damping ratios (ξ_y and ξ_θ), which are derived from load-deformation and moment-rotation loops at the mudline and from distributed reactions along the embedded depth of the monopile.

The foundation damping parameters (local and global) derived in this study are of significant importance, as they apply to large OWTs with a capacity of 15 MW, which are expected to become standard in future developments. As a result, these parameters can be incorporated directly into integrated OWT analysis tools such as OpenFAST and HAWC2 to assess the overall response of monopile-supported OWTs.

Chapter 3

Materials and Experimental Methods

3.1 Introduction

This chapter provides detailed information on the physical characteristics of the tested granular materials, triaxial apparatus used for the experiments, bender element system employed to measure small-strain stiffness, methodology for sample preparation, and the equations used for analysing the test results. The physical characteristics of the soils are discussed in terms of grain size distribution, density limits, and specific gravity. Determining these properties is essential, as they help interpret the triaxial test results and explain differences in the mechanical behaviour of the tested materials. Furthermore, to prepare samples to different relative densities (i.e., void ratios), it is necessary to determine the maximum and minimum densities along with the specific gravity of the soil. The physical characteristics of Blessington sand, which is one of the materials tested in this study, are compared with values reported in previous studies on the same soil to assess whether the results obtained in this research fall within the expected range for Blessington sand.

The various components of the triaxial testing apparatus, along with the load and displacement measurement sensors, are described in detail. In addition, the configuration and setup of the bender element testing system are also thoroughly explained. The chapter outlines the selected method for preparing the triaxial test specimens, which is moist tamping with undercompaction, and provides a rationale for choosing this technique over other available soil reconstitution methods. Furthermore, the key stages of the testing procedure, saturation, consolidation, and loading, are discussed in detail.

The methodology and equations used to determine the different types of stresses and strains, as well as to compute the dynamic parameters (i.e., the secant shear modulus and hysteretic damping ratio), are also presented. Some of the limitations encountered during the testing campaign, such as challenges associated with the radial LVDT readings, are addressed. Given that the experimental results from the triaxial tests, which are presented in Chapter 5, form the basis for calibrating soil constitutive models in the 3D FE analyses, it is important to provide the reader with a clear understanding of the laboratory procedures and how the relevant parameters were derived.

3.2 Tested materials

Two different sand materials are tested in this research, sourced from two separate quarries in the Republic of Ireland. The first sand is taken from Blessington quarry while the second is from Kilmuckridge quarry. Samples from both sites were taken from shallow depths, with Blessington sand extending to a depth of approximately 3 m below the ground, while Kilmuckridge sand was collected from the surface level. The particle size distribution (PSD) curves for Blessington and Kilmuckridge sands are shown in Figure 3.1. From the PSD curves, the average values of the mean grain size (d_{50}), the grain size at 10% finer (d_{10}), the grain size at 60% finer (d_{60}), uniformity coefficient (C_u), coefficient of curvature (C_c), and the fines content are determined for both sands and are summarized in Table 3.1. Based on the average C_u values, both Blessington and Kilmuckridge sands are uniformly graded. The average d_{50} values indicate that Blessington sand is fine, while Kilmuckridge sand is medium-coarse. Furthermore, Table 3.1 shows that Blessington sand has more fines content than that of Kilmuckridge sand.

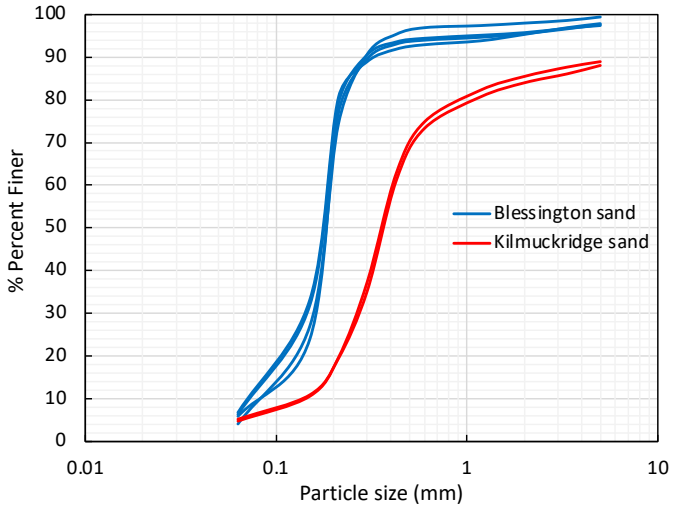


Figure 3.1: Particle size distribution curves of Blessington and Kilmuckridge sands

Kirwan (2015) performed PSD analyses on Blessington sand samples taken from depths of 1.75 m to 11.5 m below ground level. The mean values of d_{10}, d_{50}, d_{60}, C_u, and fines content were 0.093 mm, 0.191 mm, 0.21 mm, 2.42, and 8.3%, respectively. A comparison between the PSD results reported by Kirwan (2015) and those obtained in this study (Table 3.1) shows that the values are closely aligned, confirming that the grain size characteristics determined in this research are representative of Blessington sand. Although there are some minor differences, such as the slightly higher mean fines content reported by Kirwan (2015) compared to that found in this study, these variations are likely due to natural differences in the samples, as they were collected from nearby but not identical locations within the Blessington quarry. Due to the lack of published tests on the physical characteristics of Kilmuckridge soil, it is not possible to confirm whether the characteristics obtained from the samples tested in this research are fully representative of that material.

The specific gravities (G_s) of both soils are determined using the pyknometer method according to BS 1377 (Part 2: 1990). The average G_s of Blessington sand, based on three pycnometer tests, is 2.675, while that of Kilmuckridge sand is 2.640. Limiting density tests were performed according to BS 1377 (Part 4:1990) to determine the maximum and minimum dry densities and the corresponding minimum and maximum void ratios. For Blessington sand, the maximum dry density is 1793.41 kg/m³, corresponding to a minimum void ratio of 0.492, while the minimum dry density is 1351.35 kg/m³, yielding a maximum void ratio of 0.980. Kirwan (2015) also conducted limiting density tests on Blessington sand in accordance with BS 1377 (Part 4:1990), and by assuming a specific gravity (G_s) of 2.670, determined the maximum and minimum void ratios to be 0.856 and 0.412, respectively. These values are close to those determined in the present study, further supporting that the physical characteristics established in this research are representative of Blessington sand. For Kilmuckridge sand, the maximum and minimum dry densities are 1942.20 kg/m³ and 1562.19 kg/m³, corresponding to minimum and maximum void ratios of 0.360 and 0.691, respectively. Accurate determination of limiting densities is crucial as it allows recreating the soil samples to the correct relative densities in the field. Several methods exist according to different standards to estimate the limiting densities, which can yield drastically different results. Lunne et al. (2019) investigated the variation in limiting densities using different methods. Their study revealed that, for six types of sand tested across seven different standards, the variation in minimum dry density was smaller than the variation in maximum dry density. Methods for determining maximum dry density can generally be classified as vibration, compaction, or tamping methods. The ASTM standard methods for estimating maximum dry density are all vibrational, utilising a shaking table machine to apply vibration. In contrast, the British Standard method BS 1377 (Part 4:1990) employs vertical compaction, where a vibrating hammer is used to compact soil within a standard-sized mould. Although ASTM methods may be more suitable than the British Standard method, as compaction can cause grain crushing and alter the grain characteristics of soil, the lack of specialised vibration equipment required for ASTM methods necessitated the use of the British Standard method to determine the maximum dry densities.

Table 3.1: Grain size characteristics of Blessington and Kilmuckridge sands

Material	d10 (mm)	d50 (mm)	d60 (mm)	Cu	Cc	Fines content
Blessington	0.089	0.179	0.192	2.218	1.476	5.061
Kilmuckridge	0.169	0.386	0.429	2.546	1.252	0.602

It is important to note that this research primarily focuses on Blessington sand, which makes up the majority of samples used in the triaxial tests and is the material calibrated with constitutive models to simulate soil response in the 3D FE simulations. Only a limited set of cyclic triaxial tests is conducted on Kilmuckridge sand to examine differences in dynamic soil behaviour, specifically in terms of damping and shear stiffness, between the two sand types. The variation in dynamic soil

behaviour based on different particle size distributions is compared with findings from previous studies. Finally, the behaviour of Kilmuckridge sand can serve as a benchmark to verify whether the behaviour of Blessington sand is suitable as a representative material for analysing the response of OWTs installed in sandy soils.

3.3 Triaxial apparatus

The advanced cyclic triaxial apparatus used in this project, procured from Global Digital Systems (GDS), is known as the Advanced Dynamic Triaxial Testing System (DYNTTS). This high-performance testing device is designed to conduct both stress-controlled and strain-controlled tests with exceptional precision and is capable of applying cyclic loading at frequencies of up to 5 Hz. The triaxial testing system is shown in Figure 3.2 and consists of the following components:

(i) Axial actuator unit
(ii) Triaxial cell
(iii) Internal load cell
(iv) Data acquisition and control unit
(v) Cell pressure controller
(vi) Back pressure controller
(vii) Pore water pressure transducer
(viii) Local LVDTs

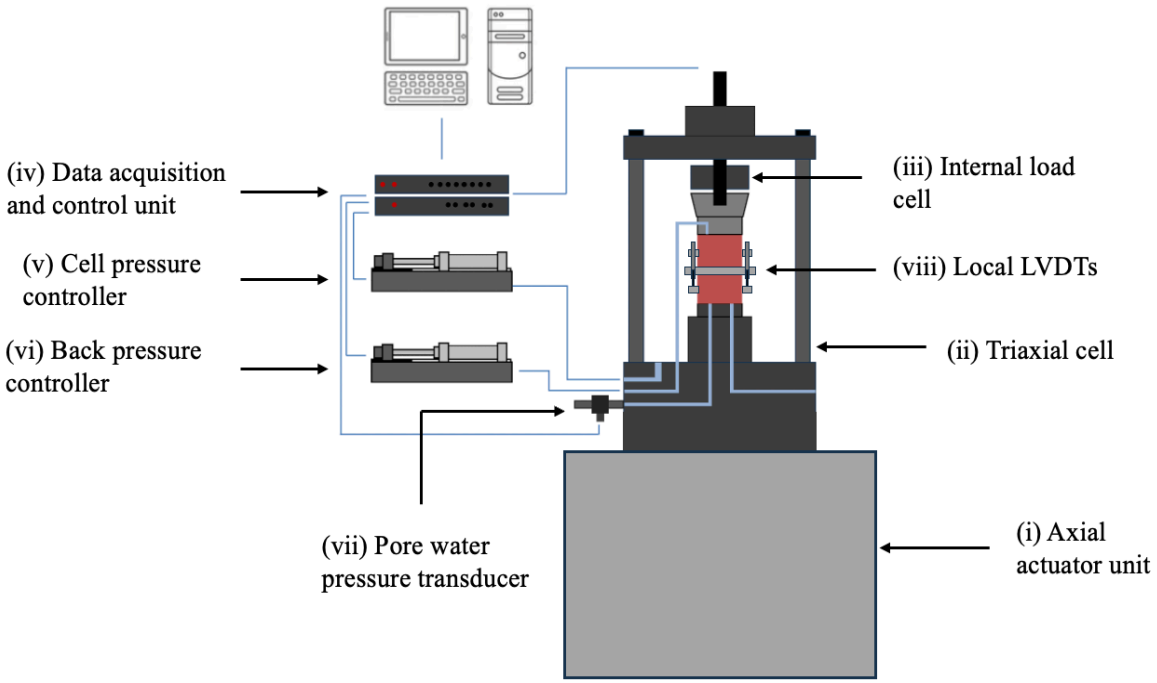


Figure 3.2: Triaxial apparatus testing system

3.3.1 Axial actuator unit

The axial actuator unit is equipped with a brushless DC servo motor that drives a ball screw via a toothed belt. The axial ram is linked to a thrust cylinder and a ball nut, both operated by the ball screw. To prevent the thrust cylinder from rotating, it is secured with a linear guide attached to the centre plate. The servo motor employs a closed-loop control system, enabling precise adjustments to the position and vertical movement speed of the axial ram. The thrust cylinder is directly connected to the axial ram, which passes through the 'balanced ram' configuration and extends out through the base of the cell. The base pedestal is also fixed to the axial ram. The axial movement range of the ram is 100 mm.

The balanced ram (illustrated in Figure 3.3) is designed to counteract the volumetric displacement caused by the loading ram entering or exiting the cell. The cell fluid is hydraulically connected via the hollow centre of the ram to a chamber where the ram passes through. Within this chamber, an annular piston is attached to the ram. The annular piston's area is precisely equal to the cross-sectional area of the ram. As the ram moves within the cell and induces a volume change, the annular piston produces an equal and opposite volume change, ensuring that the net volume change within the cell remains zero. Furthermore, the cell pressure acting on the annular piston inherently compensates for the cell pressure acting on the ram itself. This design feature ensures that the axial force capacity of the cell is unaffected by variations in cell pressure, maintaining consistent performance regardless of the applied cell pressure.

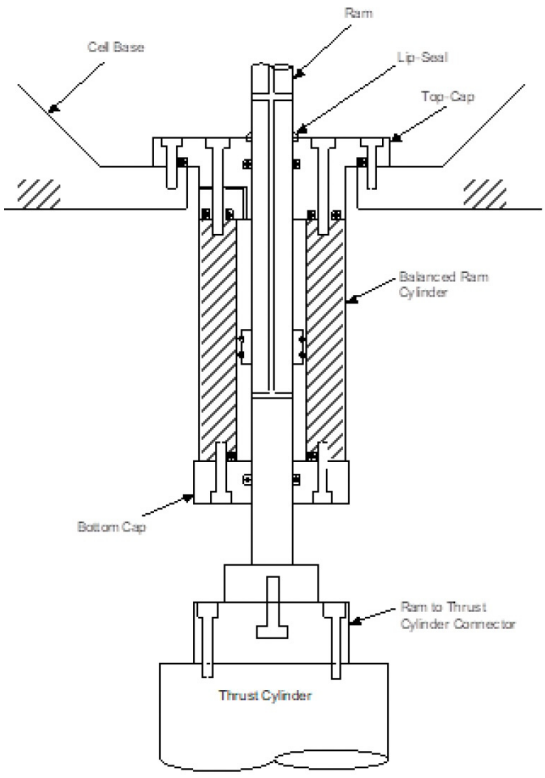


Figure 3.3: Balanced ram configuration

3.3.2 Triaxial cell

The triaxial cell (shown in Figure 3.4) is constructed from hard-anodised aluminium, offering durability and corrosion resistance. It has a maximum cell pressure capacity of 2 MPa and can accommodate samples with diameters of up to 100 mm. The triaxial cell includes an extension cap, enabling the application of extension loads. The cell is mounted and secured to the cell base with screw rods, which include ports for connecting the back pressure and cell pressure controllers, pore water pressure transducer, and allows access for the cables of the internal measuring devices such as bender elements and Linear Variable Differential Transformers (LVDTs).

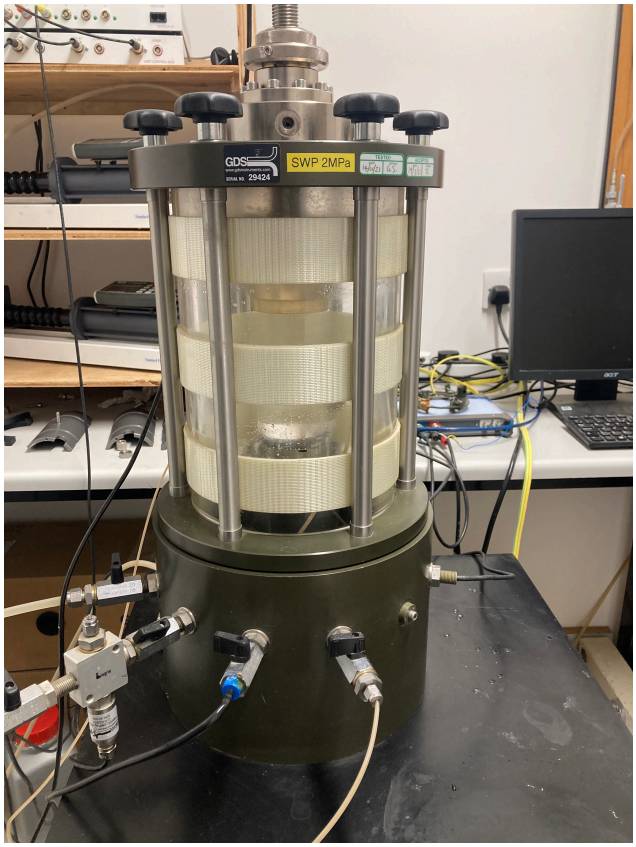


Figure 3.4: Triaxial cell

3.3.3 Internal load cell

A submersible internal load cell (shown in Figure 3.5) is used to measure the axial load subjected to the sample. The internal load cell has the unique advantage of being unaffected by pressure, removing the need for corrections for ram upthrust and ram friction. The load cell has a maximum axial load capacity of 10 kN, making it suitable for measuring the resistance of soil samples under both small and large confining stresses. The load cell was regularly calibrated using reference dead weights to ensure accurate measurements throughout the research duration.



Figure 3.5: GDS submersible load cell

3.3.4 Data acquisition and control unit

The data acquisition unit used in this research is the advanced ADVDCS V2 control system from GDS. This unit integrates a dynamic control processor with signal conditioning capabilities. The analogue signal conditioning includes an eight-channel A/D board that supplies excitation to each transducer and ensures proper zeroing and gain adjustment for each input. All inputs are processed by the dynamic control processor, which performs 24-bit analogue-to-digital conversion for high-precision data acquisition. Figure 3.6 illustrates the ADVDCS V2 control system, showing the connections for the transducers, which are plugged into the GDS ADVDCS V2 unit using individually color-coded Lemo connectors. The ADVDCS V2 control system operates with the user-friendly GDSLAB software, which facilitates test setup for various monotonic and cyclic triaxial tests while also allowing real-time monitoring of transducer readings and test results.



Figure 3.6: ADVDCS V2 control unit

3.3.5 Cell and back pressure controllers

The GDS Pressure/Volume Controllers are syringe pumps equipped with microprocessors, designed for accurate control and measurement of fluid pressure and volume changes. The cell pressure and back pressure controllers are hydraulically connected to the triaxial cell base to regulate the isotropic pressure applied to the sample and the pore water pressure within the soil sample. The pressure controller used in this setup is the Standard Pressure/Volume Controller (STDDPC), capable of applying pressures up to 2 MPa with a resolution of 1 kPa. As shown in Figure 3.7, the STDDPC pressure controller functions by pressurising and displacing liquid (typically deaerated water) within a cylinder using a moving piston. The piston is driven linearly by a ball screw

mechanism, which is rotated by an electric motor and gearbox mounted on a ball slide. Pressure is monitored through an integrated solid-state transducer. The onboard microprocessor incorporates control algorithms that allow the controller to reach a specified pressure or adjust to a desired volume change. Volume changes are accurately tracked by counting the steps of the incremental motor.

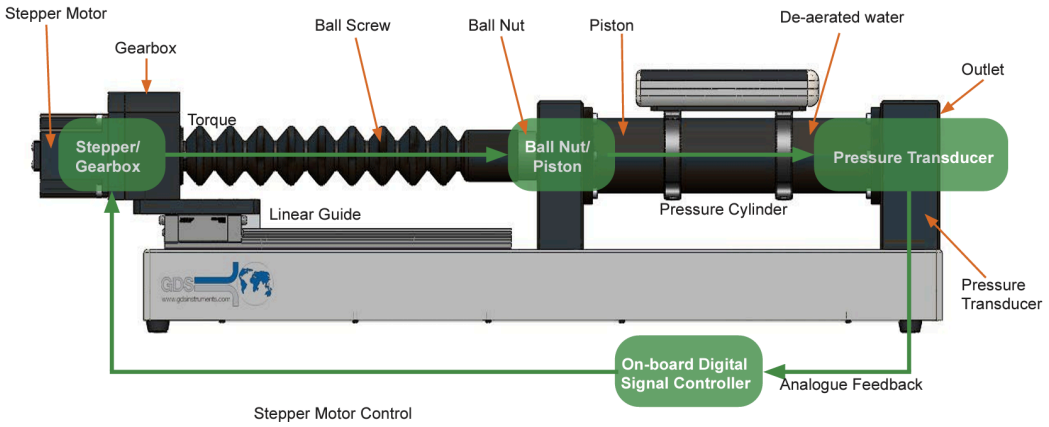


Figure 3.7: Schematic of a GDS Standard Level Controller

3.3.6 Pore water pressure transducer

The pore water pressure within the soil is measured with an external transducer attached to the cell base. The transducer (displayed in Figure 3.8), supplied by GDS, has a maximum measurement capacity of 2 MPa and a resolution of 0.01 kPa.

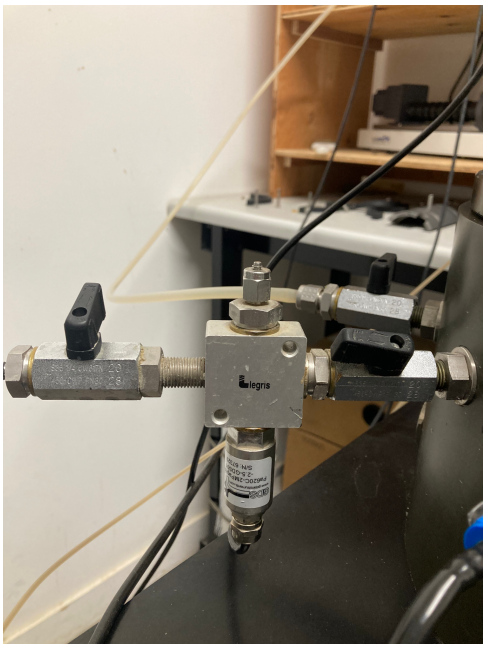


Figure 3.8: Pore pressure transducer

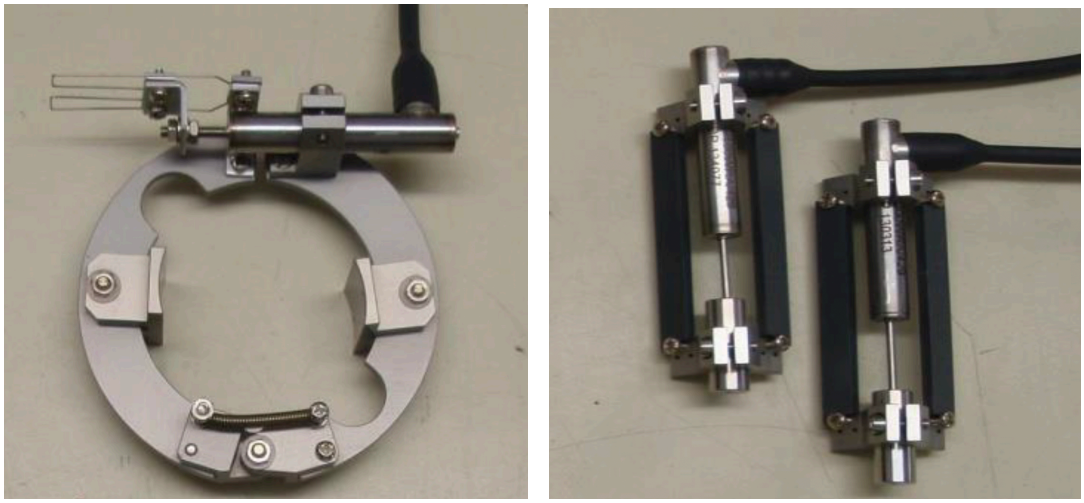
3.3.7 Local LVDTs

The determination of axial soil stiffness based on external measurements of pedestal displacement may significantly underestimate small-strain stiffness due to the compliance of various components

in the triaxial loading frame, specimen tilting, and imperfect platen-specimen bedding. These factors cause the small stress-strain behaviour to deviate from the actual behaviour of the soil in the field. To minimise errors associated with external strain measurements and accurately determine stiffness at typical strain levels below 0.1%, as experienced by most structures in the field (Burland, 1989), stiffness should be calculated using internal strain measurement methods.

Various internal strain measurement methods have been developed and utilised in the literature to accurately study the behaviour of soil. Scholey et al. (1995) provided a comprehensive review of these systems, which are generally classified into electrical and imaging methods. Electrical systems are further divided into contacting and non-contacting techniques, while imaging methods include X-ray and video tracking approaches. Examples of electrical contacting methods include mounting Local Deformation Transducers (LDTs) directly on the sample (e.g., Tatsuoka, 1988; Goto et al., 1991; Hoque et al., 1997), attaching LVDTs to measure radial strains using the radial bracket design by , or employing LVDTs to measure axial strains using the floating-type design developed by Cuccovillo and Coop (1997). Additional contacting methods involve Hall effect gauges, such as those used for measuring axial strains (e.g., Clayton and Khatrush, 1986) and radial strains (e.g., Clayton et al., 1989). Non-contacting methods include the use of proximity transducers, which operate on the principle of magnetic field attenuation as the distance between the probe and its target changes. Example of studies using proximity transducers for measuring axial and radial strains are Hird and Yung (1989), Yimsiri et al., (2009), and Ratananikom et al. (2013). The advantages and limitations of the different electrical methods are discussed by Yimsiri and Soga (2002). Imaging methods are typically employed only in highly detailed studies that focus on capturing the migration of soil grains for discrete element modelling.

The internal measurement system used in this study involves attaching LVDTs locally on the soil samples. The displacement is determined by the movement of an armature inside the core of the LVDT transducer, which induces voltage changes. A constant calibration factor is then applied to convert these voltage measurements into displacement values. The LVDTs, along with their mounting pads and brackets, are sourced from GDS. The LVDTs are attached to the middle of the soil sample to minimise the frictional effects of the end plates. Two axial LVDTs are attached to opposing sides of the sample to measure the average axial strain. The radial LVDT (shown in Figure 3.9a) is based on the design by Bishop and Henkel (1962), while the axial LVDTs (depicted in Figure 3.9b) are based on the design by Cuccovillo and Coop (1997). The LVDTs have a displacement range of ± 2.5mm and a resolution of 0.1 μm. The method used to attach the LVDTs to the sample, along with the limitations encountered in the measurements, are discussed later in this chapter.



(a) (b)

Figure 3.9: (a) Radial LVDT and (b) Axial LVDTs

3.4 Bender element testing system

Bender elements are utilised to estimate the small-strain shear modulus (G_0) of Blessington sand under varying confining stresses and relative densities. Bender elements were initially developed by Shirley and Hampton (1978) and are composed of two piezoelectric ceramic layers bonded together to function as a bimorph. Piezoelectric ceramic materials exhibit mechanical deformation when exposed to an electrical field and, conversely, generate an electric charge when they are deformed. A bender element functions as a transmitter which vibrates and propagates small strain shear waves within the soil when triggered with electrical pulses. On the other hand, a bender element acts as a receiver which produces an electrical signal when it deforms as a result of the propagated shear waves. The shear waves are generated by the bending motion of the bender elements, which occurs due to the contraction of one ceramic layer and the elongation of the other. Since the two ceramic layers are rigidly bonded together, their opposing deformations result in a bending motion. The direction of deformation of the ceramic plates is based on their orientation during manufacturing. Between the two ceramic plates, a thin metal shim layer is added for reinforcement, increasing the strength of the bender elements. Because the shear strain level resulting from bender element vibrations is generally less than 10^{-5}% (Viggiani and Atkinson, 1995), the bender element test can reliably be used to calculate G_0. Since their introduction by Shirley and Hampton (1978), bender elements have been widely adopted by researchers and integrated into various geotechnical testing devices, including the triaxial apparatus (e.g., Viggiani and Atkinson ,1995; Pennington, 1999; Fioravante, 2000; Kuwano et al., 2000), oedometer apparatus (e.g., Fam and Santamarina, 1995; Zeng and Grolewski, 2005), and resonant column apparatus (e.g., Souto et al., 1994; Fam et al., 2002).

The primary advantage of the bender element approach lies in its simplicity. It involves merely triggering a pulse at the transmitting bender element and measuring the travel time based on the output signal detected at the receiving bender element. However, interpreting the results is

challenging due to various issues associated with the hardware used, as well as near-field effects that can affect the accuracy of the results. For this reason, several studies in the literature, such as Arulnathan et al. (1998), Leong et al. (2005), and Clayton (2011), have provided recommendations for conducting the tests and interpreting the results. For example, Leong et al. (2005) proposed that to minimise near-field effects, it is recommended to apply pulses of high frequencies such that the ratio between the travel distance (from tip to tip of the two elements, L_{tt}) and the wavelength (λ) is greater than 0.33.

The setup of the bender element testing system is illustrated in Figure 3.10. The bender elements were supplied by GDS Instruments, the oscilloscope was sourced from Pico Technology, and the function generator was obtained from Thurlby Thandar Instruments (TTI). The bender elements provided by GDS Instruments are equipped with a specially designed pedestal and top cap, as shown in Figure 3.11. The bender elements are encased and securely mounted within a titanium insert, which provides high axial rigidity and resistance to corrosion. The height of the bender elements is 3 mm, ensuring adequate protrusion into the soil to effectively induce shear waves. The oscilloscope used is the PicoScope 5242D, which offers high-speed and high-resolution signal measurements. This PicoScope model features two channels, a sampling rate of 1 GS/s, and a bandwidth of up to 200 MHz. Furthermore, PicoScope 5242D can be easily connected to a computer using USB 3.0 connection, and the signals can be viewed and saved using the PicoScope 7 software which is very efficient in displaying the signals and saving them in various formats.

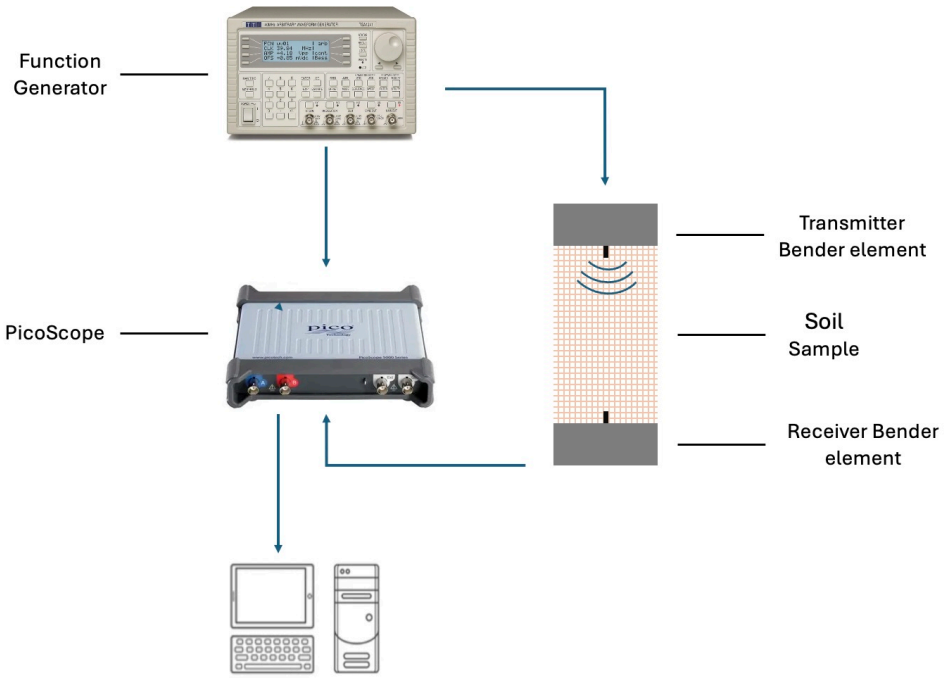


Figure 3.10: Bender element testing system

The function generator used to supply electrical pulses to the transmitter bender element is TGA 1241, which supports the generation of various arbitrary waveforms. The transmitter bender element is triggered by sinusoidal pulses with a peak-to-peak voltage of 20 volts. According to the

schematic in Figure 3.10, the function generator sends a pulse to the transmitting bender element, which produces a shear wave that propagates through the soil sample. Once the wave reaches the receiving bender element, it generates an electrical signal that is captured by the oscilloscope and displayed on the computer screen.



Figure 3.11: GDS transmitter and receiver bender elements

3.5 Triaxial test procedure

This section covers the testing procedure which is the same for both the Blessington and Kilmuckridge sands. All specimens used in the triaxial testing campaign were reconstituted to a diameter of 70 mm and a height of 140 mm. The triaxial test consists of different stages which are as follows:

(i) Sample preparation
(ii) Attaching local LVDTs
(iii) Saturation
(iv) Consolidation
(v) Shear loading

3.5.1 Sample preparation

It is widely recognised that the behaviour of two specimens prepared using different reconstitution methods at the same density varies significantly (Miura and Toki, 1982; Tatsuoka et al., 1986; Vaid et al., 1999), owing to the soil fabric, which is influenced by the deposition process. The method that is used for reconstituting the soil samples in this research is the moist tamping method. This method is chosen for its high capability to control the relative density of the reconstituted sample, as well as its ability to achieve both very loose and very dense relative densities. Due to its simplicity and reliability in consistently reconstituting samples to the same relative density, the moist tamping

method has been the preferred sample preparation method for commercial testing laboratories and research institutes, including the Norwegian Geotechnical Institute (NGI). However, the main limitation of this method is that it does not replicate the soil fabric in terms of grain orientation resulting from natural soil deposition. The grain orientation of soil samples prepared using the moist tamping method is generally random, as capillary forces restrain particle reorientation during the reconstitution process. Another limitation of the moist tamping method is that it creates a "honeycomb structure" which is susceptible to liquefaction upon saturation (Casagrande, 1976).

Several other sample reconstitution methods exist in the literature to mimic the natural soil deposition and to capture the inherent anisotropy of soil as a result of fabric effects. One such sample reconstitution method is the dry pluviation technique, which involves pouring the soil material in its dry condition from a funnel at a constant height. The method is considered suitable for reconstituting samples for soil materials of wind-blown aeolian deposits (Kuerbis and Vaid, 1988). Furthermore, depending on different techniques, the dry pluviation method can yield fairly uniform specimens (Miura and Toki, 1982). However, the method can be challenging, as it requires maintaining a constant height between the funnel tip and the soil surface, and it is difficult to reconstitute the samples to low relative densities. An additional drawback of the dry pluviation method is its tendency to consistently produce dilatative behaviour (Ishihara, 1996). Another sample preparation method is wet pluviation, in which soil is deposited into a water-filled split mould. The wet pluviation method replicates the process of sand deposition through water, commonly observed in natural environments and mechanically placed hydraulic fills. According to Oda et al. (1978), the fabric and behaviour of water pluviated soils closely resemble those of natural alluvial soils. Furthermore, studies such as that by Ghionna and Porcino (2006) compared the behaviour of undisturbed soil samples retrieved through in-situ ground freezing with that of samples prepared using various reconstitution methods. Ghionna and Porcino (2006) concluded that the wet pluviation method closely replicated the fabric of the undisturbed samples. However, while the method performs well for poorly graded soil materials, particle segregation occurs when wet pluviation is used for silty or well-graded soil samples (Kuerbis and Vaid, 1988). The wet pluviation method is also unsuitable for loose soil samples, as achieving relative densities lower than 40% is challenging (White, 2020).

Although the dry and wet pluviation methods are more representative of natural soil deposition compared to the moist tamping method, they are less effective in controlling the desired relative density and in producing loose state soil samples. For these reasons, along with simplicity and the ease of the moist tamping method, it is adopted in this research for recreating the soil samples. An additional advantage of the moist tamping method is that it produces cyclic shear strength values comparable to those of undisturbed soil samples, unlike samples prepared using other methods, which tend to exhibit lower shear strengths (Ladd, 1978).

The sample preparation method is discussed as follows with the key steps summarised in Figure 3.12:

(i) The first step in the sample preparation process involves ensuring that the tubes connected to the pedestal and top cap are clear of any blockages. This is achieved by flushing water through these tubes using the back pressure controller.

(ii) The porous stones on the pedestal and top cap must be saturated which can be done by boiling them in water for around 10 minutes. Ensuring the saturation of porous stones facilitates achieving full saturation of the soil samples.

(iii) After placing the bottom porous stone on the pedestal, a latex membrane with a thickness of 0.25 mm is stretched over the pedestal and secured with two O-rings, as shown in Figure 3.12a. The O-rings have a cross-sectional diameter of 2.5 mm and an unstretched inside diameter of approximately 85% the sample diameter.

(iv) A three-piece split mould is mounted on the pedestal, after which the membrane is pulled and folded around the top of the mould and secured with two O-rings, as shown in Figure 3.12b. The membrane is then held tightly against the split mould by applying a small vacuum.

(v) The soil is then poured and compacted into the split mould following the moist tamping procedure. This method involves adding moisture to the sample and dividing it into layers, with each layer compacted to a predetermined height. The original moist tamping method, proposed by Ladd (1978), involves dividing the sample into equal weights and compacting each layer to a predefined height within the mould, ensuring that each layer is slightly under-compacted relative to the layer above it. The moist tamping with under-compaction method was developed to achieve soil layers with homogeneous densities by compacting each layer to a lower density than the subsequent layer. This accounts for further densification that occurs in each layer as the next layer is placed and compacted. Each layer is under-compacted according to its corresponding under-compaction factor, which can be determined using the following expression proposed by Ladd (1978):

$$U_n = U_{ni} - \left[\frac{(U_{ni} - U_{nt}}{n_t - 1}\ (n-1)\right] \tag{3.1}$$

where U_n is the percent undercompaction factor, U_{ni} is the percent undercompaction factor of the bottom-most layer, U_{nt} is the percent undercompaction factor of the top-most layer, n is number of the layer being considered, and n_t is the total number of layers. The value of U_{nt} is zero, while for U_{ni}, which generally ranges between 0% and 15%, Ladd (1978) recommended performing undrained cyclic triaxial tests with varying U_{ni} values and selecting the one that yields the highest cyclic shear strength. Ladd (1978) found an optimum U_{ni} value of 5% for loose-state Monterey No. 0 sand and recommended lower U_{ni} values for soils prepared at denser states. Since conducting tests at various U_{ni} values is cumbersome, a U_{ni} value of 5% is assigned to samples prepared at 30% relative density, while samples with relative densities

of 60% and higher are assigned a U_{ni} value of 2%. The U_{ni} values used in this this research are based on the values adopted by Escribano (2014) for Hostun sand. The undercompaction approach used in this research differs slightly from the method proposed by Ladd (1978) in that the thickness of each layer is kept constant, while the mass of each layer is varied. The cumulative mass (M_n) at the top of each layer is determined based on the following expression:

$$M_n = \left(\frac{M_T}{n_t}\right) n \left(1 - \frac{U_n}{100}\right) \tag{3.2}$$

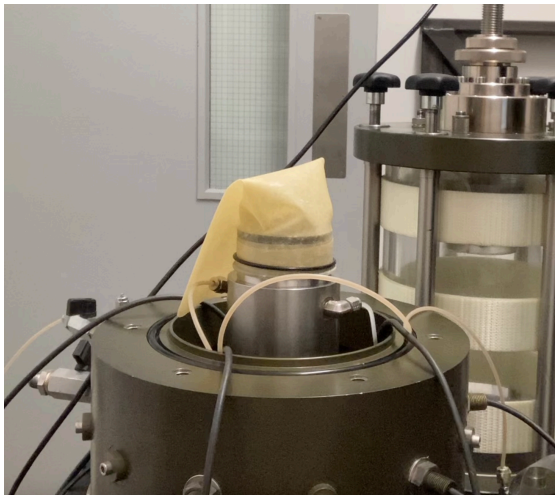
where M_T is the total mass. The moisture content is 5% for the samples prepared to 30% relative density, 10% for the samples reconstituted to 60% relative density, and 15% for the samples reconstituted to 80% and 90% relative densities. The compaction of the samples into different layers with a tamper is shown in Figure 3.12c. The diameter of the tamper is 35 mm which is half the diameter of the soil samples.

(vi) After compacting the final layer and ensuring the surface is levelled, a porous stone is placed on the top of the sample, followed by the placement of the top cap as shown in Figure 3.12d. The membrane is pulled over the top cap and secured with two O-rings. The top cap is connected to the back pressure controller, which regulates the pore water pressure within the sample and monitors the global volumetric change of the sample.

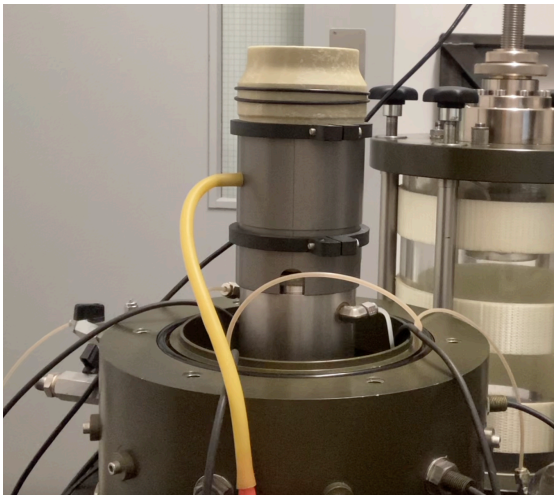
(vii) Once the top cap is secured, a small negative vacuum pressure of 20 kPa is applied. This is to ensure that the soil remains stable once the split mould is dismounted and to check if there are any leaks. If the pressure fluctuates and fails to reach -20 kPa, it indicates the presence of a leak, potentially caused by puncturing the membrane when the layers are compacted. In case a puncture is observed, it can be sealed using a Copydex glue, which is often effective in stopping the leak. Additionally, leaks may occur at the ends of the membranes. In such cases, the Copydex glue can be applied around the membrane ends to effectively seal and prevent leakage. Once it is confirmed that there are no leaks, the split mould is carefully removed from the pedestal. The soil after removing the split mould is shown in Figure 3.12e.

(viii) Measurements are taken for the diameter and height dimensions of the sample. The height is measured at four different sides of the sample and the average height is calculated. For the average diameter, measurements are taken at three different heights along the sample, with two diameter readings recorded at each height.

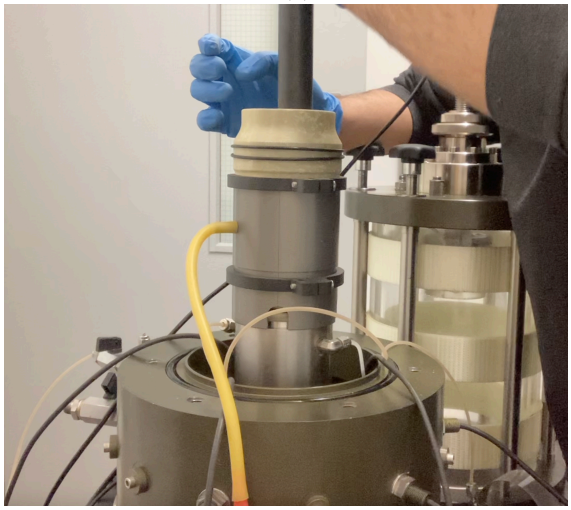
(ix) Finally, for the bender element tests, the orientation of the receiver bender element at the pedestal should be marked. This is to ensure that the orientation of the transmitter bender element at the top cap aligns with that of the receiver bender element.



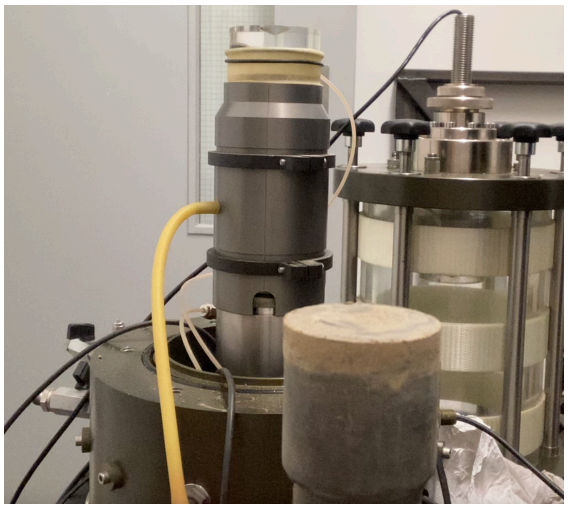
(a)



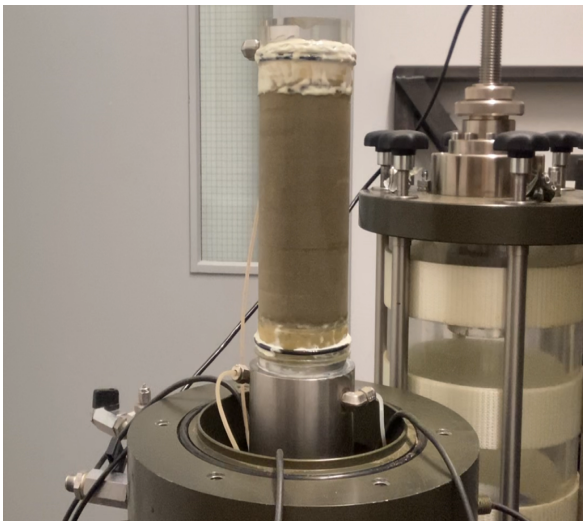
(b)



(c)



(d)



(e)

Figure 3.12: Sample preparation: (a) securing the membrane to the base pedestal, (b) setting up the split mould and securing the membrane on the split mould, (c) Compacting the soil, (d) Placing the top cap, (e) removing the split mould

3.5.2 Attaching the local LVDTs

The LVDTs are positioned in the middle third of the sample to minimise end effects, as recommended by Kirkpatrick and Younger (1970). Prior to attachment, the pad positions are marked on the sample membrane. The axial LVDTs have a gauge length of 47 mm, which corresponds to one-third of the 140 mm sample height. The LVDTs are fixed to the sample using pins that penetrate into the membrane. To prevent leakage of cell water into the sample, a silicone sealant is applied to the pads before they are attached to the sample and the pins are inserted. Additionally, the silicone sealant also functions as an adhesive, strengthening the bond between the LVDT pads and the sample. The LVDTs attached on the soil sample is presented in Figure 3.13

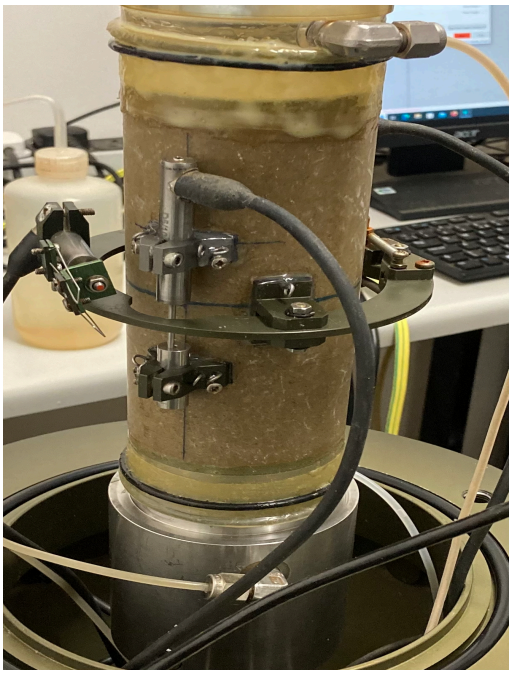


Figure 3.13: LVDTs secured on the sample

3.5.3 Saturation

After completing the sample preparation and securing the LVDTs, the cell chamber is placed onto the cell base and filled with de-aired water. The vacuum pressure is gradually reduced to 0 kPa, while simultaneously, the cell pressure is increased to 20 kPa using the cell pressure controller. To ensure a fully saturated soil sample, the saturation stage consists mainly of the following phases:

(i) CO_2 flushing
(ii) De-aired water flushing
(iii) Back pressure ramp saturation
(iv) *B*-value check

The initial step involves slowly flushing the sample with CO_2 to replace the air in the voids with CO_2, which is more soluble in water and helps to achieve saturation more quickly. The sample is flushed with CO_2 from the pedestal and the air is allowed to escape from the top cap. The CO_2

flushing rate is monitored by the number of air bubbles escaping from the sample, and it is adjusted to maintain a rate of one bubble per second. CO_2 flushing is carried out for 30 minutes. The second stage, following CO_2 flushing, involves allowing de-aired water to flow into the sample from the base pedestal via the back pressure controller. The de-aired water must flow slowly into the sample to prevent collapse and avoid disturbing its fabric. This stage is repeated at least three times to ensure and facilitate full saturation.

After completing the initial two stages, back pressure ramp saturation is performed. During this stage, both the back pressure and cell pressure are increased simultaneously, while maintaining a small 20 kPa difference between them to keep the sample stable and prevent swelling. The purpose of this step is to apply pressure to the air bubbles trapped within the voids, forcing them to dissolve into the de-aired water. This stage is carried out very slowly to avoid disturbing the sample, typically completed over the course of an entire day. For most samples, the back pressure is increased to 1000 kPa to achieve full saturation. However, full saturation can also be attained at lower back pressures by extending the duration of this stage, allowing the air bubbles to dissolve slowly over time.

The last saturation stage is checking the pore pressure coefficient *B*. As defined by Skempton (1954), the *B*-value is as follows:

$$B = \frac{\Delta u}{\Delta \sigma_3} \tag{3.3}$$

where $\Delta\sigma_3$ is the imposed change in cell pressure while Δu is associated pore water pressure change. The *B*-value is checked by increasing the cell pressure by 50 kPa and monitoring the pore water pressure rise. Based on the resulting *B*-value, the soil is considered fully saturated if the *B*-value is greater than 0.95. However, if the *B*-value is below 0.95, the back pressure ramp saturation is repeated by increasing the back pressure to a higher value, followed by rechecking the *B*-value. It is important to emphasise that the *B*-value is not solely dependent on the degree of saturation; therefore, a *B*-value lower than 1 does not necessarily indicate that the soil is not fully saturated. Other factors that influence the *B*-value are the compressibility of the soil skeleton, the porosity of the soil, the compressibility of the soil grains, and the absolute pressure of the pore fluid after application of the cell pressure increment (Lade, 2016). For very stiff materials, the compressibility of the soil skeleton is very low, allowing full saturation to occur at *B*-values below unity. This is particularly true for highly overconsolidated clays and sands with very high relative densities. For the majority of the samples tested in this research, *B*-values higher 0.97 were achieved.

3.5.4 Consolidation

All samples in this research were isotropically consolidated through increasing the cell pressure while monitoring the volume change using the back pressure controller. The cell pressure was increased in maximum increments of 50 kPa until the target mean effective stress was reached.

Given that excess pore water pressures rapidly drop to zero for sands, the samples were considered consolidated once the rate of volume change became lower than 1 mm³/minute.

3.5.5 Shearing

Shearing in the triaxial apparatus is applied by increasing the axial stress, which is controlled via the vertical movement of the pedestal. In this research, both monotonic and cyclic triaxial shear tests were conducted. The monotonic compression tests were mainly conducted under drained conditions, which required the loading rate to be very slow to allow excess pore water pressures to escape rapidly. The axial strain rate for the monotonic compression tests was set at 2% per hour, which was slow enough to prevent the development of excess pore water pressures. The primary standard used for the monotonic compression tests is ASTM D7181.

Cyclic triaxial shearing tests were carried out in both drained and undrained conditions. The loading rate was the main parameter that was varied between the drained and undrained cyclic tests. As opposed to the monotonic tests which were strain controlled, all the cyclic tests were stress controlled in this research. The undrained cyclic triaxial tests were conducted according to ASTM D3999, which provides the procedure for obtaining the relationships between damping ratio and shear modulus with cyclic shear strain.

3.6 Calculations of stresses, strains, and dynamic parameters

This section explains how the different stresses and strains are calculated using both local and global measurement systems. It also presents the equations used to calculate the dynamic parameters, namely shear modulus and damping ratio, based on the measured stresses and strains.

3.6.1 Axial strain

The axial strains can be determined locally from the LVDTs attached to the middle of sample or globally based on the vertical movements of the pedestal. The axial strains (ε_a) are calculated as follows:

$$\varepsilon_a = \frac{\Delta L}{L} \tag{3.4}$$

where ΔL is the measured displacement recorded by the axial LVDTs or the pedestal movement. L represents the gauge length of the LVDTs (centre-to-centre distance between the pads) for measuring the local axial strains, or the total height of the sample for measuring the global axial strains. For cyclic triaxial tests, axial strains are determined locally due to the relatively small deformation, and since local measurements provide more accurate and detailed insights into dynamic behaviour of soil. For monotonic tests, both local and global axial strains are calculated. However, when the samples are loaded to failure, the local axial deformations exceed the measurement range, necessitating reliance on only the global axial strain measurements to observe the response of the sample.

3.6.2 Volumetric strain

The volumetric strains of the sample during consolidation and shearing are determined using the back pressure controller. Since the soil is fully saturated and the soil grains are assumed to be incompressible, the volume of water entering or exiting the sample directly equals the volumetric change. During the saturation stage, the change of volume recorded by the back pressure controller does not reflect the volumetric change of the sample. Therefore, the volumetric strain must be determined using the local LVDTs. However, based on the LVDT readings, it was observed that the changes in the readings were very small, indicating that the volume of the sample did not change significantly during saturation. Thus, the volumetric change during saturation was neglected. The calculation of the volumetric strain (ε_v) is as follows:

$$\varepsilon_v = \frac{\Delta V}{V} \tag{3.5}$$

where ΔV is the change of volume and V is the volume of the sample. One factor that can affect the accuracy of the calculated volumetric strain is membrane penetration. As the effective confining stress increases, the rubber membrane tends to penetrate into the voids between soil grains, resulting in a recorded volumetric change that is larger than the actual volumetric change of the soil structure. Numerous experimental and theoretical studies have been conducted to evaluate the parasitic volume due to membrane penetration. Nicholson et al. (1993) provide a comprehensive summary of various membrane penetration correction methods. They also discussed the key factors influencing membrane penetration, including soil grain size, specimen geometry, specimen density, and the range of applied effective confining stresses. However, based on triaxial tests conducted on Hostun sand, Diambra (2010) found that accounting for volumetric changes caused by membrane penetration using various correction methods results in minimal variations in the void ratio, which are smaller than the margin of error associated with calculating the initial void ratio. For this reason, membrane penetration effects were disregarded in this research.

3.6.3 Shear strain

The shear strain can be determined from the local axial and radial strains as follows:

$$\gamma = \varepsilon_a - \varepsilon_r \tag{3.6}$$

where ε_r is the radial strain. Shear strains are calculated to construct the damping ratio and secant shear modulus reduction curves, which are typically represented as a function of the cyclic shear strain. However, the measured strains from the radial LVDTs cannot be considered accurate, as the recorded deformations did not reflect the typical behaviour of soil under sinusoidal cyclic deviatoric stresses. The recorded deformations from the LVDTs for small and large cyclic deviatoric stress levels are presented in Figure 3.14 and Figure 3.15, respectively. As shown in these figures, the axial LVDTs produced deformations consistent with the cyclic behaviour of soil, confirming the reliability of their measurements. For small cyclic deviatoric stress levels (Figure 3.14), the axial

LVDTs accurately captured sinusoidal deformations, whereas the radial LVDTs displayed no measurable deformations. At larger cyclic deviatoric stress levels (Figure 3.15), the axial LVDTs continued to record smooth sinusoidal deformation patterns, while the radial LVDTs exhibited sudden jumps and zones of no deformation, deviating significantly from the expected sinusoidal behaviour. This irregular deformation pattern in the radial LVDTs cannot be attributed to actual soil behaviour, rendering the measurements inaccurate and unsuitable for calculating shear strains. The anomalous response of the radial LVDTs may be attributed to the armature sticking and producing friction with the LVDT core during sample shearing.

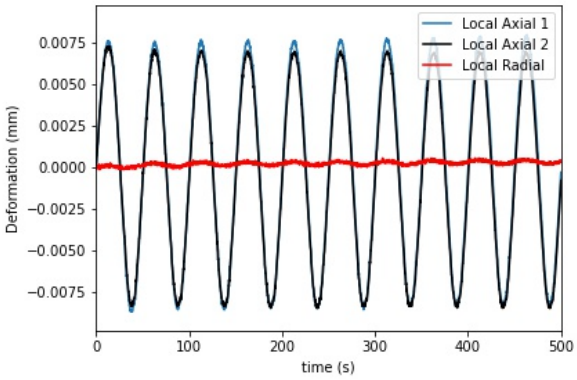


Figure 3.14: Behaviour of LVDTs at small cyclic deviatoric stress

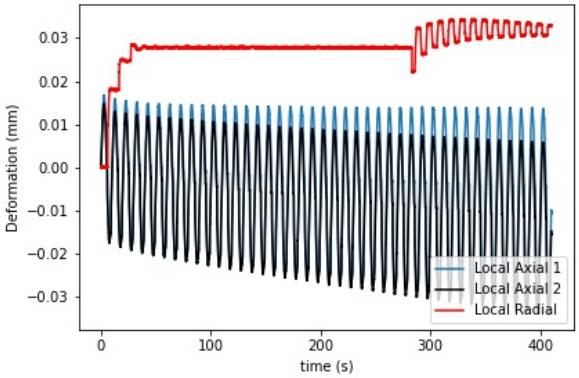


Figure 3.15: Behaviour of LVDTs at large cyclic deviatoric stress

Due to the issues related with the measurements of the radial LVDT, the cyclic shear strain is calculated using the following equation:

$$\gamma = \varepsilon_a (1 + \nu) \tag{3.7}$$

where ν is the Poisson's ratio. Poisson's ratio is theoretically 0.5 for undrained soil behaviour. Therefore, a value of 0.5 is used to calculate the cyclic shear strain in undrained cyclic triaxial tests. For the drained cyclic tests, a constant Poisson's ratio value of 0.2 is assumed to calculate the cyclic shear strain.

3.6.4 Deviatoric stress

The deviatoric stress is determined from the load cell measurements and the area of the sample. Since the cross-sectional area of the sample changes during loading, a correction is necessary to determine the corrected area. Several equations are proposed in the literature to determine the corrected area based on the assumed shape of the sample during deformation. Lade (2016) provides an equation that accounts for the bulging mode of deformation, where the sample exhibits a parabolic distribution of lateral strain. A discussion on the different equations for correcting the cross-sectional area can be found in Escribano (2014). Equation 3.4 is used in this research for calculating the corrected area (A_c) which is proposed by ASTM D7181 standard and it assumes a right cylinder mode of deformation. A_0 in Equation 3.4 is the initial area of the sample prior to shearing. Other equations are not used because the mode of deformation varies between samples of different relative, requiring different equations rather than a single one for all cases.

$$A_c = A_0 \frac{1- \varepsilon_v}{1- \varepsilon_a} \tag{3.8}$$

In addition to correcting the area, a correction is required to take into account the lateral restraint provided by the rubber membrane. Several equations have been developed in the literature (e.g., Henkel and Gilbert, 1952; Ponce & Bell, 1971) to account for the stresses carried by the membrane. These equations are derived from the theory of elasticity and are based on specific assumptions, as summarised by DeGroff et al. (1988). The following equation, proposed by Henkel and Gilbert (1952) and recommended by the ASTM D7181 standard, is used in this thesis:

$$\Delta q = \frac{4\, E_m\, t_m\, \varepsilon_a}{D_c} \tag{3.9}$$

where E_m is the Young's modulus of the membrane, t_m is the thickness of the membrane, and D_c is the diameter of the sample after consolidation. The E_m supplied from GDS is 1400 kPa and t_m is approximately 0.25 mm and is measured before each test with vernier calibre. The deviatoric stress (q) applied is calculated as follows:

$$q = \frac{P}{A_c} - \Delta q \tag{3.10}$$

where P is the load measured by the internal submersible load cell.

3.6.5 Mean effective stress

The mean effective stress (p') is the average of the effective stresses applied on the soil from all three directions and is determined as follows:

$$p' = \frac{1}{3}(\sigma_1' + 2\sigma_3') \tag{3.11}$$

where σ_1' and σ_3' are the effective vertical and horizontal stresses, respectively. σ_1' is calculated according to Equation 3.12, while σ_3' is estimated based on Equation 3.13. σ_3' is the isotropic

effective stress and is equal to the difference between the cell pressure (σ_{cell}) and the pore water pressure (u) measured by the pore pressure transducer.

$$\sigma_1' = \sigma_3' + q \tag{3.12}$$

$$\sigma_3' = \sigma_{cell} - u \tag{3.13}$$

3.6.6 Damping ratio and secant shear modulus

The damping ratio (D) and secant shear modulus are calculated from the local axial strains and the cyclic deviatoric stresses. For a typical stress-strain loop (Figure 3.16), the secant Young's modulus (E) and the corresponding secant shear modulus (G) are calculated as follows:

$$E = \frac{(q_{max} - q_{min})}{(\varepsilon_{a,max} - \varepsilon_{a,min})} \tag{3.14}$$

$$G = \frac{E}{2(1+v)} \tag{3.15}$$

where v is the Poisson's ratio. As mentioned previously, the value of v is 0.5 when the behaviour is undrained, and is assumed to be 0.2 when the soil behaviour is drained. The damping ratio (D) is determined according to the following equation:

$$D = \frac{W_D}{4\pi W_S} \tag{3.16}$$

where W_D is the amount of the dissipated energy, equal to the area of the hysteretic loop , and W_S is the elastic stored energy and is equal to the area of the grey triangle in Figure 3.16.

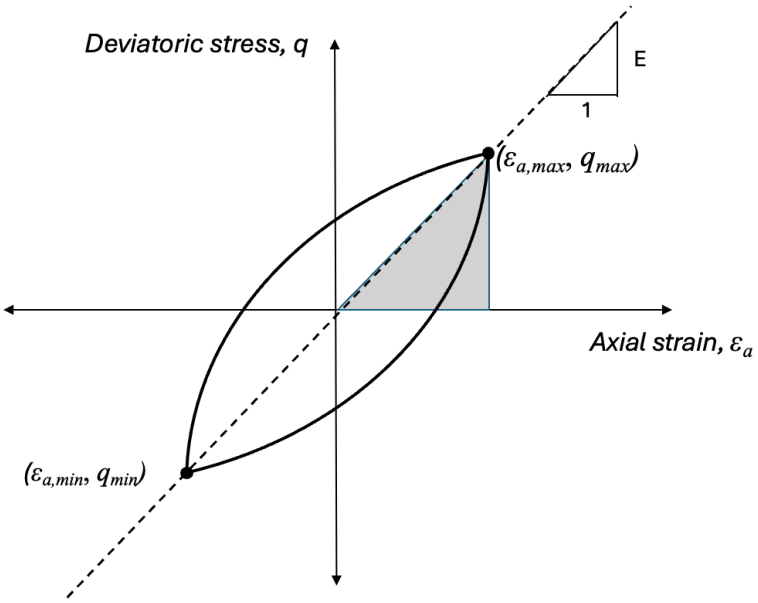


Figure 3.16: Typical hysteretic stress-strain loop

3.7 Conclusions

This chapter presented an overview of the physical characteristics of Blessington and Kilmuckridge sands, including their grain size distribution, specific gravity, and density limits. A comparison between the physical properties of Blessington sand obtained in this study and those reported in a previous study showed strong agreement. This consistency indicates that the values derived in this study are representative of the physical characteristics of Blessington sand.

The chapter also provided a detailed description of the main components of the GDS DYNTTS dynamic triaxial apparatus, such as the axial actuator, load cell, data acquisition unit, pressure controllers, pore water pressure transducer, and LVDT transducers. The components of the bender element testing system were also outlined.

A brief review of soil sample reconstitution methods was presented, discussing their respective advantages and limitations. The moist tamping method with undercompaction was selected for this study, as it offers effective control over relative density and enables the preparation of specimens with both very loose and very dense states. The stages of a triaxial test, including saturation, consolidation, and shearing, were discussed in detail. Finally, the equations used to calculate various stresses and strains, as well as the derived dynamic parameters such as secant shear modulus and hysteretic damping ratio, were presented.

This chapter serves to familiarise the reader with the soil materials tested and the procedures used to obtain both monotonic and dynamic test results, which form the core of the following chapter. Since the calibration of constitutive models relies on these laboratory results, it is essential to clearly explain how the tests were conducted and how the parameters were derived.

Chapter 4

Laboratory Tests

4.1 Introduction

This chapter presents the results of the monotonic and cyclic tests conducted during this research to inform the parameters required for calibrating the constitutive soil models. Additionally, the cyclic tests provide a database of dynamic soil parameters across different stress levels and relative densities. This database serves as an idealised representation of dynamic soil behaviour, facilitating the fatigue design of OWTs, given the high costs and extended duration associated with conducting cyclic laboratory element tests. The laboratory element tests were conducted using the advanced DYNTTS GDS cyclic triaxial apparatus, capable of performing tests under different frequencies and stress conditions. The two key dynamic parameters of primary concern for geotechnical engineers are the secant shear modulus (G) and damping ratio (D), as these significantly impact the behaviour of structures under dynamic loading. The cyclic triaxial tests were performed for various initial mean effective stresses (p_0'), relative densities (D_r), and drainage conditions. The variation of soil behaviour along the monopile depth was investigated through testing soil samples under different p_0' values. The effects of p_0' and D_r were examined for both Blessington and Kilmuckridge sands, and the observed patterns of dynamic soil behaviour were compared with findings from previous studies. The effect of drainage condition was also examined by comparing the D-γ_c curves from the undrained tests with those from drained tests. As a result, a comprehensive database was established, enabling the G-γ_c and D-γ_c curves to be fitted with commonly used empirical formulas. A limited series of large cyclic tests were also carried out to study how the dynamic parameters change with the number of cycles (N). only a few tests with large N under asymmetric stresses were conducted to inform the cyclic parameters of SANISAND-MS.

The testing campaign also involved extensive monotonic tests to obtain the stiffness and strength parameters required for the HSsmall and SANISAND-MS models. The monotonic tests focused on estimating the critical angle of shearing resistance and the variation of the peak angle of shearing resistance. Furthermore, the campaign also sought to acquire the critical state framework parameters that are necessary inputs for the SANISAND-MS model. In addition to the peak and critical angles of shearing resistance, the variation of the characteristic friction angle, which represents the stress state at the transition from contraction to dilation behaviour, was also investigated. Finally, bender element tests were also carried out on Blessington sand to obtain a database of small strain shear

modulus for different p_0' and D_r values. The database was employed in curve fitting to yield the small strain stiffness parameters for the HSsmall and SANISAND-MS constitutive models.

4.2 Undrained cyclic tests

The cyclic tests were stress-controlled and performed according to the procedure in ASTM D3999 (2013) standard. For the same sample, the cyclic deviatoric stress was increased from one loading stage to another in order to obtain the G-γ_c and D- γ_c curves. The cyclic tests were two-way symmetrical such that the mean deviatoric stress was at 0 kPa. The tests were conducted at a frequency of 0.1 Hz, which is regarded as a typical frequency for wave loading (K. Andersen, 2015). Although the soil surrounding a monopile may be subjected to different frequencies, such as those caused by the oscillation of the OWT structure at its fundamental natural frequency (f_1) or by wind loading, these frequencies are generally very low and tend to fall close to or below 0.1 Hz. Therefore, the dynamic response of the soil is not expected to differ significantly from that induced by the chosen loading frequency. As the tests mainly focused on obtaining the parameters for short-term cyclic loading, the number of cycles for each stress amplitude was 40. The obtained cyclic shear strains fell between 0.005% and 0.5%, which cover the range of shear strains that are expected for different geotechnical structures (shown in Figure 4.1).

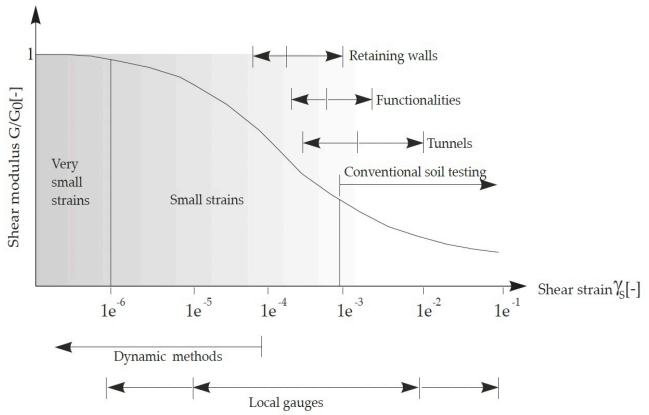


Figure 4.1: typical strain ranges for laboratory tests and structures (Atkinson & Sallfors,1991)

The undrained tests, including the target D_r, the void ratio after consolidation (e_i), and the applied p_0', are summarised in Table 4.1. The D_r of 30% represents very loose soil samples, while the medium dense state is prepared to a D_r of 60%, and the D_r values of 80% and 90% are used to indicate very dense samples. The nomenclature of the test IDs is as follows:

BCU(30)50

where the letter 'B' stands for Blessington, whereas 'K' is used to indicate Kilmuckridge sand. The abbreviation 'CU' is used to denote cyclic undrained tests. The number between the brackets corresponds to D_r, and the number outside the brackets is p_0'. Small alphabetical letters are added to the test IDs that were replicated under the same conditions to check the repeatability of the results. Prior to conducting undrained cyclic loading, the samples were consolidated to the desired value of

p_0'. After each cyclic loading stage, the drainage valve was opened to allow the excess pore water pressure to dissipate, and the sample was reconsolidated to the initial value of p_0'. Although some tests were conducted at p_0' values of 25 kPa, 100 kPa, and 200 kPa, the majority focused on p_0' values of 50 kPa, 150 kPa, and 300 kPa. These values were selected to represent the in-situ effective stress conditions near the mudline, mid-depth, and tip of a representative monopile with an embedment depth of 30 m.

Table 4.1. Database of undrained cyclic tests

Test Number	Test ID	p_0' (kPa)	D_r (%)	e_i
1	BCU(30)50	50	30	0.854
2	BCU(30)150	150	30	0.811
3	BCU(30)300	300	30	0.801
4	BCU(60)25	25	60	0.684
5	BCU(60)50a	50	60	0.677
6	BCU(60)50b	50	60	0.678
7	BCU(60)100	100	60	0.675
8	BCU(60)150a	150	60	0.677
9	BCU(60)150b	150	60	N/A
10	BCU(60)200	200	60	0.659
11	BCU(60)300	300	60	0.675
12	BCU(80)50	50	80	0.592
13	BCU(80)150	150	80	0.592
14	BCU(80)300	300	80	0.596
15	BCU(90)50a	50	90	N/A
16	BCU(90)50b	50	90	0.543
17	BCU(90)150	150	90	0.542
18	BCU(90)300	300	90	0.528
19	KCU(60)50a	50	60	0.479
20	KCU(60)50b	50	60	N/A
21	KCU(60)150a	150	60	N/A
22	KCU(60)150b	150	60	0.469
23	KCU(60)300a	300	60	0.48
24	KCU(60)300b	300	60	0.471
25	KCU(90)150	150	90	N/A
26	KCU(90)300	300	90	0.391

4.2.1 Effects of mean effective stress and relative density

The test results are initially examined to investigate the influence of p_0' on the shear modulus reduction and hysteretic damping ratio curves. The effect of p_0' on Blessington sand is shown in Figure 4.2 to Figure 4.5, while Figure 4.6 and Figure 4.7 illustrate the influence of p_0' on Kilmuckridge sand. Given that the behaviour of soil generally depends on the number of cycles (N),

the comparisons in this section for the different G-γ_c and D-γ_c curves are based on the tenth cycle (N = 10). The comparisons for the effect of p_0' are performed on samples prepared to similar D_r values. While the moist tamping method provides effective control in reconstituting the sample to the desired relative density, a small variation of 2% to 3% in relative density after consolidation was unavoidable. The small difference is unlikely to affect the results, and the variation in behaviour can entirely attributed to p_0'.

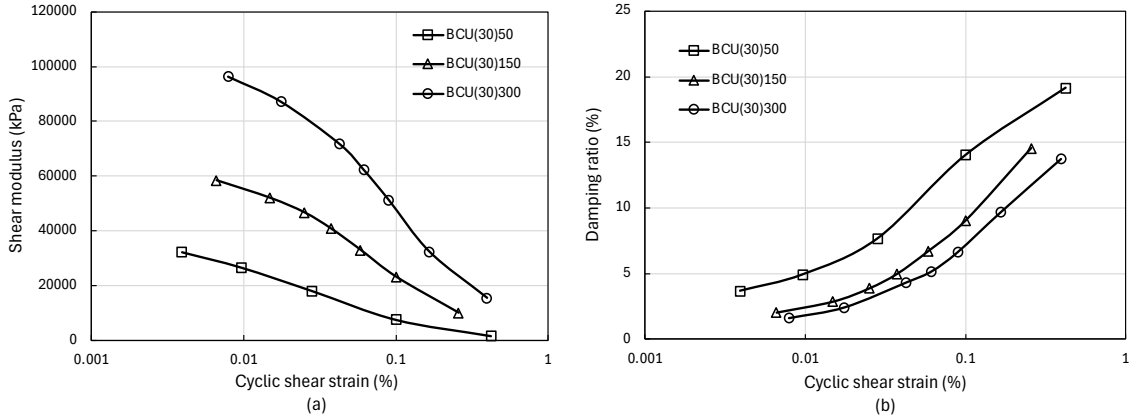


Figure 4.2: (a) Shear modulus reduction and (b) damping ratio of Blessington sand with $D_r \approx 30\%$

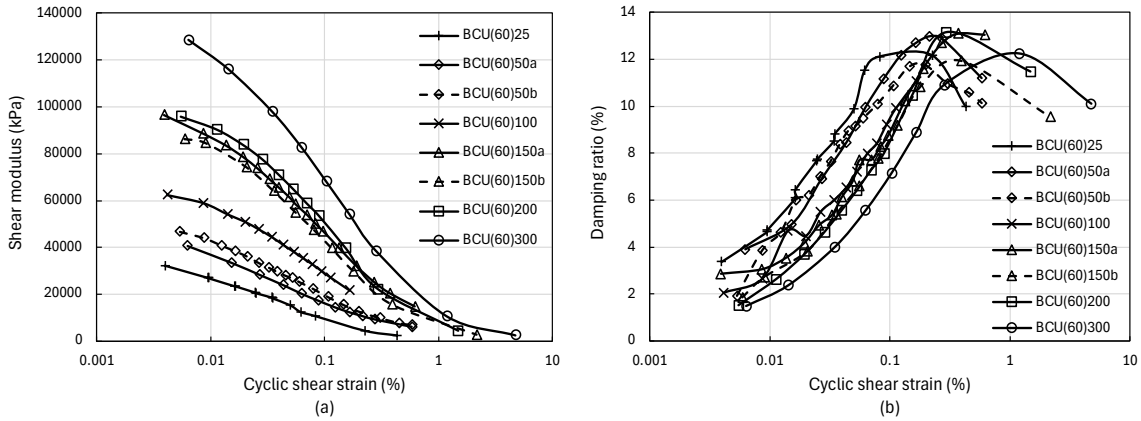


Figure 4.3: (a) Shear modulus reduction and (b) damping ratio of Blessington sand with $D_r \approx 60\%$

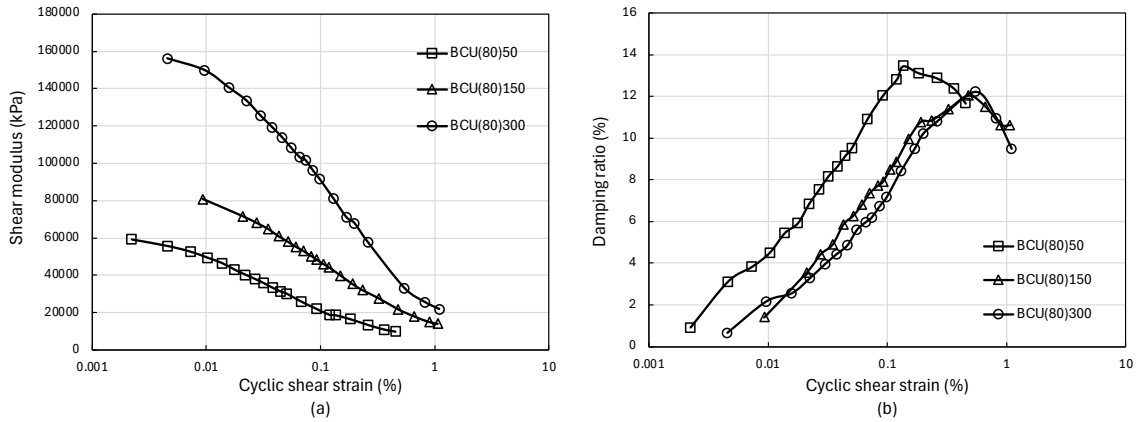


Figure 4.4: (a) Shear modulus reduction and (b) damping ratio of Blessington sand with $D_r \approx 80\%$

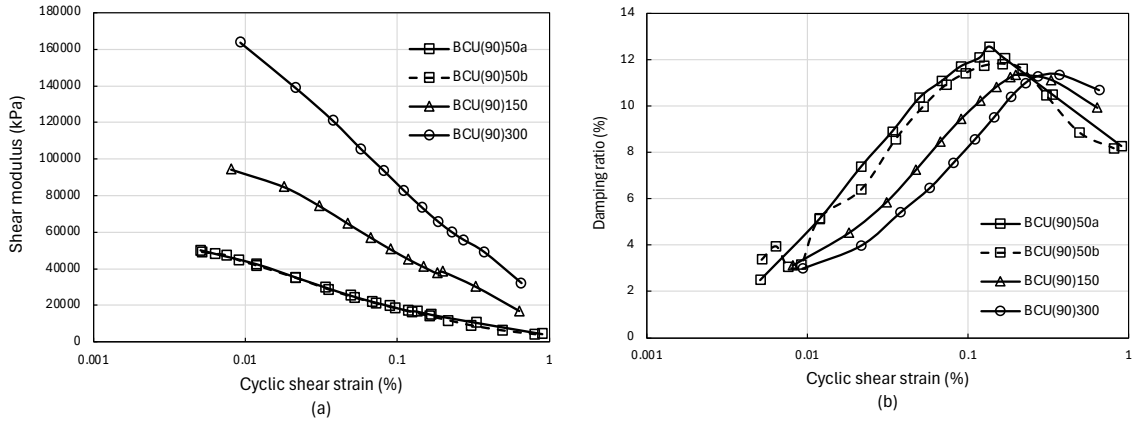


Figure 4.5: (a) Shear modulus reduction and (b) damping ratio of Blessington sand with $D_r \approx 90\%$

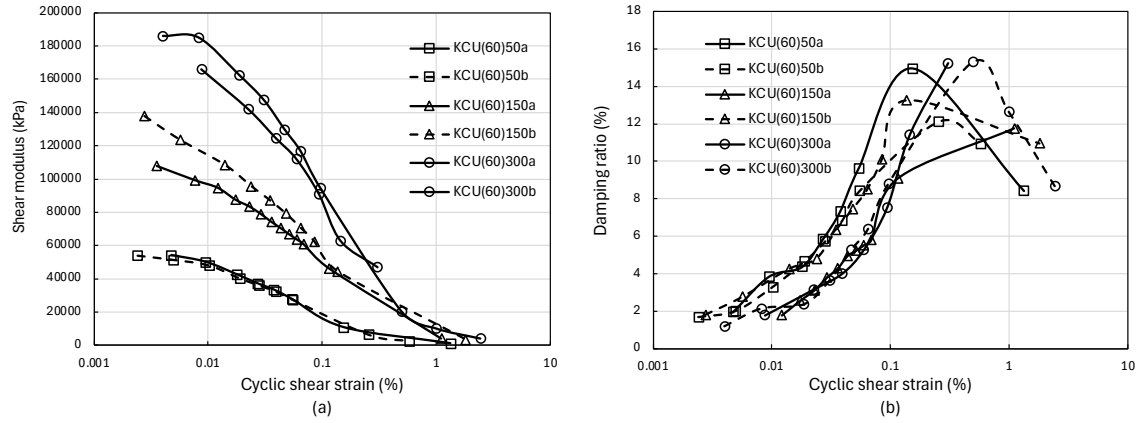


Figure 4.6: (a) Shear modulus reduction and (b) damping ratio of Kilmuckridge sand with $D_r \approx 60\%$

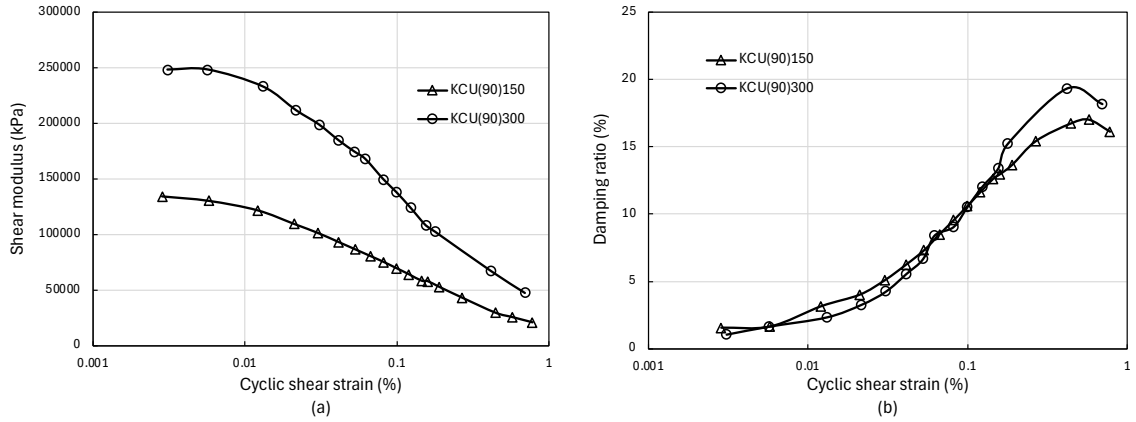


Figure 4.7: (a) Shear modulus reduction and (b) damping ratio of Kilmuckridge sand with $D_r \approx 90\%$

The results show that the dynamic behaviour of sands is highly dependent on p_0'. For the same shear strain level, the shear modulus (G) increased with p_0' for all the tested samples. Furthermore, the damping ratio curves (D- γ_c) showed that soil hysteretic damping has a decreasing trend with increasing p_0', which is in agreement with the behaviour observed from previous studies (e.g., Kokusho, 1980; Wichtmann and Triantafyllidis, 2013). Although a clear trend of the variation of G-γ_c and D-γ_c with p_0' was noted in majority of the tests, some anomalies were present. For example, the damping ratio curves from KCU(90)150 and KCU(90)300 tests show no difference

(Figure 4.7b), despite the large difference in p_0'. This anomaly could be attributed to the high sensitivity of the damping ratio parameter to discrepancies in setting up the sample and the sensors.

The effect of relative density (D_r) on the variation of the shear modulus reduction and damping ratio is also examined by comparing tests conducted under the same p_0'. This comparisons are shown in Figure 4.8 to Figure 4.10 for Blessington sand, and Figure 4.11 and Figure 4.12 for Kilmuckridge sand.

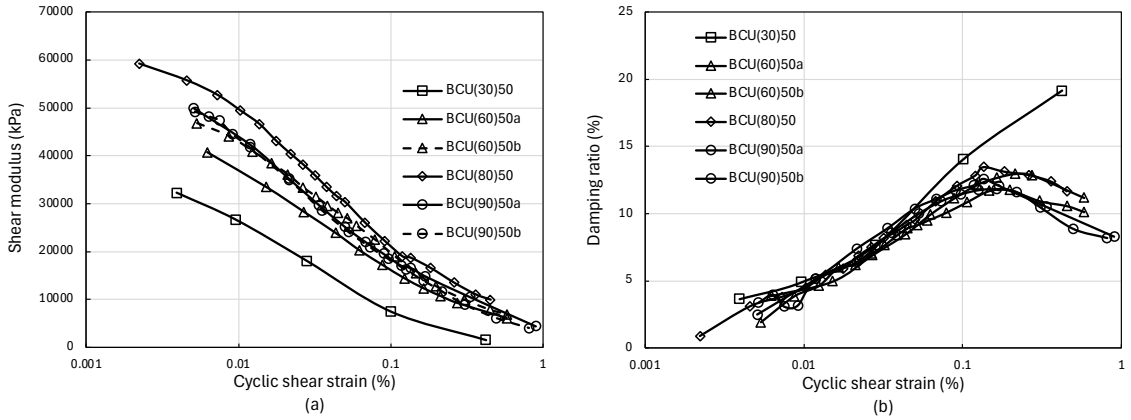


Figure 4.8: (a) Shear modulus reduction and (b) damping ratio of Blessington sand tested at p_0'=50 kPa

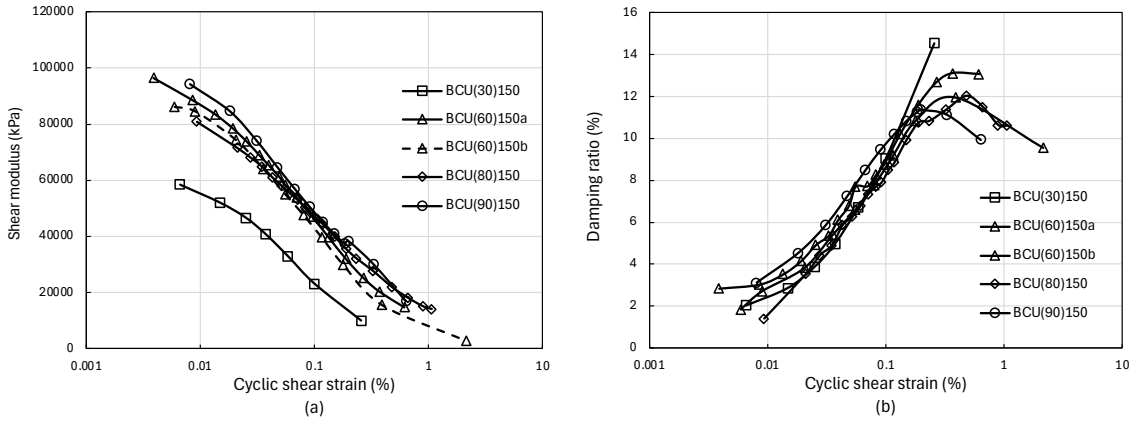


Figure 4.9: (a) Shear modulus reduction and (b) damping ratio of Blessington sand tested at p_0'=150 kPa

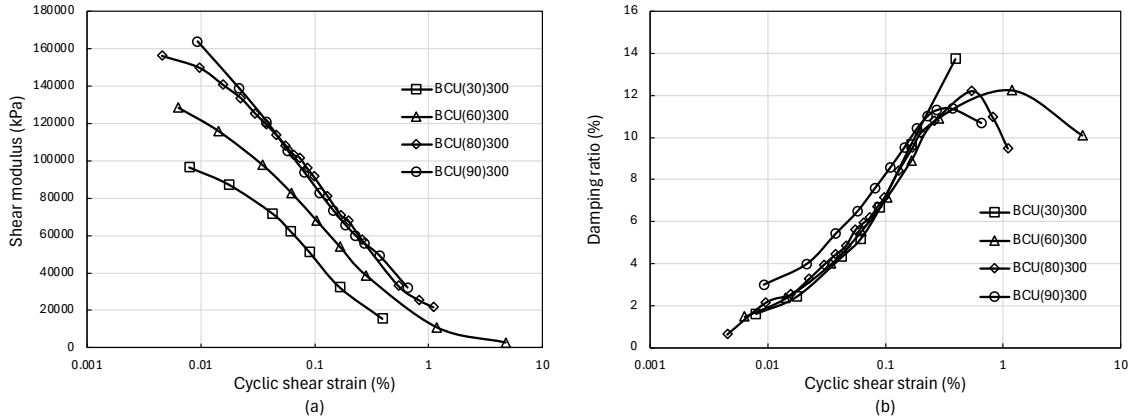


Figure 4.10: (a) Shear modulus reduction and (b) damping ratio of Blessington sand tested at p_0'=300 kPa

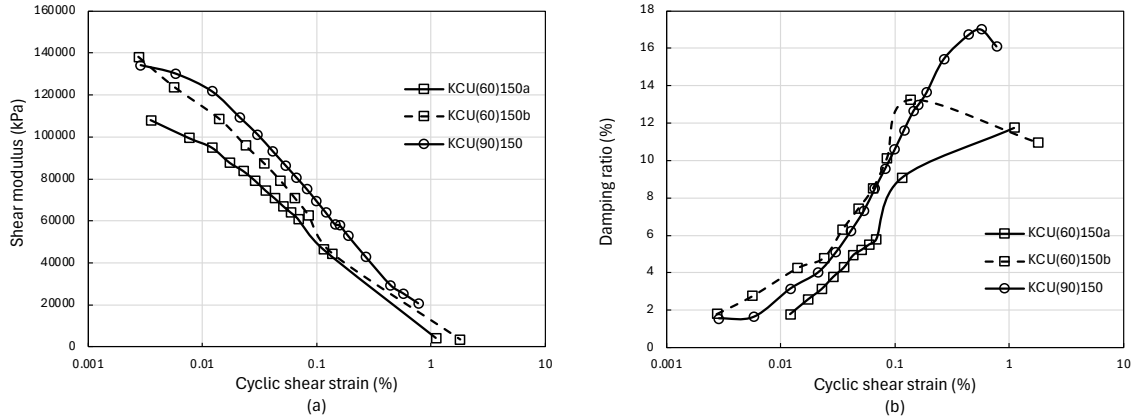


Figure 4.11: (a) Shear modulus reduction and (b) damping ratio of Kilmuckridge sand tested at p_0'=150 kPa

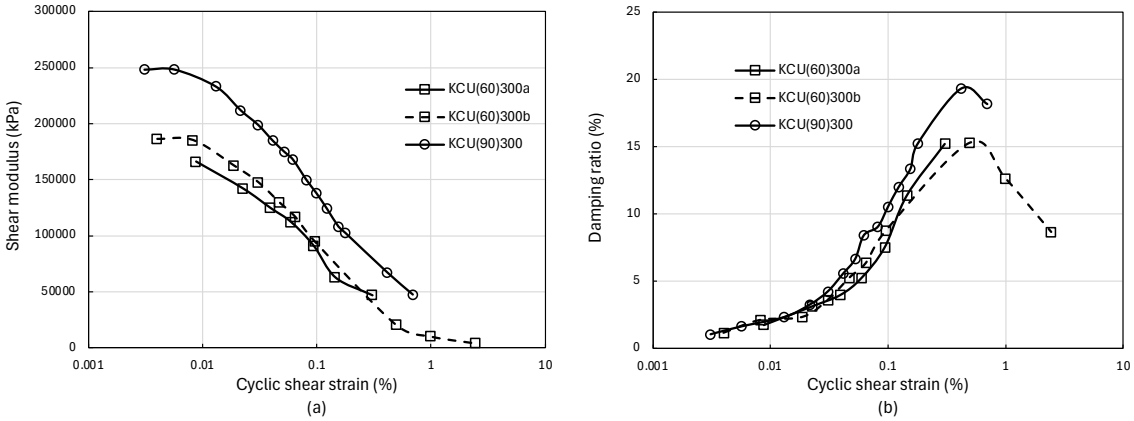


Figure 4.12: (a) Shear modulus reduction and (b) damping ratio of Kilmuckridge sand tested at p_0'=300 kPa

It is observed that the shear modulus of both Blessington and Kilmuckridge sands increase with D_r, while the damping ratio curves show no significant effect of D_r for small cyclic shear strains up to 0.1%. This observation agrees with the findings from previous research studies (e.g., Kokusho, 1980; Wichtmann and Triantafyllidis, 2013). However, as the cyclic shear strain exceeds the small strain range (shown in Figure 4.1), the influence of D_r on the damping ratio becomes evident. For example, the tests conducted on Blessington sand showed that for cyclic shear strains above 0.1%, the damping ratio for the samples reconstituted to $D_r \approx 30\%$ continues to increase, while for the denser soil samples it begins to follow a downward trend as a certain strain level is exceeded. This reduction in the damping ratio for dense soils was also reported by Rascol (2009), Blaker and Andersen (2019), and Løvholt et al. (2020). Løvholt et al. (2020) attributed the tendency of dense soils to dilate and having non-elliptical stress-strain loops to decreasing the damping ratio. The damping ratio peaks approximately occur within the shear strain range of 0.45% to 1%, as reported by Rascol (2009). Using the results from the BCU(60)300 test to demonstrate damping reduction, the shape of the elliptical loops at small strains is compared with the shape of the non-elliptical loops associated with large cyclic strains (shown in Figure 4.13). Since the empirical formulas (e.g., Hardin and Drnevich, 1972b; Ishibashi and Zhang, 1993; Zhang et al., 2005; Darendeli, 2001; Menq, 2003) were primarily derived for small strains, they do not produce the downward trend of

D-γ_c at large shear strains. The effect of dilation on the decrement of the hysteretic damping for sands was also observed in the undrained cyclic DSS test simulations performed by Liu and Kaynia (2023) using the advanced SANISAND-MS constitutive model. It is important to highlight that the variation in the damping ratio is only evident when the curves of medium and very dense samples are compared with the fully contractive soil samples prepared to a D_r of 30%, whereas the difference is shown to be marginal for the samples prepared to D_r values of 60% and higher. Overall, the repeatability and consistency of Blessington test results are higher than those of Kilmuckridge sand. For example, Figure 4.11 shows that the D-γ_c curves vary widely and the damping ratio results of KCU(60)150a and KCU(60)150b tests do not match. In this case, test KCU(60)150a could be considered to be an anomaly since the D-γ_c curves of KCU(60)150b and KCU(90)150 tests are similar.

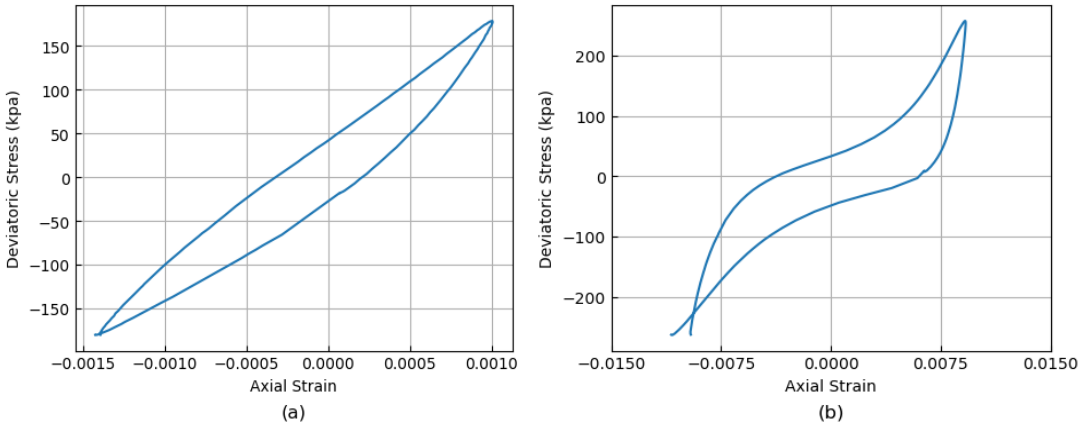


Figure 4.13: (a) stress-strain loops for small strain levels, (b) stress-strain loops for large strain levels

4.2.2 Comparison between Blessington and Kilmuckridge

The G-γ_c and D-γ_c curves are compared between Blessington and Kilmuckridge sands. Although the number of tests performed on Kilmuckridge sand is limited, it remains valuable to examine how the dynamic parameters vary from the finer Blessington sand to the coarser Kilmuckridge sand. Furthermore, this comparison is beneficial for assessing whether Blessington sand can serve as an idealised representation of sand behaviour for offshore wind farms. The dynamic curves are compared for the same p_0' and D_r as shown in Figure 4.14 to Figure 4.18. As the dynamic behaviour changes from one cycle to another, the curves are compared consistently for the tenth cycle (N = 10). It is worth noting that the sample preparation procedure and the steps leading up to dynamic loading are exactly the same.

The G-γ_c curves indicate that the stiffness of Kilmuckridge sand at the same relative density is higher than that of Blessington sand. This difference in stiffness is well depicted in Figure 4.18 showing the results for p_0' = 300 kPa and $D_r \approx 90\%$. The higher shear stiffness displayed by Kilmuckridge sand could be explained by its d_{50} value, which is larger than that of Blessington sand. The increased shear stiffness of soil due to d_{50} was observed in the resonant column tests performed

by Menq (2003). The D-γ_c curves exhibited by Kilmuckridge sand are observed to be higher than those of Blessington sand for the range of cyclic shear strains that are examined. This observation aligns with test results from Menq (2003), which showed that the D-γ_c curves of coarse-grained material are higher than those of fine sand. However, it is noteworthy to highlight that the difference between the D-γ_c curves is only significant when the shear strains are higher than 0.1%, and the difference is insignificant for lower shear strain levels.

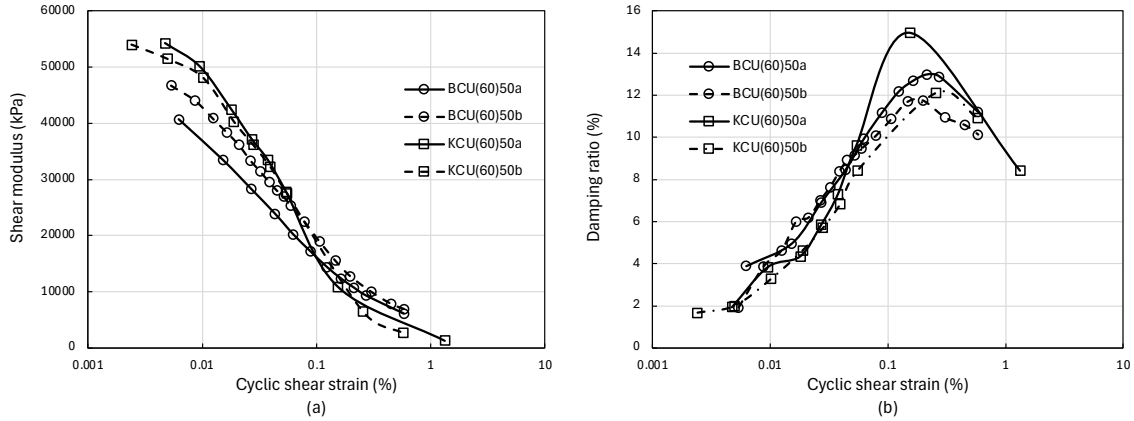


Figure 4.14: (a) Shear modulus reduction and (b) damping ratio for p_0'=50 kPa and $D_r \approx 60\%$

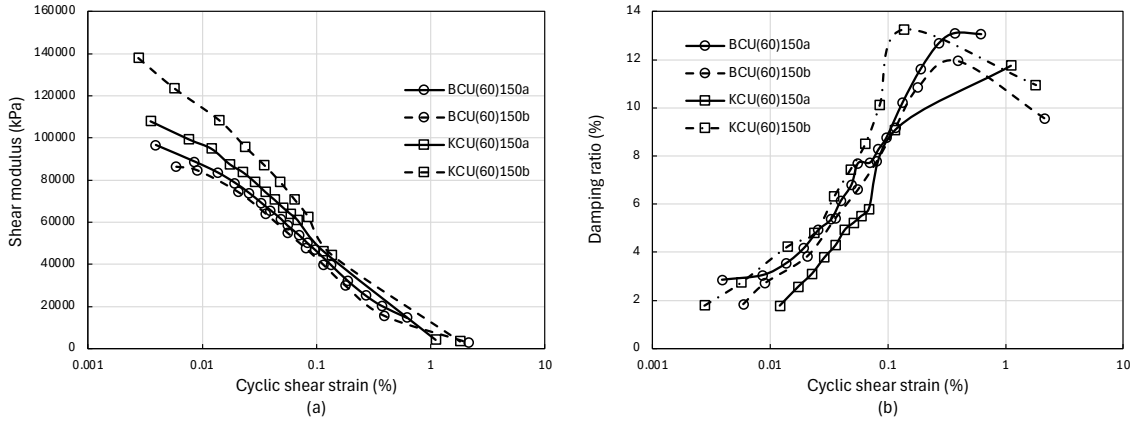


Figure 4.15: (a) Shear modulus reduction and (b) damping ratio for p_0'=150 kPa and $D_r \approx 60\%$

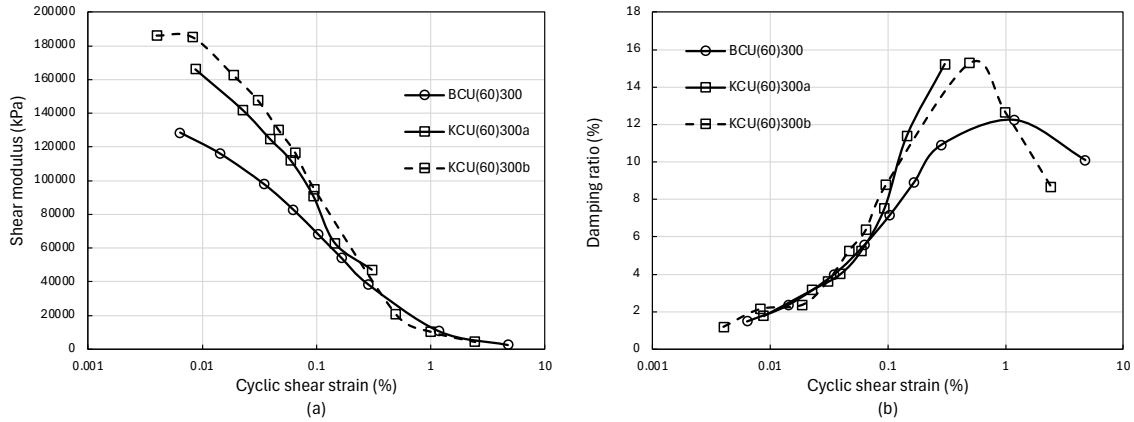


Figure 4.16: (a) Shear modulus reduction and (b) damping ratio for p_0'=300 kPa and $D_r \approx 60\%$

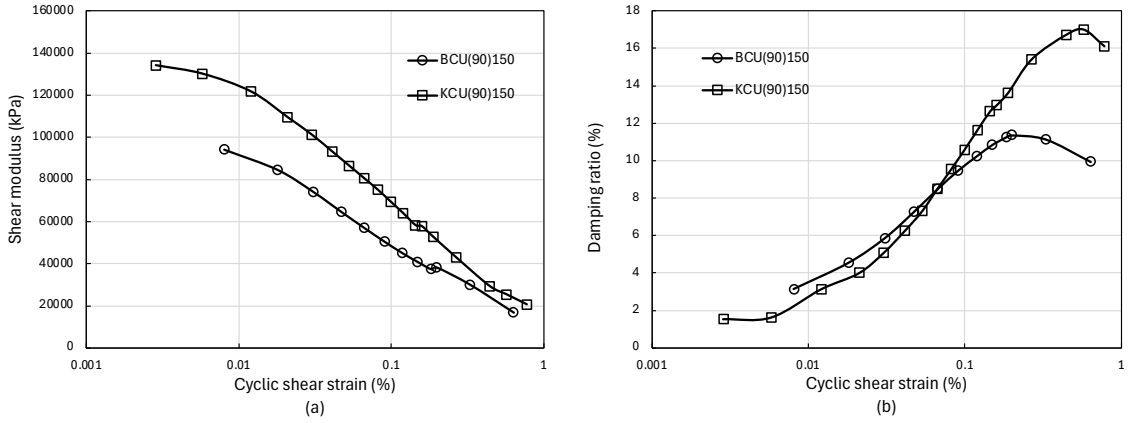


Figure 4.17: (a) Shear modulus reduction and (b) damping ratio for p_0'=150 kPa and $D_r \approx 90\%$

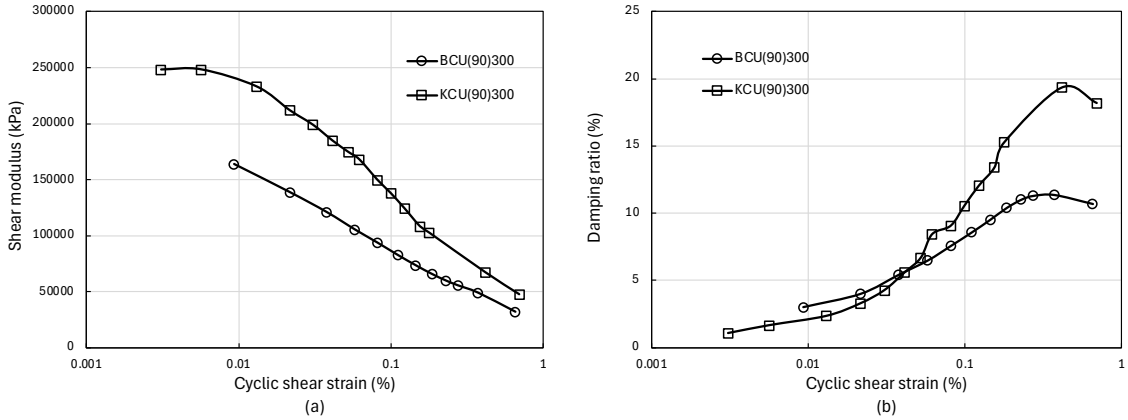


Figure 4.18: (a) Shear modulus reduction and (b) damping ratio for p_0'=300 kPa and $D_r \approx 90\%$

4.2.3 Effect of number of cycles (*N*)

Although the number of cycles (N) for the undrained tests was limited to only 40 cycles, a slight influence of N was observed for the G-γ_c and D-γ_c curves. The observed influence is attributed to the tendency of soil to either contract or dilate, resulting in the generation of negative or positive excess pore water pressures when drainage is prevented. Since the effect of N is almost the same for all tests, only a few cases for the Blessington sand are shown here. Figure 4.19 to Figure 4.21 present the G-γ_c and D-γ_c curves for samples subjected to p_0'=150 kPa, prepared to D_r values of 30%, 60% and 90%, respectively. The results show that with the increase of N, the shear modulus of the samples degrade regardless of the D_r value. This shear modulus degradation is a result of the progressive increase in positive excess pore water pressure and the associated reduction in the mean effective stress (p'). Even though negative excess pore water pressures developed in the tests conducted on medium and dense soil samples, the residual excess pore water pressures at the end of the cycles were positive, resulting in a reduction of p'. The results in this research show that the effect of N on G is greater than the minor influence reported by Darendeli (2001) for cohesive intact soils. The D-γ_c curves for all tests show that damping slightly reduces with N. The largest reduction in damping ratio occurs during the first cycle, after which the rate of reduction slows down, and the D-γ_c curves exhibit minimal changes after N = 10. This finding closely aligns with the behaviour

observed by Darendeli (2001) based on resonant column and cyclic torsional shear tests. However, damping ratio curves derived by Blaker and Andersen (2019) using cyclic simple shear tests on dense sand show a greater influence and a larger reduction in damping compared to the results presented in this thesis. As a result, the effect of the number of cycles (N) may vary between different soils. Although the effect of N on the damping ratio of Kilmuckridge sand is not presented, the observed behaviour was very similar to that of Blessington sand.

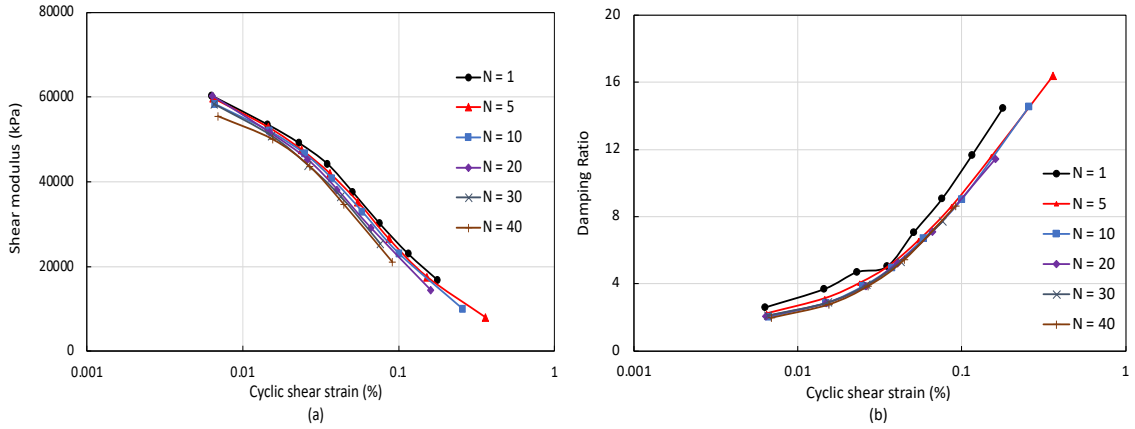


Figure 4.19: (a) Shear modulus reduction and (b) damping ratio for BCU(30)150 at N = 1, 5, 10, 20, 30, and 40

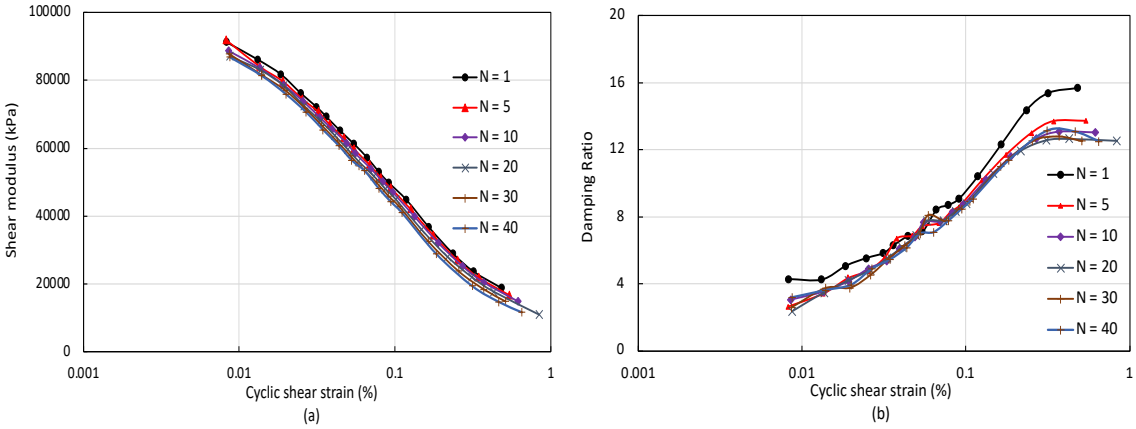


Figure 4.20: (a) Shear modulus reduction and (b) damping ratio for BCU(60)150a at N = 1, 5, 10, 20, 30, and 40

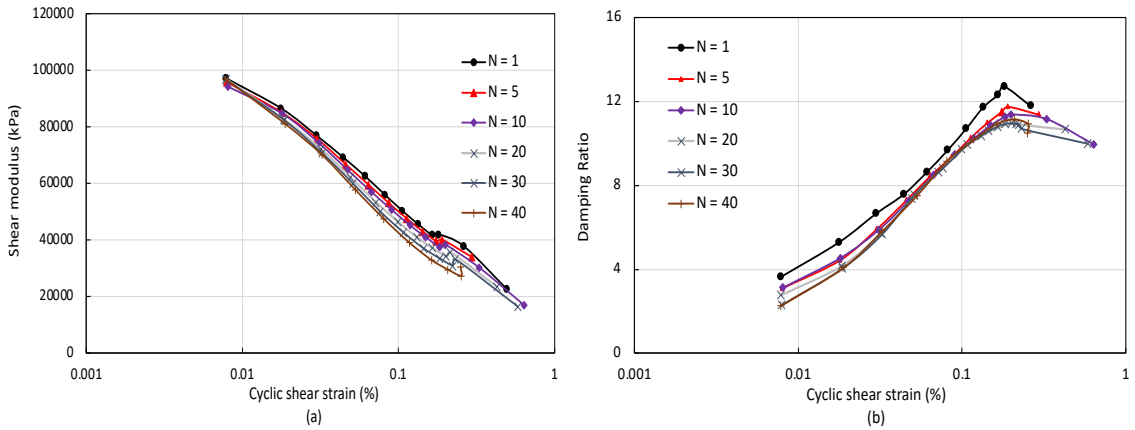


Figure 4.21: (a) Shear modulus reduction and (b) damping ratio for BCU(90)150 at N = 1, 5, 10, 20, 30, and 40

4.3 Bender element tests

Although LVDTs are capable of recording small deformations, they are not sufficiently reliable to accurately capture the value of G_0. Bender element tests are therefore required to estimate G_0 by measuring the travel time of shear waves through the soil element. The travel time is determined by measuring the time difference between the voltage signal peaks recorded by the transmitter and receiver bender elements. The shear wave velocity (V_s) of the soil is calculated by dividing the travel length, which is equal to the distance between the tips of the transmitter and receiver bender elements, by the travel time. The value of G_0 is directly related to V_s and the bulk density of the soil (ρ) according to the following formula:

$$G_0 = \rho V s^2 \tag{4.1}$$

The tests were conducted on Blessington sand to measure G_0 for D_r values of 30%, 60%, and 90% at mean effective stresses ranging from 50 kPa to 500 kPa. The G_0 values obtained are used as inputs for the parameters required for HSsmall and SANISAND-MS constitutive models. Furthermore, the values of G_0 determined from the bender element tests, based on the applied mean effective stress (p') and the void ratio (e) of the sample, were utilised in nonlinear regression analysis to determine the coefficients of the well-known empirical equation proposed by Hardin and Black (1966):

$$G_0 = Af(e)OCR^k \left(\frac{\mathrm{p}'}{P_{ref}}\right)^m \tag{4.2}$$

where P_{ref} is the reference pressure (taken as the atmospheric pressure equal to 100 kPa), OCR is the overconslidation ratio, $f(e)$ is a function of the void ratio (e), and A, m, and k are dimensionless material constants. The nonlinear regression was performed using a Python script that employs the curve_fit function from the scipy.optimize library. The script takes the mean effective stress (p') and void ratio (e) as independent variables, and the corresponding G_0 values as the dependent variable. It then determines the optimal values of A, $f(e)$, k, and m by minimising the sum of squared differences between the measured values of G_0 and those predicted using Equation (4.2). The constants A and m depend mainly on the soil type, the shape and angularity of the particles, and the gradation of the soil. The constant k is dependent on the plasticity index and is equal to 0 for granular materials. Hardin and Black (1966) proposed $f(e) = (e_g - e)^2/(1 + e)$ where e_g is determined from curve fitting the laboratory results. The authors originally suggested e_g values of 2.17 and 2.97 for rounded and angular particles, respectively.

Figure 4.22 illustrates how the travel time is determined by measuring the time lag between the peak voltage of the transmitter bender element and the first peak recorded by the receiver bender element. It is worth noting that a general sinusoidal noise was present in the receiver recordings even in the absence of transmitted pulses, likely due to inadequate shielding or grounding of the wires. For each stress level, the sample was subjected to pulses at various frequencies to assess

whether travel time varied with frequency. The travel time was selected from the frequency that produced the highest amplification in the receiver bender element. Additionally, frequency domain methods, such as the cross-correlation technique proposed by Viggiani and Atkinson (1995), were employed to analyse the recorded signals. However, this method yielded very low shear wave velocities at high *p'* values, leading to the eventual use of the peak-to-peak method. Figure 4.23 shows the increase in G_0 with respect to *p'* for the three different relative densities.

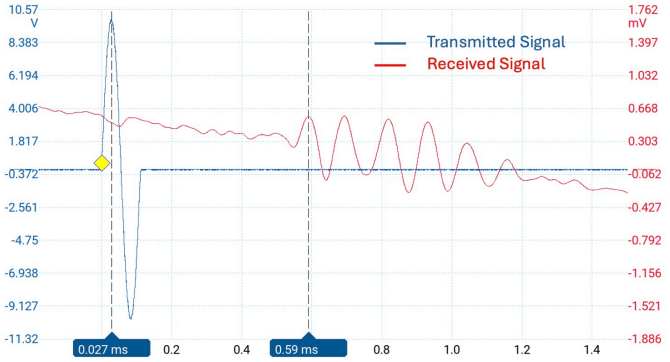


Figure 4.22: Determination of travel time from signal recordings

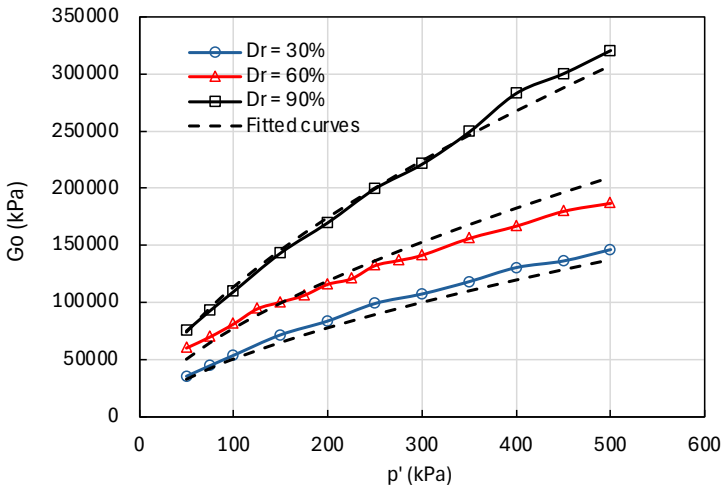


Figure 4.23: Maximum shear modulus G_0 versus mean effective stress *p'*

Figure 4.23 clearly shows the increase of G_0 with both *p'* and D_r. Furthermore, the black dashed lines show the fitted curves using equation 4.2 with the values of the parameters determined from nonlinear regression analysis of the measured data. The values of parameters A, m, and $f(e)$ are summarised in Table 4.2. Figure 4.23 confirms that the fitting parameters are appropriate, as the fitted curves closely match with the measured data.

Table 4.2: Parameters of equation 4.2 fitted with Blessington G_0 data

A	***m***	***f(e)***
149938.63	0.62	$(1.62 - e)^2/(1 + e)$

4.4 Drained triaxial tests

In addition to the undrained triaxial database, a testing campaign is also conducted to study G-γ_c and D-γ_c curves for Blessington sand under fully drained conditions. The tests were conducted under the same confining pressures and relative densities as the undrained tests. To ensure fully drained conditions, the loading frequency was reduced to 0.02 Hz, allowing the water to escape without generating excess pore water pressure. Examination of the pore pressure transducer readings indicated that the loading frequency of 0.02 Hz was sufficiently slow to prevent the development of excess pore water pressures in all tested samples. Although the majority of the database consists of tests conducted with a limited number of cycles (N = 40), three additional tests were performed to generate G-γ_c and D-γ_c curves for up to 1000 cycles. The drained cyclic tests are summarised in Table 4.3 in terms of p_0', D_r, and the consolidated void ratio (e_i). The nomenclature of the test IDs is as follows:

BCD(30)50

The letter 'B' refers to Blessington sand, as in the undrained case, while 'CD' indicates cyclic drained tests, as opposed to 'CU', which was used to refer to undrained tests. As for the undrained tests, the number inside the brackets represents the target D_r value, while the number outside indicates the applied p_0'. The test IDs which have an 'L' letter at the end indicate large cyclic tests with N = 1000. All tests are two-way symmetrical, except for BCD(30)100L and BCD(60)200L tests, which were conducted to inform the cyclic parameters of the SANISAND-MS model. Initially, the results are presented to show the effects of different p_0' and D_r values. Subsequently, the results are analysed to examine whether the cyclic behaviour of drained and undrained loading is different.

Table 4.3: Database for drained cyclic tests

Test Number	Test ID	p_0' (kPa)	D_r (%)	e_i
1	BCD(30)50	50	30	0.827
2	BCD(30)150	150	30	0.811
3	BCD(30)300	300	30	0.793
4	BCD(60)50	50	60	0.694
5	BCD(60)150	150	60	0.675
6	BCD(60)300	300	60	0.682
7	BCD(90)50	50	90	0.548
8	BCD(90)150	150	90	0.544
9	BCD(90)300	300	90	0.551
10	BCD(90)50L	50	90	0.550
11	BCD(90)150L	150	90	0.545
12	BCD(90)300L	300	90	0.571
13	BCD(30)100L	100	30	0.809
14	BCD(60)200L	200	60	0.685

4.4.1 Effects of mean effective stress and relative density

The results in this section examine the effects of p_0' and D_r on the dynamic soil behaviour in a similar manner as was done for the undrained tests. Initially, the effects of varying p_0' on G-γ_c and D-γ_c curves are presented in Figure 4.24 for the samples reconstituted to $D_r \approx 60\%$. The results in Figure 4.24a show that, at the same cyclic shear strain (γ_c), the secant shear modulus (G) increases with increasing p_0', which is consistent with the observed trend from the undrained test database. Furthermore, Figure 4.24b shows consistent trends with those observed from the undrained tests, whereby at the same cyclic shear strain (γ_c), the damping ratio (D) decreases as the value of p_0' increases.

The effect of D_r on the G-γ_c and D-γ_c curves is shown in Figure 6.25 to Figure 6.27 for tests conducted under p_0' values of 50 kPa, 150 kPa, and 300 kPa, respectively. These figures clearly show that, for a given value of p_0', the secant shear modulus (G) increases as the soil density increases. The damping ratio curves (D-γ_c) in Figure 6.25 to Figure 6.27 indicate that soil damping, across the investigated range of shear strains, is only marginally influenced by variations in D_r. This observation aligns with the behaviour noted from the undrained tests, and confirms the conclusions drawn from previous studies (e.g., Kokusho, 1980; Wichtmann and Triantafyllidis, 2013). It is important to emphasise that the minimal effect of D_r on soil damping may only be valid for shear strains in the small to medium strain range. At higher strain levels, when soil dilation becomes more pronounced, the damping behaviour could differ significantly. The maximum cyclic shear strain obtained in the drained tests was around 0.3%, which is below the level of shear strains that are required for the effect of dilation to become important. Given that the tests were stress-controlled, it was required to increase the cyclic deviatoric stress applied to achieve larger cyclic shear strains. However, increasing the cyclic deviatoric stress involved increasing the cyclic axial stress which could lead to the top platen losing contact with the soil when the effective cyclic axial stress (σ_1') exceeds the effective confining pressure (σ_3'). This limitation does not apply to undrained tests, as reversing the load into extension generates negative pore water pressures, allowing the soil sample to maintain contact with the top platen.

In addition to the shear modulus reduction (G-γ_c) and damping ratio (D-γ_c) curves, it is worthwhile to investigate the effects of p_0' and D_r on the normalised shear modulus reduction curves (G/G_0-γ_c). Although the G/G_0-γ_c curves can, in principle, be obtained by dividing the G values presented in Figure 4.24 to Figure 6.27 by the G_0 values from the bender element tests, it is important to note that the G_0 values were derived from different reconstituted samples than those used in the cyclic triaxial tests. Consequently, the relative densities in the bender element tests were slightly different from those in the cyclic triaxial tests. For this reason, the G_0 values obtained from the bender element tests cannot be reliably used to generate the normalised shear modulus reduction curves

(G/G_0-γ_c). However, one way to overcome this issue and derive representative G/G_0-γ_c curves is by extrapolating the shear modulus reduction curves (G-γ_c) in Figure 4.24 to Figure 6.27 to back-calculate appropriate values of G_0. This was accomplished by selecting a suitable function to fit the shear modulus reduction curves (G-γ_c). The hyperbolic function proposed by Darendeli (2001) was adopted for this purpose, and the fitting was performed using the same procedure in section 4.3, which involved implementing a Python script that uses the curve_fit function from the scipy.optimize library. The details regarding the hyperbolic function and its associated fitting parameters are addressed in detail in Section 4.5.

Figure 4.28 illustrates the effect of p_0' on the normalised shear modulus reduction curves (G/G_0-γ_c) based on the data presented in Figure 4.24. Figure 4.28a shows the fitting of the hyperbolic function to the actual G-γ_c data, while Figure 4.28b compares the resulting G/G_0-γ_c curves based on the back-calculated G_0 values. The main conclusion that can be drawn from Figure 4.28b is that, at the same magnitude of the cyclic shear strain (γ_c), the value of the normalised shear modulus (G/G_0) increases with increasing the applied p_0' . This finding aligns with the trend observed from previous studies (e.g., Kokusho, 1980; Wichtmann and Triantafyllidis, 2013).

The effect of D_r on the normalised shear modulus reduction curves (G/G_0-γ_c) are investigated based on the results in Figure 4.27a. Figure 4.29a demonstrates the fitting of the hyperbolic function to the actual G-γ_c data, while Figure 4.29b compares the corresponding G/G_0-γ_c curves based on the back-calculated G_0 values. The results in Figure 4.29b indicate that at the same applied p_0', the relative density (D_r) has no influence on the normalised shear modulus reduction curves (G/G_0-γ_c). This finding is consistent with observations reported by Kokusho (1980), based on cyclic triaxial tests on Toyoura sand, and by Wichtmann and Triantafyllidis (2013), from resonant column tests conducted on natural quartz sand. Since the observations presented in this section align with previous experimental studies on sands, the behaviour of Blessington sand can be regarded as representative of cohesionless materials. Furthermore, these observations were used in curve fitting to provide idealised relationships for the damping ratio and normalised shear modulus reduction curves of Blessington sand. The details regarding the empirical functions employed in fitting the laboratory results are thoroughly discussed in Section 4.5

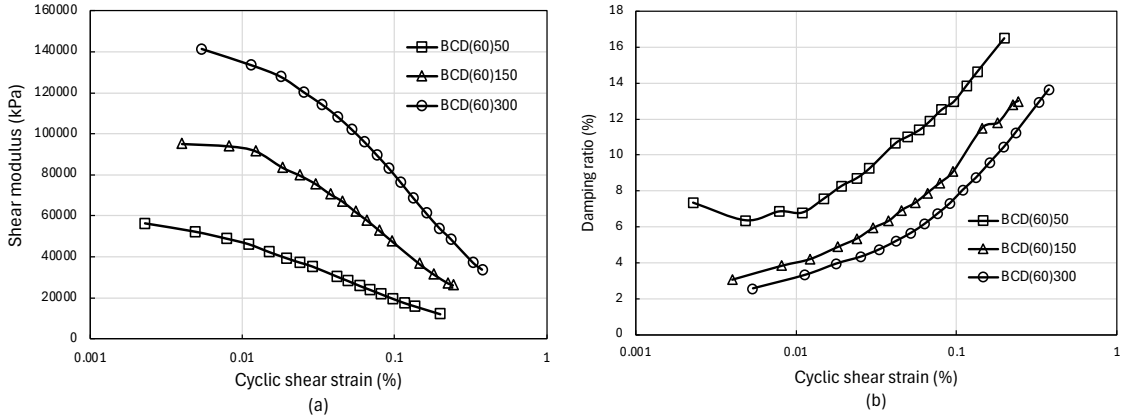


Figure 4.24: (a) Shear modulus reduction and (b) damping ratio of Blessington sand with $D_r \approx 60\%$

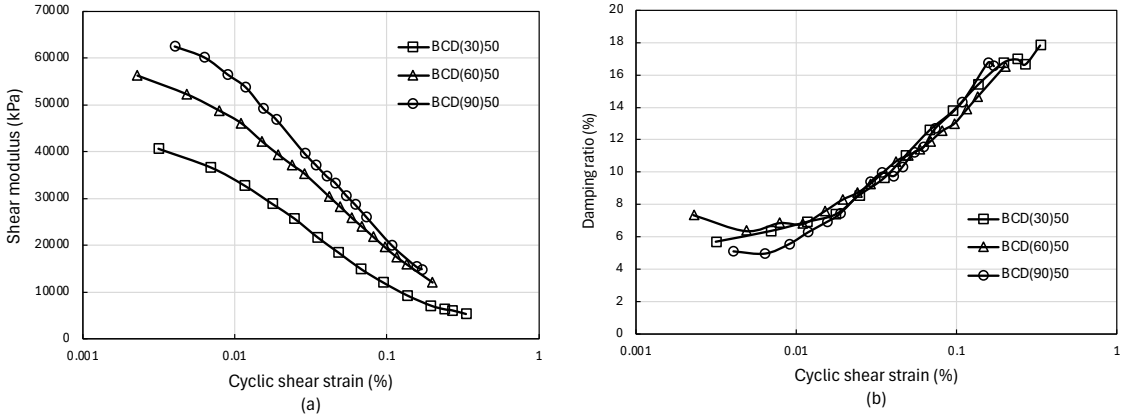


Figure 4.25: (a) Shear modulus reduction and (b) damping ratio of Blessington sand tested at p_0'=50 kPa

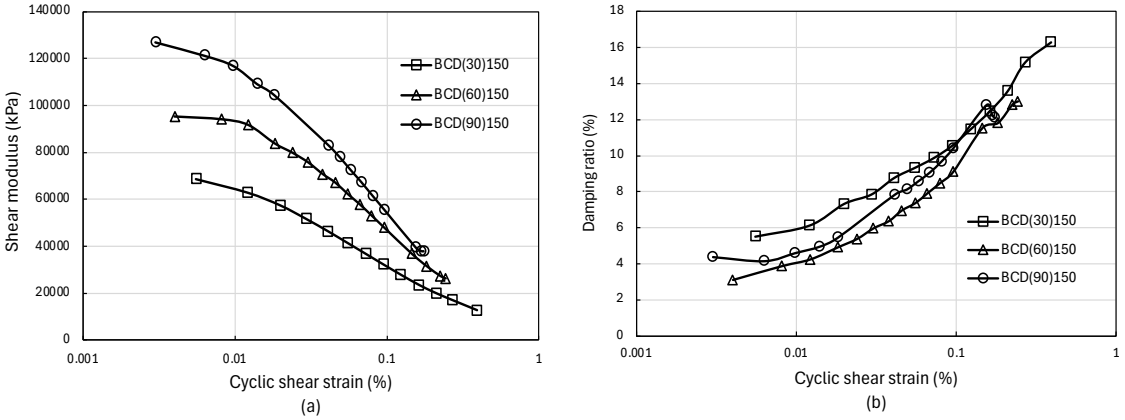


Figure 4.26: (a) Shear modulus reduction and (b) damping ratio of Blessington sand tested at p_0'=150 kPa

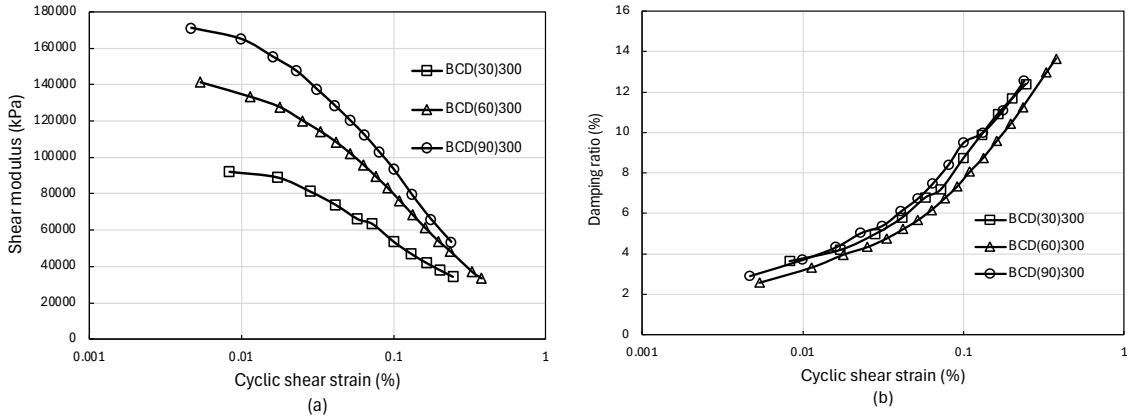


Figure 4.27: (a) Shear modulus reduction and (b) damping ratio of Blessington sand tested at p_0'=300 kPa

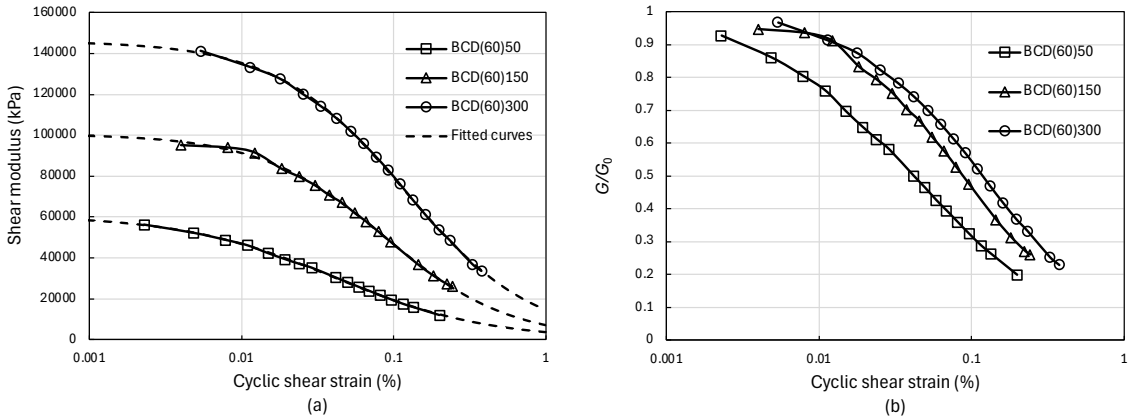


Figure 4.28: Effect of p_0' on G/G_0-γ_c curves: (a) fitting of G-γ_c curves; (b) G/G_0-γ_c curves for D_r = 60%

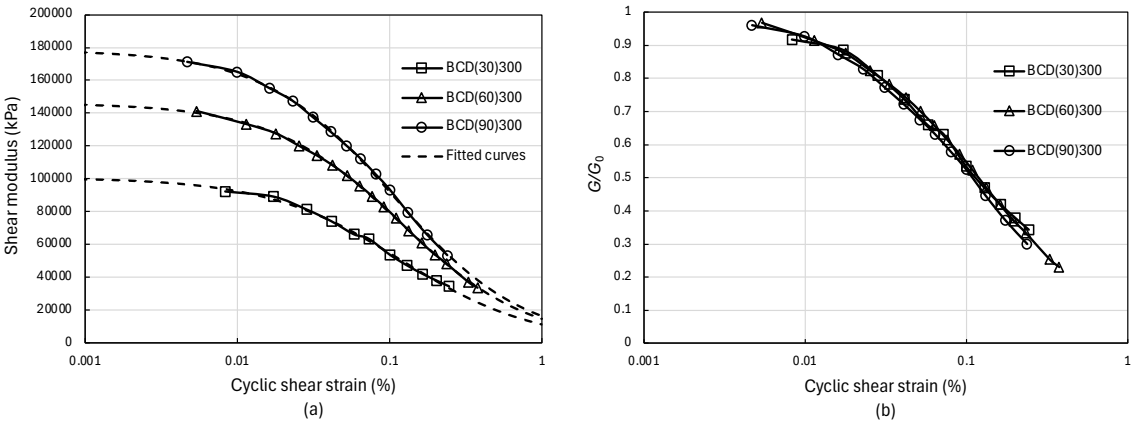


Figure 4.29: Effect of D_r on G/G_0-γ_c curves: (a) fitting of G-γ_c curves; (b) G/G_0-γ_c curves for p_0' = 300 kPa

4.4.2 Comparison between drained and undrained

The effect of drainage on the damping response of soil is investigated by comparing the damping ratio curves (D-γ_c) from both drained and undrained experiments conducted on soil samples tested under similar void ratio and effective stress conditions. There are very few studies in the literature that directly compared the behaviour between fully drained and undrained conditions. One reason is that most research studies focused on the dynamic behaviour of sand materials subjected to earthquake loads, which are rapid and the soil behaviour can be idealised as fully undrained.

However, the behaviour of soil under the loads experienced by OWTs is more complex. Traditional design standards, such as API (2010) and DNV (2014), assume that soil behaves in a fully drained manner. Additionally, most field and physical model studies on monopiles installed in sands have been carried out under drained conditions, which can be justified by the low frequency of wind and wave loads. However, finite element analyses conducted by Li et al. (2019) suggested that for large monopiles, the behaviour of sands may become fully undrained within a single load cycle. As a result, comparing drained and undrained damping becomes highly significant.

The comparisons in this section are shown for the soil samples prepared to $D_r \approx 60\%$; however, similar findings were observed for samples prepared to different relative densities. The damping ratio curves are shown in Figure 4.30 to Figure 4.32 for the samples subjected to p_0' values of 50 kPa, 150 kPa, and 300 kPa, respectively. The main conclusion that can be drawn from the observed curves is that the drained damping ratios were slightly higher than those of undrained tests. Furthermore, a clear trend is evident from the tests, which suggests that the effect of drainage condition increases with decreasing p_0'. However, it is difficult to state whether this behaviour is true for different kinds of granular materials as the existing literature lacks extensive comparisons between drained and undrained damping ratios. One study that investigated the effect of drainage was conducted by Kokusho (1980), who carried out cyclic triaxial tests on Toyoura sand and concluded that the D-γ_c curves for drained and undrained shearing are approximately identical. The higher D-γ_c obtained from the drained experiments could be attributed to calculating the damping ratio and the corresponding cyclic shear strain from the hysteresis loops of the axial LVDTs. In a fully drained condition, the axial strain loops are due to both volumetric and deviatoric hysteretic behaviour. However, volumetric hysteretic behaviour does not occur when shearing is performed under constant volume (undrained loading) since no drainage occurs and the volume of the sample remains the same.

Understanding the effect of drainage on soil damping from a micromechanical perspective is challenging and requires further testing to achieve a robust interpretation of the results. Given that damping is lower for the undrained condition, the D-γ_c curves from the undrained tests were adopted in fitting the chosen hyperbolic function and determining the associated parameters. Although the drained damping ratio curves were not used in this thesis, the observations drawn from them emphasise the importance of considering different drainage conditions and their influence on the energy dissipation behaviour of soil.

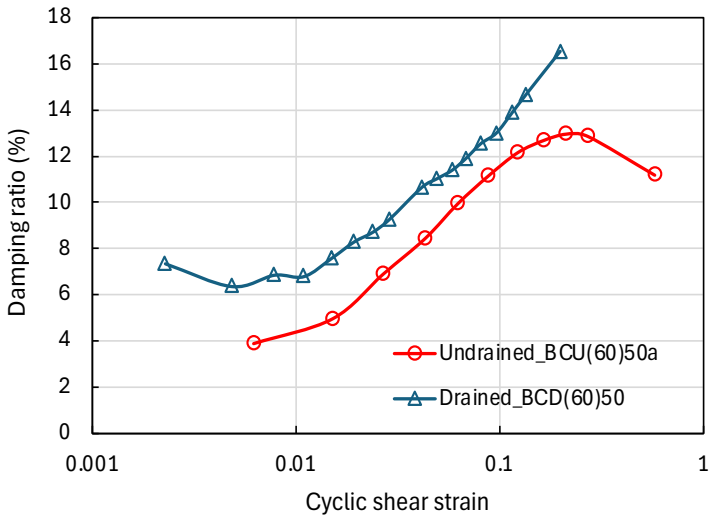


Figure 4.30: Drained and undrained damping ratio comparison (p_0'= 50 kPa)

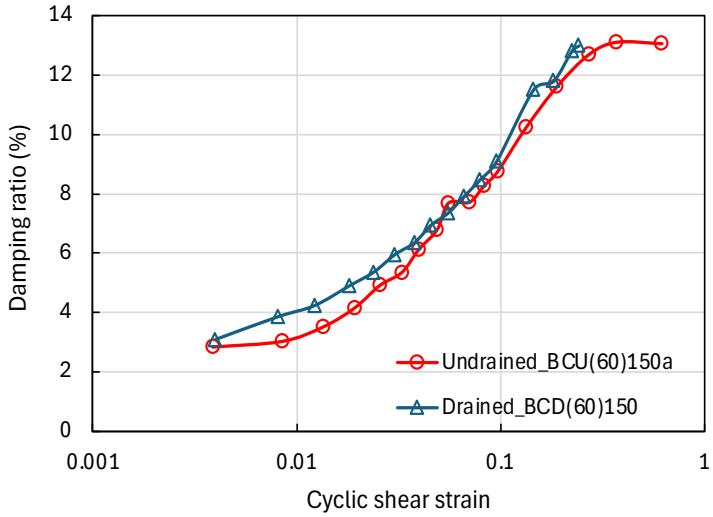


Figure 4.31: Drained and undrained damping ratio comparison (p_0'= 150 kPa)

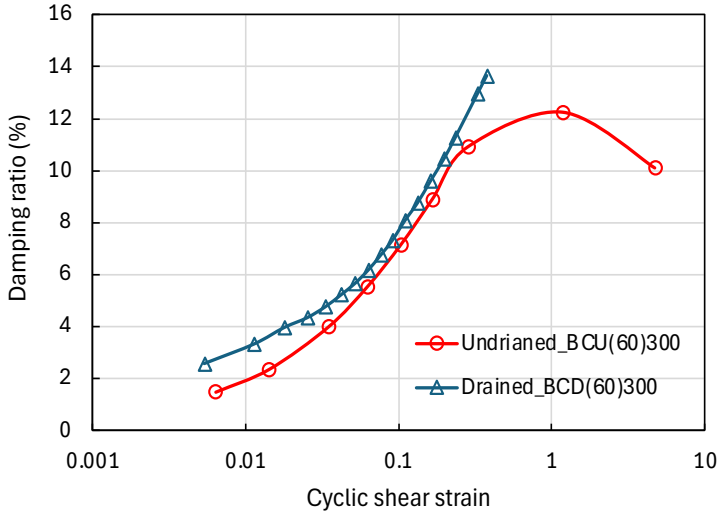


Figure 4.32: Drained and undrained damping ratio comparison (p_0'= 300 kPa)

4.4.3 Effect of number of cycles (*N*)

The effect of the number of loading cycles (*N*) was investigated using the large cyclic tests BCD(90)50L, BCD(90)150L, and BCD(90)300L, each of which was subjected to up to 1000 cycles at various deviatoric stress amplitudes. In all tests, the influence of *N* was evident, with the damping ratio (*D*) decreasing as *N* increased. Large cyclic tests were not conducted for varying relative densities, as observations from the short cyclic tests indicated that the rate of reduction in *D* was not significantly affected by relative density. Figure 4.33 presents the decay of the damping ratio for two cyclic shear strain amplitudes (γ_c = 0.05% and γ_c = 0.1%) under confining pressures of 50 kPa and 150 kPa. The horizontal axis is plotted on a logarithmic scale. To quantify the rate of damping decay, the results for each shear strain amplitude and confining pressure were fitted in Excel using natural logarithmic trendlines. This approach was chosen because the slope coefficient in the logarithmic equation represents the rate of decay, thereby offering insight into the effect of *N* on the damping ratio.

The results in Figure 4.33 show that the decay of *D* depends on both the level of p_0' and γ_c. Comparing the slope coefficients of tests BCD(90)50L and BCD(90)150L reveal that the decay of damping decreases as p_0' increases. For example, for the cyclic shear strain (γ_c) magnitude of 0.1%, the rate of decay for the sample sheared under p_0' of 50 kPa is 0.597, whereas the rate of decay for the sample sheared under p_0' of 150 kPa is 0.183. Furthermore, the results in Figure 4.33 show that rate of decay increases as the magnitude of the cyclic shear strain (γ_c) increases. For the same p_0' of 150 kPa, the rate of decay for γ_c = 0.05% is 0.118, whereas for γ_c = 0.1%, the rate of decay is 0.183.

However, it is important to note that although soil damping decreases with increasing *N*, the reduction is most significant during the first 100 cycles. Beyond this point, the rate of decay gradually diminishes, and the damping ratio eventually stabilises, showing negligible degradation by *N* = 1000 cycles. This is shown in Figure 4.34, which displays the effect of *N* on soil damping with the horizontal axis plotted with a linear scale. Large cyclic undrained tests were not examined in this study because the undrained behaviour of sand is typically limited to the first few cycles, after which the response becomes either partially or fully drained.

The effect of number of cycles (*N*) on the secant shear modulus (*G*) is not presented here as it is effect was very minimal. Given that the effect of *N* on both the secant shear modulus (*G*) and damping ratio was insignificant for the material tested in this research, the curve fitting in Section 4.5 based on the hyperbolic functions provided do not address the influence of *N*.

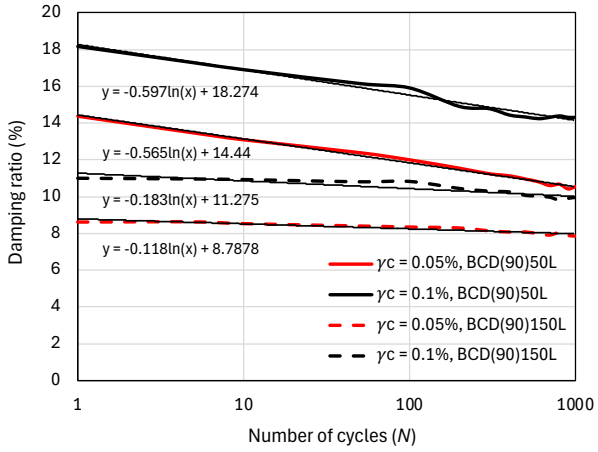


Figure 4.33: Influence of *N* on the damping ratio of soil (horizontal axis in logarithmic scale)

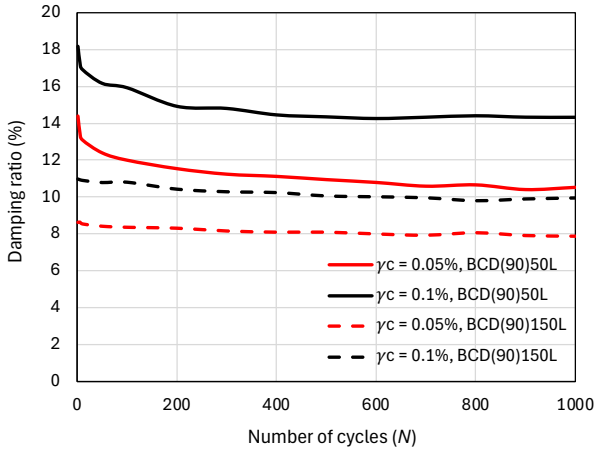


Figure 4.34: Influence of *N* on the damping ratio of soil (horizontal axis in linear scale)

4.5 Fitting empirical functions

It is common practice in the analysis of dynamic soil-structure interaction problems to use empirical functions, with their parameters determined from the initial effective stresses and the in-situ characteristics of the soil. This approach is due to the difficulty and cost associated with conducting element tests in the laboratory. This section introduces the most commonly used empirical equations in the literature and selects the most suitable ones to represent the normalised shear modulus reduction (G/G_0-γ_c) and damping ratio (D-γ_c) curves. Nonlinear regression analyses were conducted to fit the empirical equations to the laboratory results presented in this chapter. The empirical functions were fitted exclusively to Blessington sand results, as the tests conducted on Kilmuckridge sand were limited in number and showed inconsistencies under the same initial conditions. The curve-fitted empirical functions were used for calibrating the constitutive models, and are also presented to allow the shear modulus and damping ratio curves to be obtained at any mean effective stress.

4.5.1 Normalised shear modulus reduction

The earliest empirical function used to represent the normalised shear modulus reduction (G/G_0-γ_c) is the hyperbolic function proposed by Hardin and Drnevich (1972b). The hyperbolic function is as follows:

$$\frac{G}{G_o} = \frac{1}{1 + \frac{\gamma_c}{\gamma_r}} \tag{4.3}$$

where G/G_0 is the normalised shear modulus, γ represents the cyclic shear strain, and γ_r is the reference cyclic shear strain. According to Hardin and Drnevich (1972b), γ_r is defined as the ratio of the maximum shear strength (τ_{max}) to G_0. Normalising the cyclic shear strain by γ_r is highly beneficial, as it eliminates the influence of the mean effective stress, allowing a single G/G_0 curve to be obtained for different p_0' values when plotted against γ/γ_r. Furthermore, the stress-strain relationship described by the hyperbolic function (Equation 4.3) produces a curve with an initial stiffness equal to G_0, which decreases with strain and eventually becomes asymptotic to a horizontal line defined by the shear stress equal to τ_{max}. However, additional definitions of γ_r have been proposed in the literature, as measuring τ_{max} can be challenging in laboratory tests, particularly in cases where an asymptotic line is not observed. For example, Hardin and Kalinski (2005) proposed a simpler definition of γ_r, expressed as $\sqrt{p'/p_{atm}}$, where p' is the mean effective stress and p_{atm} is the atmospheric pressure. A modification of Equation 4.3 was proposed by Darendeli (2001):

$$\frac{G}{G_o} = \frac{1}{1 + (\frac{\gamma_c}{\gamma_r})^{\alpha}} \tag{4.4}$$

where α represents the curvature of the shear modulus reduction curve, and γ_r is the reference shear strain at $G/G_0 = 0.5$. The empirical function proposed by Darendeli (2001), with its two fitting parameters, provides a better fit than Equation 4.3. As a result, it has been widely adopted in research studies such as Menq (2003), Zhang et al. (2005), and Wichtmann and Triantafyllidis (2013). Equation 4.4 is the empirical function used to fit the results presented in this thesis. Oztoprak and Bolton (2013) proposed a modified hyperbolic model (Equation 4.5), which includes the elastic linear shear strain threshold (γ_{lt}) as an additional parameter, allowing more control over fitting the results.

$$\frac{G}{G_o} = \frac{1}{1 + (\frac{\gamma_c - \gamma_{lt}}{\gamma_r})^{\alpha}} \tag{4.5}$$

The hyperbolic function suggested by Darendeli (2001) (Equation 4.4) is fitted to the undrained and drained test results. The aim of the curve fitting is to determine how the values of α and γ_r change with respect to relative density (D_r) and initial mean effective stress (p_0'). For the undrained tests, the variations of α and γ_r are shown in Figure 4.35a and Figure 4.35b, respectively. Figure 4.35a shows some discrepancies, while α shows an increasing trend with p_0' for samples reconstituted to D_r values of 30% and 60%, α decreases with p_0' for the samples at $D_r \approx 90\%$. Furthermore, Figure

4.35a also shows that α decreases as the relative density becomes higher. The findings in the literature are inconsistent in regard to the influence of effective stresses and relative density on the parameter α. While studies such as Oztoprak and Bolton (2013), Wichtmann and Triantafyllidis (2013), and Darendeli (2001) observed no influence of p_0' on α, Menq (2003) noted that α increases with p_0' and provided an equation of the form $\alpha = 0.86 + 0.1\log(p_0'/p_{atm})$. For gravel and sandy soils, Darendeli (2001) suggested using a constant α value of 0.92. Based on an extensive database compiled from over 70 studies, Oztoprak and Bolton (2013) reported that the value of α for sands ranges from 0.75 to 1.0, with an average of 0.88. Wichtmann and Triantafyllidis (2013) noted that α is neither influenced by density nor effective stresses, and recommended an α value of 1.03. The value of α in Figure 4.35a varies between 0.67 and 1.17, with an average value of 0.9. Therefore, this confirms that average value of α obtained in this thesis falls within the range expected for sands, as observed in the aforementioned previous studies.

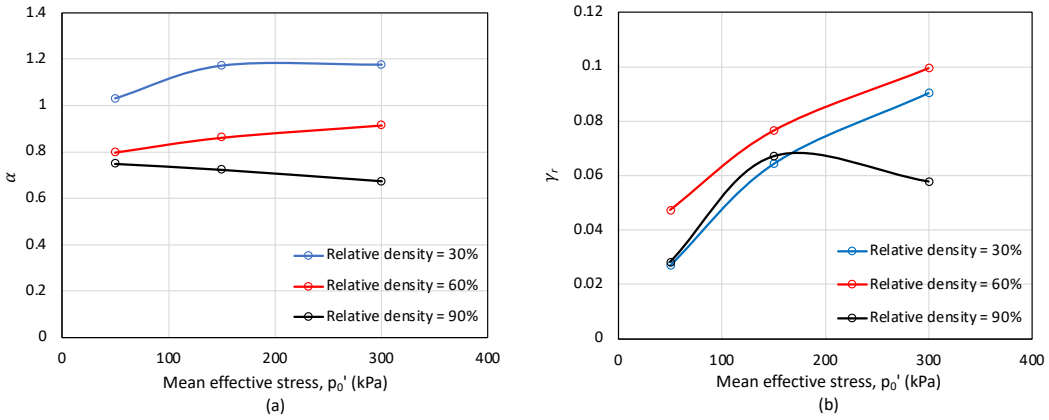


Figure 4.35: Curve fitting of the undrained tests: (a) α and (b) γ_r

The results in Figure 4.35b show that γ_r increases with p_0' and decreases with D_r. The effect of p_0' on γ_r has been observed in many studies and incorporated in various empirical functions (e.g., Darendeli, 2001; Menq, 2003; Oztoprak and Bolton, 2013; Wichtmann and Triantafyllidis, 2013). Although the influence of p_0' on γ_r is well-documented, none of the previous studies in the literature indicate that γ_r is affected by density. As a result, the drained tests are also investigated to check whether γ_r is influenced by relative density. The variation of α and γ_r for the drained test results are shown in Figure 4.36a and Figure 4.36b, respectively. Figure 4.36a shows a slight influence of the mean effective stress on α, with α increasing as the mean effective stress becomes larger. α varies between 0.86 and 1.05, with the average value equal to 0.96. In contrast to the observed influence of relative density on α in the undrained case, Figure 4.36a shows no definitive effect of relative density. Therefore, it can be concluded that, at least for the drained case, α is not governed by relative density. Figure 4.36b shows that while γ_r increases with the mean effective stress, the effect of relative density on γ_r is insignificant and can be neglected.

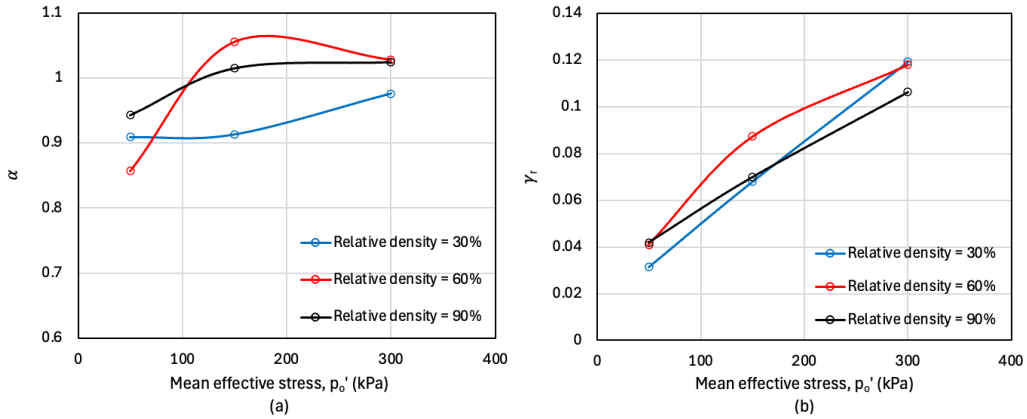


Figure 4.36: Curve fitting of the drained tests: (a) α and (b) γ_r

Although distinct correlations for α and γ_r can be provided for the drained and undrained case, the correlations provided here are only based on the drained case given that it provides simpler normalised shear modulus reduction (G/G_0-γ_c) curves without requiring the relative density as input. A constant α value of 0.96 is recommended and γ_r variation with the mean effective stress can determined with following power law:

$$\gamma_r\,(\%) \;= 0.0584\,(\frac{p_0'}{patm})^{0.615} \tag{4.6}$$

where 0.0584% is the γ_r at the reference atmospheric pressure of 100 kPa. To verify whether the correlation for γ_r and the constant value of α provide a good approximation of the G/G_0-γ_c curves obtained from the drained laboratory tests, Figure 4.37 compares the predicted G/G_0-γ_c curves derived using Equation 4.4 with the actual G/G_0-γ_c curves from tests conducted under p_0' of 150 kPa. Figure 4.37 shows that Equation 4.4 with the constant α of 0.96 and the correlated γ_r based on the power law in Equation 4.6, fits well with the drained triaxial test results and hence the correlations provided in this section can be used to obtained shear modulus reduction curves for granular materials when laboratory test results are not available.

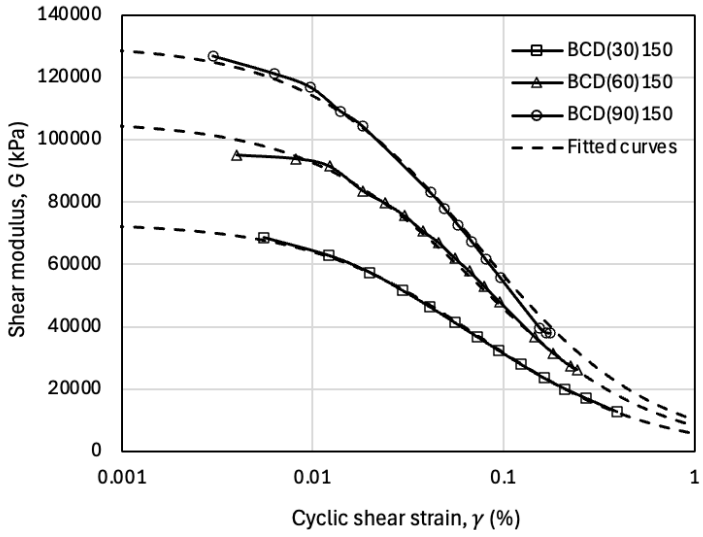


Figure 4.37: Comparison between laboratory results and the fittings with Equation 4.4

4.5.2 Damping ratio

Several functions in the literature have been developed to fit the hysteretic soil damping curves. In addition to the hyperbolic function developed for the shear modulus reduction, Hardin and Drnevich (1972b) suggested the following equation for D-γ_c:

$$\frac{D}{D_{max}} = \frac{\frac{\gamma_c}{\gamma_r}}{1 + \frac{\gamma_c}{\gamma_r}} \tag{4.7}$$

where D_{max} is an asymptotic value of damping ratio at large shear strains. A slightly more refined version of Equation 4.7 is:

$$\frac{D}{D_{max}} = \frac{\frac{\gamma_c}{\gamma_r}\left[1+\mathrm{a}\exp\left(-\mathrm{b}\frac{\gamma}{\gamma_r}\right)\right]}{1 + \frac{\gamma_c}{\gamma_r}\left[1+\mathrm{a}\exp\left(-\mathrm{b}\frac{\gamma}{\gamma_r}\right)\right]} \tag{4.8}$$

where a and b are curve-fitting parameters. Several research studies proposed to link the damping ratio with G/G_0-γ_c curves. For example, Ishibashi and Zhang (1993) proposed the following equation which takes into account the effect of soil plasticity index PI:

$$D = \frac{0.333(1+ \mathrm{e}^{-0.0145\mathrm{PI}^{1.3}})}{2}\left\{0.586\left(\frac{G}{G_0}\right)^2 - 1.547\left(\frac{G}{G_0}\right) + 1\right\} \tag{4.9}$$

Another model that also employs G/G_0 to determine D was introduced by Darendeli (2001). The model is based on adjusting the damping ratio calculated with assuming Masing-type behaviour to fit the actual measured D-γ_c from laboratory tests. The equation of the model proposed by Darendeli is as follows:

$$D = \mathrm{b}\left(\frac{G}{G_0}\right)^{0.1} D_{Masing} + D_{min} \tag{4.10}$$

where b is a curve fitting parameter, and D_{Masing} is the damping calculated assuming Masing-type behaviour.

This model was also used by Menq (2003) to fit the D-γ_c curves obtained from experiments conducted on coarse-grained granular soils. The equation used to fit the results in this chapter is equation 4.8, due to its simplicity. As suggested by Wichtmann and Triantafyllidis (2013), γ_r is taken as $\sqrt{p'/p_{atm}}$ instead of the original definition ($\gamma_r = \tau_{max}/G_0$) introduced by Hardin and Drnevich (1972b). The value for the coefficient b was taken as a constant value of 1.0. The choice of assigning a value of 1.0 to b was based on the recommendation by Wichtmann and Triantafyllidis (2013). The two parameters that are determined from curve fitting the results were D_{max} and a, which were assumed to vary with p_0'. The parameter values presented in this section are only recommended to be used for coarse-grained granular soils with fines content less than 10%, and PI around 0%. Since the undrained damping curves were slightly lower than the drained curves, making them more conservative, the nonlinear regression analyses using Equation 4.8 were

performed on the undrained test results. Based on the nonlinear regression analyses the correlated parameters of Equation 4.8 are summarised in Table 4.4. In order check whether the correlations in Table 4.4 provide reasonable damping ratio curves, Figure 4.38 compares between the fitted D-γ_c curves using Equation 4.8 and the D-γ_c curves obtained from the undrained triaxial tests conducted on the samples prepared to $D_r \approx 60\%$. Figure 4.38 shows that the D-γ_c curves derived using the empirical function in Equation 4.8 closely match the actual damping ratio curves obtained from the triaxial tests. Therefore, it can be concluded that employing Equation 4.8 with parameters taken from Table 4.4, yields representative damping ratio curves for coarse grained materials.

Table 4.4: Correlated parameters of Equation 4.8

a	b	γ_r (%)	D_{max}
19.79	1	$\sqrt{p'_o/p_{atm}}$	$-0.875\ln(p'_o/p_{atm}) + 16.039$

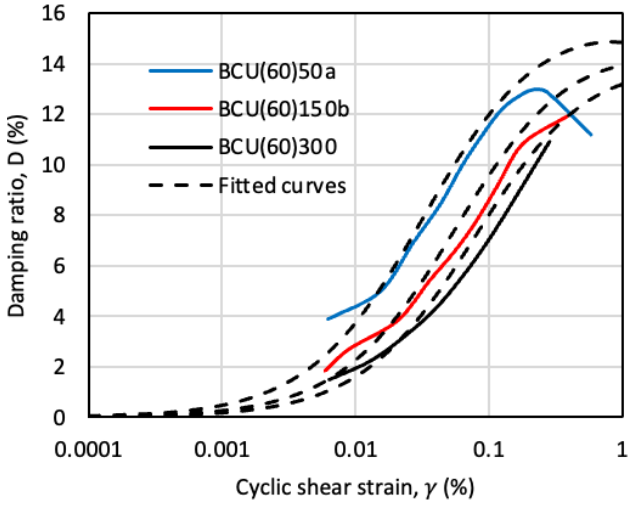


Figure 4.38: Comparing the results of the empirical function (Equation 4.8) and triaxial results

4.6 Monotonic behaviour

The monotonic tests were conducted to evaluate the strength and stiffness characteristics of Blessington sand and to calibrate the parameters of the HSsmall and SANISAND-MS constitutive models. All samples were tested under compression loading. The tests investigated the variation of the peak angle of shearing resistance (φ_p) under different mean effective stresses and relative densities. Additionally, the majority of samples were sheared to axial strains (ε_a) of approximately 25% to determine the critical angle of shearing resistance (φ_c).

Since the SANISAND-MS model is based on the critical state framework, the parameter values that determine the projection of the critical state line (CSL) onto the void ratio versus mean effective stress plane (e-p') were established. The CSL was determined from loose soil samples that undergo compaction until the critical state is reached, at which point no further changes in p' and e are observed. Furthermore, the characteristic line friction angles (φ_{cl}), which indicate the volumetric

behaviour transition from compaction to dilation, were also determined for the dilative soil samples. The monotonic tests conducted on Blessington sand are summarised in Table 4.5.

Table 4.5: Summary of Blessington monotonic tests

Test Number	Test ID	p_0' (kPa)	D_r (%)	e_i
1	BMD(30)25	25	30	0.847
2	BMD(30)40	40	30	0.832
3	BMD(30)50	50	30	0.830
4	BMD(30)120	120	30	0.817
5	BMD(30)200	200	30	0.796
6	BMD(60)20	20	60	0.682
7	BMD(60)25	25	60	0.660
8	BMD(60)50a	50	60	0.662
9	BMD(60)50b	50	60	0.687
10	BMD(60)100a	100	60	0.684
11	BMD(60)100b	100	60	0.691
12	BMD(60)150	150	60	0.657
13	BMD(60)200a	200	60	0.680
14	BMD(60)200b	200	60	0.678
15	BMD(60)300a	300	60	0.642
16	BMD(60)300b	300	60	0.665
17	BMD(60)400	400	60	0.678
18	BMD(60)500	500	60	0.676
19	BMD(60)700	700	60	0.669
20	BMU(60)300	300	60	0.677
21	BMD(90)50a	50	90	0.544
22	BMD(90)50b	50	90	0.552
23	BMD(90)150	150	90	0.534

4.6.1 Peak angle of shearing resistance (φ_p)

The peak shear resistance of soil (φ_p) primarily depends on the applied mean effective stress and relative density. Soils that tend to dilate exhibit a peak shear strength before softening, after which the strength decreases to the critical shear strength, which remains constant with further shearing. The monotonic stress-strain curves were presented in this section in terms of the mobilized angle of friction (φ_m) versus axial strain (as illustrated in Figure 4.39 and Figure 4.41). The expression used for calculating φ_m is as follows:

$$\varphi_{\mathrm{m}} = \sin^{-1}\left(\frac{3\eta}{6+\eta}\right) \tag{4.11}$$

where η is the stress ratio of the deviatoric stress (q) to the mean effective stress p' ($\eta=q/p'$). The dilatancy of Blessington sand is illustrated by the relationship between volumetric strain (ε_v) and

axial strain (ε_a) as shown in Figure 4.40 and Figure 4.42. The results of the tests conducted on the samples reconstituted to $D_r \approx 60\%$ are shown in Figure 4.39 and Figure 4.40, while the results for samples reconstituted to $D_r \approx 30\%$ are shown in Figure 4.41 and Figure 4.42. The global volumetric strain and φ_m are plotted with respect to the global axial strain, which is measured based on the movement of the pedestal and reflects the overall compression of the soil sample. The global volumetric strain (ε_v) is determined from the back pressure controller which measures the overall volume of water entering and exiting the sample.

Local LVDTs were attached to some soil samples to investigate the small-strain response. However, these tests had to be terminated shortly after the measurement range of the local LVDTs was exceeded. As deformations increased, gaps formed between the LVDT pads and the soil sample, allowing water from the cell to gradually seep into the sample through the pinholes used for LVDT attachment. This infiltration would cause the volumetric strain measurements to become inaccurate, as higher volumetric strains could be recorded by the back pressure controller. As a result, the stress-strain and volumetric behaviour of the samples with local LVDTs are not included in Figure 4.39 to Figure 4.42; however, their φ_p values are recorded and employed in analysing the variation of φ_p with relative density and mean effective stress. The stress dependent behaviour of soil can be clearly observed in Figure 4.39 and Figure 4.40 for soil samples reconstituted to $D_r \approx 60\%$. As p_0' increases, the peak φ_m value decreases, and the volumetric behaviour changes from dilation to compression. For applied p_0' values lower than 400 kPa, distinct peaks appear in the φ_m versus axial strain graph, and the samples experience dilation with further shearing. However, for p_0' values of 500 kPa and 700 kPa, the soil behaviour is completely contractive, given that no peaks occur and the volume of the samples steadily reduces until the critical state is reached at large axial strains. The results in Figure 4.39 illustrate that φ_m softens for the dilative samples and eventually converges with that of the contractive samples, which exhibit a monotonic hardening response. The goal of the comprehensive tests conducted in this research is to calibrate the constitutive soil models by applying appropriate parameter values to accurately capture the softening and hardening of soil behaviour.

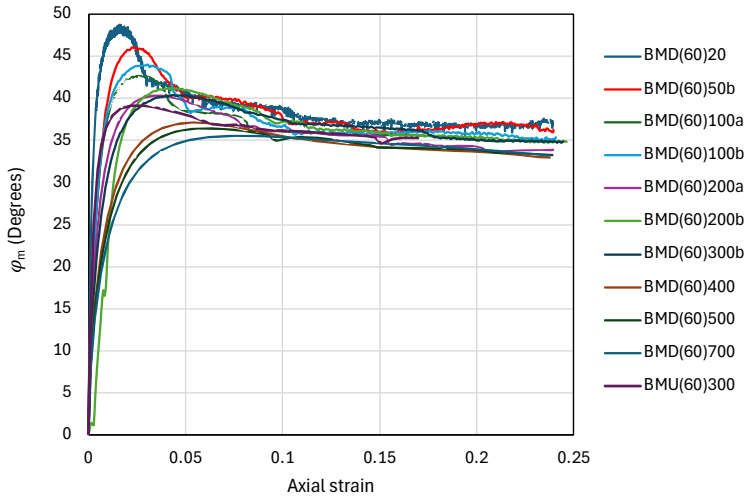


Figure 4.39: φ_m versus axial strain for samples reconstituted at $D_r \approx 60\%$

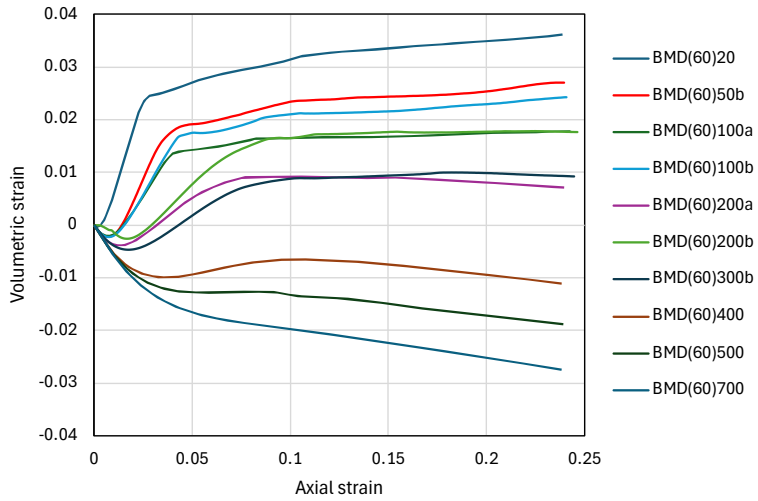


Figure 4.40: Volumetric strain versus axial strain for samples reconstituted at $D_r \approx 60\%$

Figure 4.42 shows that the behaviour of loose samples reconstituted to $D_r \approx 30\%$ is predominantly contractive, with all samples experiencing a reduction in volume until reaching the critical state. Furthermore, Figure 4.41 shows that φ_m increases gradually for all samples, tending to approach φ_c at large axial strains, without any indication of softening response. Figure 4.43 presents φ_p values plotted against p_0' for all monotonic tests, including the samples with local LVDTs that were sheared to axial strains below 10%. A clear reduction in φ_p with increasing p_0' is observed for dense soil samples reconstituted to relative densities of 60% and 90%.

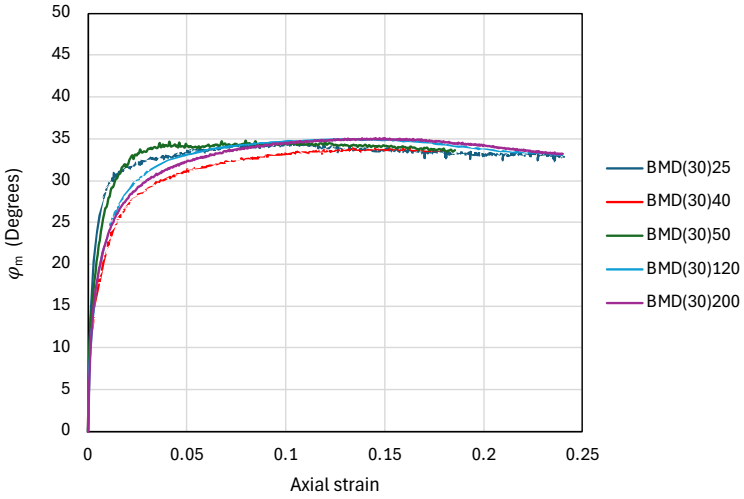


Figure 4.41: φ_m versus axial strain for samples reconstituted at $D_r \approx 30\%$

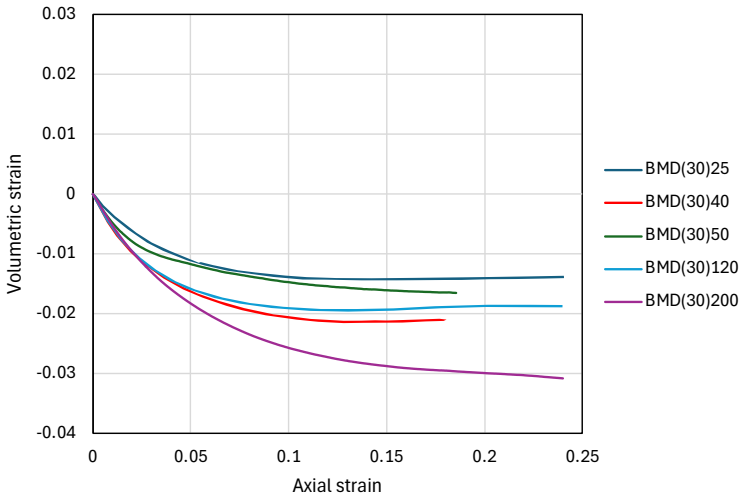


Figure 4.42: Volumetric strain versus axial strain for samples reconstituted at $D_r \approx 30\%$

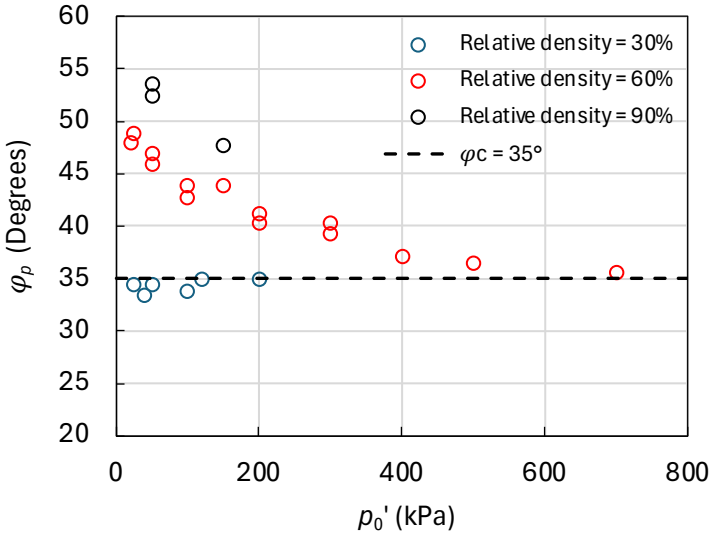


Figure 4.43: φ_p versus p_0' for all the monotonic tests

4.6.2 Critical state parameters

The results in Figure 4.43 show that φ_p decreases with increasing stress level and void ratio, ultimately approaching the critical angle of shearing resistance (φ_c). φ_c is considered a material constant, independent of void ratio and mean effective stress, and is reached at large shear strains when the behaviour stabilises and shows no further changes in strength and volume. For most samples, the deviatoric stress (q) begins to plateau once the axial strain exceeds 10%; therefore, φ_c is calculated at an axial strain of 15%. The measured φ_c values range between 33.61° and 37.19° and can be approximated to a representative value of 35° for Blessington sand. The slope of the critical state line (M_c) in the q-p' stress space is equal to 1.418 according to the following equation:

$$M_c = \frac{6 \sin \varphi_c}{3 - \sin \varphi_c} \tag{4.12}$$

Although the HSsmall constitutive model lacks inputs for critical state parameters, the SANISAND-MS model is based on the critical state framework and requires critical state parameters to be determined from monotonic compression tests.

The projection of the critical state line (CSL) in the *e-p'* space is also established from the database of the monotonic tests. The CSL determines whether the behaviour of the soil is dilative or contractive based on the void ratio and applied effective stresses. At the same mean effective stress, a given soil is dilative if its void ratio (e) is lower than critical state void ratio (e_c), and is contractive if e is higher than e_c. The value determined from the difference between e and e_c is the state parameter (Ψ), which was discussed thoroughly in Chapter two. The mean effective stress corresponding to e_c is denoted as p_c'. In critical state soil mechanics, soil behaviour in the *e-p'* space is described as "denser than critical" if it lies below the Critical State Line (CSL) and "looser than critical" if it lies above the CSL.

Ideally, a soil reconstituted at two different e values and subjected to the same p_0' would arrive at the same e_c and p_c' values. However, several studies (e.g., White, 2020; Bakri, 2021) reported that samples prepared to loose and dense states do not converge to a unified CSL in the *e-p'* space. White (2020) attributed the discrepancy to the tendency of dense samples to underpredict the critical state void ratio (e_c) due to the occurrence of shear bands and zones of strain localization. Furthermore, authors such as Klotz and Coop (2002) highlighted that the formation of premature strain localization, as a result of dilation when shearing at low confining stress levels, is a major challenge that leads to inaccuracies in identifying the CSL.

To mitigate strain localization and allow accurate identification of the CSL, Jefferies and Been (2015) recommended preparing samples to very low relative densities (i.e., high void ratios) and shearing them under high effective stress levels. Thus, the CSL for Blessington sand is derived from the samples reconstituted to $D_r \approx 30\%$. The axial strain level of 15% is used to obtain the values of e_c and p_c' from each test sample.

The power law proposed by Li et al. (1999) is adopted to fit the curve of the CSL in the *e-p'* space, as the parameter values from this power law are needed as inputs for the SANISAND-MS model. The expression of the power law (Equation 2.6) and the associated parameters are presented in Chapter two. Figure 4.44 shows the CSL determined with fitting the power law to the critical state data points from the tests. The parameter values of power law function are summarised in Table 4.6.

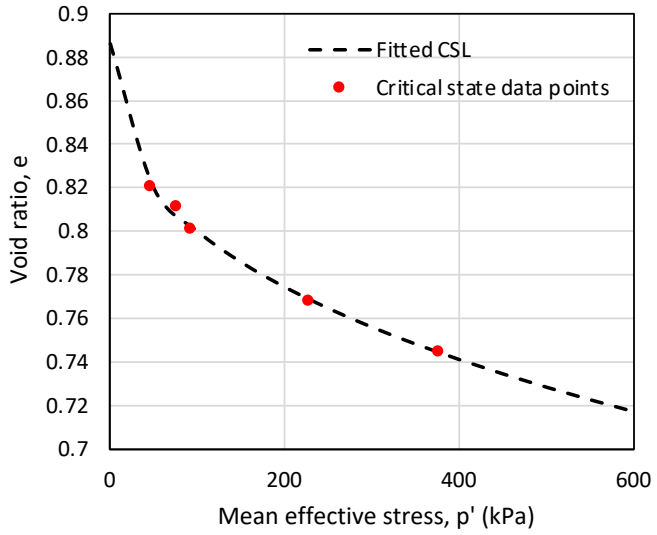


Figure 4.44: Identification of CSL for Blessington sand

Table 4.6: CSL parameters in the *e-p'* space for Blessington sand

Parameters	Fitting values
e_0	0.886
λ_c	0.086
ξ	0.376

4.6.3 Characteristic line

As discussed in the literature review chapter, the characteristic line defines the stress ratio (η_{cl}) in the *q-p'* stress space at which volumetric behaviour transitions from contraction to dilation. The value of η_{cl} is calculated from graphs of volumetric strain (ε_v) versus axial strain (ε_a) and is taken at the point where the ratio $\Delta\varepsilon_v/\Delta\varepsilon_a$ approaches zero. When the soil is denser than the critical state, the characteristic state is reached at small strain levels. However, when the soil lies above the CSL, the characteristic state coincides with the critical state, as both occur when $\Delta\varepsilon_v/\Delta\varepsilon_a$ is zero.

This state of soil behaviour transition is very similar to another state which is commonly referred to as the phase transformation line. Various studies in the literature attempted to accurately identify the two states and to check whether they are density or stress dependent (e.g., Chu, 1995; Lade and Ibsen, 1997). Lade and Ibsen (1997) found that the characteristic line is unaffected by density but varies with the effective confining stress level and the applied stress path. This section aims to investigate the variation of the characteristic line and its corresponding friction angle (φ_{cl}) with respect to different mean effective stresses and relative densities.

Figure 4.45 plots the characteristic line friction angle (φ_{cl}) versus p_0' for all the monotonic samples that have experienced dilation. Although there is considerable scatter in the plot, several conclusions can be drawn when the data for the respective relative densities are fitted with a linear trend line. The two linear trend lines indicate that φ_{cl} increases with increasing p_0'. This trend is expected, as at higher mean effective stresses, the value of φ_{cl} approaches and becomes equivalent to the critical state angle of shearing resistance (φ_c). This increase in φ_{cl} with applying higher p_0' was similarly reported by Lade and Ibsen (1997) based on drained triaxial compression tests conducted on Santa Monica Beach sand. However, other experimental studies, such as those by White (2020), who performed triaxial tests on Leighton Buzzard sand, contradicted this finding, reporting that φ_{cl} shows a decreasing trend with p_0'. Even though a limited number of tests are conducted on the very dense samples reconstituted to 90% relative density, the results are still sufficient to draw an observation regarding the effect of density on the variation of φ_{cl}. According to the fitted linear trend lines, φ_{cl} for the samples prepared at $D_r \approx 90\%$ is lower than that of the samples prepared at $D_r \approx 60\%$. The observed reduction in φ_{cl} with increasing relative density can be attributed to the earlier onset of dilation as relative density becomes higher. At higher relative densities, dilation initiates at smaller axial strains, which corresponds to a lower mobilized stress ratio, ultimately resulting in a reduced φ_{cl}. However, given that the experimental study by Lade and Ibsen (1997) observed no influence of relative density on φ_{cl}, and the limited tests conducted on $D_r \approx 90\%$ in this research, it is difficult to confidently confirm that φ_{cl} decreases with increasing relative density. Finally, it is crucial to note that only one undrained monotonic test was conducted in this research and hence no comparisons can be made to check whether the characteristic state and the phase transformation state are different or the same.

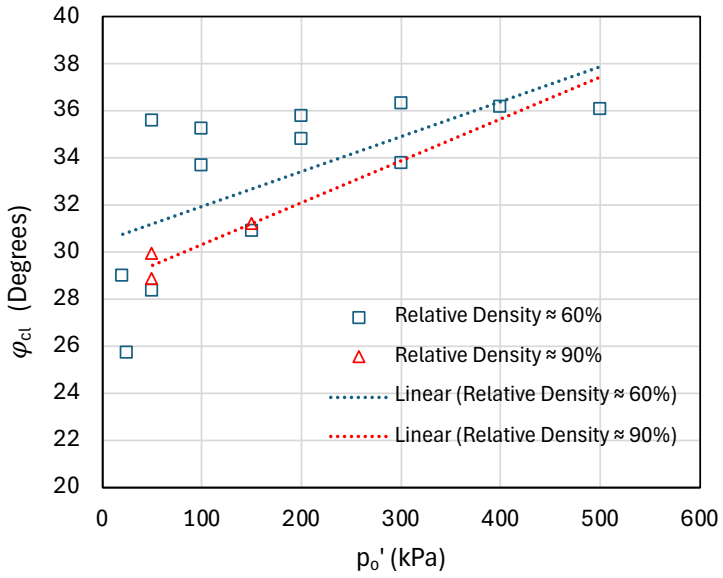


Figure 4.45: φ_{cl} versus p_o' for all the monotonic tests at $D_r \approx 60\%$ and $D_r \approx 90\%$

4.7 Summary

This chapter presented the results of both cyclic and monotonic tests, aiming to identify patterns and compare the findings with those of previous studies to determine whether similar conclusions can be drawn. The study primarily focused on the influence of mean effective stress, relative density, and drainage on the variation of shear modulus reduction and damping ratio. Additionally, the shear modulus reduction and damping ratio curves of Blessington sand were compared with those of Kilmuckridge sand to evaluate how the dynamic parameters differ between the two soils. Furthermore, the effect of the number of cycles on the dynamic parameters was investigated using the results of drained and undrained cyclic tests. The calibration of the HSsmall and SANISAND-MS constitutive model parameters, discussed in Chapter Five, was performed based on the results presented in this chapter. Nonlinear regression analyses were also conducted to derive the parameters of empirical functions, enabling the generation of representative normalised shear modulus reduction and damping ratio curves for granular materials. These curves are particularly valuable in the early stages of design when actual laboratory data are unavailable.

For the undrained cyclic tests, the effects of mean effective stress and relative density on the shear modulus reduction and damping ratio of Blessington and Kilmuckridge sands were initially investigated. The results indicated that, at a given cyclic shear strain, the damping ratio decreases, and the shear modulus increases as the mean effective stress rises. The observed reduction in damping ratio with increasing mean effective stress is consistent with findings reported in numerous studies in the literature. With respect to relative density, the results demonstrated that, at small cyclic shear strains, the influence of relative density on the damping ratio is minimal. However, as the cyclic shear strain increases, the effect of relative density becomes more pronounced: the damping ratio decreases for dense samples and increases for loose samples as shear strain grows. This reduction in damping for dense soils is attributed to their tendency to dilate, which causes stress-strain loops to transition from elliptical to non-elliptical shapes, as previously reported by Rascol (2009), Blaker and Andersen (2019), and Løvholt et al. (2020). A comparison of Blessington and Kilmuckridge sands revealed that, at the same cyclic shear strain, the shear modulus and damping ratio of Kilmuckridge sand are higher than those of Blessington sand. However, it is important to note that the difference in damping between the two sands is marginal at small and medium shear strains below 0.1%. The higher shear stiffness of Kilmuckridge sand can be attributed to its larger mean particle size (d_{50}). The effect of the mean particle size (d_{50}) on shear stiffness was reported by Menq (2003). Finally, the close agreement between the damping ratios of Kilmuckridge and Blessington sands confirms that Blessington sand is representative of cohesionless soil materials. Therefore, it can be reliably used as a reference material for studying foundation damping in monopile-supported OWTs.

Examining the effect of the number of cycles in the undrained tests revealed that both the shear modulus and damping ratio degrade as the loading cycles increase. Notably, the damping ratio

decreases with the number of cycles, regardless of whether the soil is reconstituted to a loose or dense state. Moreover, the influence of the number of cycles appears to vary with soil type. For example, Darendeli (2001) reported only marginal effects of cycle number on the damping ratio, whereas the dynamic test results of Blaker and Andersen (2019) demonstrated a significant reduction in damping with an increasing number of cycles.

Regarding the drained test results, the damping ratio exhibits a similar trend with respect to the effect of mean effective stress as observed in the undrained tests. Additionally, the drained test results indicate that the damping ratio does not vary significantly with relative density. However, since the maximum cyclic shear strain achieved in the drained tests was approximately 0.3%, it cannot be conclusively determined whether the drained damping ratios remain consistent across different relative densities at higher cyclic shear strain levels. The impacts of mean effective stress and relative density on the normalised shear modulus reduction were also examined. The results showed that, at a given cyclic shear strain level, the normalised shear modulus increases with higher mean effective stress, aligning with findings from numerous previous studies. Regarding the influence of relative density, the normalised shear modulus curves for different relative densities were observed to overlap, suggesting that the effect of relative density on the normalised shear modulus is negligible.

The effect of the number of cycles on the damping ratio was also investigated. The results of the large cyclic tests indicated that soil damping decreases as the number of cycles increases. However, the effect is insignificant, and the damping ratio stabilises by 1000 cycles. Furthermore, a comparison of the large cyclic test results across different mean effective stresses and cyclic shear strain levels showed that the rate of damping ratio decay increases as the mean effective stress decreases, while it also increases as the cyclic shear strain becomes larger.

Nonlinear regression analyses were conducted to fit commonly used empirical functions to the damping ratio and shear modulus reduction curves obtained from the cyclic tests. The patterns and values of the fitting parameters, such as the curvature coefficient (α), were in good agreement with those derived from previous studies. As a result, the fitting parameters and empirical functions can be used to estimate the damping ratio and shear modulus reduction curves when actual laboratory data are not available.

Extensive monotonic tests were conducted to examine the variation of peak friction angles and to determine the critical state angle of shearing resistance. These tests were performed at various mean effective stress levels to evaluate the hardening and softening behaviour of Blessington sand. The results revealed that, for samples reconstituted to 60% relative density, the peak friction angle decreases as the mean effective stress increases. Eventually, the peak friction angle converges to the critical state angle of shearing resistance at high mean effective stress levels. Based on monotonic tests conducted to large axial strains of 25%, the critical state angle of shearing resistance of

Blessington sand was approximated to 35°. Furthermore, since the SANISAND-MS model is developed within the critical state framework, the parameters of the critical state line (CSL) in the compressibility plane were determined from tests performed on soil samples reconstituted to 30% relative density. The variation of the characteristic angle of friction with mean effective stress and relative density was also examined. The results showed that the characteristic friction angle increases as the mean effective stress increases and eventually coincides with the critical angle of shearing resistance when the behaviour becomes fully contractive at very high mean effective stress levels. However, due to the limited number of tests conducted on very dense soil samples, the effect of relative density on the characteristic friction angle is unclear.

Chapter 5

Constitutive Model Calibration

5.1 Introduction

Prior to examining the dynamic behaviour of monopiles using 3D FE analyses, the parameters given to the constitutive soil models must be determined accurately such that the soil-structure interaction problem is adequately represented. The interaction of the soil continuum with the monopile greatly affects the dynamic characteristics of the overall OWT structure and failure to incorporate appropriate soil stiffness and damping values may lead to results that do not reflect the actual behaviour of OWTs. This chapter covers the calibration of both the HSsmall and SANISAND-MS models. The parameters are determined based on the monotonic and cyclic triaxial results which were introduced in the previous chapter. Although triaxial tests were conducted on Kilmuckridge sand, its strength and stiffness variation was not investigated as thoroughly as that of Blessington sand. Therefore, the constitutive models are calibrated exclusively for Blessington sand.

This chapter is divided into two parts. The first part involves the calibration of HSsmall parameters while the second part covers the calibration of the SANISAND-MS model. For each model, the limitations of the selected parameter values and the impacts they likely have on the simulation results are discussed. The calibration is carried out with the soil test facility in Plaxis 3D software which allows simulating monotonic and cyclical triaxial tests under different stress conditions. The Plaxis 3D test facility was used to calibrate the parameter values such that the triaxial test simulations with the constitutive models match the actual results obtained from the laboratory triaxial tests. The 3D FE analyses in Chapter six are based on the parameter values introduced in this chapter.

5.2 HSsmall model calibration

The theoretical background of the HSsmall model is not discussed here given that it was covered in the literature review chapter. This section discusses the procedure for determining the values of each parameter. Furthermore, the numerical simulations of HSsmall for different relative densities and confining pressures are compared with the corresponding laboratory test results. The calibration of the HSsmall model is discussed initially since the model is relatively simple when compared to the SANISAND-MS model and requires only a few parameters that are straight forward to determine. The general limitations of the HSsmall model are also discussed, primarily regarding its

ability to capture softening behaviour in monotonic tests and the increase in damping ratio in cyclic tests. The initial objective of the research was to calibrate the HSsmall model for soil relative densities of 30%, 60%, and 90%. However, due to the limited number of samples reconstituted to 90% relative density, the parameter values are determined only for relative densities of 30% and 60%.

5.2.1 HSsmall model parameters

The parameters of the HSsmall model are summarised in Table 5.1. The parameters can generally be divided into stiffness and strength parameters. The first three stiffness parameters can be determined from conventional monotonic triaxial and oedometer tests without requiring any special instrumentation for capturing stiffness variation at small strains. The two parameters (G_0^{ref} and $\gamma_{0.7}$) are used to simulate the dynamic behaviour of soil and capture the nonlinear reduction in stiffness with shear strain. These two parameters are determined from sensors capable of measuring stiffness at small strains such as bender elements and local strain gauges. The three parameters (c, φ, and ψ) are determined from monotonic triaxial or direct simple shear tests to failure. Apart from G_0^{ref} and $\gamma_{0.7}$, all other parameters in the HSsmall model are identical to those in its predecessor, the Isotropic Hardening Soil (HS) model.

Table 5.1: HSsmall mode parameters

Parameter	Symbol	Unit
Secant stiffness in standard drained triaxial test	E_{50}^{ref}	[kPa]
Tangent stiffness for primary oedometer loading	E_{oed}^{ref}	[kPa]
Unloading / reloading stiffness	E_{ur}^{ref}	[kPa]
Power for stress-level dependency of stiffness	m	[-]
Poisson's ratio for unloading-reloading	v_{ur}	[-]
Reference stress for stiffnesses	P_{ref}	[kPa]
Reference shear modulus at very small strains	G_0^{ref}	[kPa]
Threshold shear strain	$\gamma_{0.7}$	[-]
Cohesion	c	[kPa]
Angle of internal friction	φ	[Degrees]
Dilatancy angle	ψ	[Degrees]
Coefficient of lateral earth pressure (normal consolidation)	K_0^{NC}	[-]

5.2.2 c, φ, ψ, and K_0^{NC} Parameters

These parameters are determined directly from the monotonic tests and do not require calibration. The Blessington sand is a cohesionless material, and hence c is equal to zero. φ is taken as the peak angle of shearing resistance (φ_p) and is determined for different initial mean effective stress (p_0') values based on Figure 4.43. For relative density (D_r) of 30%, Blessington sand does not show much softening in the monotonic stress-strain curves, and φ was taken as the critical angle of shearing resistance (φ_c) which is approximated to 35° for Blessington sand. Furthermore, since the

volumetric behaviour of Blessington sand at D_r = 30% is primarily contractive, the dilatancy angle (ψ) was considered to be zero.

The test results in Figure 4.43 for the samples prepared at D_r = 60% are replotted in Figure 5.1 to obtain the variation of φ with p_0'. To fit the results in Figure 5.1, a logarithmic function is suggested as follows:

$$\varphi = -3.804 \ln p_0' + 60.932 \tag{5.1}$$

The coefficient of determination (R^2) for the fitting of Equation 5.1 to the data in Figure 5.1 is 0.952, indicating that Equation 5.1 effectively captures the variation of φ with p_0'. ψ is calculated according to the following equation presented in PLAXIS 3D Manual (2023a):

$$\sin\psi = \frac{\sin\varphi - \sin\varphi_c}{1 - \sin\varphi \sin\varphi_c} \tag{5.2}$$

The fourth parameter in this section, K_0^{NC}, can be determined from the well-known equation by Jaky (1944) which is presented as follows:

$$K_0^{NC} = 1 - \sin\varphi \tag{5.3}$$

Using Equations 5.1, 5.2, and 5.3, the values of φ, ψ, and K_0^{NC} parameters with depth for the soil profile at D_r = 60% can be calculated. One additional parameter is K_0, which is the coefficient of lateral earth pressure and is calculated based on K_0^{NC} and the over-consolidation ratio (OCR). Although the in-situ OCR of Blessington soil is expected to be greater than one (i.e., overconsolidated), the structure of the extracted samples was fully disturbed. Therefore, the laboratory samples were reconstituted to simulate normally consolidated soil behaviour in the triaxial tests. Since this research focuses solely on the behaviour of monopiles installed in normally consolidated soil profiles, the values of K_0 are taken to be equal to those of K_0^{NC}. Although Equation 5.1 is formulated to calculate φ based on the value of p_0' at the midpoint of each soil layer, this calculation requires the value of K_0^{NC} to be known a priori. Hence an initial assumption of K_0^{NC} is required and then iterations need to be carried out between Equations 5.1 and 5.3 until the values of K_0^{NC} and p_0' do not further change. However, for the purpose of simplifying the problem, the initial vertical effective stress (σ_{v0}') is used in Equation 5.1 in place of p_0'.

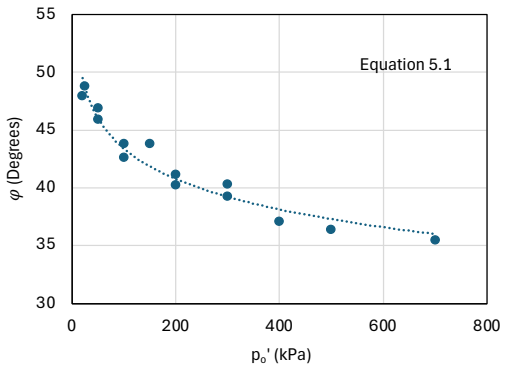


Figure 5.1: Angle of internal friction (φ) versus initial mean effective stress (p_0') for D_r = 60%

5.2.3 E_{50}^{ref}, E_{oed}^{ref}, E_{ur}^{ref}, m, and ν_{ur} Parameters

The parameters presented in this section significantly influence the monotonic stress-strain behaviour of soil. The HSsmall model is formulated such that its three stiffness parameters (E_{50}^{ref}, E_{oed}^{ref}, and E_{ur}^{ref}) are determined at a reference confining stress (P_{ref}) and automatically adjusted according to a power law relative to the effective confining stress (σ_3') in the field. In this research, P_{ref} is taken as 100 kPa. The most influential parameter among the three stiffness parameters is E_{50}^{ref}, which represents the reference young's modulus of the soil corresponding to the deviatoric stress (q) at 50% of its value at failure. The parameter E_{50}, which represents the confining stress-dependent young's modulus, is related to E_{50}^{ref} by the following power law equation, as presented in the PLAXIS 3D Manual (2023a):

$$E_{50} = E_{50}^{ref}\left(\frac{c\cos\varphi - \sigma_3' \sin\varphi}{c\cos\varphi - P_{ref}\sin\varphi}\right)^{m} \tag{5.4}$$

Since $c = 0$, Equation 5.4 simplifies to:

$$E_{50} = E_{50}^{ref}\left(\frac{\sigma_3'}{P_{ref}}\right)^{m} \tag{5.5}$$

where m is a parameter that denotes the effective confining stress dependency of the three stiffness parameters (E_{50}^{ref}, E_{oed}^{ref}, and E_{ur}^{ref}). For Norwegian sands and silts, Janbu (1963) reported values of m around 0.5, whereas Von Soos (1990) found values of m within the range $0.5 < m < 1.0$. Oztoprak and Bolton (2013) reported that for the majority of sandy m is equal to 0.5. E_{50}^{ref} and m were determined for the relative densities of 30% and 60% by fitting Equation 5.5 to the measured values of E_{50} with respect to the normalised effective confining stress (σ_3'/P_{ref}).

The fitting was performed in Microsoft Excel by inputting the values of E_{50} and the corresponding σ_3'/P_{ref} values, and applying a power law trendline. Figure 5.2 shows the fitting of the test results for the samples prepared at $D_r \approx 30\%$ using equation 5.5. According to the fitted curve in Figure 5.2, the values of E_{50}^{ref} and m are 15,785 kPa and 0.586, respectively. However, the values of E_{50}^{ref} and m were adjusted to provide a better match of the triaxial simulations with the laboratory results in terms of q versus deviatoric strain (ε_q).

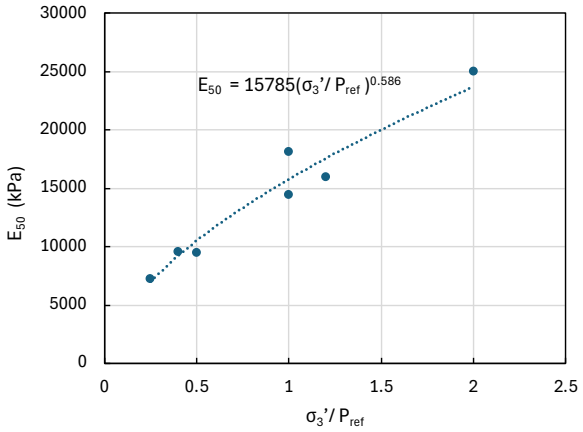


Figure 5.2: E_{50} versus normalised effective confining stress (σ_3'/P_{ref}) for $D_r \approx 30\%$

The fitting of the test results for the samples prepared at $D_r \approx 60\%$ using Equation 5.5 is shown in Figure 5.3. The results in Figure 5.3 show some scatter which is attributed to compiling the values of E_{50} calculated from the global and local axial strains. The E_{50} values determined from the local axial strains were slightly larger than those determined from the global axial strains, due to the compliance of the porous stones and the triaxial apparatus loading frame. The maximum recorded difference between the two approaches of calculating E_{50} is around 10 MPa. According to the fitted curve in Figure 5.3, the values of E_{50}^{ref} and m are 38,528 kPa and 0.534, respectively. However, these values do not yield a satisfactory match between the triaxial simulations and the laboratory results, indicating that E_{50}^{ref} needs to be slightly increased to achieve a closer agreement with the monotonic behaviour observed from the local axial strains. Therefore, the selected values of E_{50}^{ref} and m to represent the monotonic behaviour of Blessington sand at D_r = 60% are 45,000 kPa and 0.5, respectively.

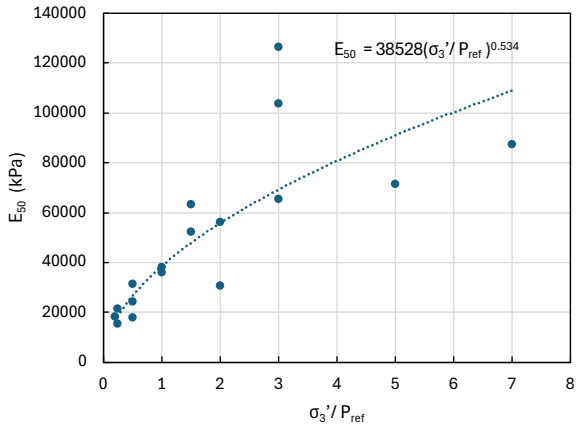


Figure 5.3: E_{50} versus normalised effective confining stress (σ_3 '/ P_{ref}) for $D_r \approx 60\%$

Since no oedometer tests were conducted in this research, the values of E_{oed}^{ref} are assumed equal to those of E_{50}^{ref} ($E_{oed}^{ref} = E_{50}^{ref}$), as recommended by Panagoulias et al. (2018). Hence the E_{oed}^{ref} value for the case of the soil at D_r = 30% is equal to 16,500 kPa. However, for the soil at D_r = 60%, Plaxis 3D software did not permit assigning the E_{oed}^{ref} value of 45,000 kPa and suggested either lowering the E_{oed}^{ref} value or increasing the K_0^{NC} value. Given that decreasing E_{oed}^{ref} does not significantly impact the monotonic q-ε_q response, the value of E_{oed}^{ref} was gradually reduced until it became valid in Plaxis 3D. Consequently, E_{oed}^{ref} was set equal to 31,500 kPa for the soil at D_r = 60%. The reason why PLAXIS 3D does not permit an input value of 45,000 kPa for E_{oed}^{ref} is unclear, as the PLAXIS 3D Manual (2023a) does not provide any explanations for this.

The unloading/reloading stiffness (E_{ur}) in the standard Hardening Soil (HS) model is used to simulate the elastic stiffness of the soil during unloading and reloading. During stress reversal, the HS model behaviour is fully linear elastic. However, for the HSsmall model, E_{ur} is used to limit the reduction of the tangent shear modulus (G_t). The cut-off limit of G_t is defined by the unloading-

reloading stiffness (G_{ur}), which is calculated from the material parameters E_{ur} and the unloading/reloading Poisson's ratio (v_{ur}) using the following equation:

$$G_{ur} = \frac{E_{ur}}{2(1+ v_{ur})} \tag{5.6}$$

Additionally, the ratio of the initial shear stiffness (G_0) to G_{ur} controls the maximum hysteretic soil damping in the HSsmall model. Therefore, the value of E_{ur} at P_{ref} (E_{ur}^{ref}) could be selected such that the maximum hysteretic soil damping in the HSsmall model matches the maximum damping ratio obtained from the laboratory triaxial tests. In practice the value E_{ur}^{ref} is often determined from E_{50}^{ref}, and the ratio ($E_{ur}^{ref}/E_{50}^{ref}$) usually varies within the range of 2 to 6, while the default value of E_{ur}^{ref} in Plaxis 3D software is set to $3E_{50}^{ref}$. As result, the value of E_{ur}^{ref} for the case of 30% relative density is set to 49,500 kPa, which corresponds to the ratio of $E_{ur}^{ref}/E_{50}^{ref} = 3$. As will be shown in the next section, the value of E_{ur}^{ref} = 49,500 kPa yields a satisfactory maximum damping ratio compared to the damping ratio curves derived from laboratory tests. However, assigning the value of E_{ur}^{ref} as $3E_{50}^{ref}$ for a relative density of 60% results in a low (G_0/G_{ur}) ratio, which significantly underestimates the maximum damping ratio. Thus, a lower ratio of $E_{ur}^{ref}/E_{50}^{ref} = 2$ is adopted, resulting in an E_{ur}^{ref} value of 90,000 kPa for the case of 60% relative density.

Accurate estimation of v_{ur} was not achievable in this research due to the significant sticking and friction in the radial strain LVDT, rendering the values unreliable. However, the value of v_{ur} for sands usually falls within the range of 0.1-0.3 (Shibuya et al., 1994). In this study, the value assigned to v_{ur} is 0.2, which is the recommended value of v_{ur} for the HSsmall model according to Panagoulias et al. (2018).

Since all the monotonic parameters of the HSsmall model are discussed and determined, triaxial simulations are conducted using the test facility in Plaxis 3D, and the results are compared with the corresponding laboratory test results, as shown in Figure 5.4 to Figure 5.7. The parameter values of G_0^{ref} and $\gamma_{0.7}$ are discussed in the next section, as the influence of $\gamma_{0.7}$ on the monotonic response is minimal, and the values of G_0^{ref} are determined from the bender element results presented in the previous chapter. Figure 5.4 and Figure 5.5 present comparisons for samples prepared to $D_r \approx 30\%$, while Figure 5.6 and Figure 5.7 show comparisons between the triaxial simulations and the laboratory results for samples prepared to $D_r \approx 60\%$. The suitability of the selected parameter values is assessed by comparing the triaxial simulations with both the laboratory tests conducted to failure (Figure 5.4 and Figure 5.6) and the tests examining small-strain behaviour, measured using the locally attached LVDTs (Figure 5.5 and Figure 5.7). The triaxial simulations and the corresponding laboratory test results, presented in Figure 5.4 and Figure 5.6, are compared in terms of q versus ε_q, with ε_q calculated using the following equation:

$$\varepsilon_q = \frac{2}{3}(\varepsilon_a - \varepsilon_r) \tag{5.7}$$

where ε_a and ε_r are the axial and radial strains, respectively. ε_r is calculated from the global axial and volumetric strains, assuming the sample deforms as a right cylinder. The global axial strains are measured based on the movement of the pedestal, reflecting the overall compression of the soil sample, while the global volumetric strains (ε_v) are determined by the back pressure controller, which tracks the volume of water entering and exiting the sample. As previously mentioned, the readings from the local radial LVDT are unreliable, and hence the comparisons in Figure 5.5 and Figure 5.7 are in terms of q versus the average local axial strain measured by two opposing side axial LVDTs.

Figure 5.4 and Figure 5.5 show that the simulations closely match the laboratory results, confirming that the assigned parameter values are appropriate to accurately reproduce the behaviour of the loose state soil at D_r = 30% for both large and small strain levels. Although Figure 5.4 shows slight softening, this is likely due to grain crushing rather than dilation, as all samples in the figure exhibited contractive volumetric behaviour. However, because the softening is minimal, it will not be discussed further in this research.

Figure 5.6 and Figure 5.7 show that the simulations, based on the assigned parameter values, reasonably match with laboratory tests reconstituted to $D_r \approx 60\%$. Achieving a satisfactory fit of the simulations to the monotonic behaviour is challenging, as the parameter values must be iteratively adjusted to balance the observed behaviour at both large and small strain levels. This compromise is evident, as the simulations are slightly stiffer than the behaviour observed in Figure 5.6, yet align well with the behaviour in Figure 5.7, which is measured by the local axial LVDTs. In conclusion, the selected parameter values represent the monotonic behaviour of soil sufficiently well and can be confidently adopted to examine the soil-structure interaction of OWTs using 3D FE numerical analyses.

Comparisons between the triaxial simulations and laboratory results reveal that the main inherent limitation of the HSsmall model is its innate inability to capture the softening response typically observed in dilative soil samples. This limitation can lead to an overestimation of the maximum load-bearing resistance of monopiles. The inability of the HSsmall model to capture softening stems from its formulation, which is based on the following simple hyperbolic stress-strain relationship:

$$-\varepsilon_1 = \frac{1}{E_i} \frac{q}{1-\frac{q}{q_a}} \tag{5.8}$$

where ε_1 is the major principal strain, E_i is initial Young's modulus, and q_a is the asymptotic value of the deviatoric strength. Although a significant advantage of the HSsmall model over other commonly used models is its stress-dependent stiffness, the angles φ and ψ must be manually adjusted to account for variations in σ_3' and relative density with soil depth. Consequently, constitutive models like SANISAND-MS, which are based on the critical state framework, are

gaining popularity for their ability to capture variations in strength and stiffness implicitly, based on the effective stresses and in-situ density conditions.

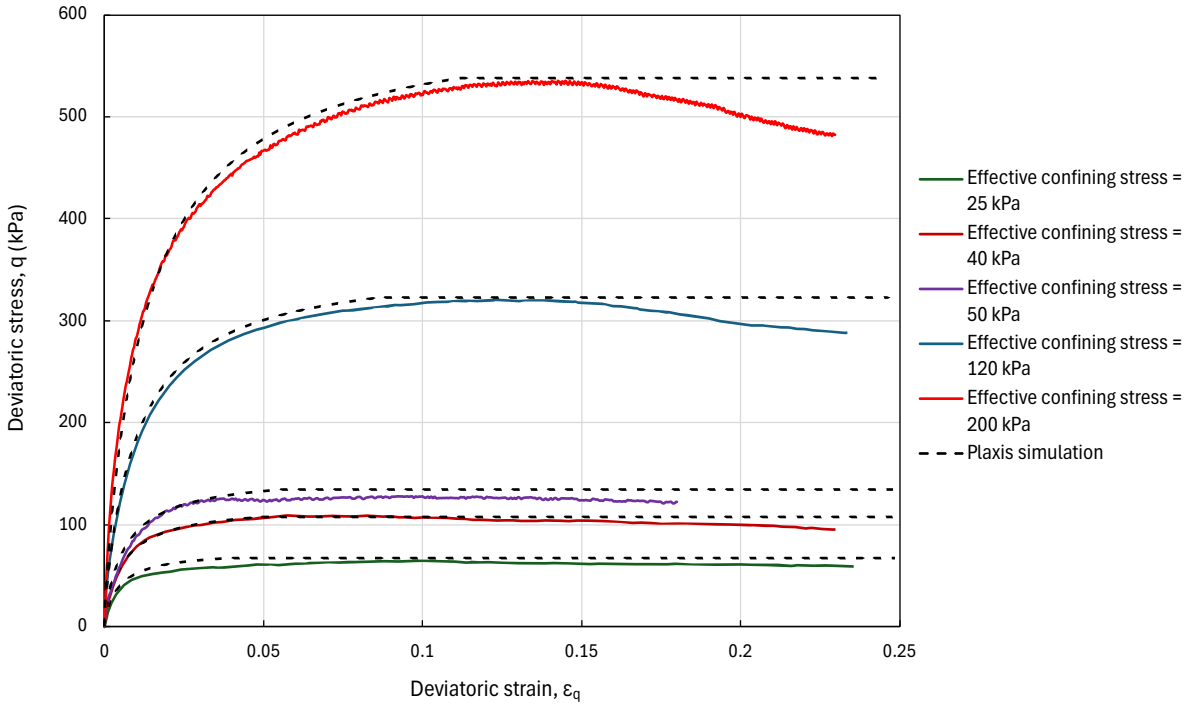


Figure 5.4: Comparing monotonic q-ε_q curves between triaxial simulation and laboratory results for $D_r \approx$ 30%

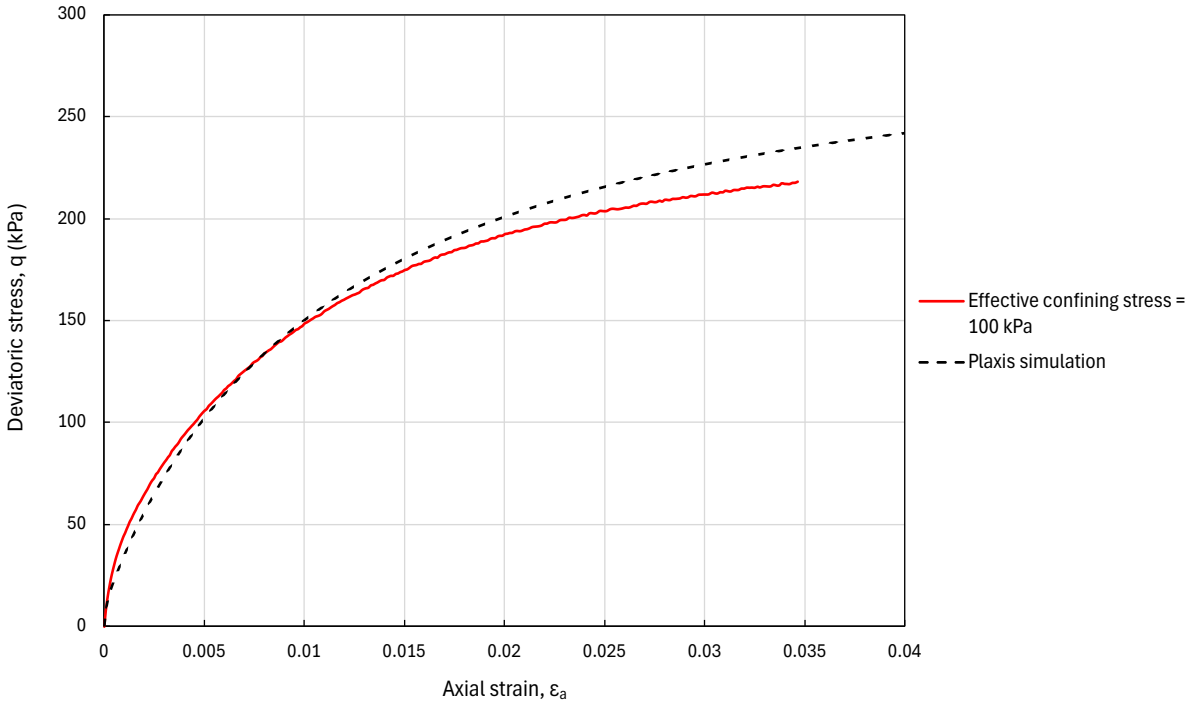


Figure 5.5: Comparing monotonic q-ε_a curves between triaxial simulations and laboratory results for $D_r \approx$ 30%

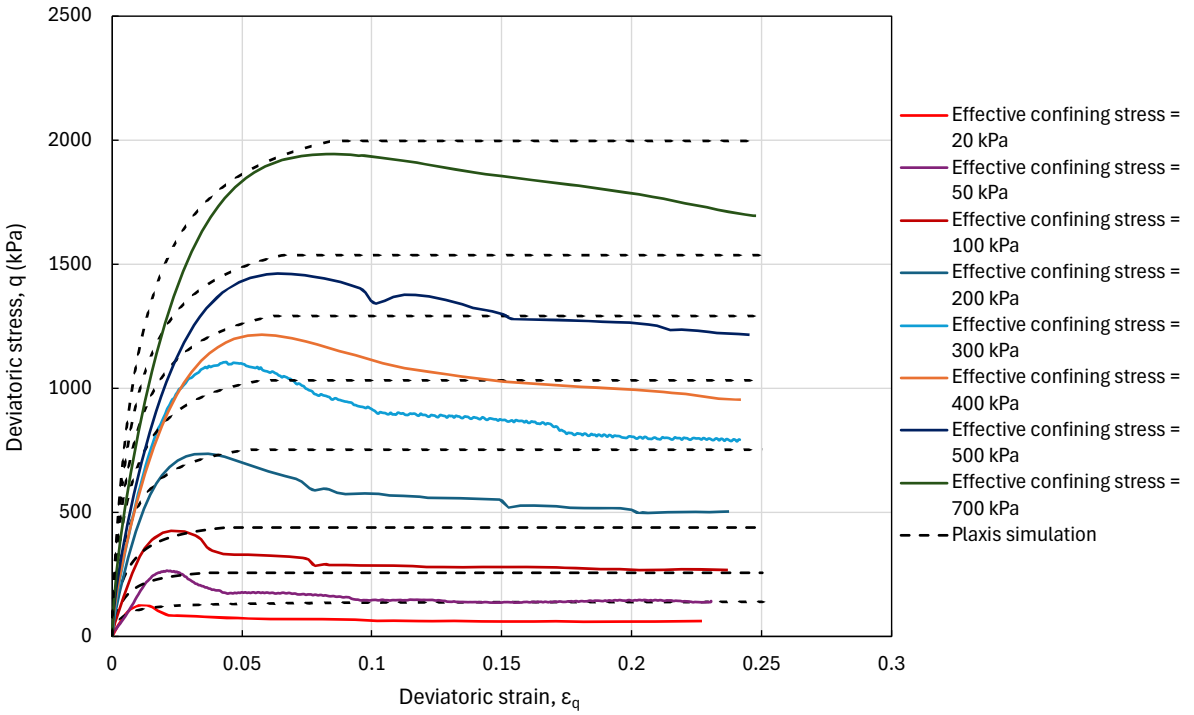


Figure 5.6: Comparing monotonic q-ε_q curves between triaxial simulation and laboratory results for $D_r \approx$ 60%

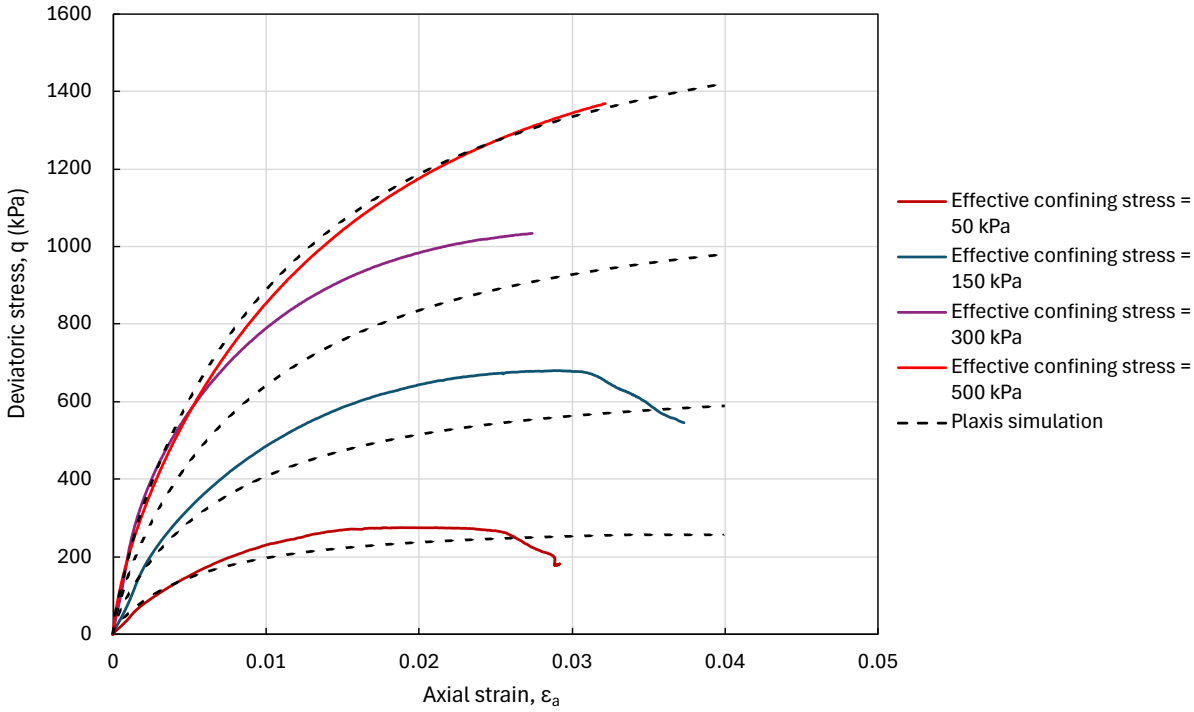


Figure 5.7: Comparing monotonic q-ε_a curves between triaxial simulations and laboratory results for $D_r \approx$ 60%

5.2.4 G_0^{ref} and $\gamma_{0.7}$ Parameters

The parameters G_0^{ref} and $\gamma_{0.7}$ characterise the hysteretic behaviour of soil by capturing the nonlinear reduction in stiffness and the increase in the hysteretic damping ratio with the cyclic shear strain. The G_0^{ref} values were simply determined from the bender element test results in Figure 4.23 through fitting the following power law function, with an m value fixed at 0.5:

$$G_0 = G_0^{ref}\left(\frac{\sigma_3'}{P_{ref}}\right)^m \tag{5.9}$$

The values of G_0^{ref} for Blessington sand at 30% and 60% relative densities are 54112 kPa and 82511 kPa, respectively. In addition to controlling small-strain shear stiffness, the value of G_0^{ref} also determines the maximum hysteretic soil damping ratio, as discussed in the previous section. The damping ratio curves within the elastic limit of the HSsmall overlay model, based on the assigned values of G_0^{ref} and $\gamma_{0.7}$, closely align with the laboratory derived D-γ_c curves.

The $\gamma_{0.7}$ parameter, as previously mentioned in Chapter 2, defines the cyclic shear strain level at which the normalised shear modulus ratio (G/G_0) reduces to 0.722. Previous studies investigating foundation damping of OWTs, using the HSsmall model (e.g., Vo, 2022) calculated $\gamma_{0.7}$ based on the empirical equation proposed by Brinkgreve et al. (2010):

$$\gamma_{0.7} = \left(2 - \frac{D_r}{100}\right)10^{-4} \tag{5.10}$$

According to Equation 5.10, $\gamma_{0.7}$ depends on the relative density. However, as was discussed in Chapter Four, the normalised shear modulus reduction curves (G/G_0-γ_c) are stress dependent and are unaffected by the soil relative density. This was illustrated in Figure 4.29b, which showed that the G/G_0-γ_c curves for three samples prepared to different relative densities but subjected to the same p_0' closely overlap, confirming that G/G_0-γ_c does not vary with relative density. Thus, a better approach to determine $\gamma_{0.7}$ is to rely on G/G_0-γ_c derived directly from laboratory tests or to adopt the empirical equations developed from studies based on dynamic laboratory tests (e.g., Darendeli, 2001; Menq, 2003; Zhang et al., 2005; Oztoprak and Bolton, 2013; Akeju et al., 2019; Ciancimino et al., 2020). Generally, increasing the value of $\gamma_{0.7}$ shifts the G/G_0-γ_c curves to the right and increases the G/G_0 ratio at a given cyclic shear strain level (γ_c). Similarly, higher values of $\gamma_{0.7}$ shifts the D-γ_c curves to the right and causes the damping ratio (D) to decrease at a particular cyclic shear strain level (γ_c). Ideally, the value of $\gamma_{0.7}$ could be calibrated such that the HSsmall model captures both the G/G_0-γ_c and D-γ_c curves to simulate the dynamic behaviour of soil accurately. However, achieving a balanced fit for both the laboratory derived G/G_0-γ_c and D-γ_c curves is challenging, as the resulting HSsmall curves may accurately fit one curve while underestimating or overestimating the other. Since this research primarily aims to study hysteretic foundation damping, the value of $\gamma_{0.7}$ for each soil layer at different depths is chosen to capture the D-γ_c curve by fitting Equation 4.8 to the laboratory results. Unlike G_0, which is stress-dependent and varies automatically according

to G_0^{ref} and the exponent m, the value of $\gamma_{0.7}$ must be manually adjusted for the representative value of p_0' at the midpoint of each soil layer. The variation of $\gamma_{0.7}$ to fit the D-γ_c curves derived from the laboratory results using Equation 4.8 is shown in Figure 5.8 for p_0' values of 50 kPa, 150 kPa, and 300 kPa. It is important to highlight that the coefficients of Equation 4.8 were determined solely from the undrained laboratory tests, as the D-γ_c curves from these tests were lower and therefore more conservative than the curves from the drained tests. The HSsmall D-γ_c curves are derived using the following relation:

$$D = \frac{2\gamma_{0.7}\left(2\gamma_c - \frac{\gamma_c}{1+a\frac{\gamma_{0.7}}{\gamma_c}} - \frac{2\gamma_{0.7}}{a}\ln\left(1+\frac{a\gamma_c}{\gamma_{0.7}}\right)\right)}{a\pi\left(\frac{\gamma_c^2}{1+\frac{a\gamma_c}{\gamma_{0.7}}}\right)} \tag{5.11}$$

where a is set as a constant value of 0.385 in the HSsmall model. The damping ratio (D) of the soil, as represented by the HSsmall model, is calculated using Equation 5.11 up to a specific threshold. Once D reaches this predefined limit, which is illustrated by the horizontal lines in Figure 5.8, it is no longer governed by Equation 5.11. The cut-off shear strain ($\gamma_{cut\text{-}off}$), beyond which soil damping is not expressed with Equation 5.11, is calculated as follows:

$$\gamma_{cut\text{-}off} = \frac{\gamma_{0.7}}{a}\left(\sqrt{\frac{G_0}{G_{ur}}} - 1\right) \tag{5.12}$$

Beyond this point, the damping ratio is not governed by an explicit function and instead is influenced by plastic hardening and the yield surface evolution. The same $\gamma_{0.7}$ values used to plot the curves in Figure 5.8 are also used in Figure 5.9 to compare the G/G_0-γ_c curves obtained from the HSsmall model with those derived by fitting Equation 4.4 to the cyclic triaxial test results. Since the coefficients of Equation 4.4 determined from the drained triaxial tests agree better to values reported in previous studies than those from the undrained tests, the representative G/G_0-γ_c curves in this research are based on the drained test results. Figure 5.9 illustrates that while the values of $\gamma_{0.7}$ are calibrated using the damping ratio curves, the HSsmall G/G_0-γ_c curves provide an adequate fit to the G/G_0-γ_c curves obtained from the drained triaxial tests within the small shear strain range of 0.001 to 0.05. The fit of the G/G_0-γ_c curves is not ideal, but it can be considered satisfactory for the purpose of conducting the 3D FE analyses. Figure 5.8 shows that the maximum damping ratio is approximately 10% based on the G_0/G_{ur} ratio for Blessington sand at 30% relative density. However, since the resulting G_0/G_{ur} ratio is slightly lower for the 60% relative density, the maximum damping ratio is approximately 8.5%. The HSsmall G/G_0-γ_c curves in Figure 5.9 are expressed with the following relation:

$$\frac{G}{G_0} = \frac{1}{1+\frac{a\gamma_c}{\gamma_{0.7}}} \tag{5.13}$$

The normalised shear modulus reduction curves (G/G_0-γ_c) are governed by Equation 5.13 up to the cut-off shear strain ($\gamma_{cut\text{-}off}$). Similar to the simplification made in section 5.2.2 for determining φ,

the value of $\gamma_{0.7}$ for each layer is calculated based on the initial vertical effective stress (σ_{v0}') at the midpoint of the layer. Because p_0' is lower than σ_{v0}' throughout the soil profile, using σ_{v0}' to determine $\gamma_{0.7}$ results in a conservatively lower damping ratio (D) at any given cyclic shear strain (γ_c)

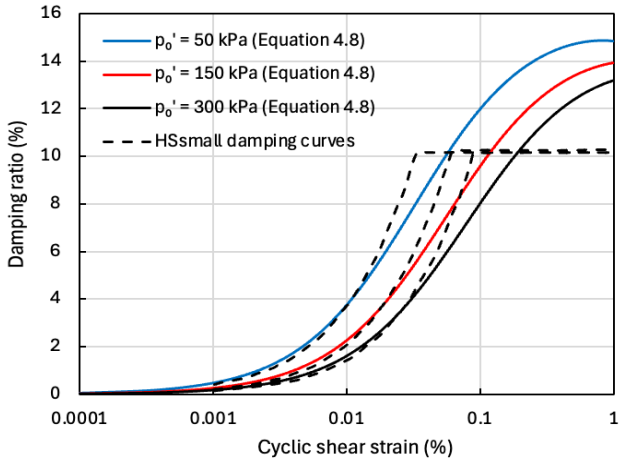


Figure 5.8: HSsmall and laboratory derived damping ratio curves

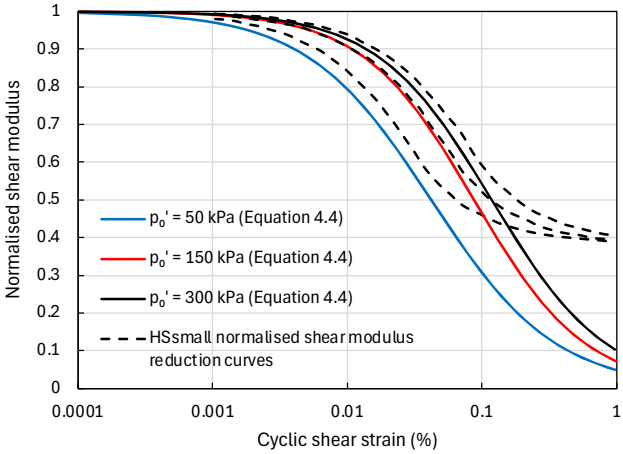


Figure 5.9: HSsmall and laboratory derived normalised shear modulus reduction curves

The same soil profile is used for both the 30% and 60% relative densities in terms of layer thickness and depth to the bottom boundary. Table 5.2 summarises the HSsmall parameters for Blessington sand at D_r = 30%, while

Table 5.3 provides the HSsmall parameters for Blessington sand at D_r = 60%. The final parameter is the strength reduction factor (R_{inter}), which accounts for the reduction in interface shear strength when slip occurs between the soil and the pile wall. The R_{inter} value chosen for both relative densities is 0.7. To simulate the behaviour of drained saturated soil, one common approach is to place the water table at or above the mudline and assign the saturated unit weight as the soil's unit weight. Alternatively, equivalent behaviour can be reproduced by assigning the effective buoyant unit weight (γ') to the soil and positioning the water table at the base of the FE model. In this research, the latter method was adopted, following the recommendation of Panagoulias et al. (2018). Because σ_{v0}' does not vary significantly between the two different relative densities, the same $\gamma_{0.7}$ values were assigned for both.

Table 5.2: HSsmall model parameter for 30% relative density

From (m)	To (m)	γ' [kN/m^3]	E_{50}^{ref} [kPa]	E_{oed}^{ref} [kPa]	E_{ur}^{ref} [kPa]	m	φ [Deg]	ψ [Deg]	G_0^{Ref} [kPa]	$\gamma_{0.7}$
0	5	8.96	16500	16500	49500	0.5	35	0	54112	0.000165
5	10	8.96	16500	16500	49500	0.5	35	0	54112	0.00024
10	15	8.96	16500	16500	49500	0.5	35	0	54112	0.00034
15	20	8.96	16500	16500	49500	0.5	35	0	54112	0.000415
20	25	8.96	16500	16500	49500	0.5	35	0	54112	0.00045
25	30	8.96	16500	16500	49500	0.5	35	0	54112	0.000525
30	35	8.96	16500	16500	49500	0.5	35	0	54112	0.00055
35	40	8.96	16500	16500	49500	0.5	35	0	54112	0.00058
40	-	8.96	16500	16500	49500	0.5	35	0	54112	0.00063

Table 5.3: HSsmall model parameter for 60% relative density

From (m)	To (m)	γ' [kN/m^3]	E_{50}^{ref} [kPa]	E_{oed}^{ref} [kPa]	E_{ur}^{ref} [kPa]	m	φ [Deg]	ψ [Deg]	G_0^{Ref} [kPa]	$\gamma_{0.7}$
0	5	9.74	45000	31500	90000	0.5	48.69	18.18	82511	0.000165
5	10	9.74	45000	31500	90000	0.5	44.51	12.31	82511	0.00024
10	15	9.74	45000	31500	90000	0.5	42.57	9.67	82511	0.00034
15	20	9.74	45000	31500	90000	0.5	41.29	7.97	82511	0.000415
20	25	9.74	45000	31500	90000	0.5	40.33	6.72	82511	0.00045
25	30	9.74	45000	31500	90000	0.5	39.57	5.73	82511	0.000525
30	35	9.74	45000	31500	90000	0.5	38.93	4.92	82511	0.00055
35	40	9.74	45000	31500	90000	0.5	38.39	4.22	82511	0.00058
40	-	9.74	45000	31500	90000	0.5	37.29	2.84	82511	0.00063

Each layer is 5 m thick down to a depth of 40 m, after which a single layer extends to the boundary of the 3D FE models. The total depth of the soil profiles depends on whether the analyses are dynamic or static, as well as on the geometry of the monopiles. Further details on the boundaries of the 3D FE models are provided in Chapter 6, which examines the foundation damping of OWTs using the soil parameters established in this chapter.

The main limitation of the HSsmall model for dynamic load applications is selecting appropriate values for $\gamma_{0.7}$ and G_0/G_{ur}. As shown in Figure 5.8 and Figure 5.9, the ratio G_0/G_{ur} introduces an upper limit for the D-γ_c curves and a lower limit for G/G_0-γ_c curves. Using a low G_0/G_{ur} ratio to fit the G/G_0-γ_c curves may significantly overestimate soil damping. For shear strains below the strain level at which G_{ur} is reached, the cyclic behaviour is governed by the HSsmall model constitutive relations. However, when the shear stiffness reduces to G_{ur}, the soil material no longer follows the elastic constitutive relations of the HSsmall model, and plasticity occurs as a result of deviatoric and isotropic strain hardening. This means that the hysteretic soil damping varies after reaching the upper limit, unlike the elastic HSsmall curves in Figure 5.8. Figure 5.10 compares the damping obtained from the elastic HSsmall relations with the damping determined from cyclic triaxial

simulations at various shear strain levels, using the soil test facility in Plaxis 3D software. The damping ratio at different shear strain levels is determined based on the cyclic shear stress-strain loops shown in Figure 5.10. The figure illustrates that, above the cut-off strain where the shear modulus G_{ur} is reached, the damping ratio first decreases slightly before rising sharply. Once strain hardening occurs, the damping ratio is no longer a simple function of the cyclic shear strain level and depends on all the specified parameter values. For this reason, the HSsmall model is often used for small cyclic loads, as assigning suitable parameters for accurate soil damping and stiffness at large shear strains is challenging. The sharp increase in damping, as noted in previous studies (e.g., Brinkgreve et al., 2007; Panagoulias et al., 2023), could lead to overestimation of soil damping and hence unconservative simulation results.

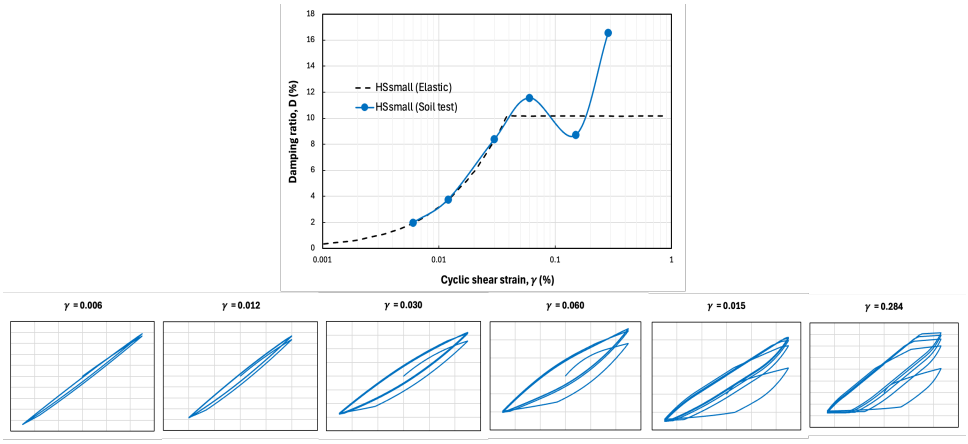


Figure 5.10: Comparison between damping from HSsmall relations and triaxial simulations

5.3 SANISAND-MS model calibration

SANISAND-MS model is an advanced constitutive model that belongs to the bounding surface plasticity models and obeys the critical state framework of soil. The model framework is based on the well-known SANISAND04 model (Dafalias and Manzari, 2004), which was further enhanced by Liu (2020) through incorporating a memory surface (MS) to track the loading history, variation of density, and the accumulation of cyclic deformations (ratcheting). Since SANISAND-MS is a critical state-based model, the behaviour of sand at different relative densities can be simulated with a single set of parameters. Although advanced bounding surface constitutive models are not commonly used in standard geotechnical design practice, 3D FE studies (e.g., Taborda et al., 2019; Pisanò et al., 2024) have demonstrated the capability of these soil models to simulate boundary value problems, such as the behaviour of laterally loaded monopiles. Taborda et al. (2019) highlighted that the accuracy of critical state based bounding surface models depend on rigorous integration of soil data from laboratory and field investigations, and applying sound engineering judgment. Furthermore, the authors emphasized that accurately simulating monopile behaviour, including the load-displacement response at ground level, along with the deflected shape and bending moment below the ground, depend on the capability of the soil model to reproduce the

dependency of sand behaviour on stress level and void ratio. Given that the theoretical background of the SANISAND-MS model was discussed in Chapter two, this chapter will focus solely on describing the parameters and how they are determined. Although determining the values of the SANISAND-MS parameters may be perceived as challenging due to the large number of parameters, they can be easily derived from conventional triaxial tests. The SANISAND-MS model employed in Plaxis 3D software consists of 21 parameters, which are summarised in Table 5.4.

Table 5.4: SANISAND-MS model parameter

Parameter	Symbol	Unit
Shear modulus coefficient	G^*	-
Poisson's ratio	ν	-
Stress ratio at critical state in triaxial compression	M_c	-
Ratio between critical stress ratios in triaxial extension and compression	c	-
Slope of the CSL in the compressibility plane	λ_c	-
Void ratio of the CSL at p' = 0kPa	e_0	-
Critical state line constant	ξ	-
Size of the yield surface	m	-
Hardening parameter	h_0	-
Hardening parameter	c_h	-
Bounding parameter	n^b	-
Dilatancy parameter	A_0	-
Dilatancy surface parameter	n^d	-
MS surface parameter	μ_0	-
MS surface parameter	ζ	-
MS surface parameter	β	-
Initial void ratio of the layer	e_{ini}	-
Maximum void ratio	e_{max}	-
Minimum void ratio	e_{min}	-
Maximum bounding stress ratio in triaxial compression	${M_c}^b{}_{max}$	-
Toggle	Elscheme	-

The initial 16 parameters in Table 5.4 were originally proposed by Liu (2020), comprising 13 constitutive parameters of the SANISAND04 (Dafalias and Manzari, 2004) and 3 additional parameters associated with the MS and ratcheting effects. The last 4 parameters in Table 5.4 (e_{min}, e_{max}, ${M_c}^b{}_{max}$, and Elscheme) were added to improve the numerical accuracy and implementation in Plaxis 3D software. Parameters (e_0, λ_c, ξ, M_c, and c) are the critical state parameters used to define the void ratio and stresses when the soil reaches the critical state zone under shearing. These parameters primarily define the location of the critical state line (CSL) in the compressibility plane (e-p') and in the triaxial stress space (q-p'). Parameters (G^*, ν, and m) govern the elastic behaviour of the soil and the small strain shear stiffness. The evolution of the bounding and dilatancy surfaces

based on the state parameter (ψ) is governed by the n^b and n^d parameters, respectively. The parameters (h_0, c_h, and A_0) control the hardening and dilatancy of the soil and can be determined iteratively by fitting the monotonic q-ε_a and volumetric behaviour of the soil. Finally, parameters that distinguish the SANISAND-MS model from SANISAND04 (Dafalias and Manzari, 2004) are (μ_0, ζ, and β), which simulate the ratcheting behaviour of sand. The following sections will provide a detailed description of each parameter and its determined value.

The SANISAND-MS parameters in Table 5.4 are determined from the triaxial tests presented in Chapter 4 and are informed by the parameter values of the SANISAND04 model (Dafalias and Manzari, 2004), as summarised by Kowalczyk (2020) in Table 5.5 for various types of sands.

Table 5.5: SANISAND04 (Dafalias and Manzari, 2004) parameter values summarised by Kowalczyk (2020)

Parameter	Toyoura sand	Nevada sand	Sacramento sand	Ottawa F-65 sand	Monterey sand	Quartz sand
G^* [-]	125	150	200	82.35	130	110
ν	0.05	0.05	0.2	0.01	0.05	0.05
m	0.01	-	-	0.02	0.01	
e_0	0.934	0.83	0.96	0.8	0.858	0.845
λc	0.019	0.027	0.028	0.055	0.02	0.049
ξ	0.7	0.45	0.7	0.5	0.69	0.27
M_c	1.25	1.14	1.35	1.46-1.6	1.27	1.27
c	0.712	0.78	0.65	0.47-1.0	0.712	0.712
h_0	7.05	9.7	5	15.114-17.0	8.5	5.95
ch	0.968	1.02	1.03	0.996	0.968	1.01
n^b	1.1	2.56	1.2	0.64	1.05	2
A_0	0.704	0.81	0.8	0.45	0.6	1.06
n^d	3.5	1.05	2	0.1-0.5	2.5	1.17
$zmax$	4	5	-	14.6-15	4	-
cz	600	800	2000-4000	-	-	-

5.3.1 e_0, λ_c, ξ, M_c, and c parameters

The critical state framework of the SANISAND-MS model is taken into account with the parameters presented in this section. The three parameters (e_0, λ_c, and ξ) are used to locate the CSL in the *e-p'* compressibility plane. According to the critical state theory, a soil element at a given density and applied effective stresses must either dilate or contract under shearing to reach the CSL. The procedure and tests used to determine the CSL are not discussed in this section, as they were covered in detail in Section 4.6.2 of Chapter 4. Figure 5.11 replots the CSL of Blessington sand from Figure 4.44 and includes the parameter values (e_0, λ_c, and ξ) summarised in Table 4.6.

As mentioned in Section 4.6.2 of Chapter 4, the critical state stress ratio in triaxial compression (M_c) is 1.418, based on a representative critical angle of shearing resistance (φ_c) of 35° for Blessington

sand. Since no triaxial extension tests were conducted in this research, the value of the ratio between the critical stress ratios in triaxial extension and compression (c) is selected according to values reported in previous studies. According to Table 5.5, the parameter c falls within the range 0.47-1. Since calibrated values of c are often close to 0.7 (Plaxis SANISAND-MS Manual, 2023), the value of 0.7 is used in this research for c.

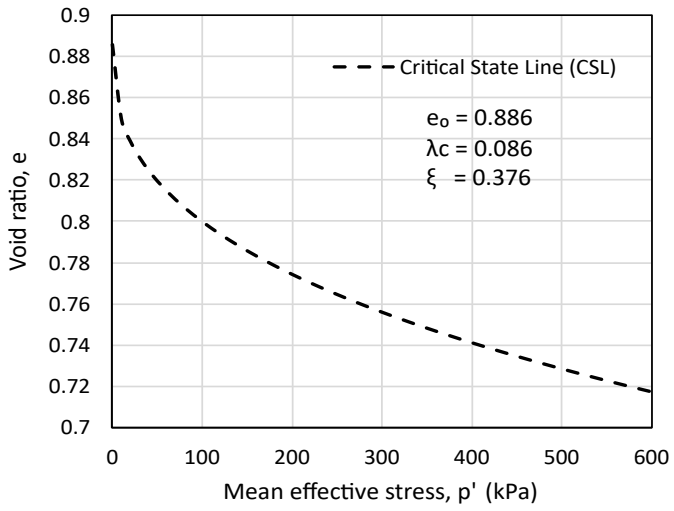


Figure 5.11: Critical state line (CSL) for Blessington sand

5.3.2 *G**, *v*, and *m* parameters

The parameters in this section describe the elastic response of the soil. The coefficient G^* controls the small strain shear modulus (G_0) and can be calibrated based on shear wave measurements from bender element tests in the laboratory or from seismic cone penetration (SCPT) and cross-hole tests in the field. Furthermore, when laboratory and field shear wave measurements are unavailable, the coefficient G^* can be estimated by fitting the initial q-ε_a response from monotonic triaxial tests. The relation between the small strain shear modulus (G_0) and the coefficient G^* is as follows:

$$G_0 = G^* p_{atm} \left[\frac{(2.97-e)^2}{(1+e)}\right] \left(\frac{p}{p_{atm}}\right)^{0.5} \tag{5.14}$$

The G^* coefficient is similar to the A parameter in Equation 4.2 previously shown in Chapter 4. Although the value of G^* can be easily determined from the bender element results, it is calibrated in this research based on the initial q-ε_a response from the monotonic triaxial tests, which is selected as 125. The value assigned to Poisson's ratio (v) is 0.2, which is similar to the value of v_{ur} in the HSsmall model. The parameter m defines the size of the yield surface in the deviatoric stress ratio plane. Dafalias and Manzari (2004) suggested using an m value in the order of M_d/100. As a result, the value assigned to m is 0.0142.

5.3.3 n^b and n^d parameters

The bounding stress ratio (M^b) and dilatancy stress ratio (M^d) correspond to the stress ratios at which the peak shear strength and phase transformation take place, respectively. The evolution of M^b and M^d as a function of ψ is as follows:

$$M^b = M_c \exp(-n^b \psi) \tag{5.15}$$

$$M^d = M_c \exp(n^d \psi) \tag{5.16}$$

where n^b and n^d are model parameters that control the dependency of M^b and M^d on ψ. Knowing the M^b and M^d stress ratios and the corresponding state parameters ψ^b and ψ^d, the values of n^b and n^d can be easily determined from Equations 5.15 and 5.16.. Using nonlinear regression analysis to fit Equation 5.15 to the M^b and ψ^b data, the value of n^b was equal to 2.222. This value can be considered satisfactory, as it falls within the range of 0.64–2.56 shown in Table 5.5 for different sand types.

The dilatancy surface represents the stress ratio at which phase transformation occurs. The phase transformation state appears in undrained tests when *p'* reaches its minimum value and the stress direction in the *p'-q* space begins to change. This transient state marks the transition of soil behaviour from contractive to dilative. However, since only a single undrained test was conducted in this research, the parameter n^d is determined from the stress ratios corresponding to the characteristic state, due to its similarity to the phase transformation state. Unlike the phase transformation state, the characteristic state stress ratio is determined at the point where the incremental volumetric strain changes from contraction to dilation. Using nonlinear regression analysis to fit equation 5.16 to the M^d and ψ^d data, the value of n^d was equal 0.827. This value is satisfactory since is falls with the range of 0.1-3.5 shown in Table 5.5.

5.3.4 h_0, c_h, and A_0 parameters

The parameters h_0 and c_h govern the hardening of the soil and influence the hardening modulus K_p which is proportional to the distance between the current stress ratio (η) and its corresponding image η on the bounding surface. These two parameters are fitting parameters and can be determined by iteratively adjusting them to best fit the monotonic q-ε_a response from triaxial experiments conducted at different relative densities and mean effective stresses. The parameter values chosen for h_0 and c_h for Blessington sand are 8.25 and 1.0, respectively. The parameter A_0 influences the dilatancy of the soil can be estimated from the procedure provided in the Plaxis SANISAND-MS Manual (2023). However, the value of A_0 in this research is iteratively adjusted to fit the monotonic response, rather than following the procedure in the Plaxis SANISAND-MS Manual (2023), as the obtained value did not closely match the laboratory results. The value selected for A_0 is 1.1 which is slightly above the range of 0.704-1.06 in Table 5.5.

5.3.5 e_{ini}, e_{min}, e_{max} parameters

These three parameters represent the void ratio at different states. e_{ini} is the initial void ratio of the sample, and it is the parameter that is varied to reflect different relative densities in the field, while the other parameters remain constant, as the SANISAND-MS model is based on the critical state theory of soil. e_{min} and e_{max} are the minimum and maximum void ratios corresponding to the maximum and minimum densities of the soil. As mentioned in Chapter 3, the values of e_{min} and e_{max} are 0.492 and 0.980, respectively.

The calibration of the monotonic parameters of the SANISAND-MS model is checked by comparing the monotonic test results with triaxial simulations conducted using the soil test facility in Plaxis 3D. Figure 5.12 and Figure 5.13 display comparisons for samples prepared at a relative density of approximately $D_r \approx 30\%$, while Figure 5.14 and Figure 5.15 present comparisons between triaxial simulations and laboratory results for samples prepared at $D_r \approx 60\%$. Figure 5.12 and Figure 5.14 compare the triaxial simulation results with laboratory results in terms of q-ε_q behaviour for large strain levels up to failure. While Figure 5.13 and Figure 5.15 present comparisons at small strain levels, measured with local axial strains, in terms of q-ε_a. The comparisons at both small and large strain levels indicate that the selected SANISAND-MS parameters effectively capture the monotonic behaviour of Blessington sand for both loose and dense samples across a wide range of mean effective stresses.

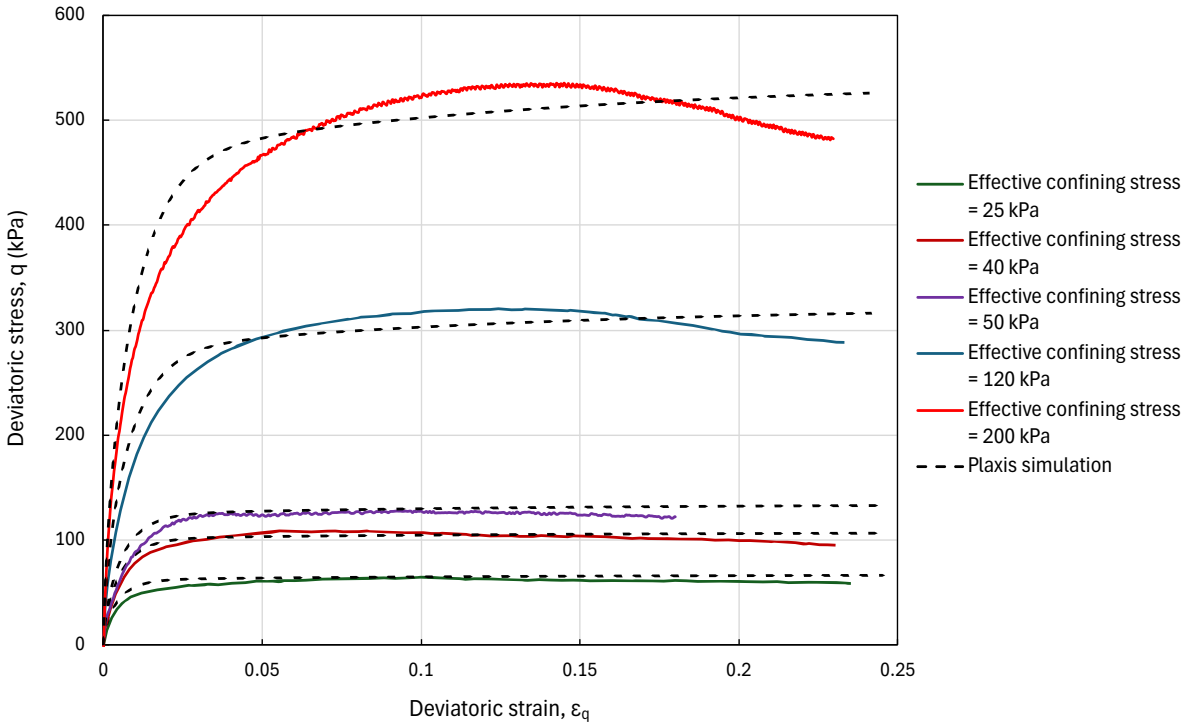


Figure 5.12: Comparing monotonic q-ε_q curves between triaxial simulation and laboratory results for $D_r \approx$ 30%

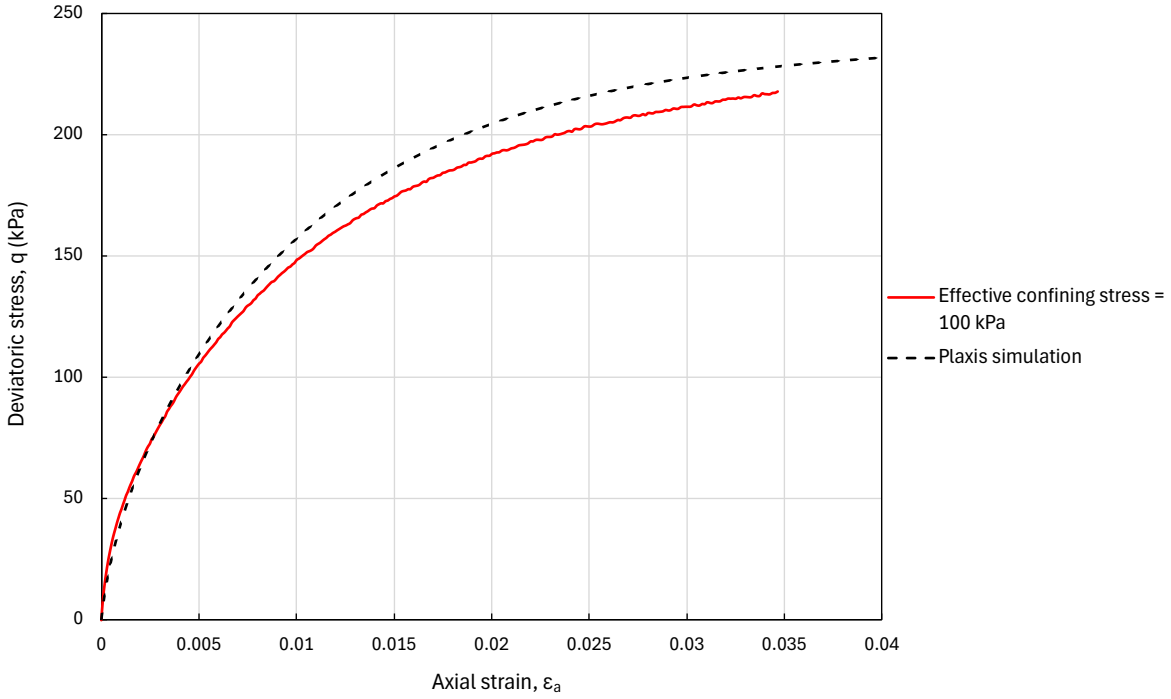


Figure 5.13: Comparing monotonic q-ε_a curves between triaxial simulations and laboratory results for $D_r \approx$ 30%

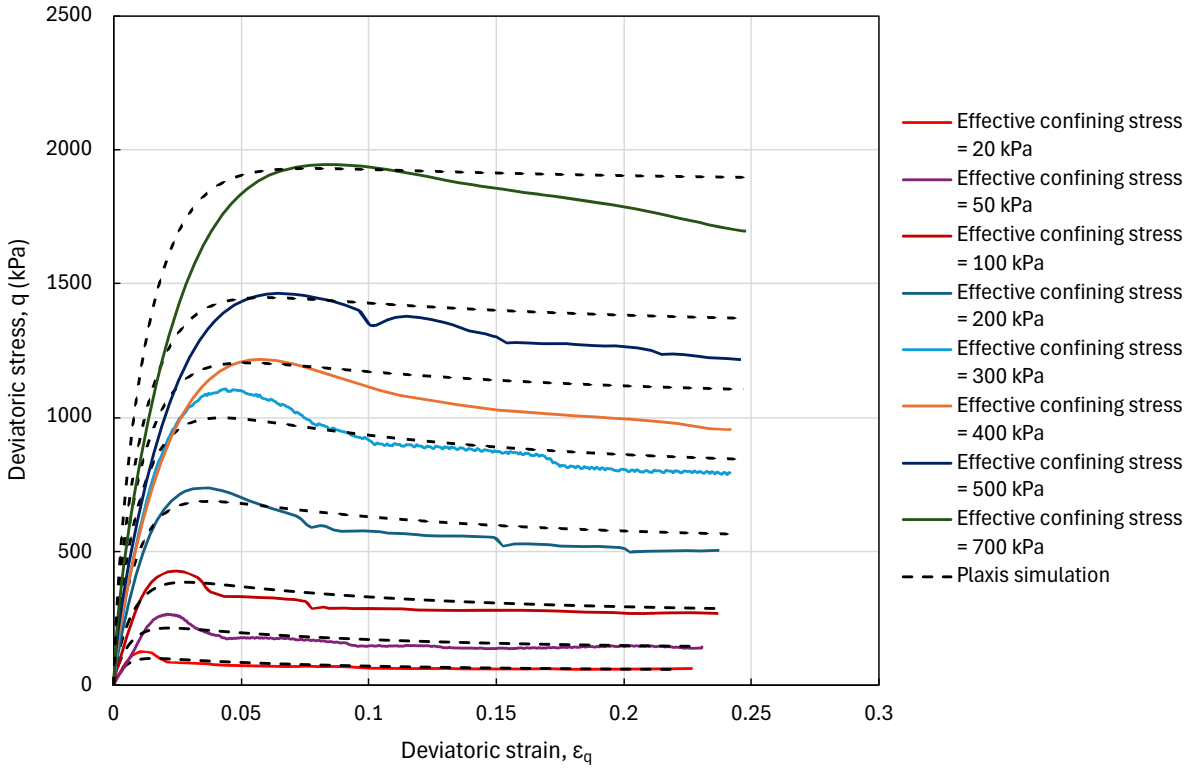


Figure 5.14: Comparing monotonic q-ε_q curves between triaxial simulation and laboratory results for $D_r \approx$ 60%

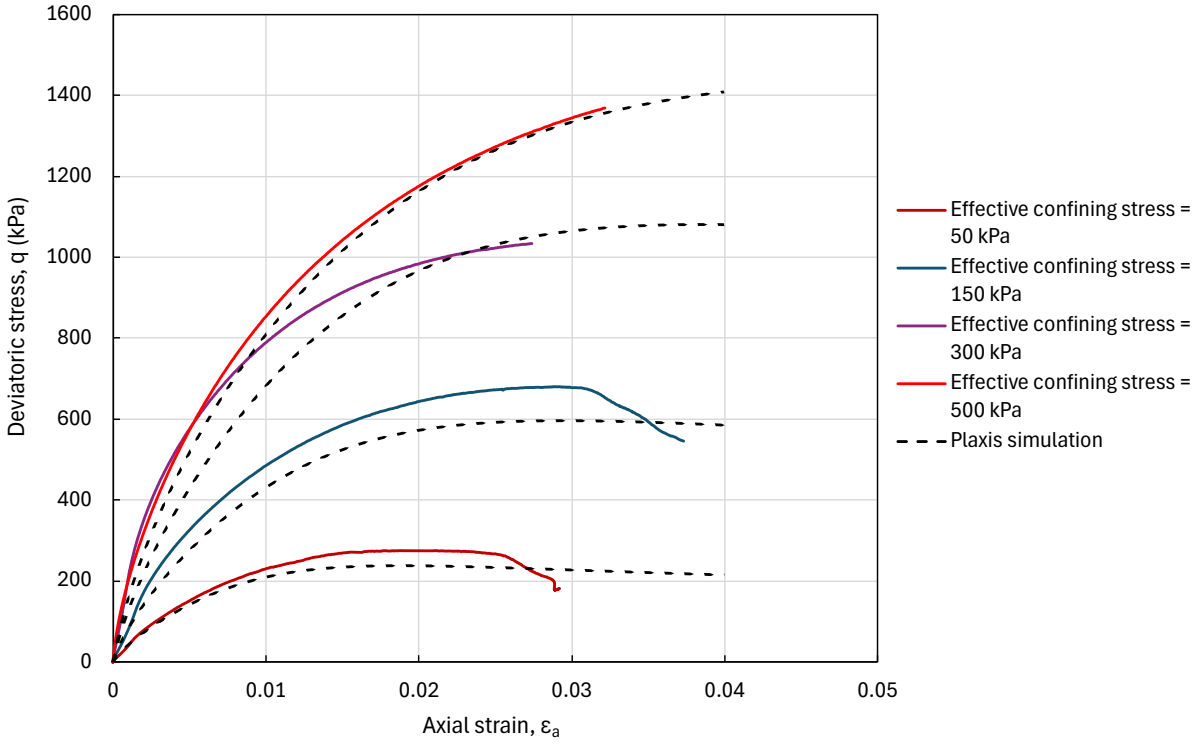


Figure 5.15: Comparing monotonic q-ε_a curves between triaxial simulations and laboratory results for $D_r \approx 60\%$

Some concluding remarks regarding the calibration process and results are as follows:

(iv) The calibration process was conducted manually and involved a degree of subjectivity. Rather than using an automated calibration method that objectively determines parameter values based on laboratory results, the author manually adjusted the parameters to fit the observed data. While implementing an automated approach could improve objectivity, it can be time-consuming, and the implementation script requires thorough initial verification.

(v) Due to the large number of parameters in the SANISAND-MS model, alternative sets of parameter values can produce the same simulation results shown in Figure 5.12 to Figure 5.15. Although an alternative set of parameters is presented later, it will not be used because it results in excessively high hysteretic soil damping.

5.3.6 μ_0, ζ, and β parameters

The three parameters discussed in this section govern the cyclic behaviour of the soil, particularly in terms of cyclic strain accumulation. According to the Plaxis SANISAND-MS Manual (2023), these parameters can be calibrated using asymmetric cyclic triaxial tests. While most experiments conducted in this research involve symmetrical cyclic tests, a limited number of asymmetric tests were performed to aid in the calibration of these parameters. The parameter μ_0 controls ratcheting at stress ratios below the dilation surface, while the parameter ζ governs soil ratcheting when the stress ratio reaches or exceeds the dilation surface, thereby activating dilative soil behaviour. The last parameter β primarily affects undrained cyclic behaviour and has minimal influence when the

behaviour is drained. Since the 3D FE simulations were conducted in drained condition, a value of 1.0 was assigned to the parameter β. The asymmetrical cyclic tests were performed only for stress ratios below the dilative surface to calibrate the value of the μ_0 parameter. This is because the 3D FE simulations were conducted for mudline displacement levels associated with the fatigue limit state, where significant dilation in the soil continuum around the monopile is unlikely to occur. The value assigned to ζ is 0.0005, which is the value calibrated for Karlsruhe Quartz sand by Liu (2020).

In order to select a suitable value for μ_0, asymmetric cyclic triaxial simulations were carried out with the soil test facility in Plaxis 3D, and the axial strain accumulation results were compared with actual results obtained from the laboratory tests. The two asymmetric cyclic triaxial tests conducted in this research are BCD(30)100L and BCD(60)200L. The BCD(30)100L test was performed on Blessington sand at a relative density of 30%, while the BCD(60)200L test was carried out at a relative density of 60%. The stress paths of BCD(30)100L and BCD(60)200L tests in the *q-p'* stress space are presented in Figure 5.16. The initial stage of both tests involved shearing the soil under a constant *p'*, achieved by increasing the deviatoric stress while simultaneously decreasing the confining stress to maintain a constant *p'*. This was followed by the application of a cyclic deviatoric stress (q_{cyc}) for 1000 cycles. For both tests, the average stress ratio (η_{av}), defined as the ratio of the average deviatoric stress (q_{av}) to the average mean effective stress (p_{av}'), is equal to 0.6 ($\eta_{av} = 0.6$). On the other hand, the cyclic stress ratio (η_{cyc}), defined as the ratio of the cyclic deviatoric stress (q_{cyc}) to the average mean effective stress (p_{av}'), is equal to 0.3 ($\eta_{cyc} = 0.3$). The accumulated axial strains against the number of cycles (N) are compared between the triaxial simulations using different μ_0 values and the results from BCD(30)100L and BCD(60)200L tests, as shown in Figure 5.17 and Figure 5.18, respectively. The comparisons indicate that a suitable μ_0 for the soil at 30% relative density lies between 50 and 100. However, for the soil at 60% relative density, a μ_0 value greater than 300 is required.

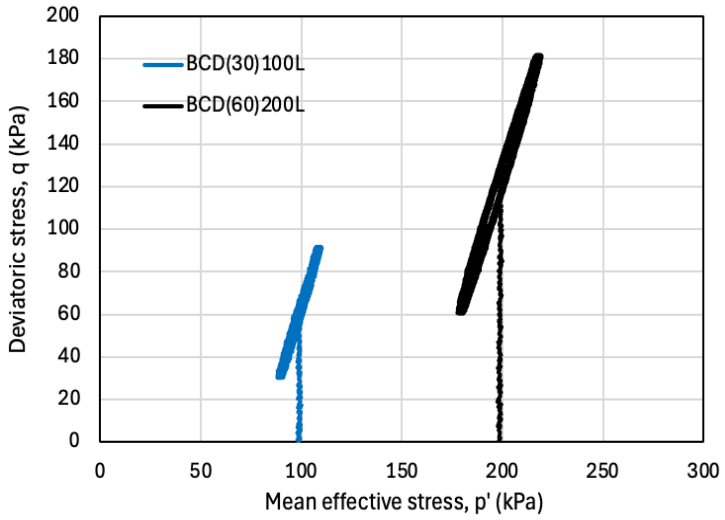


Figure 5.16: the *q-p'* stress paths for BCD(30)100L and BCD(60)200L tests

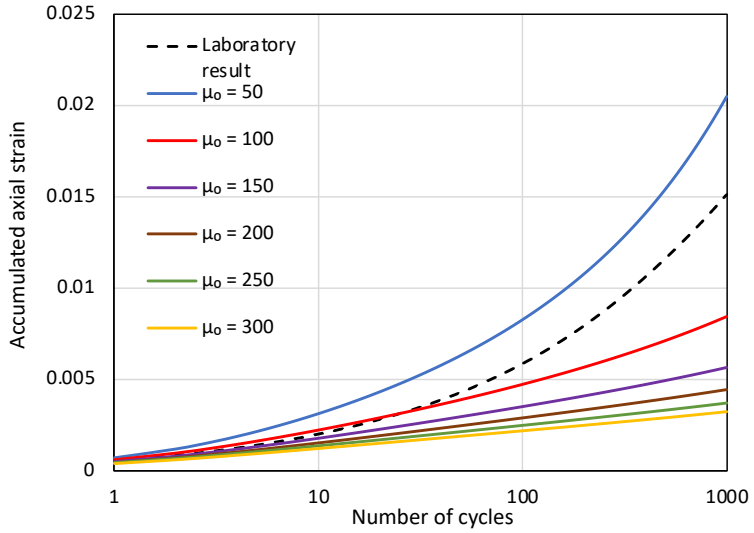


Figure 5.17: Axial strain accumulation from laboratory and triaxial simulations for BCD(30)100L

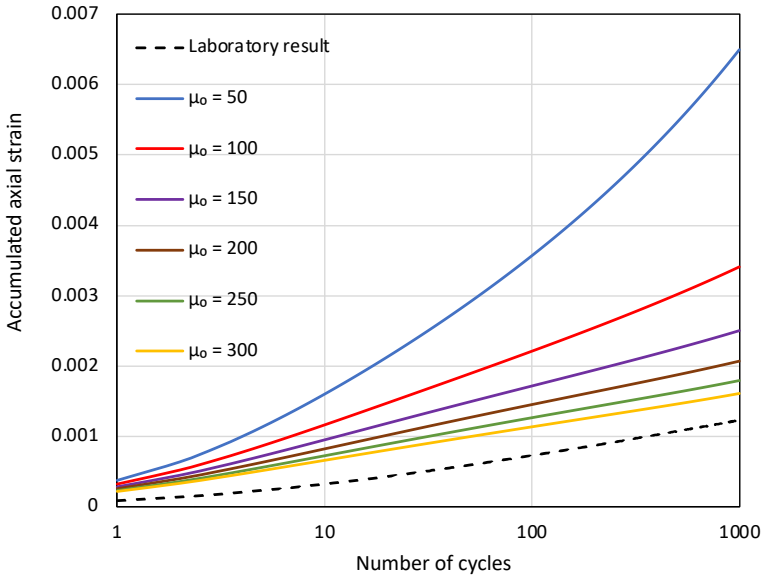


Figure 5.18: Axial strain accumulation from laboratory and triaxial simulations for BCD(60)200L

Due to the discrepancy between the required μ_0 values for the two different relative densities and the lack of representative μ_0 values for other sand materials in the literature, the μ_0 value used in this study is 265 which is the value of μ_0 calibrated by Liu (2020) to represent the cyclic behaviour of Karlsruhe Quartz sand. Furthermore, in addition to influencing ratcheting, μ_0 also affects the damping ratio (D) of soil. To represent this clearly, Figure 5.19 shows D-γ_c curves obtained from triaxial simulations for the soil at 60% relative density using different μ_0 values, alongside the D-γ_c curve calculated using Equation 4.6 for a p_0' value of 50 kPa. According to the trend observed from Figure 5.19, the damping ratio (D) at the same cyclic shear strain (γ_c) reduces as μ_0 increases. Furthermore, Figure 5.19 reveals that at cyclic shear strains below 0.1%, D-γ_c curves obtained from SANISAND-MS model tend to be lower than the D-γ_c curve obtained from Equation 4.6. However, as the cyclic shear strain exceeds 0.1%, the damping ratio obtained from SANISAND-MS exceeds that of Equation 4.6 which is curve fitted to the laboratory results. As a result, this suggests that for

large deformations, the SANISAND-MS results may be unconservative, as they overestimate the hysteretic energy dissipation.

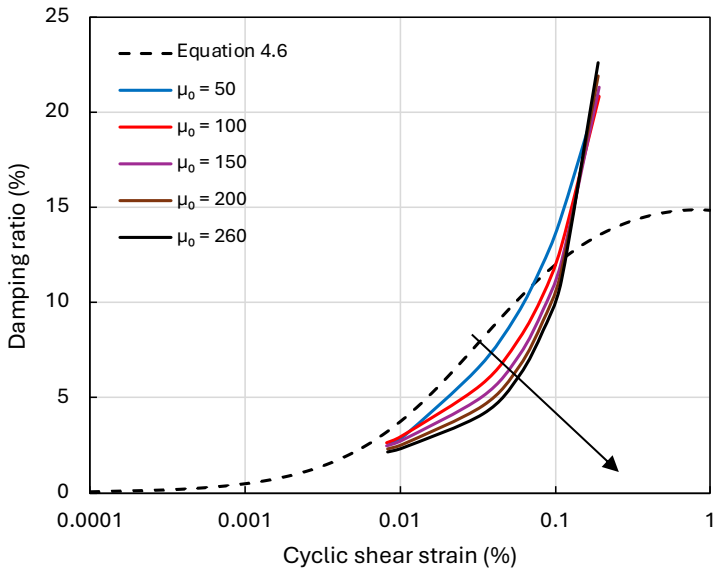


Figure 5.19: D-γ curves obtained from SANISAND-MS and laboratory derived curve fit

5.3.7 Alternative set of parameters

Since the SANISAND-MS model has many parameters, it is possible to obtain a different set of parameter values that yield the same simulation results as the parameter values presented previously. The new set of parameters discussed herein is referred to as Parameter set 2 (PS2), while the previously mentioned parameter values are referred to as Parameter set 1 (PS1). Having multiple parameter sets that produce identical simulation results is a common feature of advanced soil constitutive models, as these models, in addition to physical parameters, include various curve-fitting parameters that can be adjusted to achieve approximately the same outcomes. The differences between PS1 and PS2 are only in terms of the values assigned to parameters G_0 and h_0. The values given to G_0 and h_0 for PS2 are 265 and 3.25, respectively. Comparisons of monotonic triaxial simulations conducted using both parameter sets are presented in Figure 5.20. The monotonic triaxial simulations are performed for Blessington sand at 60% relative density under different p_0' values to check whether the simulation results of both parameter sets are consistent across different cases. From the comparisons in Figure 5.20 it can be seen that the simulation results from PS1 and PS2 closely overlap which suggests that both parameter sets can be used to represent the monotonic behaviour of Blessington sand. However, a comparison of the damping ratio curves obtained from drained cyclic simulations, as shown in Figure 5.21, reveals that while PS1 and PS2 yield identical monotonic results, their cyclic behaviours differ significantly. The comparison in Figure 5.21 is conducted for Blessington sand at 60% relative density, consolidated under a p_0' value of 50 kPa. Since the D-γ_c curve obtained from PS2 is higher than that of PS1, which could suggest than 3D FE simulations with PS2 could yield unconservative results, the parameter values of PS1 are used in this research to represent the dynamic behaviour of Blessington sand. The reason for presenting the

behaviour obtained from different parameter sets is to illustrate the complexity involved in capturing soil behaviour using advanced constitutive material models.

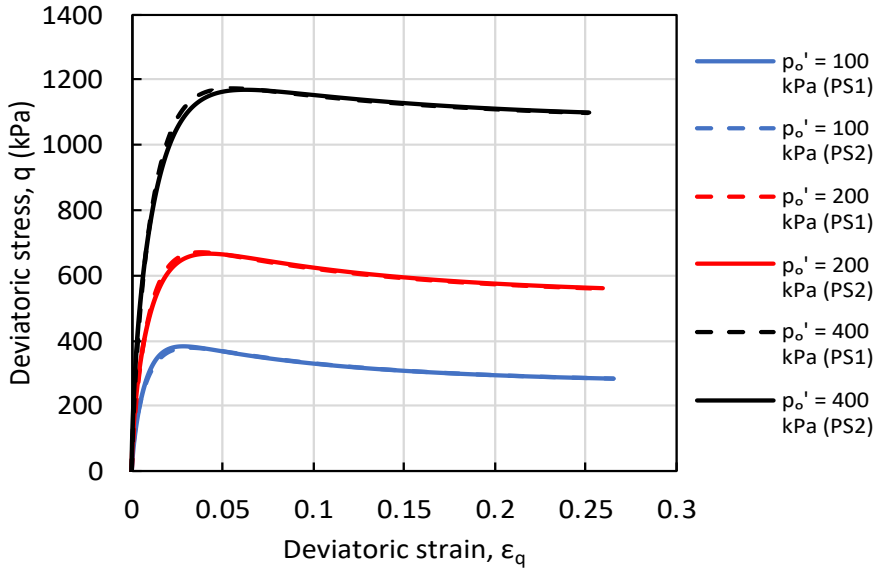


Figure 5.20: Monotonic simulation results obtained using PS1 and PS2 parameters

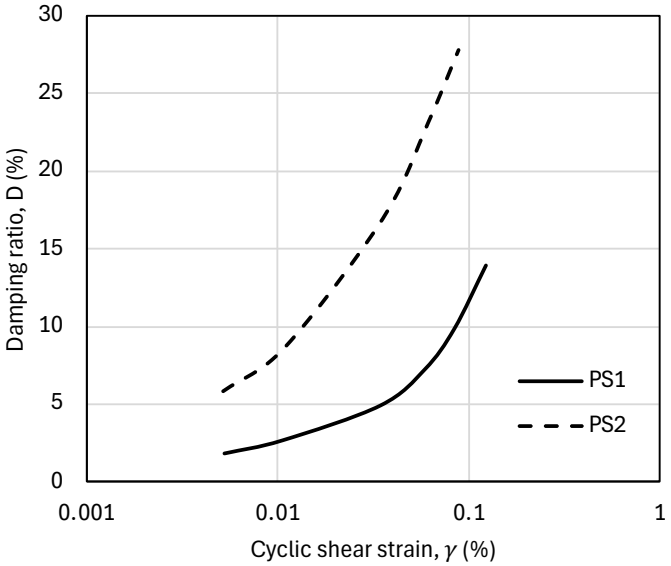


Figure 5.21: Damping ratio curves obtained using PS1 and PS2 parameters

5.3.8 Issue related to SANISAND-MS model

This section discusses the limitations of the SANISAND-MS model for cyclic soil behaviour. Two main inherent limitations are observed which could drastically impact the monopile behaviour. These two limitations are:

(i) Reduction of damping ratio with N

(ii) Strain accumulation bias

5.3.8.1 Reduction of damping ratio with *N*

Although the damping ratio of soil decreases with the number of cycles (*N*), the SANISAND-MS model tends to overestimate this reduction. This phenomena of the SANISAND-MS model is clearly shown in Figure 5.22, which shows the reduction of damping ratio as a function of *N* for a representative cyclic shear strain level of 0.1%. The rate of reduction is significantly higher than that observed in the laboratory results of this research and in other experimental studies, such as those by Darendeli (2001), Blaker and Andersen (2019), and Andersen et al. (2023). Although this could impact the analysis results, the simulations are only conducted for small number of cycles (*N* < 10) and thus the results of the simulations are representative of the behaviour of monopiles in the field.

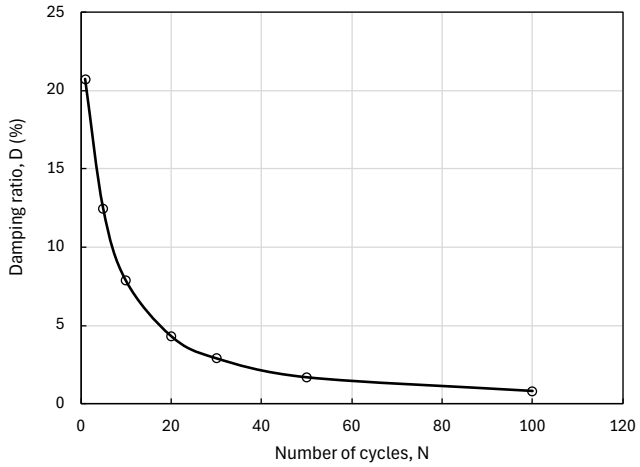


Figure 5.22: Damping ratio (*D*) against number of cycles (*N*)

5.3.8.2 Strain accumulation bias

An additional limitation of the SANISAND-MS model is its tendency to overestimate the accumulated axial strain on the extension side under two-way symmetrical cyclic deviatoric stresses. This bias of axial strain accumulation towards the extension side is illustrated in Figure 5.23, which compares the stress-strain response of a representative triaxial experiment (BCD(30)50) with the corresponding simulated response using the SANISAND-MS model. Figure 5.23 demonstrates that while the stiffness predicted by the SANISAND-MS model aligns closely with the experimental stiffness of Blessington sand, the simulated behaviour indicates that the model overestimates axial strain accumulation on the extension side. Similarly, Wichtmann et al. (2019) observed that the SANISAND model (version 2004) has a tendency to display large axial strain accumulation in the extension side, and attributed this behaviour to the model having different failure lines for compression and extension in the *q-p'* space. The same reasoning provided by Wichtmann et al. (2019) can be applied to the SANISAND-MS model, as it is based on the SANISAND model (version 2004) and creates distinct failure lines for compression and extension due to the *c* parameter. To limit the extension-side axial strain accumulation, one could assign a higher *c* value, but this would require the other parameters to be adjusted accordingly.

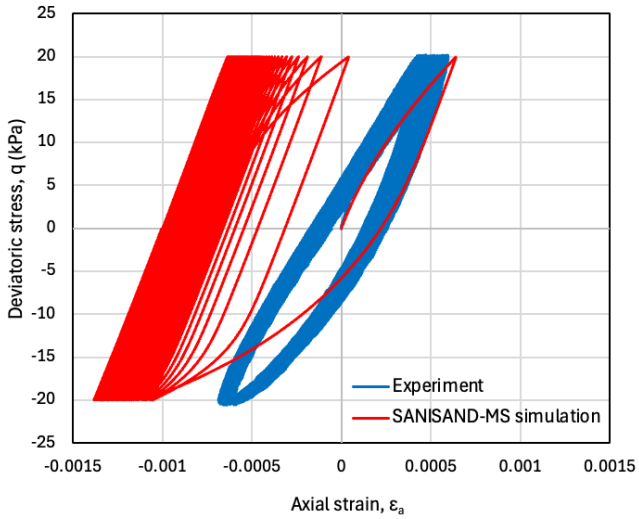


Figure 5.23: Comparing the stress-strain response of laboratory experiment and SANISAND-MS simulation

5.3.9 Selected SANISAND-MS parameters

Although different sets of parameter values could produce the same behaviour, the 3D FE analyses in Chapter six are conducted with values of parameter set 1 (PS1), which are summarised in Table 5.6.

Table 5.6: Values of parameter set 1 (PS1)

Parameter	Symbol	Unit
Shear modulus coefficient	G^*	125
Poisson's ratio	v	0.2
Stress ratio at critical state in triaxial compression	M_c	1.418
Ratio between critical stress ratios in extension and compression	c	0.7
Slope of the CSL in the compressibility plane	λ_c	0.08597
Void ratio of the CSL at p' = 0kPa	e_0	0.8858
Critical state line constant	ξ	0.376
Size of the yield surface	m	0.0142
Hardening parameter	h_0	8.25
Hardening parameter	c_h	1
Bounding parameter	n^b	2.222
Dilatancy parameter	A_0	1.1
Dilatancy surface parameter	n^d	0.827
MS surface parameter	μ_0	50
MS surface parameter	ζ	0.0005
MS surface parameter	β	1
Initial void ratio of the layer	e_{ini}	-
Maximum void ratio	e_{max}	0.98
Minimum void ratio	e_{min}	0.492
Maximum bounding stress ratio in triaxial compression	${M_c}^b{}_{max}$	0
Toggle	Elscheme	0

5.4 Summary

The calibration of the parameter values for two constitutive models was covered in detail, given the importance of the local behaviour of soil on the global behaviour of monopiles supporting OWTs. Some parameters, such as the peak friction angle values required by the HSsmall model, were obtained directly from monotonic tests, while others were either derived from recommendations in the literature or iteratively adjusted to align with the laboratory results. Comparisons between triaxial simulations and laboratory results showed that the parameters of HSsmall and SANISAND-MS models accurately reproduce the monotonic soil behaviour. Furthermore, the dynamic parameters of HSsmall and SANISAND-MS models were adjusted to achieve a reasonable match with the damping ratio curves derived from fitting the laboratory results.

The limitations of both constitutive models were also thoroughly examined. A key drawback of the HSsmall model is its inability to capture the softening response of soil, which may result in an overestimation of the ultimate capacity of monopiles. Additionally, the model requires the explicit input of peak friction angle values for varying mean effective stresses and relative densities. With regard to dynamic behaviour, the HSsmall model uses two parameters to represent the shear modulus and damping ratio as functions of cyclic shear strain. However, this relationship is only valid within the elastic region. Once strain hardening occurs, the dynamic behaviour becomes influenced by all model parameters, which could cause the damping ratio to increase sharply and potentially lead to an unconservative simulation of the dynamic response. As a result, the model is mostly suitable for small strain loading applications.

Although the SANISAND-MS model addresses most of the monotonic behaviour issues of the HSsmall model, it has some limitations in simulating dynamic soil response. The main drawback observed is that the SANISAND-MS model results in a rapid decay of soil damping ratio, with the damping almost completely diminishing after 100 cycles. Another limitation of the SANISAND-MS model is that it overestimates strain accumulation on the extension side when the soil is subjected to two-way symmetrical stresses, which is attributed to the distinct failure lines in the triaxial space for compression and extension.

Finally, it is important to note that, although both models have limitations and certain aspects of soil behaviour from the experiments could not be fully calibrated, the aim of this thesis is to provide an adequate and reasonable representation of soil-structure interaction, and thus examine the impact of soil damping on monopile-supported OWTs. Even if the models were perfect and the calibrated parameters accurately simulated all aspects of soil behaviour, modelling monopile behaviour remains challenging due to the highly complex loading and ground conditions in the field, making detailed simulation virtually impossible.

Chapter 6

3D Finite Element Modelling

6.1 Introduction

This chapter investigates foundation damping using results from 3D FE numerical simulations. The analyses employ constitutive models calibrated in the previous chapter using triaxial experiments conducted as part of this study. The use of calibrated constitutive soil models ensures that the simulated monopile behaviour closely reflects field conditions. The chapter begins by describing the development of the numerical models, including the elements used to represent the soil domain, the monopile below the mudline, and the OWT support structure above the mudline. Foundation damping was examined through dynamic free-decay and cyclic push-over simulations. The 3D FE analyses were conducted for the reference IEA 15 MW wind turbine (Gaertner et al., 2020), which is considered representative of typical large-scale OWTs expected to be widely used in future deployments. Accordingly, the findings from this study aim to support the economic viability of both current and next-generation offshore wind systems. Dynamic free-decay simulations were performed to evaluate the global foundation damping ratios (ζ_f), which were determined from the attenuation of the OWT response at the RNA level and calculated with respect to the lateral displacement of the monopile at the mudline during free vibration. The global damping ratio (ζ_f) reflects energy dissipation in the surrounding soil continuum and the elastic energy stored in the soil, monopile, and OWT structure. These analyses involve performing free vibration simulations in which the OWT structure is displaced monotonically by applying a lateral load (H) at the RNA level, then allowed to oscillate freely upon load release. Since the structure deforms predominantly in the first mode during both the loading and free vibration stages, the damping ratio (ζ_f) estimated using the logarithmic decrement method corresponds to the first-mode global foundation damping. In monopiles with low damping, the structural response is concentrated around the fundamental natural frequency (f_1), due to the high dynamic amplification at that frequency, while higher modes typically lie outside the dominant frequency range of environmental loading (Seidel, 2014). Therefore, this study focuses exclusively on evaluating ζ_f for the first mode of vibration.

Before performing free-decay simulations with the calibrated HSsmall and SANISAND-MS constitutive models, a preliminary free vibration analysis was carried out using a linear elastic soil model. This step aimed to confirm that, at typical OWT response frequencies near f_1, energy

dissipation is predominantly governed by soil hysteresis, with radiation damping effects being negligible.

Hysteretic foundation damping ratios (ξ_y and ξ_θ) were computed from the force-displacement and moment-rotation hysteresis loops obtained through cyclic push-over simulations. These simulations involved applying two-way symmetrical cyclic loads at the RNA level, with the analyses conducted under static conditions to eliminate inertial effects. The damping ratios were evaluated at both the mudline and along the embedded portion of the monopile shaft.

The hysteretic foundation damping ratios derived in this study can be incorporated into integrated wind turbine simulation tools (e.g., Bladed and OpenFAST) to account for foundation damping effects. To assess whether the hysteretic foundation damping ratios obtained from cyclic push-over simulations yield global foundation damping ratios (ζ_f) comparable to those obtained from the 3D FE free-decay analyses, the mudline hysteretic damping ratios (ξ_y and ξ_θ) were converted into equivalent viscous dashpots and incorporated in 1D FE analyses. Global foundation damping ratios (ζ_f) were then calculated using the logarithmic decrement approach and compared to the ζ_f values derived from the original 3D FE free-decay simulations.

It is important to note that although different foundation damping parameters are presented in this thesis, they are inherently interrelated. For example, while the global foundation damping ratio (ζ_f) represents the effect of the foundation on the overall dynamic response of the OWT, it is influenced by the local damping ratios (ξ_y and ξ_θ), which are derived from load-deformation hysteresis loops. Generally, when ξ_y and ξ_θ are large for a given foundation displacement, the corresponding ζ_f is also large, as greater plastic energy is dissipated within the soil surrounding the monopile. The relationship between the foundation damping parameters and how they affect each other are addressed in this chapter.

The numerical analysis results presented in this chapter aim to address the research gap identified in the literature review, specifically the evaluation of how monopile dimensions and ground conditions influence foundation damping in monopile-supported OWTs. The study investigates the effects of monopile diameter (D_p), embedment depth (L_p), and soil relative density (D_r) on the global and local foundation damping behaviour. Additionally, since the analyses were performed using two different soil constitutive models, results were compared to evaluate the sensitivity of foundation damping to the chosen constitutive model.

6.2 3D FE numerical models

The 3D FE models were developed using the Plaxis 3D software Version (2024.1), selected for its user-friendly interface, robustness, and extensive support resources. Numerical analyses were conducted to investigate foundation damping for the reference IEA 15 MW wind turbine (Gaertner et al., 2020). A representative 3D FE model, created using Plaxis 3D, is shown in Figure 6.1, which

includes the soil domain, the monopile below the mudline, and the support structure above the mudline. Taking advantage of the symmetry of the OWT structure, the 3D FE models were constructed as half-space models to reduce computational time. The discretised soil mesh is modelled using 10-node tetrahedral volume elements, which employ second-order interpolation for displacements and incorporate four Gaussian integration points. The monopile below the mudline was modelled with plate elements, which are 6-node triangular elements with three Gaussian integration points. The plate elements representing the steel monopile were assigned four key properties: wall thickness (t), Young's modulus (E), effective unit weight (γ'), and Poisson's ratio (v). A constant thickness of 0.1 m was applied to the plate elements. The assumed values for Young's modulus (E) and submerged unit weight (γ') of the steel monopile were 210 GPa and 67.19 kN/m³, respectively, while the Poisson's ratio (v) was assumed to be 0.3.

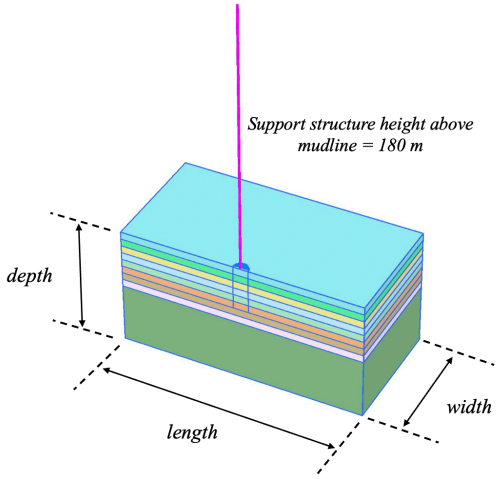


Figure 6.1: 3D FE numerical model

Interface elements were also added to the monopile plates. The interfaces have zero thickness and are composed of 12-node elements which consist of pairs of nodes that connect the 6-noded plate elements to the soil. For each node pair, one node belongs to the structure and the other node belongs to the soil. The interaction between these two nodes consists of two elastic-perfectly plastic springs. One elastic-perfectly plastic spring to model the gap displacement and one elastic-perfectly plastic spring to model slip displacement of the pile as it moves against the soil. The interfaces were added on both the inside and the outside of the monopile. For the HSsmall model, the reduction in interface shear strength and stiffness when slip occurs is accounted for using the strength reduction factor R_{inter}, which was set to 0.7 for both 30% and 60% soil relative densities. For the SANISAND-MS model, the interface shear strength reduction is taken into account using the effective cohesion (c'_{ref}), the effective friction angle (φ'), the dilatancy angle (ψ'). A small value of 0.1 was assigned to c'_{ref} for numerical stability, while a value of 29° was used for φ', as per the recommendation by Panagoulias et al. (2018), and a value of 0° was chosen for ψ'. The interface stiffness for the SANISAND-MS model is determined using a power law, which is formulated in terms of the reference primary oedometric modulus (E_{oed}^{ref}), reference stress level ($UD\text{-}P^{ref}$), and stress rate

dependency (*UD-Power*). The values of E_{oed}^{ref} were derived from the G_0^{ref} values of Blessington sand presented in Chapter 5, using the following equation:

$$E_{oed}^{ref} = 2\ G_0^{ref} \frac{1-v}{1-2v} \tag{6.1}$$

where a Poisson's ratio (v) value of 0.45 was adopted, as the Plaxis 3D software calculates the interface shear stiffness based on this v value. The values of *UD-P*^{ref} and *UD-Power* which account for the variation of the primary oedometric modulus (E_{oed}) with stress level were taken as 100 kN and 0.5, respectively. To evaluate the suitability of the SANISAND-MS interface parameter values for modelling the interaction between the soil and the pile wall, monotonic analyses were carried out on the model shown in Figure 6.1 using both the HSsmall and SANISAND-MS constitutive models. These analyses were conducted on the case of 30% relative density, as the soil in this loose state does not exhibit dilation, enabling a meaningful comparison between the numerical simulations produced by the SANISAND-MS and HSsmall models. The comparison of the monotonic response at the mudline, in terms of lateral force versus mudline displacement (H-y_g), based on lateral loading applied at the RNA level of the tower, for the two constitutive models is shown in Figure 6.2.

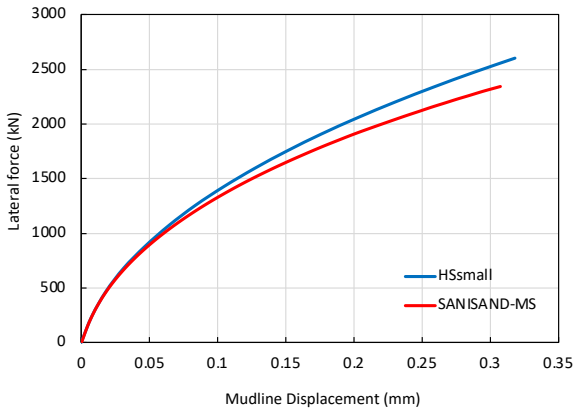


Figure 6.2: Comparison between the monotonic simulation of SANISAND-MS and HSsmall

The results in Figure 6.2 demonstrate that the monotonic behaviour predicted by the SANISAND-MS model closely aligns with that of the HSsmall model. This indicates that the interface parameter values used in the SANISAND-MS model provide comparable interface shear strength and stiffness to those obtained from the HSsmall model through the application of the strength reduction factor (R_{inter}). According to Equation 6.1 and the G_0^{ref} values presented for Blessington sand in Section 5.2.4, the assigned E_{oed}^{ref} values for Blessington sand at 30% and 60% relative densities were 595,232 kPa and 907,621 kPa, respectively.

The boundaries of the models were positioned based on the dimensions of the monopiles to minimise boundary effects. The size of the models in terms of length, width, and depth were larger for the dynamic analyses than those for the monotonic simulations to mitigate the impact of wave reflections. For the static analyses, the model dimensions were defined as follows: the length was

set to 12 times the monopile diameter, the width to 6 times the monopile diameter, and the depth was equal to the monopile embedment depth plus 3 times the monopile diameter. For the dynamic analyses, the dimensions were adjusted to account for wave reflection, with the length set to 16 times the monopile diameter, the width to 8 times the monopile diameter, and the depth to the monopile embedment depth plus 5 times the monopile diameter. To further ensure that no wave reflections take place, viscous boundaries were activated for the dynamic analyses. Boundary deformation conditions were assigned such that the vertical boundaries were fixed in the normal direction (allowing vertical movement), while the bottom horizontal boundary was fully fixed to restrain deformations in all directions. The choice and positioning of the model boundaries were informed by preliminary sensitivity analyses to ensure they did not influence monopile behaviour, while also avoiding unnecessarily large models that would increase computational cost.

While the monopile below the mudline was modelled using plate elements, the rest of the support structure, which includes the portion of the monopile above the mudline and the tower, was represented using discretised beam elements. Although plate elements provide a more detailed representation of the support structure, their use would significantly increase the total number of elements in the model, leading to longer computational times. The beam elements used to model the support structure above the mudline had a uniform length of 2.0 m. Four key parameters were assigned to the beam elements: the effective unit weight (γ'), cross-sectional area (A), second moment of area (I), and elastic Young's modulus of the steel (E). The value of E was taken as 210 GPa, while the values of A, I, and γ' for each beam element were derived from the dimensions and distributed mass of the support structure of the reference IEA 15 MW wind turbine (Gaertner et al., 2020). Details on the variation of distributed mass and dimensions along the height of the support structure of the refence 15 MW OWT are provided in Appendix A.

The unit weight values assigned to the discretised beam elements depend on the distributed mass of the support structure and the assumed sea water depth. The assumed sea water depth for this research was 30 m, which falls within the typical range of depths considered suitable for monopile foundations. Above the sea water level, the unit weight of the discretised beam elements was set to 77 kN/m³. Below the sea water level, the unit weight was adjusted to account for the submersion of the structure and the hydrodynamic added water mass (m_w), which reflects the effect of sea water participating in the OWT vibration. The following equation, proposed by Newman (2018) and used by Corciulo et al. (2017) and Kementzetzidis et al. (2019) for soil-structure interaction of OWTs, was employed in this study to calculate m_w:

$$m_w = 2\rho_w \frac{\pi {D_p}^2}{4} d \tag{6.2}$$

where ρ_w is the density of water and was taken as 1025 kg/m^3 for saline water, D_p is the monopile diameter, and d is the sea water depth. The total m_w calculated using Equation 6.2 was distributed uniformly across the beam elements below the sea water depth. The factor of 2 in Equation 6.2

accounts for the hydrodynamic mass contribution from both the water inside and outside the monopile.

The mass of the RNA at the top of the tower, equal to 1,016,645 kg for the reference IEA 15 MW OWT, was represented by a beam element assigned an equivalent unit weight of 204,270.87 kN/m^3. This unit weight was calculated based on a short beam element with a length of 0.1 m, a diameter of 6.5 m, and a wall thickness of 24 mm.

The foundation and structure were connected using a stiff plate element with a very high Young's modulus to ensure effective transfer of bending moments and shear forces to the monopile below the mudline. To prevent interaction with the soil surface, the stiff plate was elevated by 1 m, as shown in Figure 6.3. In all models, the mesh size around the monopile area was refined by factor of 0.1 times the size of the largest element in the mesh domain. This ensured that the obtained results were accurate and the calculation time was reasonable The water table was positioned at the lower model boundary, and since the analyses were conducted under fully drained conditions, the buoyant effective unit weight of the soil was assigned for both dry and saturated unit weights, following the recommendations of Panagoulias et al. (2018). Finally, although Plaxis 3D allows Rayleigh damping to be applied to plate and beam elements to account for structural damping in the OWT components, this study focuses exclusively on foundation damping, excluding energy dissipation from other sources. Therefore, Rayleigh damping coefficients for the structural elements of the beams and the plates were set to zero.

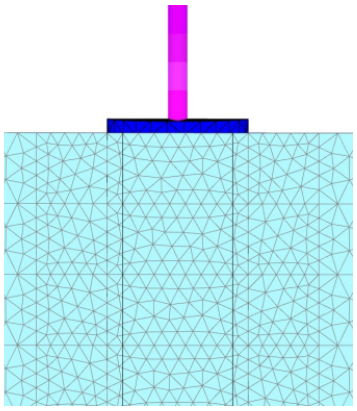


Figure 6.3: Stiff plate connecting the foundation and the structure

Since this research aims to investigate the effects of monopile dimensions and soil relative density on foundation damping, a large number of 3D FE analyses were performed, varying both monopile dimensions and soil relative densities. The analyses were conducted using two soil profiles with relative densities of 30% and 60%. The 30% profile represents a sandy soil in a very loose state, while the 60% profile corresponds to medium-dense soil, which is the ground condition commonly encountered at OWT installation sites. To replicate in-situ soil behaviour for these two profiles, the parameters of the HSsmall and SANISAND-MS constitutive models were calibrated based on monotonic and cyclic triaxial tests conducted on soil samples with relative densities of

approximately 30% and 60%. Although the initial plan included analysing a third soil profile with a relative density of 90% to capture monopile behaviour in very dense conditions, only a limited number of triaxial tests were conducted on Blessington sand at this relative density. As a result, it was not feasible to reliably calibrate the constitutive models for the 90% case, and this scenario was excluded from the numerical analyses. A single set of calibrated parameters for the SANISAND-MS model was presented in Table 5.6, while the calibrated parameters of the HSsmall constitutive model for relative densities of 30% and 60% were summarised in Table 5.2 and Table 5.3, respectively. Since the SANISAND-MS model is state-independent, one set of parameters was used to represent the 30% and 60% soil relative densities. To simulate the behaviour of the soil at relative densities of 30% and 60% using the SANISAND-MS constitutive model, the values assigned to the initial void ratio (e_{ini}) parameter were 0.834 and 0.687, respectively. Although the 30% relative density profile represents a very loose condition not typically encountered at OWT installation sites, it was considered to enable comparison with the more common 60% case and to clarify the influence of relative density on foundation damping.

Analyses were performed for various monopile dimensions below the mudline to investigate their influence on foundation damping resulting from soil-monopile interaction. To isolate the effect of the foundation, the dimensions of the support structure above the mudline, represented by discretised beam elements, were kept the same as those of the reference IEA 15 MW OWT (summarised in Appendix A). Only the foundation dimensions, modelled using plate elements, were varied to assess the effects of the monopile embedment depth and diameter. Although the foundations represented with plate elements in the 3D analyses extend 1 m above the mudline, this extension is not expected to significantly affect the response. Therefore, the observed variations in foundation damping can be attributed primarily to the changes in monopile dimensions below the mudline, where soil-monopile interaction governs the system behaviour.

The dimensions of the monopile foundations, in terms of diameter (D_p), embedment depth (L_p), and slenderness ratio (L_p/D_p), are summarised in Table 6.1. Each monopile geometry is referred with a unique identifier (ID). For example, MP10-30 refers to a monopile having a diameter of 10 m and embedment depth of 30 m. The number before the dash denotes the monopile diameter, while the number after the dash refers to the embedment depth. Although these dimensions were not checked against design requirements for a specific loading scenario, they were selected to fall within the typical range of monopile sizes used in current practice. Furthermore, designing a monopile is an iterative process, in which an initial design is used in dynamic analyses of OWTs to estimate the moments and forces at the mudline, which are then used to update the monopile dimensions. Given that the dimensions of the monopile influence foundation damping which in turn affects the mudline forces and moments, estimating the variation of foundation damping for different monopile dimensions is integral to optimise the monopile design.

As a result, the aim of this research was to investigate how foundation damping varies for the range of monopile adopted in the industry for large size OWTs such as the reference IEA 15 MW OWT. The smaller diameter of 10 m was selected based on the monopile diameter specified for the IEA 15 MW reference turbine.

Table 6.1: Monopile dimensions

Monopile No.	Monopile ID	D_p (m)	L_p (m)	L_p/D_p
1	MP10-30	10	30	3
2	MP10-40	10	40	4
3	MP10-50	10	50	5
4	MP12-30	12	30	2.5
5	MP12-36	12	36	3
6	MP12-48	12	48	4
7	MP12-60	12	60	5

6.3 Radiation damping

Since the foundation dissipates dynamic energy either by radiating elastic waves away from the structure or through hysteretic behaviour in the surrounding soil, it is important to evaluate whether radiation damping contributes at the low response frequencies typical of large OWTs. Although the literature (e.g., Carswell et al., 2015, Malekjafarian et al., 2021) suggests that radiation damping becomes significant at response frequencies above 1 Hz, which are generally higher than those experienced by OWTs under environmental loading from wind and waves, it is still necessary to confirm whether the global foundation damping ratios (ζ_f) obtained in this study, based on the analyses conducted using the HSsmall and SANISAND-MS constitutive models, can be attributed entirely to soil hysteresis around the monopile.

To investigate this, the soil domain was modelled using a linear elastic constitutive model that follows a linear stress-strain relationship during both loading and unloading, without generating nonlinear hysteretic loops. The Young's modulus assigned to the model was set equal to the E_{ur}^{ref} value for Blessington sand at 60% relative density, as given in Table 5.3. The Poisson's ratio was taken as 0.2. A free vibration simulation was carried out by first applying a monotonic lateral load at the RNA level to displace the OWT structure, and then releasing the load to allow the structure to oscillate freely under dynamic analysis. This simulation was performed for the MP10-30 monopile. However, the findings are unlikely to differ if any of the other monopile dimensions in Table 6.1 were used in the analysis.

The contribution of radiation damping was assessed based on the time history of the lateral displacement at the RNA level, shown in Figure 6.4, during the free vibration simulation. The OWT structure was displaced by 2 m at the RNA level. Since the analysis was conducted using a linear elastic soil model, the response would not be expected to vary significantly with larger or smaller displacements. Based on the simulation results in Figure 6.4, the maximum amplitudes of the lateral

displacement at the RNA level show no noticeable variation or decay over time. Therefore, the effect of radiation damping for the first mode vibration of the large size 15 MW OWT can be considered to be negligible. This confirms that the global foundation damping ratios (ζ_f) obtained as part of this study can regarded as fully governed by soil hysteresis around the monopile. The main aim of this section was to validate that ζ_f is entirely dependent on hysteretic soil energy dissipation and the topic of radiation damping will not be address further in the remainder of the thesis. Given that the analysis discussed in this section was only a preliminary analysis, the details regarding dynamic simulations are presented in the next section.

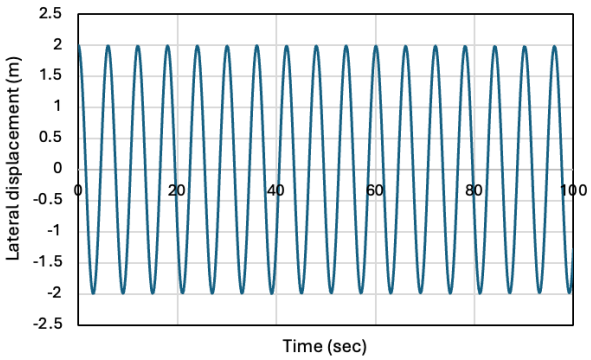


Figure 6.4: Lateral displacement time history at the RNA level

6.4 Free-decay analyses

This section presents the results of the dynamic free-decay analyses that were conducted to investigate the variation of the global foundation damping ratio (ζ_f) due to the effects of soil relative density and the monopile dimensions. The influence of soil relative density was examined by comparing the results of two soil profiles with relative densities of 30% and 60%. The analyses conducted for the different monopile dimensions (summarised in Table 6.1) aim to evaluate the influence of the monopile diameter (D_p) and embedment depth (L_p) on ζ_f. Although various numerical studies have been carried out to estimate representative values of ζ_f, very few have assessed how site-specific conditions or the selected monopile dimensions impact ζ_f. Furthermore, since each soil constitutive model has limitations in its ability to capture specific aspects of cyclic soil behaviour, this study employed two different models to evaluate the sensitivity of foundation damping to the chosen soil model and to assess the potential range of variation in ζ_f between them. By comparing ζ_f values obtained from both models, this approach provides a realistic range within which actual foundation damping values are likely to fall for large-scale OWTs in the field. Additionally, the use of two distinct models helps to validate the findings and reinforces the consistency of the trends observed in the analysis results.

The logarithmic decrement method was used to calculate the global foundation damping ratios (ζ_f) through conducting dynamic free-decay simulations and analysing the attenuation of the lateral displacement of the OWT at the RNA level. From the lateral displacement time history of the RNA,

the logarithmic decrement (δ) was computed using Equation 2.14, which was then substituted into Equation 2.15 to determine ζ_f. For clarity, Equations 2.14 and 2.15 are re-presented below:

$$\delta = \frac{1}{n} \cdot ln\left(\frac{A_0}{A_n}\right) \tag{6.3}$$

$$\zeta_f = \frac{1}{\sqrt{1+\left(\frac{2\pi}{\delta}\right)^2}} \tag{6.4}$$

where, as stated previously in Chapter 2, A_0 and A_n are two successive amplitudes of the lateral displacement of the RNA, and n is the number of cycles between them (see Figure 6.6).

Before conducting the dynamic free-decay simulations in the 3D FE models, static analyses were first performed by applying a monotonic lateral load at the RNA level to displace the entire OWT support structure. Once a certain lateral displacement was achieved at the RNA level, the applied load was removed, and the structure was allowed to vibrate freely. This was accomplished by changing the analysis type in Plaxis 3D from *Plastic*, which was used during the loading phase, to *Dynamics* for the subsequent free vibration stage. For the numerical implementation of dynamic analyses, the Plaxis 3D software adopts the Newmark implicit time integration scheme which generally provides a reliable calculation procedure and a stable solution when using appropriate α and β Newmark coefficients. The Newmark coefficients were kept as the standard values ($\alpha = 0.25$ and $\beta = 0.5$) as recommended by PLAXIS 3D Manual (2023c). The numerical control parameters for all the dynamic analyses conducted in this research are shown in Figure 6.5. The selected solver type was Pardiso since it provides the most robust way to solve equations as stated by PLAXIS 3D Manual (2023b) and was the recommended solver by Panagoulias et al. (2018). The remaining control parameters were chosen based on preliminary sensitivity analyses to balance computational efficiency with numerical accuracy.

Numerical control parameters	
Solver type	Pardiso (multicore direct)
Max cores to use	256
Max number of steps store	1
Use compression for result	☐
Use default iter parameters	☐
Max steps	10000
Time step determination	Semi-automatic
Number of sub steps	Automatic
Tolerated error	0.01000
Max unloading steps	50
Max load fraction per step	0.5000
Over-relaxation factor	1.200
Max number of iterations	90
Desired min number of itera	4
Desired max number of iter	30
Use subspace accelerator	☐
Subspace size	3
Use line search	☐
Use gradual error reduction	☐

Figure 6.5: Numerical control parameters

A representative time history of the lateral displacement of the tower at the RNA level during free vibration is shown in Figure 6.6. This result corresponds to the MP10-30 monopile, analysed for the soil relative density (D_r) of 30% using the SANISAND-MS constitutive model. Based on this simulation, the foundation damping ratio (ζ_f) was calculated as 1.083%, using Equation 6.3 to determine the logarithmic decrement (δ), followed by Equation 6.4 to compute ζ_f. In this study, the damping ratios (ζ_f) for all monopile models and displacement magnitudes at the mudline were computed following the same approach applied to the case shown in Figure 6.6. The amplitude A_0 was taken as the second peak of the lateral displacement response at the RNA level, while A_n corresponded to the peak after n cycles, with n = 5 adopted throughout the analyses.

Although the logarithmic decrement method is primarily intended for estimating damping in linear systems with viscous damping characteristics, it has also been widely applied to evaluate damping in nonlinear systems, such as those that arise due to soil-structure interaction. As discussed in the literature in Chapter 2, the logarithmic decrement method has been extensively used in field monitoring studies to estimate ζ_f for OWTs during rotor stop tests or emergency shutdowns. Furthermore, the approach has been also used in numerical modelling studies (e.g., Kementzetzidis et al., 2019; Malekjafarian et al., 2019; Carswell et al., 2022; Panagoulias et al., 2023) to compute representative values of ζ_f for monopile-supported OWTs modelled using different soil-structure interaction methods. Given that OWTs are highly underdamped systems, the variation in deformation amplitudes at the mudline level is relatively small. Therefore, for a given free vibration time history, the calculated value of ζ_f using the logarithmic decrement method can adequately represent the attenuation of the OWT structural response. Although alternative methods such as the half-power bandwidth technique exist, they are generally unsuitable for highly underdamped systems like OWTs, as they require high frequency resolution, and the narrow spectral peaks make accurate estimation of ζ_f from the frequency response function unreliable.

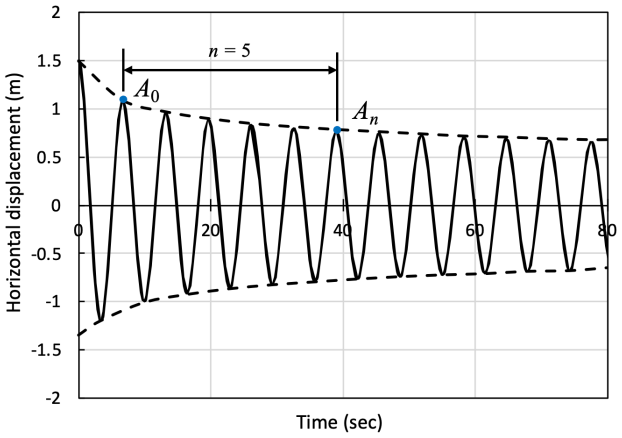


Figure 6.6: Lateral displacement of the tower at the RNA level

Since the dissipated plastic energy in the soil domain is governed by foundation deformation, the values of ζ_f were calculated with respect to the amplitudes of the lateral displacement of the

monopile at the mudline (y_g). The evaluation of ζ_f as a function of foundation displacement has been also addressed in previous numerical modelling studies. For example, Panagoulias et al. (2023) performed 3D FE analyses to investigate the relationship between ζ_f and y_g, using the HSsmall model to capture soil behaviour. Ryan et al. (2025), on the other hand, studied the same relationship using 1D FE analyses, incorporating distributed soil reactions along the foundation depth to represent soil hysteresis. Both studies found that ζ_f increases with increasing foundation deformation. The time history of lateral displacement at the mudline (y_g), corresponding to the RNA displacement shown in Figure 6.6, is presented in Figure 6.7. In this study, the amplitudes of y_g were calculated over the same duration of n = 5 cycles used for the computation of ζ_f. These amplitudes were obtained by separately averaging the positive and negative peaks of the displacement signal (e.g., the one shown in Figure 6.7), taking the difference between the two averages, and dividing the result by two. The values of ζ_f determined in this research are plotted against the amplitudes of y_g normalised by the monopile diameter (D_p). This normalisation enables comparison of the response across monopiles with different diameters.

To evaluate the evolution of ζ_f with different normalised mudline displacements (y_g/D_p), multiple free vibration simulations were conducted by first applying monotonic lateral loads to achieve varying displacements at the RNA level during the static loading stage preceding the onset of free vibration. For each model, four values of ζ_f were computed from simulations initiated with RNA-level lateral displacements of 0.5 m, 1.0 m, 1.5 m, and 2.0 m. The corresponding free vibration responses for these displacement levels, obtained for the MP10-30 monopile using the SANISAND-MS constitutive model to represent soil behaviour at D_r = 30%, are presented in Figure 6.8. The RNA-level lateral displacements were selected such that the resulting mudline-level displacement of the foundation (y_g) fell within the range required to satisfy the fatigue and serviceability limit states.

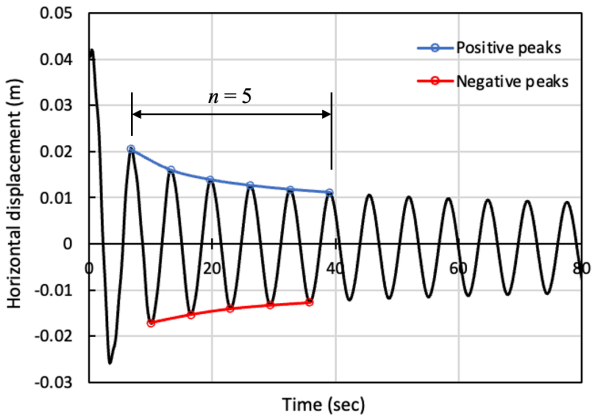


Figure 6.7: Time history of the lateral displacement of the foundation at the mudline level

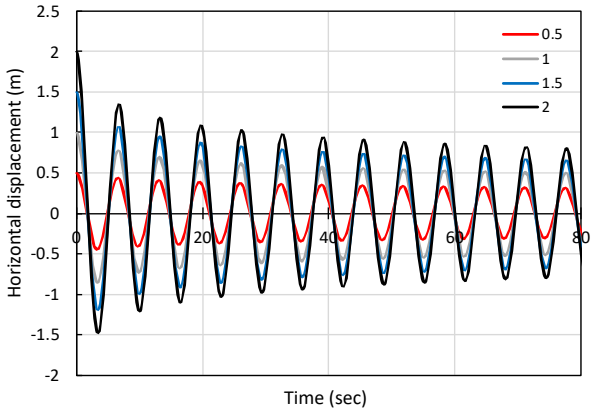


Figure 6.8: Free vibration simulations of the tower at RNA level

6.4.1 HSsmall simulations

This section presents the HSsmall simulations for the effects of monopile geometry in terms of embedment depth and monopile diameter on ζ_f. Comparisons are also made between the simulation results of 30% and 60% relative densities to examine the influence of relative density on ζ_f.

6.4.1.1 Effect of embedment depth (L_p)

Increasing the monopile embedment depth alters the deformation behaviour below the mudline, affecting the strain distribution within the soil domain and, consequently, changing the global foundation damping ratio (ζ_f). The impact of embedment depth on ζ_f was examined for monopile diameters of 10 m and 12 m, considering soil relative densities of 30% and 60%. For the soil profile with D_r = 30%, Figure 6.9a compares the variation of ζ_f with y_g/D_p for monopiles MP10-30, MP10-40, and MP10-50, while Figure 6.9b presents the same comparison for monopiles MP12-30, MP12-36, MP12-48, and MP12-60. Similarly, Figure 6.10a and Figure 6.10b present the corresponding comparisons for the same monopile dimensions as in Figure 6.9a and Figure 6.9b, respectively, but for the soil profile with D_r = 60%.

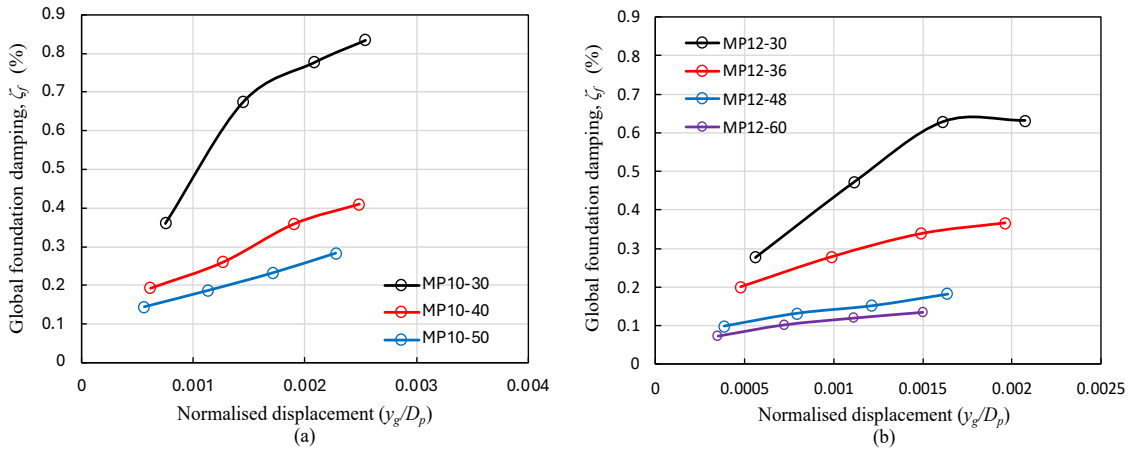


Figure 6.9: Effect of embedment depth on ζ_f for soil profile with D_r = 30%: (a) D_p = 10 m; (b) D_p = 12 m

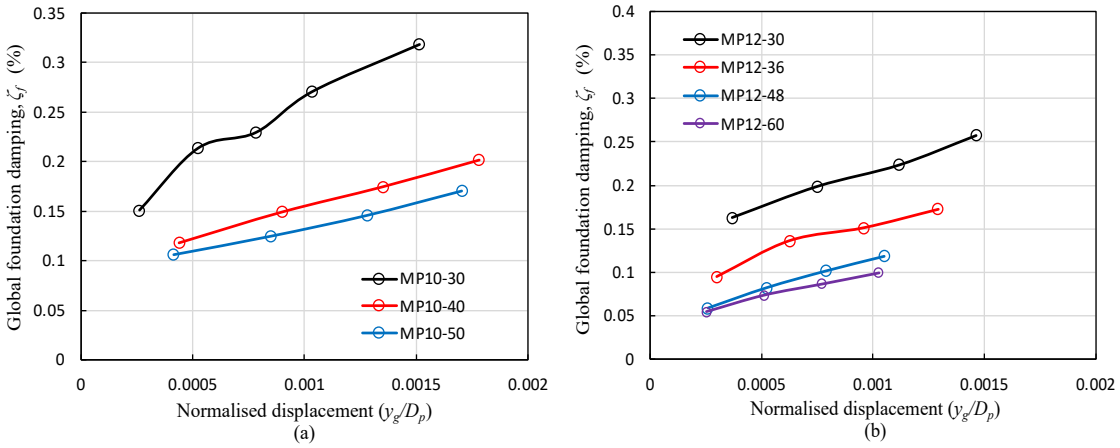


Figure 6.10: Effect of embedment depth on ζ_f for soil profile with D_r = 60%: (a) D_p = 10 m; (b) D_p = 12 m

According to Figure 6.9 and Figure 6.10, ζ_f decreases as L_p increases. However, the rate of decrease in ζ_f gradually diminishes as L_p becomes larger, suggesting that beyond a certain embedment depth, further increases in L_p may have little to no impact on ζ_f. This observation is consistent with the findings of Vo (2022), whose 3D FE simulations revealed that once the monopile depth exceeds the critical embedment depth (defined as the depth at which pile head displacement no longer changes with further increases in embedment), there is no influence of the embedment depth (L_p) on ζ_f.

6.4.1.2 Effect of monopile diameter (D_p)

Given that L_p has a significant impact on foundation damping, the effect of monopile diameter (D_p) on ζ_f should also be investigated. This effect is examined by comparing ζ_f values for two monopiles with the same L_p but different diameters. Figure 6.11a compares the ζ_f values for monopiles MP10-30 and MP12-30, based on analyses conducted for the soil profile with D_r = 30%. Based on the comparison in Figure 6.11a, the analysis results show that for a given normalised mudline displacement (y_g/D_p), ζ_f reduces as D_p increases. Although not strictly necessary, the same comparison is presented in Figure 6.11b for the soil at D_r = 60%, demonstrating that the same finding applies for higher relative densities.

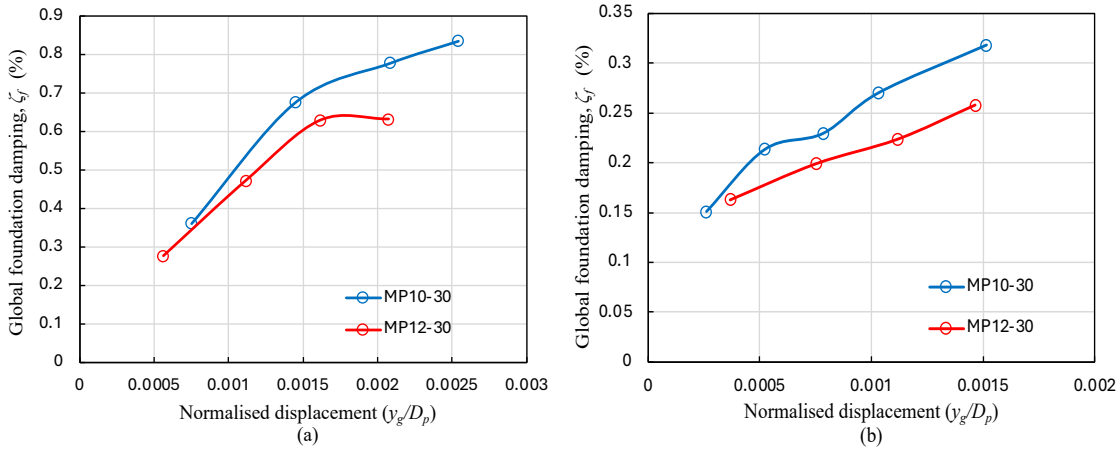


Figure 6.11: Effect of D_p on ζ_f: (a) D_r = 30%; (b) D_r = 60%

6.4.1.3 Effect of relative density (D_r)

Along with foundation dimensions, which have been shown to significantly impact the global foundation damping ratio (ζ_f), it is also important to examine the influence of the relative density (D_r) of the supporting soil on ζ_f. Although studies such as Kementzetzidis et al. (2019) investigated the variation of ζ_f using dynamic free-decay simulations at three relative densities (40%, 60%, and 80%), the resulting values were calculated and compared at different amplitudes of lateral displacement at the mudline (y_g), leading to an inconsistent comparison. As with the analyses conducted for the effects of monopile diameter and embedment depth, the comparisons in this section are also carried out by evaluating the evolution of ζ_f with normalised mudline displacement (y_g/D_p) for the two relative density cases (30% and 60%). Relative density influences the deformation of the monopile below the mudline and, consequently, the hysteresis loops of the surrounding soil, which in turn affects the total plastic energy dissipated within the soil domain.

Figure 6.12a and Figure 6.12b show plots of ζ_f versus y_g/D_p based on the analyses conducted for the two relative densities, for monopiles MP10-30 and MP10-50, respectively. Similarly, Figure 6.13a and Figure 6.13b present the same comparison for monopiles MP12-36 and MP12-60, respectively.

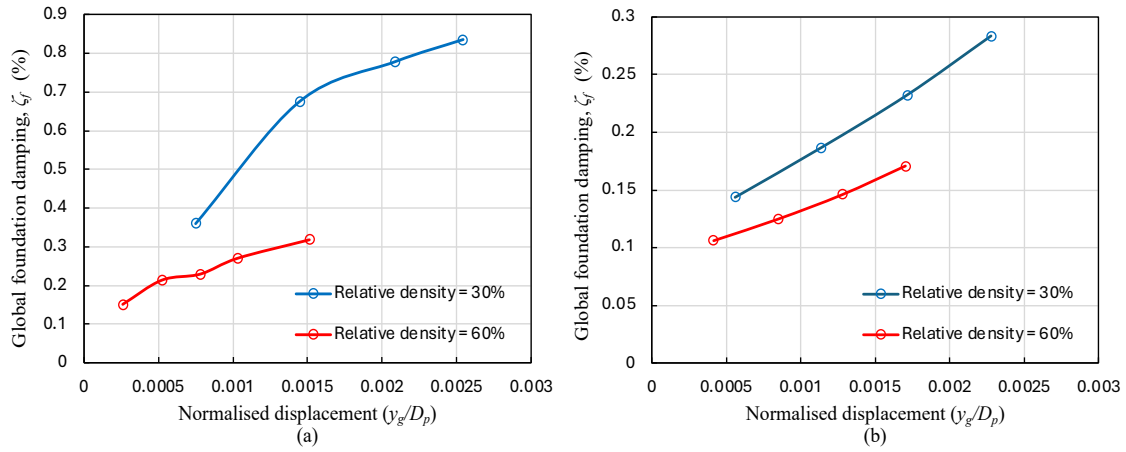


Figure 6.12: Effect of D_r on ζ_f: (a) MP10-30; (b) MP10-50

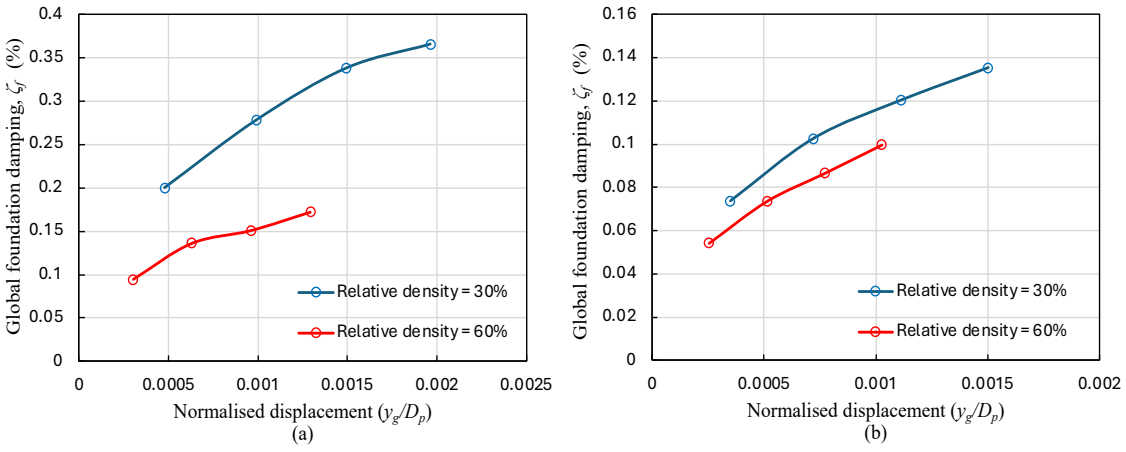


Figure 6.13: Effect of D_r on ζ_f: (a) MP12-36; (b) MP12-60

The main conclusion that can be drawn from Figure 6.12 and Figure 6.13 is that the global foundation damping ratio (ζ_f) decreases with increasing soil relative density at a given y_g/D_p. This finding is significant, as it implies that when performing integrated analyses for a full OWT system, variations in ζ_f due to differences in soil relative density (D_r) at the installation site must be taken into account.

Based on the results of the HSsmall simulations examining the effects of monopile embedment depth (L_p), diameter (D_p), and relative density (D_r), the following conclusions are derived:

i. The global foundation damping ratio (ζ_f) decreases with increasing embedment depth (L_p). However, this reduction becomes negligible once L_p exceeds a certain threshold, beyond which further increases in embedment have little to no effect on ζ_f. Vo (2022) found that this threshold corresponds to the critical pile embedment depth, defined as the depth beyond which additional embedment no longer influences the displacement response at the pile head.
ii. For the same L_p, ζ_f decreases as the monopile diameter becomes larger.
iii. For the same monopile dimensions, ζ_f decreases as the relative density of the soil increases.

These findings from the free-decay simulations can be attributed to variations in the numerator and denominator terms of Equation 2.13, which are governed by the geometry of the foundation and the mechanical properties of the surrounding soil continuum. Equation 2.13 is restated below:

$$\zeta_f = \frac{1}{4\pi} \frac{W_{D,soil}}{W_{S,(soil+foundation+tower)}} \tag{6.5}$$

where $W_{D,soil}$ is the total dissipated plastic energy in the soil domain, and $W_{S,(soil+foundation+tower)}$ is the total stored elastic energy in the overall soil-OWT system. Although the original form of Equation 2.13 includes the letter i, which denotes the mode of vibration, it has been omitted in Equation 6.5 since the ζ_f results presented in this chapter refer only to the fundamental (first) mode of vibration. While the free-decay simulations are useful for estimating ζ_f, they do not provide detailed insight into why ζ_f varies with changes in soil relative density and monopile geometry. To gain a more complete understanding of the underlying mechanisms, cyclic push-over simulations were conducted to evaluate local hysteretic foundation damping ratios (ξ_y and ξ_θ). In this study, these damping ratios were determined at the mudline level, which is useful for modelling soil-structure interaction using the macro-element approach, and also distributed along the monopile depth, which is relevant for the Winkler-based distributed soil reaction method. Although increases in ξ_y and ξ_θ would typically suggest an increase in ζ_f, this is not always the case. Changes in foundation geometry and soil properties that enhance local damping may also increase the total stored elastic energy $W_{S,(soil+foundation+tower)}$. As a result, the overall ratio in Equation 6.5 may decrease, leading to a lower calculated value of ζ_f despite increases in local hysteresis.

The findings presented in this section indicate that the global foundation damping ratio (ζ_f) decreases as foundation stiffness increases, whether due to larger monopile dimensions or higher

soil relative density (i.e., stiffer soil). This inverse relationship between foundation stiffness and ζ_f can be attributed to the corresponding increase in $W_{S,(soil+foundation+tower)}$, as the foundation stiffness increases. For a given lateral deformation at the mudline, a stiffer foundation system results in greater stored elastic energy because a larger displacement of the support structure is required to achieve the same mudline deformation.

6.4.2 SANISAND-MS simulations

The simulations conducted using the HSsmall model were also performed with the SANISAND-MS model to assess whether the same conclusions hold with a different constitutive model and to compare the values of ζ_f obtained from the two models. The procedure for estimating ζ_f is consistent with that used with the simulations conducted with the HSsmall model.

6.4.2.1 Effect of embedment depth (L_p)

The effect of L_p is examined for monopiles with diameters of 10 m and 12 m, installed in ground conditions with relative densities of 30% and 60%. For the soil profile with D_r = 30%, ζ_f values for different embedment depths are compared in Figure 6.14a and Figure 6.14b for monopiles with diameters of 10 m and 12 m, respectively. Similar comparisons for D_r = 60% are presented in Figure 6.15.

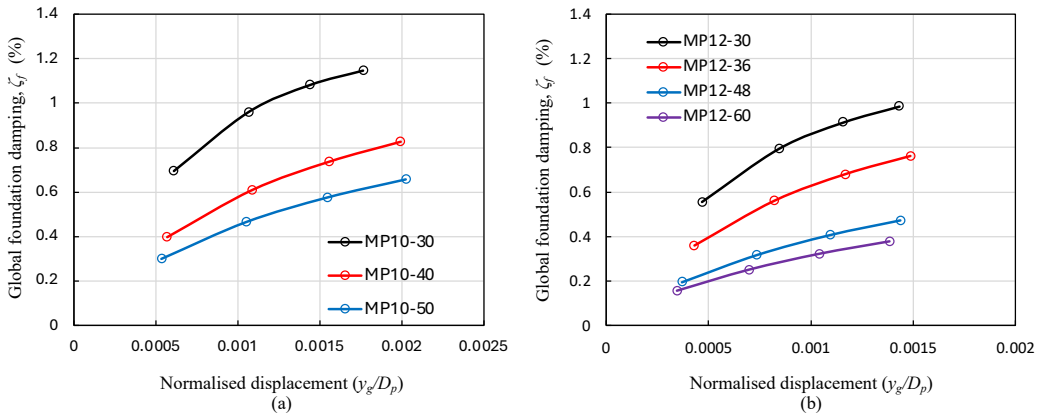


Figure 6.14: Effect of embedment depth on ζ_f for soil profile with D_r = 30%: (a) D_p = 10 m; (b) D_p = 12 m

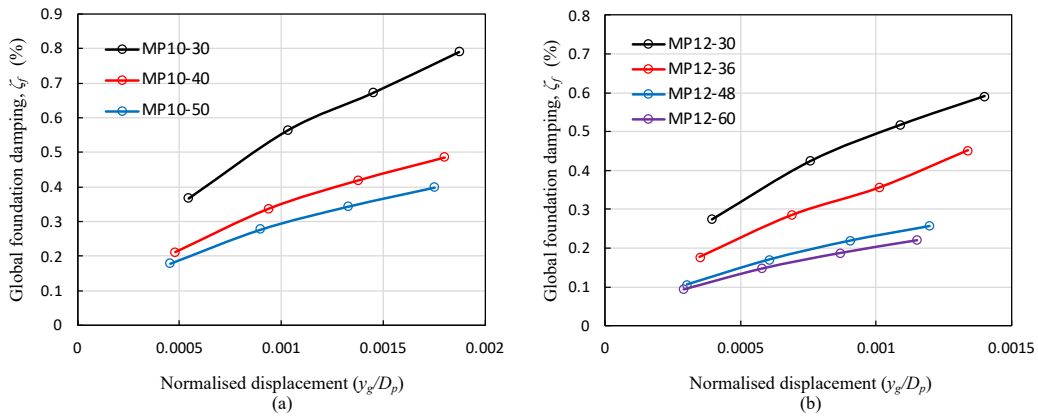


Figure 6.15: Effect of embedment depth on ζ_f for soil profile with D_r = 60%: (a) D_p = 10 m; (b) D_p = 12 m

According to Figure 6.14 and Figure 6.15, the results obtained using the SANISAND-MS model lead to the same conclusions as those derived from the simulations performed with the HSsmall model regarding the decreasing trend of the foundation damping ratio (ζ_f) with increasing monopile embedment depth (L_p). Additionally, the results from the SANISAND-MS model simulations confirm the same finding as those from the HSsmall model simulations: beyond a certain embedment depth (L_p), the foundation damping ratio (ζ_f) no longer varies significantly as the monopile is embedded deeper into the ground.

6.4.2.2 Effect of monopile diameter (D_p)

Similar to the comparisons performed for the HSsmall analyses regarding the effect of D_p, the foundation damping ratio (ζ_f) versus normalised displacement (y_g/D_p), obtained from free-decay simulations using the SANISAND-MS model, is evaluated for monopiles MP10-30 and MP12-30, which have an embedment depth (L_p) of 30 m and diameters of 10 m and 12 m, respectively. Figure 6.16a shows the analysis results for the case of the soil profile with D_r = 30%, while Figure 6.16b presents the results for the analyses conducted for the monopiles installed in the soil profile with D_r = 60%. The results from the simulations conducted with the two relative densities show that for a given normalised displacement (y_g/D_p), the foundation damping ratio (ζ_f) decreases as D_p increases for the same L_p.

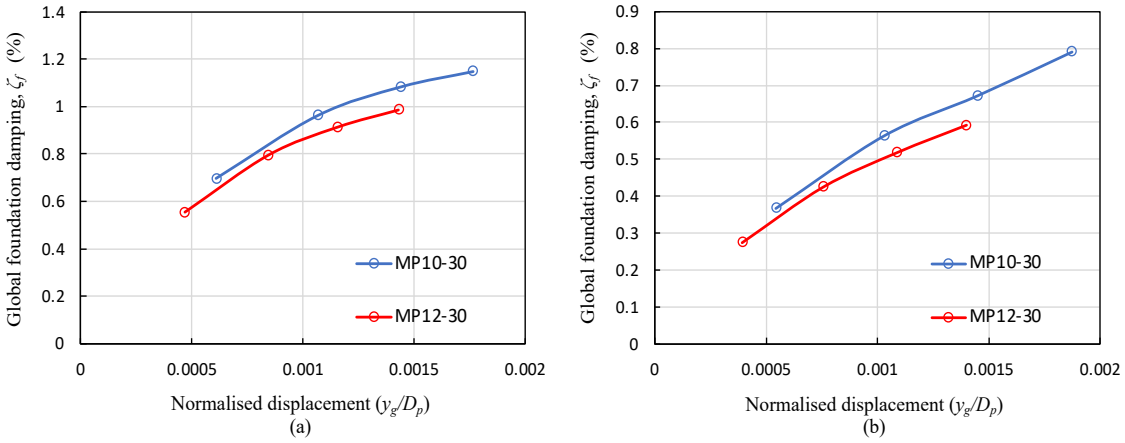


Figure 6.16: Effect of D_p on ζ_f: (a) D_r = 30%; (b) D_r = 60%

6.4.2.3 Effect of relative density (D_r)

To confirm the findings from the HSsmall model simulations regarding the effect of relative density (D_r) on ζ_f, free-decay analysis results using the SANISAND-MS model are compared in terms of foundation damping ratio (ζ_f) versus normalised displacement (y_g/D_p) for monopiles of the same dimensions embedded in soil profiles with D_r values of 30% and 60%. For monopiles with a diameter (D_p) of 10 m, Figure 6.17a and Figure 6.17b illustrate the influence of D_r by comparing ζ_f versus y_g/D_p for MP10-30 and MP10-50, respectively. Similarly, Figure 6.18a and Figure 6.18b show the effect of D_r for monopiles MP12-36 and MP12-60, which both have a diameter of 12 m. Based on the simulation results in Figure 6.17 and Figure 6.18, the foundation damping ratio (ζ_f)

reduces as D_r increases for monopiles with the same dimensions. It is important to conclude here that the trends observed for the effects of monopile dimensions and relative density on ζ_f based on the SANISAND-MS simulations align very well with those obtained from the HSsmall simulations. Although the ζ_f values may differ significantly between the two models, the consistency in trends supports the reliability of how ζ_f is expected to vary in the field based on ground conditions and the selected monopile dimensions.

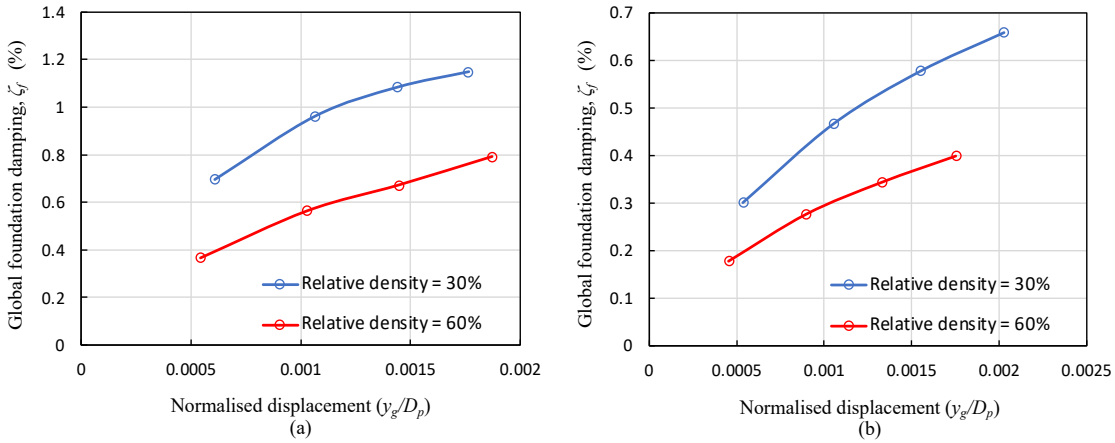


Figure 6.17: Effect of D_r on ζ_f: (a) MP10-30; (b) MP10-50

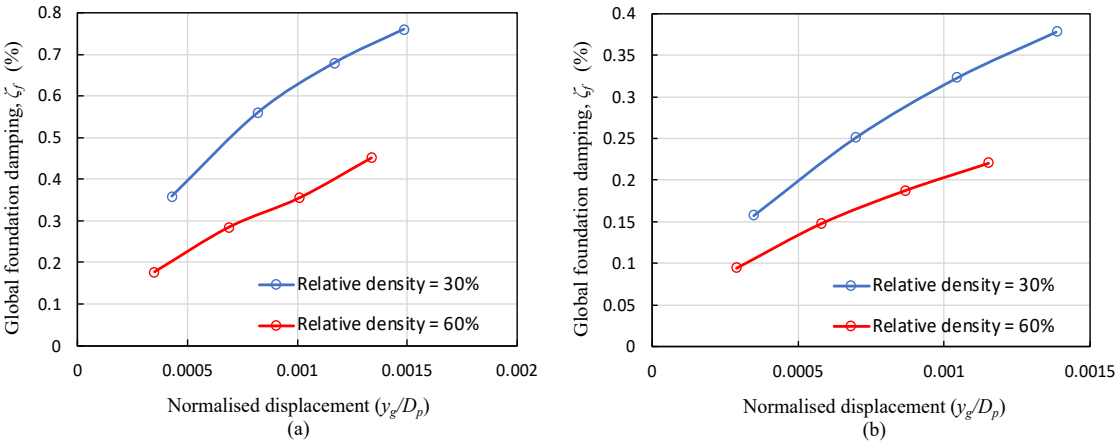


Figure 6.18: Effect of D_r on ζ_f: (a) MP12-36; (b) MP12-60

6.4.3 Comparison between HSsmall and SANISAND-MS results

Comparing the global foundation damping ratios (ζ_f) obtained from simulations using the HSsmall and SANISAND-MS models is important, as it allows for investigating whether the ζ_f values are similar or significantly different. Since both models were applied to the same 15 MW OWT with identical dimensions and structural properties, any variation in ζ_f can be attributed to differences in the simulated soil hysteresis around the monopile. Although examining the hysteretic stress-strain loops in the soil would provide deeper insight into the reasons behind differences in ζ_f, this analysis is beyond the scope of the thesis. Instead, the focus will be on comparing ζ_f as a function of y_g/D_p for the HSsmall and SANISAND-MS results. For the loose soil profile with D_r = 30%, Figure 6.19

and Figure 6.20 show ζ_f versus y_g/D_p based on the simulations performed for the monopile diameters of 10 m and 12 m, respectively. The dashed lines represent the simulation results obtained using the SANISAND-MS model, while the solid lines correspond to ζ_f versus y_g/D_p based on the dynamic free-decay analyses conducted with the HSsmall constitutive model. Figure 6.21 and Figure 6.22 show the same comparisons as Figure 6.19 and Figure 6.20, but for the case of the medium-dense soil profile with D_r = 60%.

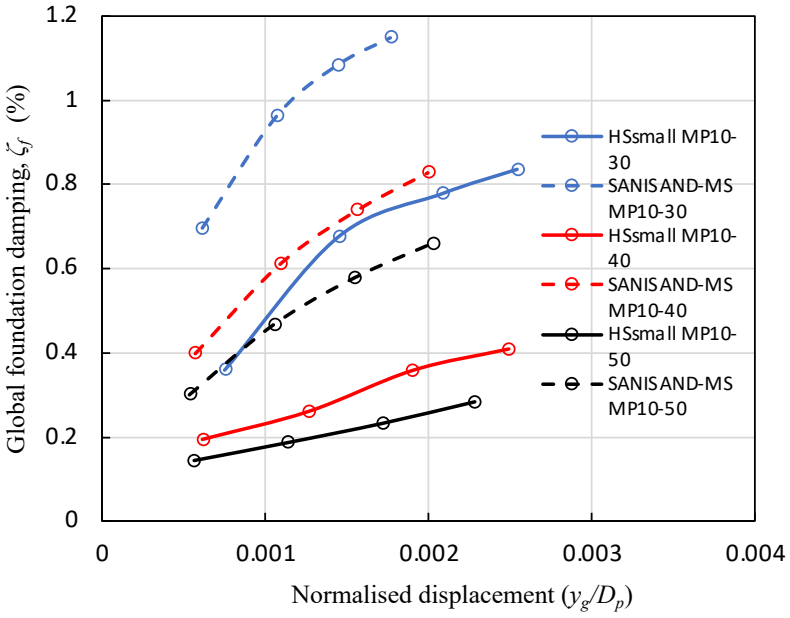


Figure 6.19: Comparison of ζ_f versus y_g/D_p using HSsmall and SANISAND-MS models (D_r=30% and D_p=10m)

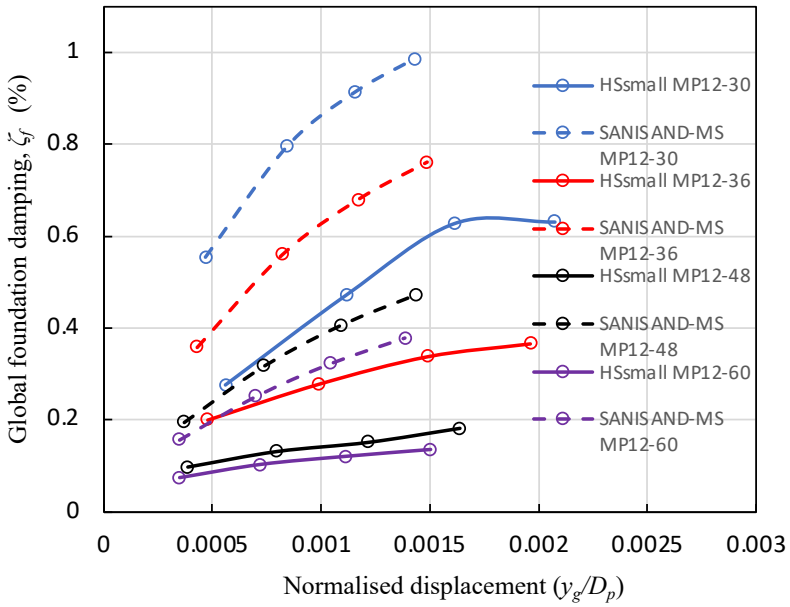


Figure 6.20: Comparison of ζ_f versus y_g/D_p using HSsmall and SANISAND-MS models (D_r=30% and D_p=12m)

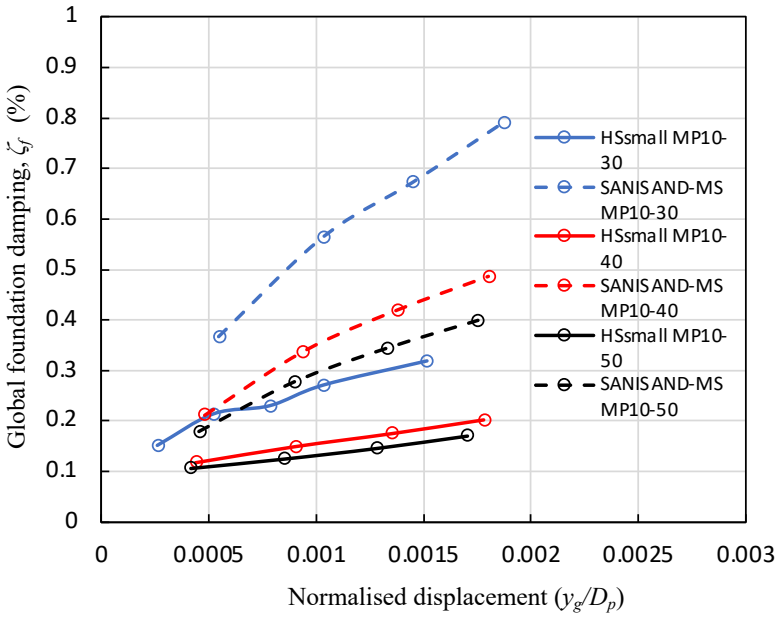


Figure 6.21: Comparison of ζ_f versus y_g/D_p using HSsmall and SANISAND-MS models (D_r=60% and D_p=10m)

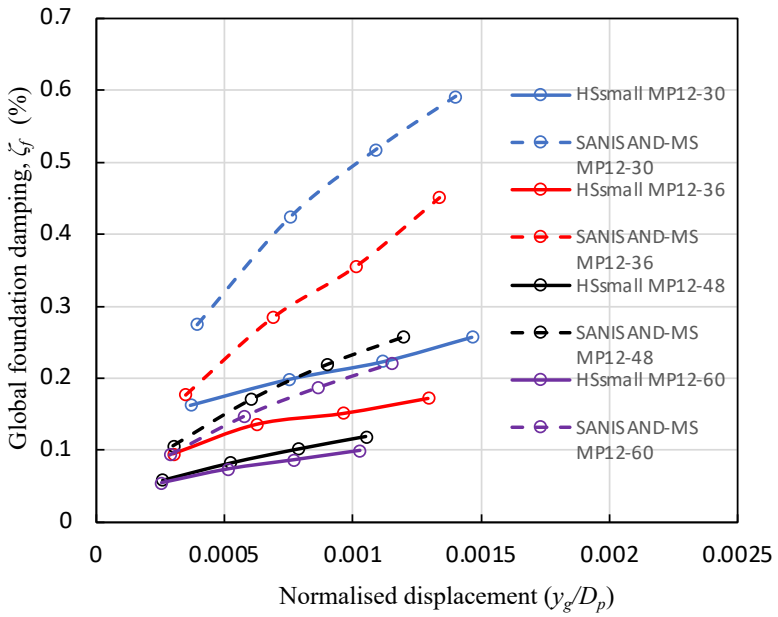


Figure 6.22: Comparison of ζ_f versus y_g/D_p using HSsmall and SANISAND-MS models (D_r=60% and D_p=12m)

According to the analysis results in Figure 6.19 to Figure 6.22, the values of ζ_f determined using the SANISAND-MS model are higher than those obtained using the HSsmall model. However, it is challenging to identify a definitive reason for this difference based solely on the dynamic free-decay simulations. In general, soil constitutive models have inherent limitations in capturing the full range of dynamic soil behaviour. A model may perform well in simulating certain aspects of soil response, yet fall short in others. For instance, one model may accurately capture cyclic accumulation of deformation (i.e., ratcheting), while another may be more effective in simulating the build-up of

excess pore water pressure during undrained dynamic loading. For this reason, two models were employed in this study to account for their respective limitations and to provide a range of ζ_f values rather than a single estimate. As a result, for a given normalised mudline displacement (y_g/D_p), the actual value of ζ_f for an OWT in the field may lie between the values of ζ_f determined from the simulations conducted using the HSsmall and SANISAND-MS models. Based on the results presented, ζ_f values obtained using the SANISAND-MS model can be considered an upper bound, while those computed with the HSsmall model may be regarded as a lower bound. Obtaining a bounded range of ζ_f values, while acknowledging that each model has limitations in fully capturing all aspects of dynamic soil behaviour, can be considered an important contribution and a key novelty of this research.

6.5 Cyclic push-over simulations

Cyclic push-over simulations were conducted to determine the local hysteretic foundation damping ratios based on cyclic load-deformation hysteresis loops. These hysteretic foundation damping ratios are useful since they can be converted into viscous dashpots and applied in integrated OWT simulation tools to account for the influence of foundation damping on the distribution of internal forces within the OWT support structure. The damping ratios were calculated from load-deformation loops at the mudline level, which is useful when considering soil-structure interaction using the macro-element approach, and they were also computed along the depth of the monopile based on the cyclic soil reaction loops, which is beneficial when representing soil-structure interaction using the distributed Winkler approach. The hysteretic foundation damping ratio is divided into a lateral foundation damping ratio (ξ_y) and a rotational foundation damping ratio (ξ_θ). At the mudline level, ξ_y and ξ_θ are calculated from the horizontal force-deformation and moment rotation hysteresis loops, respectively. Along the depth of the monopile, ξ_y and ξ_θ are derived from the p-y loops (distributed lateral load versus lateral displacement) and the m-θ loops (distributed moment versus rotation), respectively. It is important to highlight that the cyclic push-over simulations were conducted under static conditions, ensuring that no inertial effects were included. Similar to the logarithmic decrement analyses, the cyclic push-over analyses were performed using the HSsmall and SANISAND-MS models to investigate whether the same findings could be observed from both models. Furthermore, 1D FE analyses were performed by converting the hysteretic foundation damping ratios at the mudline into viscous dashpots, in order to determine the global foundation damping ratios (ζ_f) and compare them with those obtained from the original 3D FE free-decay simulations. This comparison allows for checking whether the derived hysteretic foundation damping ratios can incorporate the effect of foundation damping on the global behaviour of large-sized OWTs.

The cyclic push-over simulations were carried out by applying a lateral load at the RNA level, followed by unloading and reloading (as shown in Figure 6.23), in order to generate load-

deformation hysteresis loops in the foundation. Different symmetrical loads at the RNA were applied to evaluate the variation of the hysteretic foundation damping ratios with the deformation level of the foundation. Since the cyclic push-over analyses were conducted without considering inertial effects, static analyses were performed using the *Plastic* calculation type in Plaxis 3D. Appropriate numerical control parameters (as shown in Figure 6.24) were selected for the simulations to ensure high accuracy and computational robustness, following the guidelines provided in the MoDeTo Plaxis manual by Panagoulias et al. (2018).

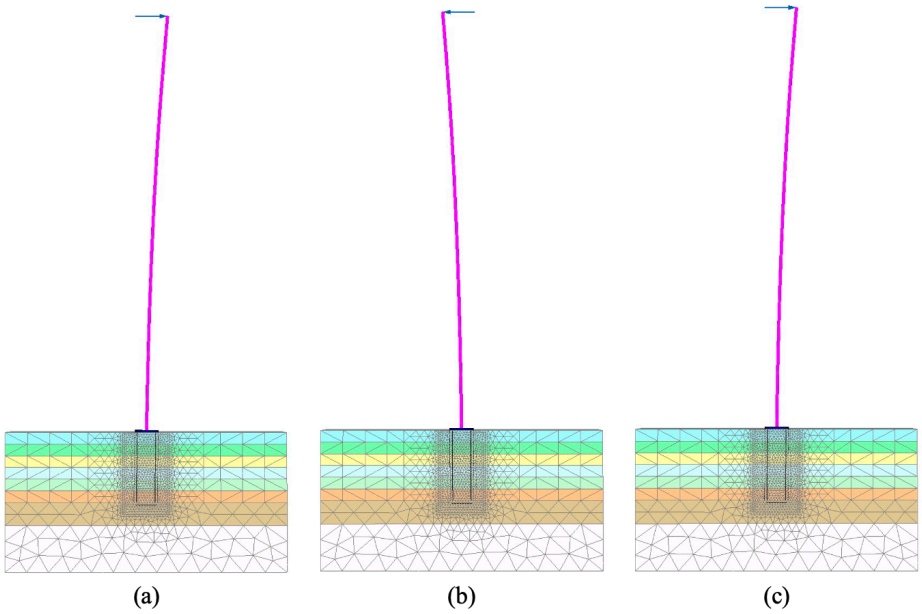


Figure 6.23: Cyclic push-over simulations: (a) Loading; (b) Unloading; (c) Reloading

Numerical control parameters	
Solver type	Pardiso (multicore direct
Max cores to use	256
Max number of steps store	1000
Use compression for result	☐
Use default iter parameters	☐
Max steps	10000
Tolerated error	0.01000
Max unloading steps	10000
Max load fraction per step	0.02500
Over-relaxation factor	1.200
Max number of iterations	90
Desired min number of itera	4
Desired max number of iter	30
Arc-length control type	On
Use subspace accelerator	☐
Subspace size	3
Use line search	☐
Use gradual error reduction	☐

Figure 6.24: Numerical control parameters for the cyclic push-over analyses

6.5.1 Mudline hysteretic foundation damping ratios

The hysteretic foundation damping ratios at the mudline were determined from the lateral force-displacement and moment-rotation loops. The damping ratios (ξ_y and ξ_θ) were obtained from simulations using both the HSsmall and SANISAND-MS models, providing a range of values within which the actual damping ratio for an OWT in the field is expected to fall. Similar to the logarithmic decrement analyses, the analyses conducted here sought to evaluate the effects of the monopile dimensions and soil relative density on ξ_y and ξ_θ. Furthermore, some limited analyses were carried out using only the HSsmall model to evaluate the effect of load eccentricity on the hysteretic foundation damping ratios. The local hysteretic foundation damping ratios (ξ_y and ξ_θ) at the mudline level influence the global foundation damping ratio (ζ_f) of the entire OWT system, including the soil, foundation, and the part of the support structure above the mudline. Higher values of ξ_y and ξ_θ, resulting from variations in monopile dimensions and relative densities, generally lead to a higher ζ_f. However, as will be shown later, it is possible for higher values of ξ_y and ξ_θ to result in a lower ζ_f. This occurs because the hysteretic foundation damping ratios at the mudline do not account for the elastic energy stored in the support structure above the mudline, which can increase and, in turn, reduce ζ_f despite the higher ξ_y and ξ_θ values. For an idealised hysteresis loop (shown in Figure 6.25), the hysteretic foundation damping ratios (ξ_y and ξ_θ) are calculated as follows:

$$\xi_f = \frac{1}{4\pi}\frac{W_{D,soil}}{W_{S,(soil+foundation)}} \tag{6.6}$$

where $W_{D,soil}$ is the dissipated energy in the soil continuum and is equal to the area of the enclosed hysteresis loop, while $W_{S,(soil+foundation)}$ is the stored energy of the soil-foundation system and is equal to the area of the grey triangle in Figure 6.25. Comparisons in this section regarding the effects of monopile dimensions and relative densities are made by plotting ξ_y and ξ_θ versus the amplitudes of the normalised lateral displacement (y_g/D_p) and rotation (θ_g), respectively. The amplitudes for a hysteresis loop is determined by taking the difference between the maximum and minimum deformations and dividing it by two.

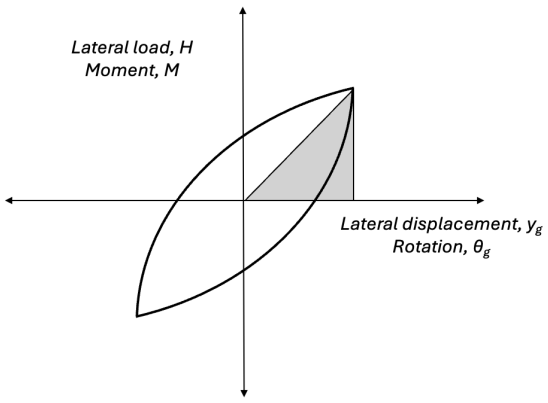


Figure 6.25: Representative load-deformation hysteresis loop at the mudline

For each load level, five cycles of unloading and reloading were conducted, and the fifth hysteresis loop was used to calculate the values of ξ_y and ξ_θ. Although the values of ξ_y and ξ_θ may vary with the number of cycles, this variation is not considered in this thesis. The aim is simply to provide representative hysteretic foundation damping ratios for short-term cyclic loading.

6.5.1.1 HSsmall simulations

This section presents the cyclic push-over analyses conducted with the HSsmall model for the monopile dimensions listed in Table 6.1, considering soil profiles with relative densities of 30% and 60%. In addition to investigating the effects of monopile dimensions and relative densities, the elevation of the lateral load along the tower height is varied to study the effect of load eccentricity on ξ_y and ξ_θ.

Effect of embedment depth (L_p)

Given that the logarithmic decrement analyses showed that L_p significantly influences the global foundation damping ratio (ζ_f), it is crucial to investigate its effect on the local hysteretic damping ratios (ξ_y and ξ_θ) at the mudline level. As mentioned previously, the results in this section are presented in terms of ξ_y and ξ_θ values plotted against the amplitudes of the normalised lateral displacement (y_g/D_p) and rotation (θ_g), respectively. For the soil profile with D_r = 30%, Figure 6.26 shows the effect of embedment by comparing the hysteretic foundation damping ratios for the monopiles with a 10 m diameter and varying embedment depths, while Figure 6.27 presents the same comparison for the monopiles with a 12 m diameter. Similarly, Figure 6.28 and Figure 6.29 compare the hysteretic foundation damping ratios for the same monopiles as in Figure 6.26 and Figure 6.27, respectively, but for analyses considering the soil profile with D_r = 60%.

The results in Figure 6.26 to Figure 6.29 show that, for a given deformation at the mudline level, ξ_y and ξ_θ reduce as the monopile embedment depth (L_p) increases. However, Figure 6.27 and Figure 6.29 clearly indicate that this decrease becomes progressively less significant at greater depths, suggesting that additional embedment beyond a certain point yields minimal changes in ξ_y and ξ_θ.

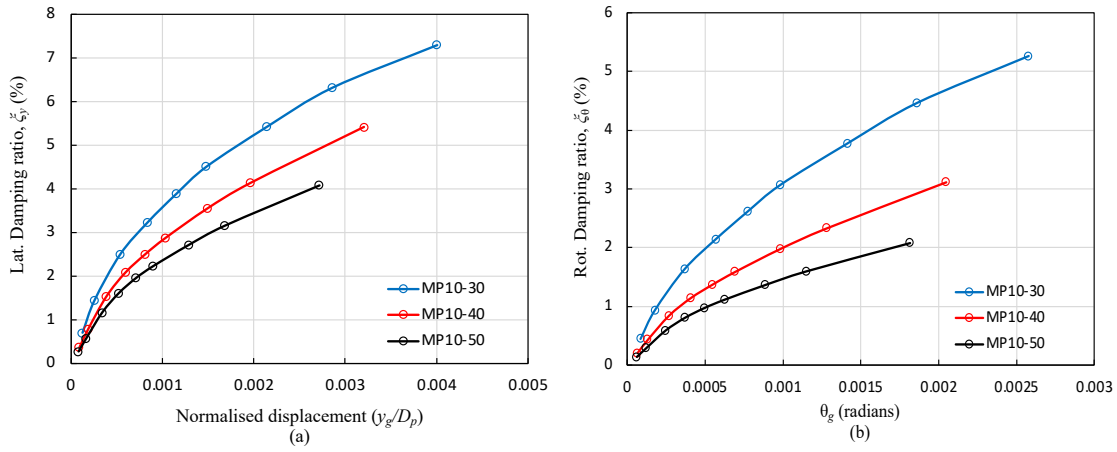


Figure 6.26: Effect of L_p on (a) ξ_y versus y_g/D_p, and (b) ξ_θ versus θ_g, for the monopiles with D_p =10 m and soil D_r = 30%

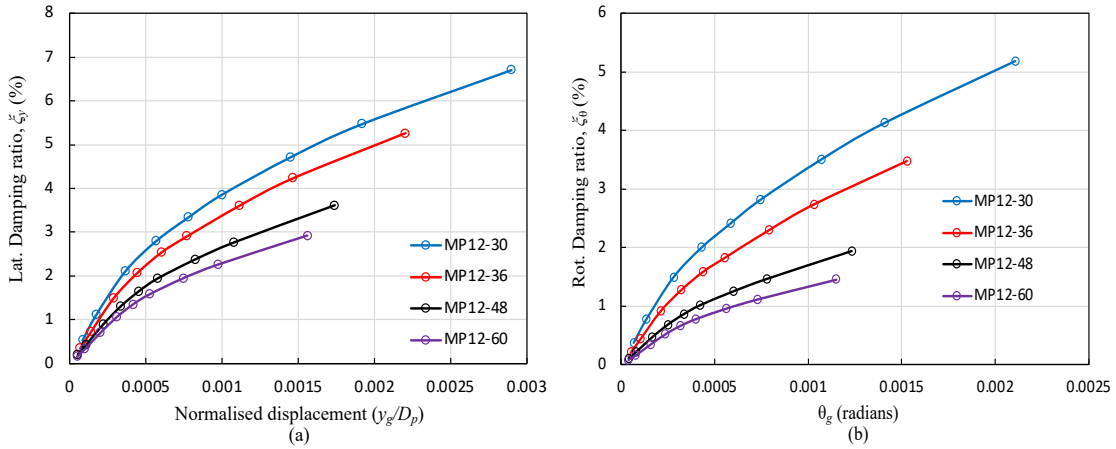


Figure 6.27: Effect of L_p on (a) ξ_y versus y_g/D_p, and (b) ξ_θ versus θ_g, for the monopiles with D_p =12 m and soil D_r = 30%

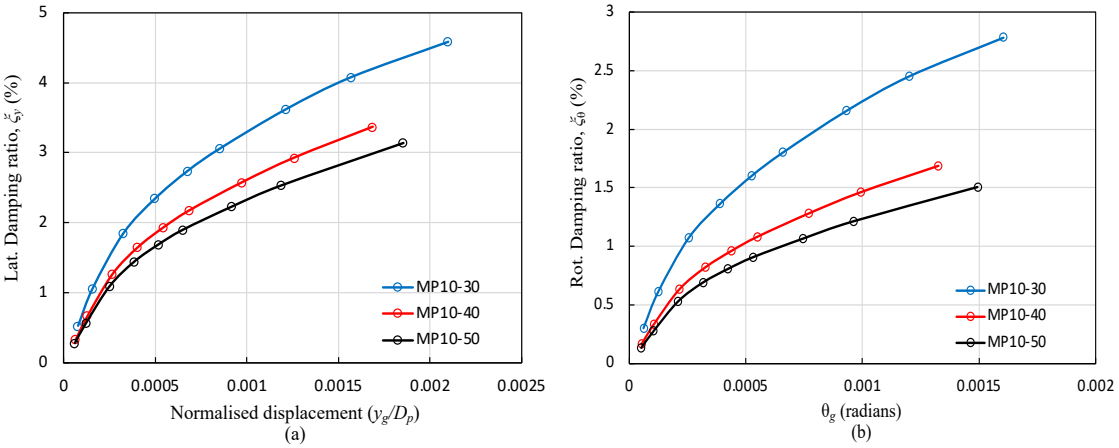


Figure 6.28: Effect of L_p on (a) ξ_y versus y_g/D_p, and (b) ξ_θ versus θ_g, for the monopiles with D_p =10 m and soil D_r = 60%

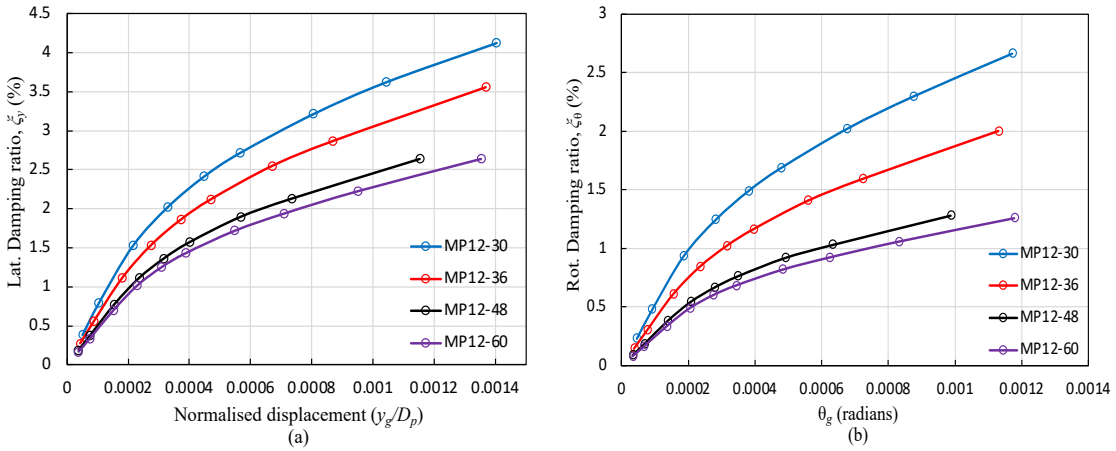


Figure 6.29: Effect of L_p on (a) ξ_y versus y_g/D_p, and (b) ξ_θ versus θ_g, for the monopiles with D_p =12 m and soil D_r = 60%

Hysteretic foundation damping ratios depend on the deformation behaviour of the monopile below the mudline. For the same deformation at the mudline, a short monopile tends to rotate more rigidly below the mudline, while a longer monopile exhibits less rigid rotation and more bending. To achieve rigid rotation, a short monopile must displace a larger volume of surrounding soil and mobilise greater nonlinearity in the soil compared to a longer monopile. Long piles that deform primarily through bending tend to induce only minor nonlinearity in the soil at greater depths and near the pile tip. In contrast, short piles that deform rigidly can experience toe-kick, allowing the nonlinear stress-strain hysteresis in the soil close to the pile tip to contribute to the total dissipated plastic energy. Since the nonlinearity of the soil decreases as the pile behaviour becomes more flexible, the hysteretic foundation damping ratios reduce with increasing the embedment depth (L_p). However, once the L_p exceeds the critical pile depth, the load-deformation hysteresis loops at the mudline remain unchanged with further embedment and the influence of L_p on the hysteretic foundation damping ratios (ξ_y and ξ_θ) becomes negligible.

The global foundation damping ratio (ζ_f), which represents the damping of the overall OWT system due to energy dissipation in the foundation, is influenced by ξ_y and ξ_θ. As ξ_y and ξ_θ decrease with increasing embedment depth (L_p), indicating reduced hysteretic damping at the foundation level, ζ_f also decreases as the monopile is embedded deeper. However, it is important to note that ζ_f also depends on the total elastic energy stored in the OWT system, which increases as the foundation becomes stiffer due to deeper monopile installation. For monopiles of the same diameter and installed in the same soil profile, ζ_f decreases with increasing L_p due to the reduction of ξ_y and ξ_θ and the increase of the total elastic stored energy. The relationship between ζ_f and the local hysteretic damping ratios (ξ_y and ξ_θ) is further discussed in this chapter.

Effect of monopile diameter (D_p)

As the free-decay simulations revealed that the global foundation damping ratio (ζ_f) is influenced by the monopile diameter (D_p), the results of the cyclic push-over simulations were compared for monopiles with the same embedment length (L_p) but different diameters, to examine the influence of D_p on ξ_y and ξ_θ. Figure 6.30 presents the hysteretic foundation damping ratios for monopiles MP10-30 and MP12-30, based on analyses conducted using constitutive parameter values corresponding to the soil relative density (D_r) of 30%. Figure 6.31 shows the comparison for the same monopiles, using parameters corresponding to D_r = 60%. The results in Figure 6.30 and Figure 6.31 indicate that both ξ_y and ξ_θ increase as monopile diameter increases. This trend contradicts the observations from the free-decay simulations, which showed that, for monopiles with identical embedment depths and subjected to the same normalised displacement (y_g/D_p) at the mudline, ζ_f decreases with increasing monopile diameter. This reduction of ζ_f with increasing D_p, when comparing monopiles displaced to the same y_g/D_p, could be attributed to the increase in total stored elastic energy. A larger diameter monopile requires greater lateral displacement of the support structure above the mudline to reach the same y_g/D_p, value, resulting in a higher amount of stored

elastic energy. Therefore, although a larger diameter monopile dissipates more plastic energy at the foundation level than a smaller diameter monopile, it also stores more elastic energy overall, leading to a lower value of ζ_f.

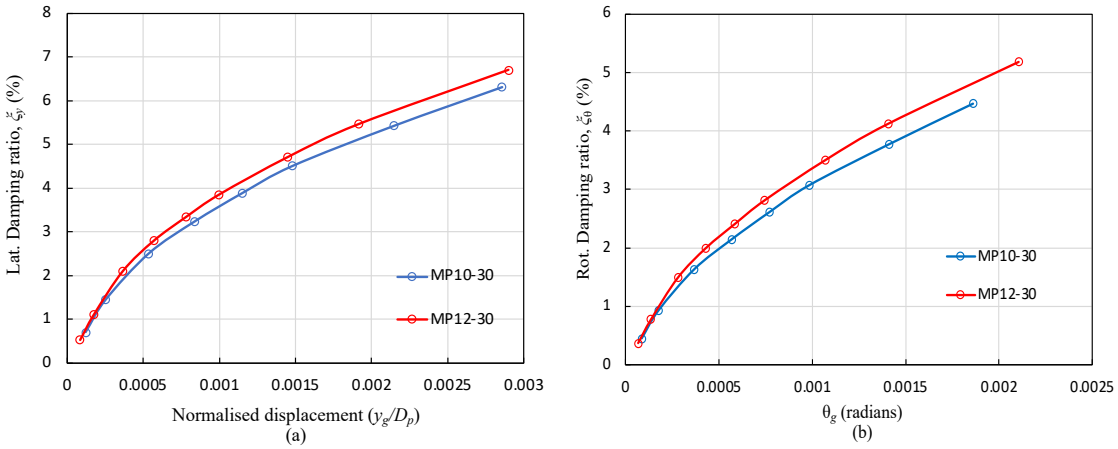


Figure 6.30: Effect of D_p on (a) ξ_y versus y_g/D_p, and (b) ξ_θ versus θ_g, for the soil profile with D_r = 30%

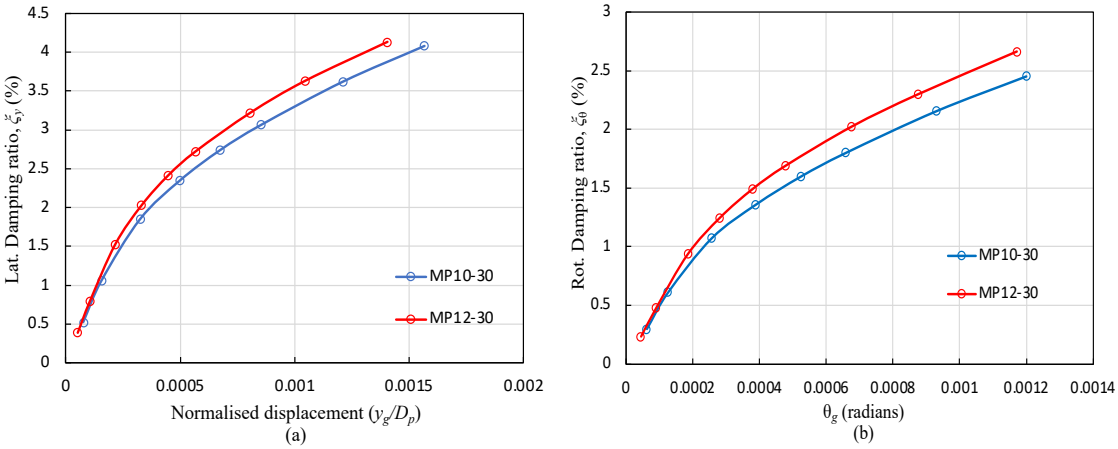


Figure 6.31: Effect of D_p on (a) ξ_y versus y_g/D_p, and (b) ξ_θ versus θ_g, for the soil profile with D_r = 60%

To confirm the influence of D_p on ζ_f, the local hysteretic damping ratios (ξ_y and ξ_θ) of monopiles MP10-30 and MP12-30 were converted into equivalent viscous dashpots to represent foundation damping at the mudline. These dashpots were then incorporated into dynamic 1D FE simulations, and the corresponding ζ_f values were determined using the logarithmic decrement method. The 1D FE models consist of beam elements, and the soil-structure interaction at the foundation level was represented using a macro-element approach, in which the foundation stiffness and hysteretic damping were modelled with springs and viscous dashpots lumped at the mudline. The Python script used for superimposing the matrices of the beam elements and performing the dynamic and modal analyses is provided in Appendix B. The details regarding the procedure for conducting the dynamic 1D FE analyses are not discussed in this section, as they will be presented later. Instead, this section focuses solely on the results obtained for ζ_f, in order to evaluate whether the logarithmic decrement analyses, conducted using 1D FE models with equivalent viscous dashpots derived from the hysteretic damping ratios (ξ_y and ξ_θ), produce the same outcome as the 3D FE analyses regarding

the effect of monopile diameter on ζ_f. The lateral viscous dashpot (c_y) and rotational viscous dashpot (c_θ) are calculated as follows:

$$c_y = \frac{2\xi_y K_y}{\omega} \tag{6.7}$$

$$c_\theta = \frac{2\xi_\theta K_\theta}{\omega} \tag{6.8}$$

where k_y is the lateral secant stiffness, determined from the ratio of the lateral load (H) to mudline displacement (y_g), while k_θ is the rotational secant stiffness, determined from the ratio of the moment to the rotation at the mudline (θ_g), and ω is the frequency of the applied load. This procedure of incorporating the effect of foundation damping into 1D FE simulations by converting the hysteretic damping ratios (ξ_y and ξ_θ) obtained from 3D FE analyses into viscous dashpots is similar to the approach adopted by Carswell et al. (2015). However, instead of using both a lateral dashpot and a rotational viscous dashpot, Carswell et al. (2015) employed only a single rotational dashpot, arguing that the moment load has a governing influence on the monopile head response. During free vibration, the OWT structure oscillates predominantly at its first-mode natural circular frequency (ω_1), so ω is typically taken as ω_1. However, under stochastic loading, which includes multiple frequency components from various sources, ω is generally selected as the dominant frequency identified from the Fourier spectrum of the applied loads. Since this dominant frequency is often close to the structure's first-mode natural frequency, it is common practice to adopt $\omega = \omega_1$. Carswell et al. (2022) followed this approach to obtain the equivalent rotational viscous dashpot for simulating the OWT response under stochastic loading events. The damping dashpot coefficients were calculated using Equations 6.7 and 6.8, based on hysteretic damping ratios presented in Figure 6.30 and Figure 6.31 and the corresponding foundation secant stiffness values. The lateral and rotational secant stiffness values corresponding to the hysteretic damping ratios in Figure 6.30 and Figure 6.31 are shown Figure 6.32 and Figure 6.33, respectively.

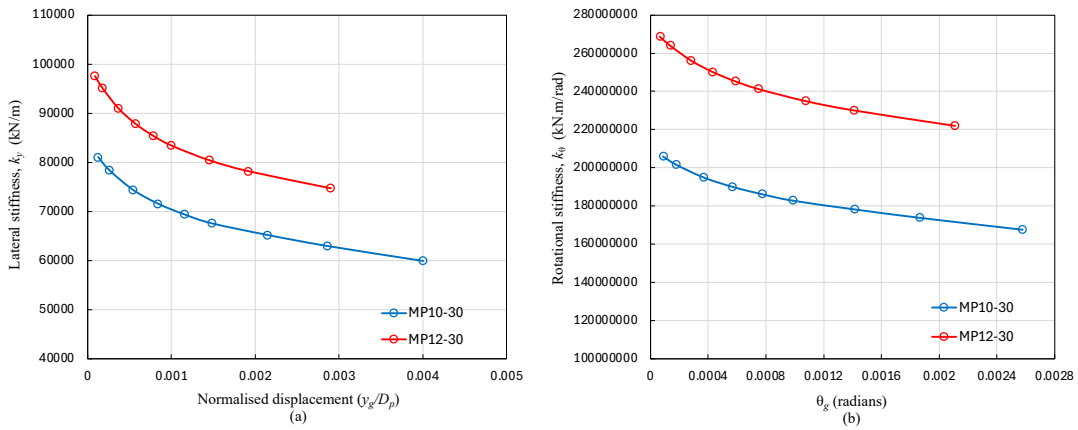


Figure 6.32: Foundation stiffness for D_r = 30%: (1) k_y versus y_g/D_p; (2) k_θ versus θ_g

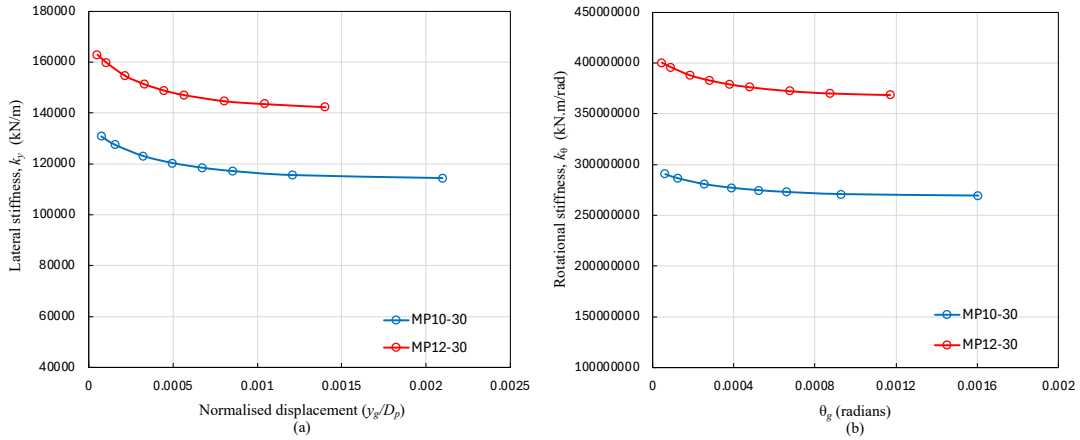


Figure 6.33: Foundation stiffness for D_r = 60%: (1) k_y versus y_g/D_p; (2) k_θ versus θ_g

In order to estimate ω_1, modal analyses were carried out by solving the following eigenvalue-eigenvector problem:

$$([K] - \omega_n^2[M])\{u\} = \{0\} \tag{6.9}$$

where K is the global stiffness matrix, M is the global mass matrix, u is the vector of modal shapes, and ω_n is angular natural frequency associated with the n-th mode of vibration. ω_1 is the angular natural frequency of the first-mode and is equal to the lowest value of ω_n. The global stiffness and mass matrices were assembled by superimposing the local stiffness and mass matrices. The mathematical eigenvalue-eigenvector problem requires a non-trivial solution such that the determinant of the characteristic matrix (|[K] - ω_n^2 [m]|) is equal to zero. The parameters of the local stiffness and mass matrices were determined to represent the mass and stiffness distribution along the height of the support structure of the reference IEA 15 MW wind turbine. Details regarding the support structure of the reference IEA 15 MW wind turbine are summarised in Appendix A. As with the 3D FE models, the mass at the RNA level at the top of the tower was accounted for in the 1D FE models by using a short beam element with a length of 0.1 m, to which an equivalent distributed mass was assigned. The effect of foundation flexibility was incorporated into the global stiffness matrix (K) by adding the lateral and rotational stiffness values to the corresponding terms at the local node representing the mudline level. To solve Equation 6.9, the linalg.eig function from the NumPy library in Python was used, which returns the values of ω_n^2 as its output. The lowest value of ω_n, representing the fundamental angular natural frequency (ω_1), was used in Equations 6.7 and 6.8 to determine the values of c_y and c_θ, respectively.

The logarithmic decrement method was used to calculate the global foundation damping ratios (ζ_f) from the dynamic 1D FE simulations. This involved displacing the OWT support structure by applying a monotonically increasing lateral load at the RNA level, followed by suddenly dropping the load to zero and allowing the structure to vibrate freely. A representative free vibration of the OWT response at the RNA level is shown in Figure 6.34. Since the foundation in the 1D FE analyses was modelled using linear springs and viscous dashpots, the same value of ζ_f is obtained regardless

of the magnitude of the lateral displacement applied at the RNA level before the structure is unloaded and allowed to oscillate freely. Figure 6.35 compares the values of ζ_f for monopiles MP10-30 and MP12-30, as determined from the dynamic 1D FE simulations using the values of ξ_y and ξ_θ from Figure 6.30, which were obtained from the soil profile with D_r = 30%. Similarly, Figure 6.36 compares the values of ζ_f for the same monopile diameters but derived from the values of ξ_y and ξ_θ shown in In order to estimate ω_1, modal analyses were carried out by solving the following eigenvalue-eigenvector problem: for the soil profile with D_r = 60%.

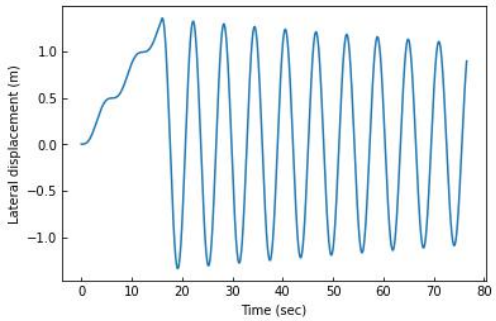


Figure 6.34: Free-decay simulation at the RNA level

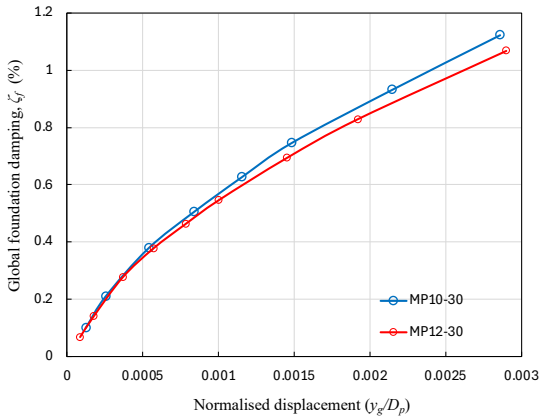


Figure 6.35: ζ_f derived from 1D FE analyses (30% relative density)

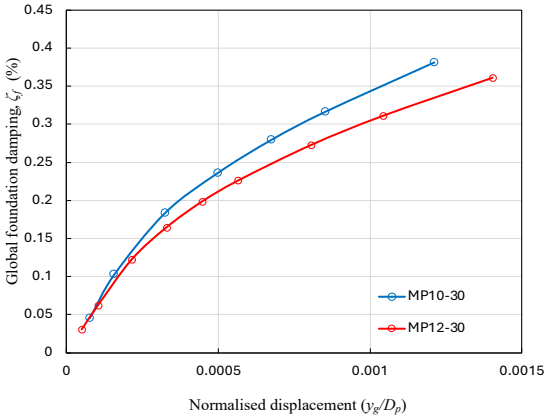


Figure 6.36: ζ_f derived from 1D FE analyses (60% relative density)

The comparisons in Figure 6.35 and Figure 6.36 reveal that, at the same normalised displacement (y_g/D_p) at the mudline, the smaller 10 m diameter monopile yields a higher ζ_f than the larger 12 m diameter monopile. This confirms the findings from the 3D FE analyses regarding the effect of

monopile diameter on ζ_f. As a result, it can be concluded that, as the monopile diameter increases, the global foundation damping ratio (ζ_f) decreases, while the local hysteretic damping ratios ξ_y and ξ_θ at the mudline level increase. The primary reason for the reduction in ζ_f with increasing D_p, despite the higher local hysteretic damping at the mudline, is the increase in the total elastic energy stored in the OWT structure. Although several studies, such as those by Vo (2022) and Shirzoi et al. (2025), also observed a decrease in ζ_f with increasing monopile diameter, they did not investigate the variation of hysteretic damping ratios at the mudline level. Therefore, the findings in this research, which examine the effect of monopile diameter on both the local and global foundation damping ratios, provide a more detailed and comprehensive understanding of foundation damping for monopile-supported OWTs.

Effect of relative density (D_r)

The effect of D_r on ξ_y and ξ_θ is investigated by comparing results for monopiles with identical dimensions, based on analyses conducted using soil profiles with D_r of 30% and 60%. For monopiles with a diameter of 10 m, Figure 6.37 presents the ξ_y and ξ_θ results for the MP10-50 monopile, obtained from analyses performed with D_r = 30% and 60%. Figure 6.38 shows the corresponding comparison for the MP12-48 monopile. The results in Figure 6.37 and Figure 6.38 indicate that for monopiles subjected to the same deformation level at the mudline, the values of ξ_y and ξ_θ decrease as D_r increases. This variation in local hysteretic damping ratios can be attributed to changes in monopile deformation below the mudline, which is strongly influenced by D_r. As the relative density of the soil increases, the soil becomes stiffer, causing the monopile response below ground level to become more slender and to undergo greater bending compared to the same monopile installed in softer (lower-density) soil. In conclusion, since monopile bending below ground level generates less nonlinearity and strains in the soil compared to rigid rotation, the values of ξ_y and ξ_θ decrease as the soil relative density increases.

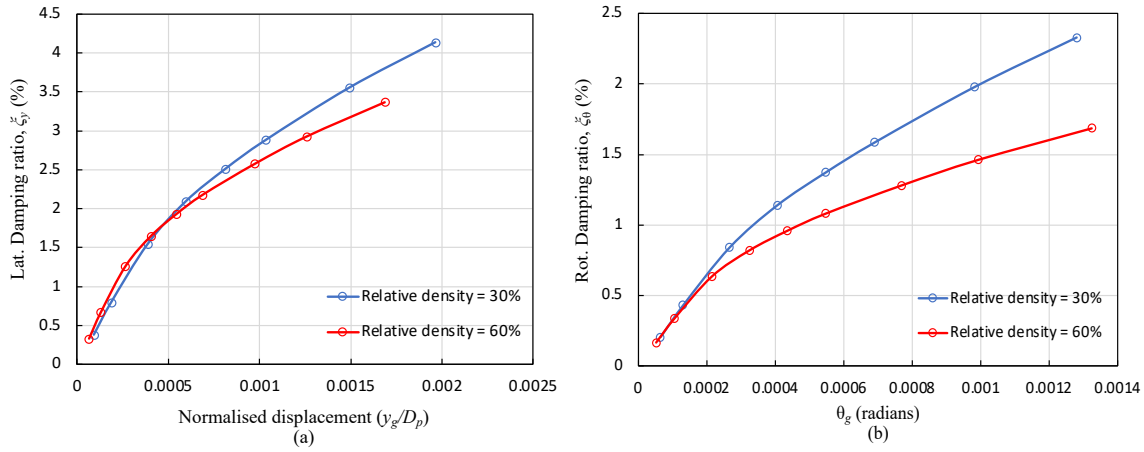


Figure 6.37: Effect of relative density on MP10-40: (1) ξ_y versus y_g/D_p; (2) ξ_θ versus θ_g

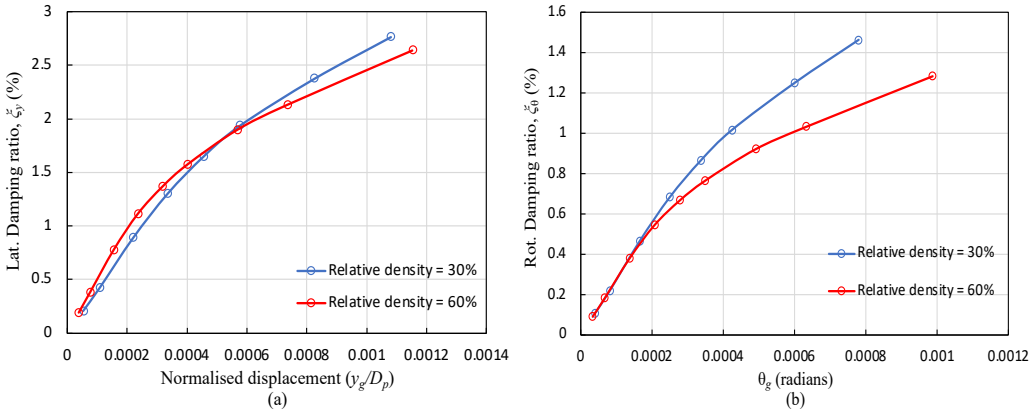


Figure 6.38: Effect of relative density on MP12-48: (1) ξ_y versus y_g/D_p; (2) ξ_θ versus θ_g

The effect of relative density on local hysteretic damping is similar to that of monopile embedment depth. For a monopile with given dimensions, one embedded in higher relative density soil behaves like a longer pile, while the same monopile in lower relative density soil responds more like a rigid (i.e., short) pile. Consequently, determining the hysteretic damping ratios associated with site-specific soil relative density is crucial to estimate the response of OWTs accurately.

Effect of load eccentricity

This section investigates the effect of load eccentricity on the variation of the hysteretic foundation damping ratios (ξ_y and ξ_θ). Lateral loads were applied at different heights along the OWT tower, and the resulting ξ_y and ξ_θ were determined from the load-deformation hysteresis loops at the mudline. Eccentricity id the lever arm of the applied lateral load (H), and is equal to the moment (M) at the mudline divided by H (eccentricity = M/H). Several analyses were performed for eccentricity values of 180 m, 135 m, 90 m, and 45 m. Based on the eccentricity level, the structural response could be wind or wave load dominated. For eccentricity values of 180 m, 135 m, and 90 m, the structure can be regarded as wind-load dominated, whereas for an eccentricity of 45 m, the structural response is primarily wave-load dominated. Figure 6.39 presents the ξ_y and ξ_θ results for the MP10-30 monopile, comparing different eccentricity values based on analyses performed with D_r = 60%.

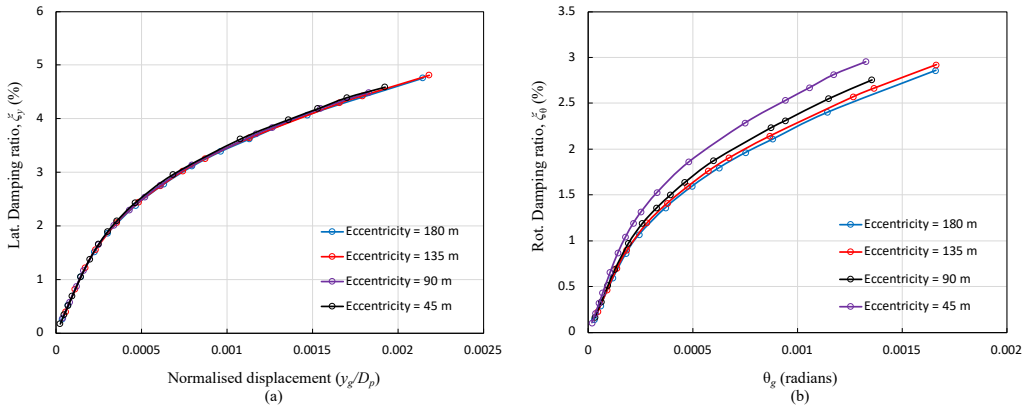


Figure 6.39: Effect of load eccentricity on: (a) ξ_y versus y_g/D_p; (2) ξ_θ versus θ_g

According to the results in Figure 6.39a, the lateral hysteretic damping (ξ_y) curves overlap, indicating that eccentricity has no influence on ξ_y. On the other hand, the results in Figure 6.39b show that eccentricity has a slight influence on the rotational damping ratio (ξ_θ) curves, with ξ_θ increasing as the eccentricity value decreases. However, the influence of eccentricity is minimal, as the rotational damping ratio (ξ_θ) curves show negligible variation between eccentricity values of 180 m and 90 m. A noticeable change only occurs when the eccentricity is reduced to 45 m, indicating a shift in the loading regime from wind-dominated to wave-dominated. Given the considerable height of modern OWTs, the effect of wind action is significant, making the structural response predominantly wind-dominated. As a result, the influence of load eccentricity on the hysteretic foundation damping rations can be disregarded. Furthermore, due to the minimal effect of load eccentricity on the foundation damping ratios, the effect of foundation damping on OWT structures can be taken into account with only lateral and rotation damping ratios without requiring a cross-coupling damping ratio. As a result of the analyses conducted with 3D FE simulations using the HSsmall soil model, the effects of the monopile embedment depth (L_p), diameter (D_p), relative density (D_r), and load eccentricity can be summarised as follows:

i. The local foundation damping ratios (ξ_y and ξ_θ) decrease with increasing the monopile embedment depth (L_p). However, this reduction becomes progressively less pronounced as L_p increases, indicating that beyond a certain embedment depth, further increases in L_p have little influence on the local foundation damping at the mudline level.
ii. As the monopile diameter increases, the local foundation damping ratios (ξ_y and ξ_θ) at the mudline also increase. This contradicts the trend observed for the global foundation damping ratio (ζ_f), which decreases as the monopile diameter becomes larger. This finding derived from the 3D FE analyses was confirmed by the logarithmic decrement analyses conducted with dynamic 1D FE simulations. For the same applied deformation at the mudline, the 1D FE analyses demonstrated that although larger diameter monopiles exhibit higher local hysteretic damping ratios (ξ_y and ξ_θ), converting these into equivalent lumped viscous dashpots at the mudline results in lower global foundation damping ratios (ζ_f) compared to smaller diameter monopiles, which have lower local damping ratios.
iii. The local foundation damping ratios (ξ_y and ξ_θ) decrease as the soil relative density (D_r) increases. This trend is primarily attributed to the change in the monopile's deformation behaviour below the mudline. In higher relative density (i.e., stiffer) soils, the monopile experiences more bending, whereas in lower relative density (i.e., softer) soils, it tends to undergo less bending and instead exhibits more rigid-body rotation. Since a monopile that bends generates less strains and nonlinearity in the soil domain compared to a monopile that rigidly rotates, the values of ξ_y and ξ_θ decrease as D_r increases.

iv. Finally, the 3D FE analyses revealed that the effect of load eccentricity is minimal and can be disregarded allowing the monopile damping to be represented without a cross coupling damping factor.

6.5.1.2 1D FE simulations

This section outlines the methodology used for conducting the 1D FE analyses and compares the global foundation damping ratios (ζ_f) obtained from their free-decay simulations with those derived from the 3D FE analyses. The 1D FE analyses were performed using a python script that assembles the global stiffness and mass matrices from the local beam elements. The OWT structure was discretised into several beam elements, each with a length of 2 m to represent the variation of the mass and cross-sectional dimensions of the OWT support-structure along its height. The beam elements were represented using the Euler-Bernoulli beam theory. The local mass (m) and stiffness (k) matrices are as follows:

$$[\mathrm{m}] = \frac{\bar{m}L}{420}\begin{bmatrix} 156 & 22L & 54 & -13L \\ 22L & 4L^2 & 13L & -3L^2 \\ 54 & 13L & 156 & -22L \\ -13L & -3L^2 & -22L & 4L^2 \end{bmatrix} \tag{6.10}$$

$$[\mathrm{k}] = \frac{EI}{L^3}\begin{bmatrix} 12 & 6L & -12 & 6L \\ 6L & 4L^2 & -6L & 2L^2 \\ -12 & -6L & 12 & -6L \\ 6L & 2L^2 & -6L & 4L^2 \end{bmatrix} \tag{6.11}$$

where $\bar{m}$ is the mass per unit length (kg/m), L is the length of the element, E is the Young's modulus, and I is the second moment of area. After assembling the global mass and stiffness matrices from the local beam element matrices, the equation of motion is solved as follows:

$$[\mathrm{M}](\ddot{\mathrm{x}}) + [\mathrm{C}](\dot{\mathrm{x}}) + [\mathrm{K}]\,(\mathrm{x}) = [\mathrm{F}] \tag{6.12}$$

where x, $\dot{\mathrm{x}}$, and $\ddot{\mathrm{x}}$, are the vectors of displacement, velocity, and acceleration, respectively. [C] is the global damping matrix that is assembled from the local damping [c] matrices. The global damping matrix consists of only the foundation contribution which is incorporated by converting the hysteretic foundation damping ratios (ξ_y and ξ_θ) into viscous dashpot coefficients and assigned to the nodal degrees of freedom at the mudline level. The response of the dynamic OWT structure is obtained by solving Equation 6.12, using the constant acceleration time-stepping method. A small time step (Δt) of 0.005 seconds is used to ensure the accuracy of the dynamic analyses. The Python script used for assembling the global matrices, calculating the eigenvalues, and computing the dynamic response of the structure using the constant acceleration time-stepping method is provided in the Appendix B. The values of ζ_f obtained from the 1D FE simulations were compared with those from the 3D FE analyses for monopiles with a diameter of 10 m, modelled using the soil profile scenario with D_r = 60%. Figure 6.40 shows the comparison of ζ_f obtained from the 3D FE and 1D FE analyses for the MP10-30 monopile, while Figure 6.41 and Figure 6.42 show the corresponding

comparison for monopiles MP10-40 and MP10-50, respectively. The comparisons in Figure 6.40 to Figure 6.42 show that the global foundation damping ratios (ζ_f) derived from the 1D FE analyses are slightly larger than those obtained from the 3D FE simulations. However, the difference between the two analysis methods is minimal, with the maximum difference in ζ_f being approximately 0.10%, which can be considered acceptable. Since the global foundation damping ratios (ζ_f) obtained from the 1D FE analyses closely match those from the 3D FE analyses, the local hysteretic foundation damping ratios (ξ_y and ξ_θ) presented in this research can be effectively used in integrated OWT analysis tools, such as Bladed and OpenFAST, to accurately incorporate the contribution of soil hysteretic energy dissipation.

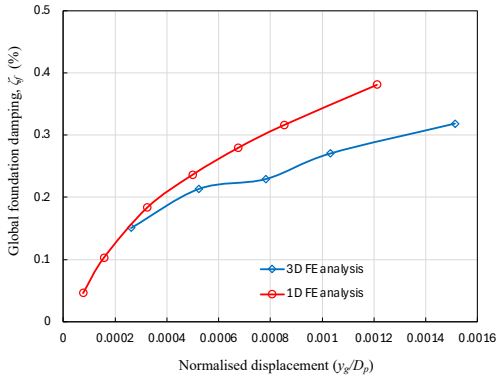


Figure 6.40: Comparison of ζ_f obtained from 1D FE and 3D FE (MP10-30)

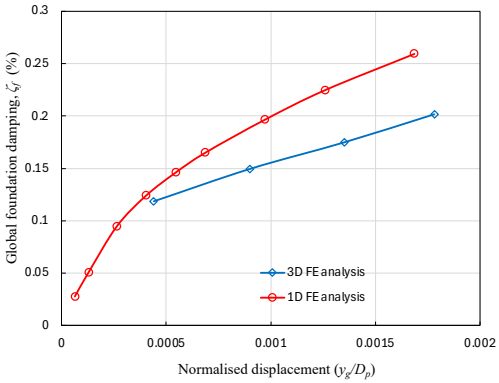


Figure 6.41: Comparison of ζ_f obtained from 1D FE and 3D FE (MP10-40)

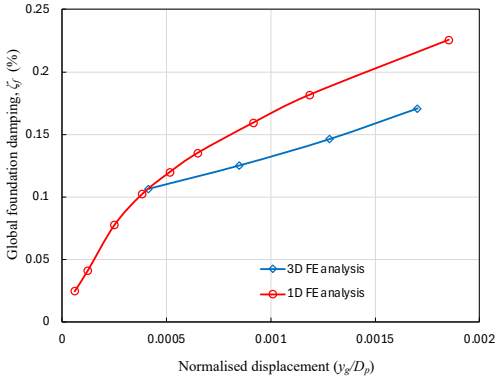


Figure 6.42: Comparison of ζ_f obtained from 1D FE and 3D FE (MP10-50)

6.5.1.2 SANISAND simulations

This section is organised similarly to the previous one, covering the effects of monopile embedment depth, diameter, and soil relative density, to examine whether the findings obtained from the HSsmall model also hold true for analyses conducted using the SANISAND-MS model. As with the HSsmall model, Simulations using the SANISAND-MS model were performed for ground conditions of 30% and 60% relative densities. The effect of load eccentricity was not considered here, as the HSsmall model simulations indicated its effect is insignificant, and this result is unlikely to differ with the SANISAND-MS model. Additionally, 1D FE simulations were not performed because previous comparisons using the HSsmall model demonstrated that global foundation damping ratios (ζ_f) from 1D FE analyses closely match those from 3D FE simulations, a result expected to remain consistent with the SANISAND-MS model. Although 3D FE analyses using the SANISAND-MS constitutive model have been conducted in the literature to investigate monopile behaviour, the majority of these studies have focused exclusively on the monotonic response. Therefore, the results presented in this section can be considered novel, as no previous research has explored foundation damping using the advanced SANISAND-MS model.

Effect of embedment depth (L_p)

The effect of the monopile embedment depth is illustrated in Figure 6.43, which presents the results of ξ_y versus y_g/D_p and ξ_θ versus θ_g, for monopiles MP10-30, MP10-40, and MP10-50. These results are based on analyses conducted using the soil profile with the relative density (D_r) of 30%. Similarly, Figure 6.44 shows the corresponding results for monopiles with a diameter of 12 m, also analysed under the ground condition of D_r = 30%. Figure 6.45 and Figure 6.46 present the results for the same monopiles shown in Figure 6.43 and Figure 6.44, respectively, but based on the analyses conducted for the soil profile with D_r = 60%.

The results in Figure 6.43 to Figure 6.46 show that 3D FE analyses conducted using the SANISAND-MS model yield the same findings observed from the HSsmall model. Both the lateral (ξ_y) and rotational (ξ_θ) damping ratios clearly reduce with increasing the embedment depth (L_p).

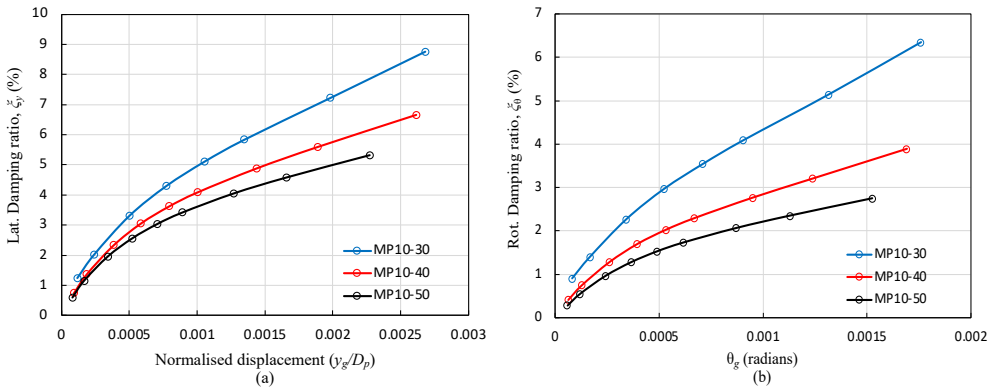


Figure 6.43: Effect of L_p on (a) ξ_y versus y_g/D_p, and (b) ξ_θ versus θ_g, for D_p =10 m and soil D_r = 30%

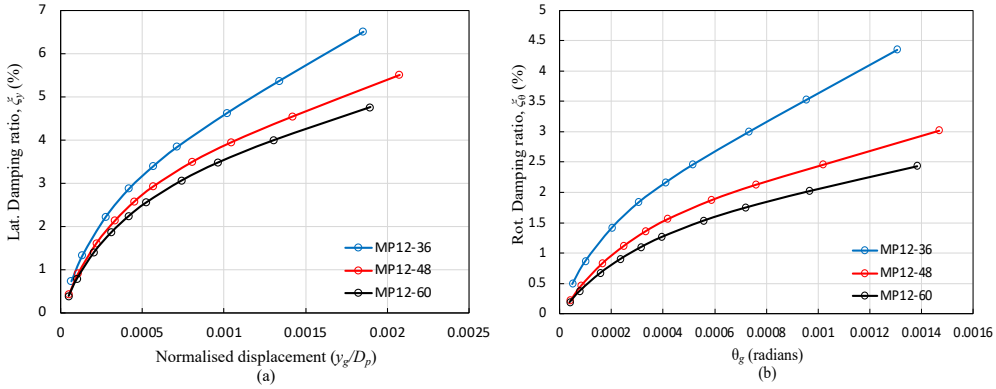


Figure 6.44: Effect of L_p on (a) ξ_y versus y_g/D_p, and (b) ξ_θ versus θ_g, for D_p =12 m and soil D_r = 30%

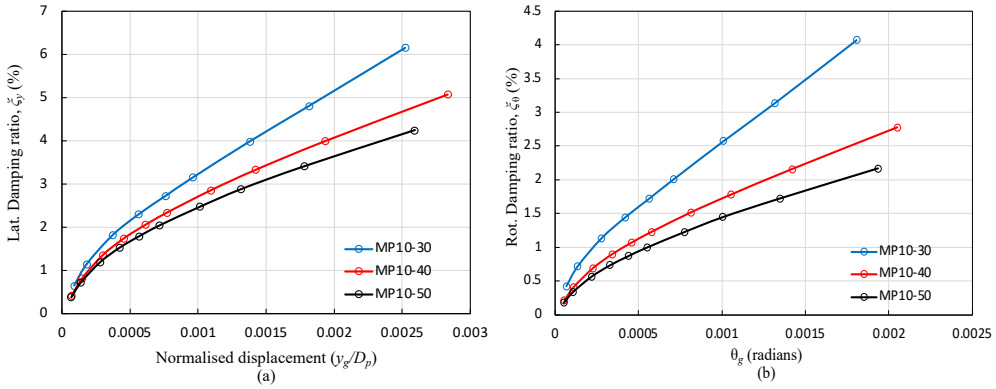


Figure 6.45: Effect of L_p on (a) ξ_y versus y_g/D_p, and (b) ξ_θ versus θ_g, for D_p =10 m and soil D_r = 60%

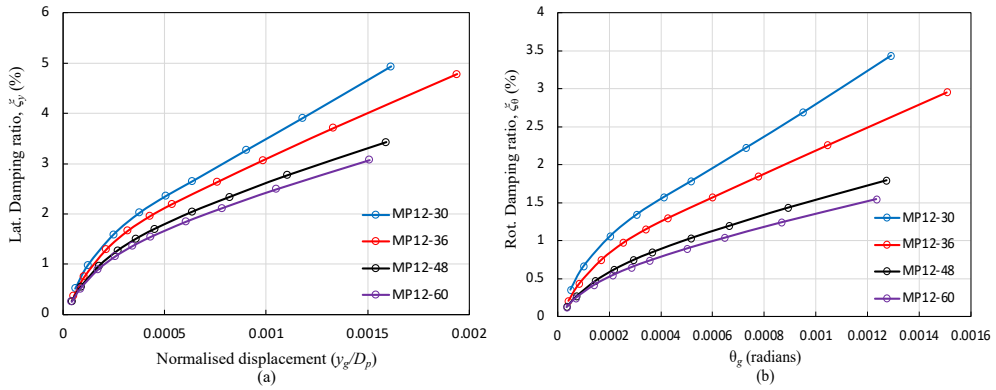


Figure 6.46: Effect of L_p on (a) ξ_y versus y_g/D_p, and (b) ξ_θ versus θ_g, for D_p =12 m and soil D_r = 60%

Effect of monopile diameter (D_p)

The effect of monopile diameter is investigated by comparing analyses conducted on monopiles with identical embedment depths and ground conditions (i.e., relative density). Figure 6.47 compares the local hysteretic damping ratios (ξ_y and ξ_θ) for monopiles MP10-30 and MP12-30, based on the analyses conducted for the soil profile with D_r = 60%. The results in Figure 6.47 show that for the same applied normalised displacement (y_g/D_p) and rotation (θ_g) at the mudline, both ξ_y and ξ_θ increase as the monopile diameter becomes larger. This confirms the trend observed from the analyses conducted using the HSsmall constitutive model.

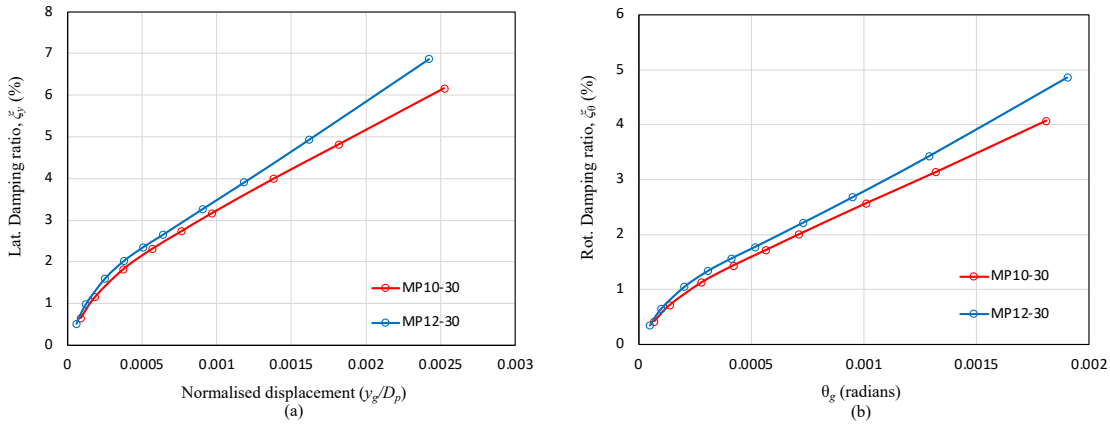


Figure 6.47: Effect of monopile diameter (D_p) on: (a) ξ_y versus y_g/D_p; (b) ξ_θ versus θ_g

Effect of relative density (D_r)

Unlike the analyses conducted using the HSsmall model, which required calibrating different parameter values for soil relative densities of 30% and 60%, the analyses performed with the SANISAND-MS model required only a single set of parameter values for both relative densities. This is because the SANISAND-MS model is state-independent, allowing the same parameter values to reproduce the behaviour under different in-situ densities and applied stresses. The analyses results presented in this section investigate the variation of the local hysteretic damping ratios due to the influence of the soil relative density. Figure 6.48 compares the hysteretic damping ratios obtained from analyses using relative densities of 30% and 60% for the monopile MP10-40. The results based on the SANISAND-MS simulations align with those obtained from the HSsmall model, showing that for the same applied deformations at the mudline, the local hysteretic damping ratios (ξ_y and ξ_θ) decrease as the relative density increases. As previously mentioned, the difference in ξ_y and ξ_θ between the two relative densities can be attributed to the influence of the soil relative (i.e., stiffness) on varying the pile deformation behaviour. for the same mudline deformation, a monopile embedded in a dense-state soil experiences more bending than rigid rotation. Since bending causes less nonlinearity in the soil domain compared to rigid rotation, the local hysteretic damping ratios reduce as the relative density increases.

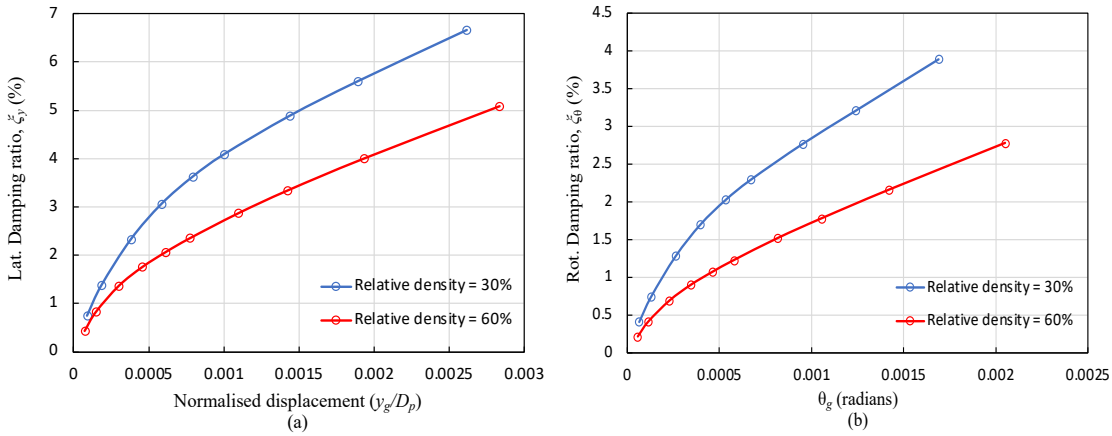


Figure 6.48: Effect of relative density on MP10-40: (1) ξ_y versus y_g/D_p; (2) ξ_θ versus θ_g

6.5.2 Distributed hysteretic foundation damping ratios

This section investigates the distributed foundation damping ratios along the monopile embedment depth. At any given depth, foundation damping is characterised by a lateral damping ratio (ξ_y) and a rotational damping ratio (ξ_θ). In contrast to the damping ratios presented in the previous section, which were derived from load-deformation loops at the mudline and represent the integrated hysteretic damping of the entire foundation, the damping ratios discussed here correspond to discrete depths. Each damping ratio represents the local hysteretic energy dissipation at a specific point along the monopile. While the previous section provided valuable insights into how the integrated hysteretic damping varies with different geometries and ground conditions, gaining a more detailed understanding requires examining the distributed damping behaviour along the embedment depth. The overall damping ratio at the mudline results from integrating the hysteretic energy dissipated through the distributed soil reactions along the depth of the monopile. At each depth, the lateral damping ratio (ξ_y) is determined from the hysteretic *p*-*y* loop, where *p* is the distributed lateral soil reaction and *y* is the corresponding lateral displacement of the monopile section. Similarly, the rotational damping ratio (ξ_θ) is derived from the *m*-θ hysteresis loop, where *m* is the distributed moment and θ is the rotation of the monopile section at the same depth. An illustration of the *p*-*y* and *m*-θ loops along the monopile embedment depth is shown in Figure 6.49. This section begins by outlining the procedure for extracting the *p*-*y* and *m*-θ loops from the 3D FE analyses and then explores the variation of ξ_y and ξ_θ in relation to changes in monopile diameter (D_p) and embedment depth (L_p). The influence of relative density on ξ_y and ξ_θ is not considered here. The focus is primarily on simulations conducted with D_r = 60%, as this relative density represents a medium-dense soil, which is typical of the ground conditions encountered for OWTs. Furthermore, only results obtained using the HSsmall model are presented here. A comparison between the HSsmall and SANISAND-MS model outcomes is left for future work.

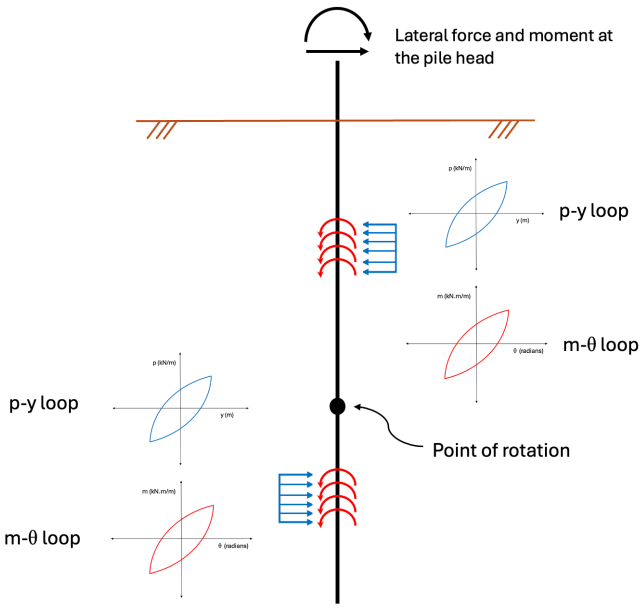


Figure 6.49: *p*-*y* and *m*-θ loops along the monopile length

6.5.2.1 Procedure for extracting *p-y* and *m*-θ loops

The soil distributed reactions were determined according to the PISA framework as shown in Figure 6.50. The lateral distributed reaction (p) arises from the passive soil resistance generated by the lateral movement of the monopile, while the distributed moment (m) is generated from the vertical shear tractions induced at the soil-pile interface due to the pile rotation. Additionally, two reaction components develop at the pile tip: the base shear (H_b) and the base moment (M_b). However, this thesis does not address the base reaction components, focusing instead on the variation of the distributed foundation damping ratios generated by p and m reactions along the pile. The distributed reactions and the corresponding deformation were extracted using a Python script.

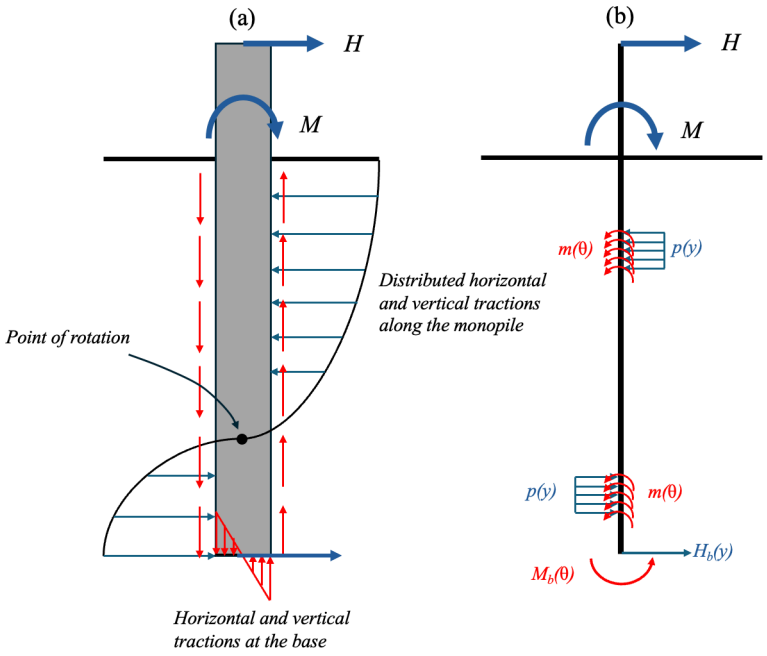


Figure 6.50: PISA design model: (a) components of soil reactions; (b) 1D FE implementation

The detailed procedure for extracting the *p-y* and *m*-θ loops are as follows:

(i) The first step involved discretising the monopile into plate sections with a maximum length of 1.0 m. This step was performed at the initial stage, during the creation of the 3D FE model, and prior to running the analyses. Discretising the monopile into multiple sections significantly simplifies the extraction process and provides a great control over creating fine mesh plate elements.

(ii) To extract p and m for each depth increment after the analyses were completed, the vectors of the normal stress (σ_n), the vertical shear stress (τ_1), and the horizontal shear stress (τ_2) for each interface element were extracted. Each interface element has 6 Gaussian integration stress points and hence 6 normal, horizontal stresses, and vertical shear stresses. The interface stresses represent the stresses exerted by the soil on the pile wall.

(iii) The interface element stresses (σ_n, τ_1, and τ_2) were then integrated across the element to obtain the corresponding average stresses. This was done by taking the dot product of the stress vectors

and weight vector (W). The average normal (σ_{nav}) , horizontal shear (τ_{2av}), and vertical shear stresses (τ_{1av}) are as follows:

$$\sigma_{nav} = \sum_{i=1}^{6} \sigma_{ni} W_i$$

$$\tau_{2av} = \sum_{i=1}^{6} \tau_{2avi} W_i \quad (6.13)$$

$$\tau_{1av} = \sum_{i=1}^{6} \tau_{1avi} W_i$$

where the vector W = [0.109952, 0.109952, 0.109952, 0.223382, 0.223382, 0.223382], as taken from the PLAXIS 3D Manual (2023b).

(iv) Once the average stresses were determined the lateral force (F_y) and the vertical traction shear force (F_z) were calculated for each interface element. The lateral force (F_y) is calculated using the following equation based on coordinates of the system in Figure 6.51:

$$F_y = \sigma_{nav} A \cos(\theta) - \tau_{2av} A \sin(\theta) \quad (6.14)$$

where A is the area of the interface element. The vertical traction shear force (F_z) is as follows:

$$F_z = \tau_{1av} A \quad (6.15)$$

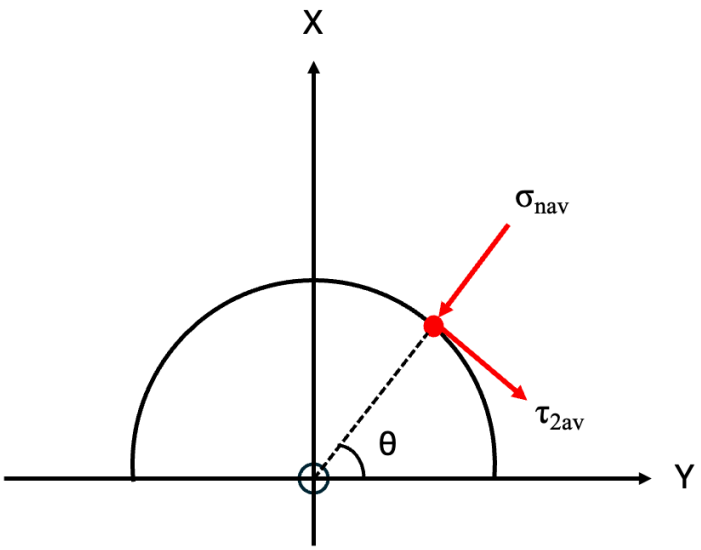


Figure 6.51: Coordinates of the monopile model

(v) After calculating the lateral force (F_y) and vertical traction shear force (F_z) for each interface element, the distributed lateral reaction (p) and distributed moment (m) was easily determined for each section along the monopile depth. The distributed lateral reaction (p) as function of depth (Z) was calculated as follows:

$$p(Z) = \frac{\int_{Z-\Delta z/2}^{Z+\Delta z/2} Fy(Z)dz}{\Delta z} \quad (6.16)$$

where Δz is the depth increment which was equal to 1 for all the models developed in this research. The distributed moment as function of depth (Z) is as follows:

$$m(Z) = \frac{\int_{Z-\Delta z/2}^{Z+\Delta z/2} d\ Fz(Z)dz}{\Delta z} \tag{6.17}$$

where d denotes the lever arm taken from the centroid of the element to the origin of coordinate system in Figure 6.51.

(vi) The lateral displacement (y) and rotation (θ) corresponding to the distributed lateral reaction (p) and distributed moment (m) were determined. Although the reactions were computed from the interfaces, the deformations were calculated from the nodes of the plate elements. For a pile element section (shown in Figure 6.52), at a given depth Z, the lateral displacement (y) at the centre of the section is simply determined by taking the average of all the lateral displacements of the nodes within the pile section. The rotation (θ) was calculated by taking the difference between the average vertical displacements at the two opposing sides of the pile divided by the monopile diameter.

(vii) Once the p-y and m-θ hysteresis loops were obtained, the distributed damping ratios were calculated using Equation 6.6. The distributed ratios were determined from the same cyclic push-over simulations that were performed to determine the damping ratios lumped at the mudline level.

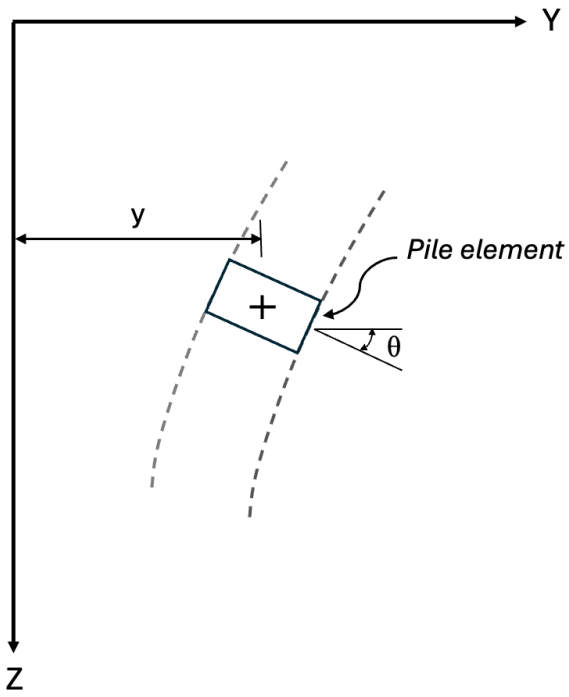


Figure 6.52: Pile element section

6.5.2.2 General characteristic of distributed damping ratios

Although several studies have investigated the variation of distributed foundation damping ratios for monopiles, most have focused solely on the lateral foundation damping component (ξ_y), without considering the contribution of the rotational damping ratio (ξ_θ), which can be significant for large-diameter monopiles. Thus, this research builds on previous studies by equally studying ξ_y and ξ_θ damping ratios. This section introduces the general characteristics related to the shape of the distributed *p-y* and *m*-θ hysteresis loops and the corresponding foundation damping ratios. The subsequent sections examine the influence of monopile diameter and embedment depth on the profiles of ξ_y and ξ_θ. Furthermore, the effects of monopile dimensions were evaluated in terms of their impact on the relationships between ξ_y and normalised displacement (y/D_p), and between ξ_θ and rotation (θ), at specific sections along the monopile.

For a representative monopile, in this case MP10-30, the shapes of the *p-y* and *m*-θ hysteresis loops are shown in Figure 6.53 to Figure 6.55 for different depths along the monopile. Figure 6.53 shows the *p-y* and *m*-θ hysteresis loops for the depths near the mudline, ranging from 0.5 m to 4.5 m in depth, while Figure 6.54 shows the hysteresis loops around the point of rotation, and Figure 6.55 shows the hysteresis loops close to the monopile tip. Figure 6.53 demonstrates that the soil reaction-deformation loops become progressively stiffer with increasing depth, reflecting the larger stiffness of the soil surrounding the corresponding pile sections at greater depths. Furthermore, since the *p-y* and *m*-θ hysteresis loops form enclosed areas, the distributed foundation damping ratios (ξ_y and ξ_θ) for depths near the mudline level can be easily calculated using Equation 6.6. Figure 6.54 presents the hysteresis loops near the point of rotation, which, for the MP10-30 monopile with a diameter of 10 m and an embedment depth of 30 m, is located approximately 20 m below the mudline. Figure 6.54a shows that around the point of rotation, the direction of the lateral distributed reaction (*p*) gradually changes to the opposite direction, rather than reversing abruptly. This transient zone around the point of rotation leads to the formation of irregular shaped *p-y* hysteresis loops. Determining the damping ratios from these hysteresis loops produces unreasonably large damping values, and as a result, they are excluded from this study.

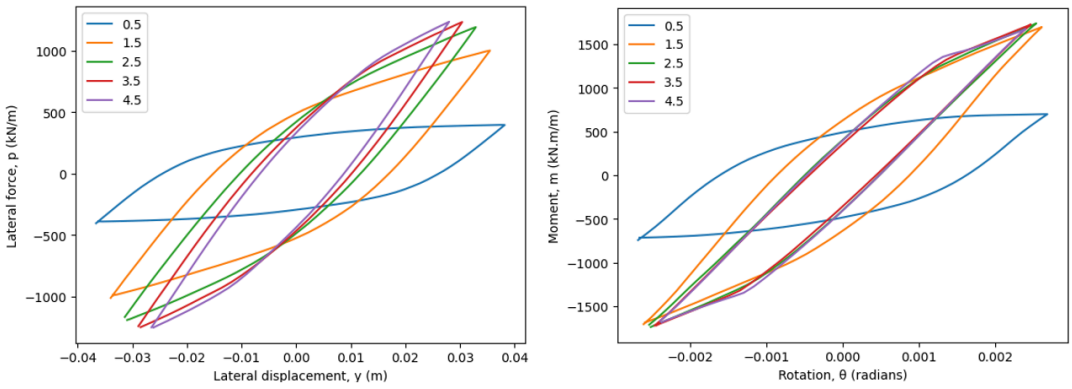


Figure 6.53: Soil reaction-deformation loops near the mudline: (a) *p-y*; (b) *m*-θ

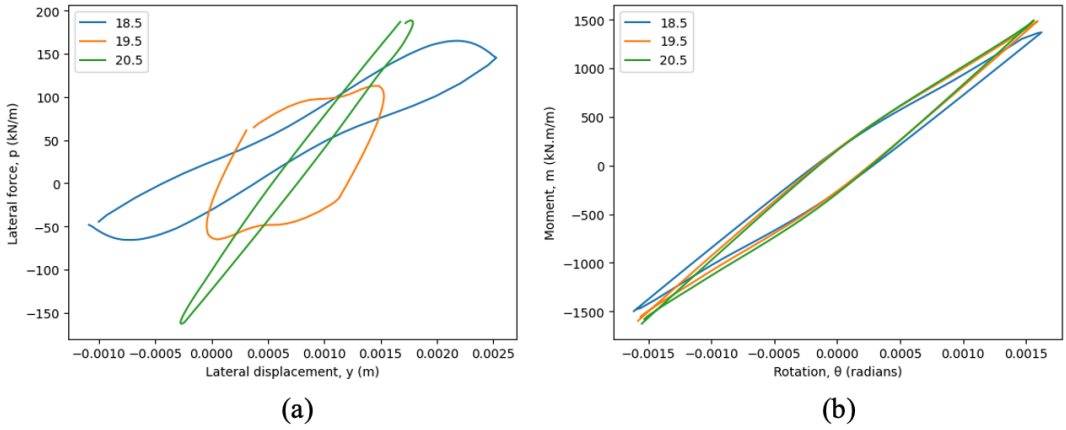


Figure 6.54: Soil reaction-deformation loops near the point of rotation: (a) *p*-*y*, (b) *m*-θ

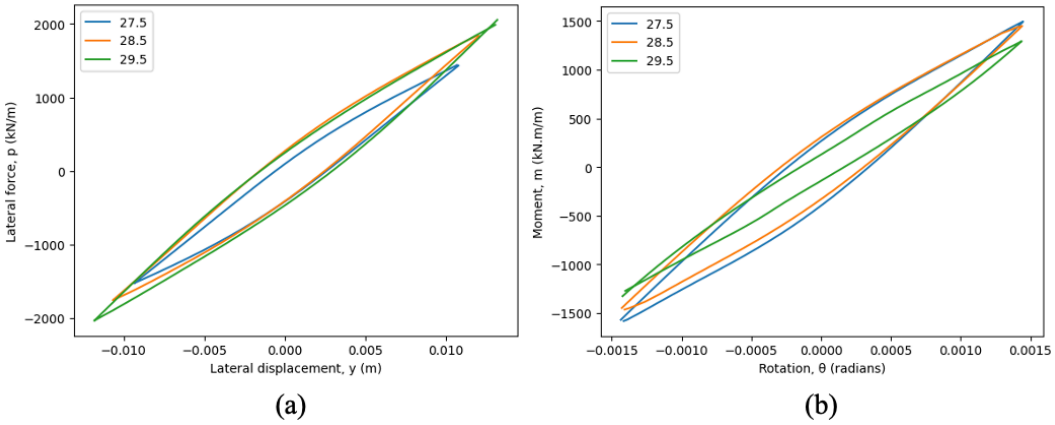


Figure 6.55: Soil reaction-deformation loops near the monopile tip: (a) *p*-*y*, (b) *m*-θ

It is important to note that the reversal in the direction of soil reactions occurs only for the lateral reaction (*p*) component, while the direction of the distributed moment (*m*) component remains unchanged both above and below the point of rotation. Given that Figure 6.54b reveals that the *m*-θ hysteresis loops remain elliptical in shape and having enclosed areas, the rotational damping ratios (ξ_θ) were computed for all depths including the pile sections that are closely around the point of rotation. The transient zone, which includes the pile elements around the point of rotation and is associated with irregularly shaped closed loops and consequently very large values of ξ_y, was considered to extend 2.5 m above and below the point of rotation.

For the MP10-30 monopile, the profiles of the lateral (ξ_y) and rotational (ξ_θ) damping ratios with depth are presented in Figure 6.56a and Figure 6.56b, respectively. Those profiles are based on a normalised mudline displacement (y_g/D_p) and a rotation of 0.0021 and 0.0016 radians, respectively. The profile in Figure 6.56 reveals that the maximum ξ_y and ξ_θ occur close to the mudline. This result is considered reasonable, as the deformation of the monopile is greatest in this region. Additionally, soil elements near the mudline produce higher damping ratios (*D*) compared to the soil elements at greater depths since they are subjected to lower mean effective stresses. The increase in soil damping ratio (*D*) with decreasing mean effective stress was discussed in Chapter 2 and confirmed by the cyclic triaxial test results presented in Chapter 3.

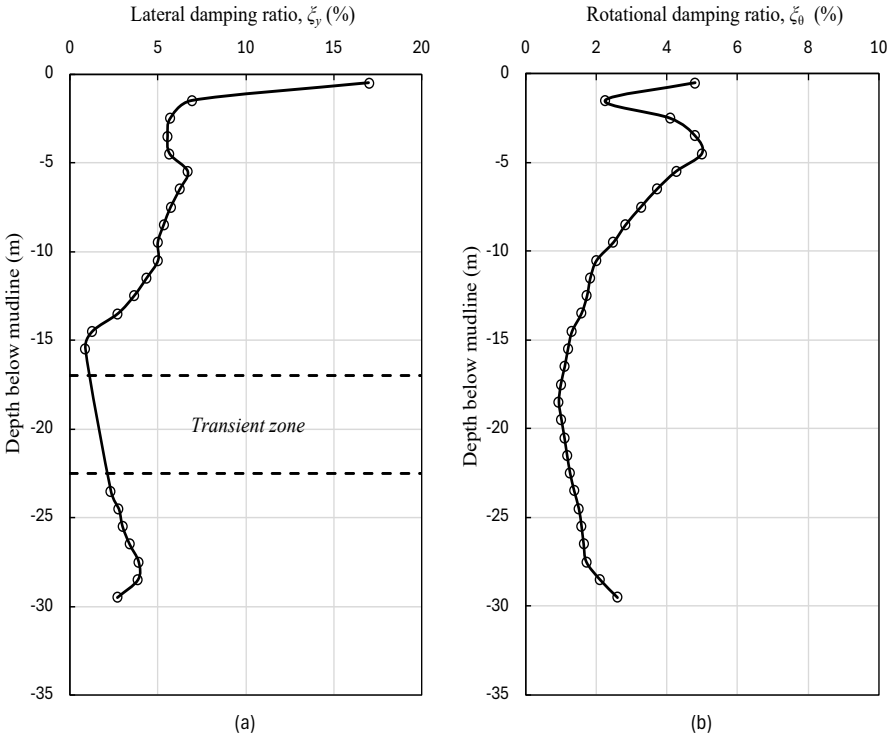


Figure 6.56: Distributed foundation damping ratios with depth: (a) ξ_y; (b) ξ_θ

6.5.2.3 Effect of embedment depth (L_p)

Analyses using different monopile geometries revealed that embedment depth (L_p) significantly influences the local damping ratios at the mudline. Therefore, it is crucial to examine how L_p affects the distribution of discrete damping ratios along the depth of the monopile. This effect is assessed by comparing the profiles of the distributed foundation damping ratios for monopiles with identical diameters but varying embedment depths. Furthermore, the influence of L_p on the relationships between damping ratios and their corresponding deformations at a given depth is also investigated. For a given pile section at any depth, it is important to examine how L_p affects the relationships between ξ_y and the normalised displacement (y/D_p), and between ξ_θ and the rotation (θ), since these relationships can be used to incorporate foundation damping as distributed viscous dashpots connected to the pile beam elements, following the Winkler modelling approach.

For an average normalised mudline displacement (y_g/D_p) of 0.0012 and an average rotation (θ_g) of 0.00096 radians, Figure 6.57a and Figure 6.57b compare the profiles of ξ_y and ξ_θ, respectively, for monopiles MP10-30 and MP10-50. To understand the results in Figure 6.57 in more detail, the profiles of the normalised lateral displacements and rotations are shown for the two monopiles in Figure 6.58a and Figure 6.58b, respectively.

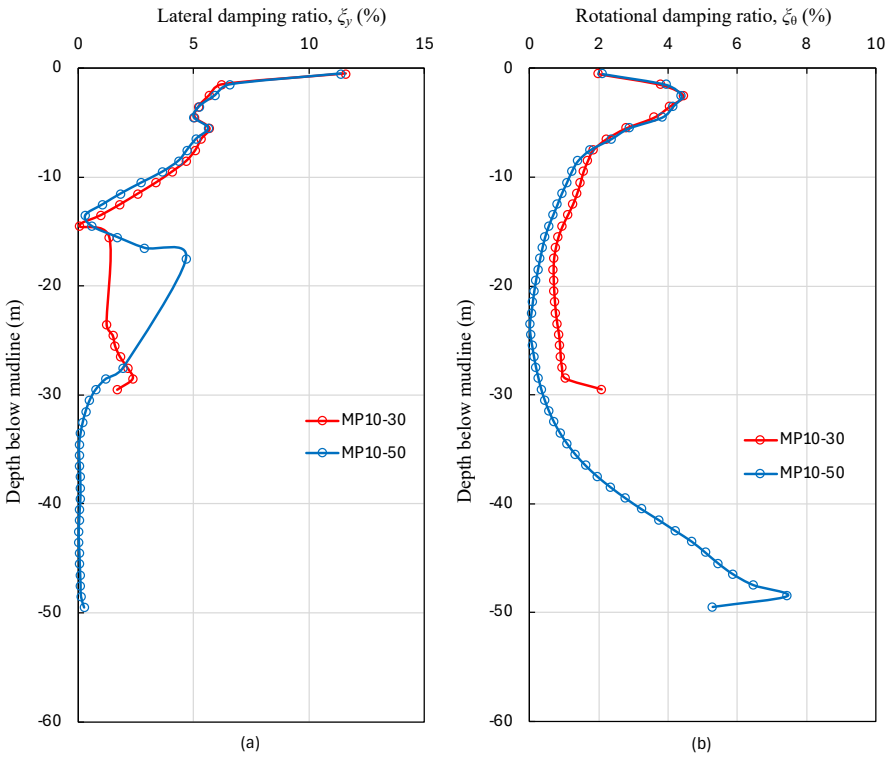


Figure 6.57: Foundation damping ratios with depth for monopiles MP10-30 and MP10-50: (a) ξ_y; (b) ξ_θ

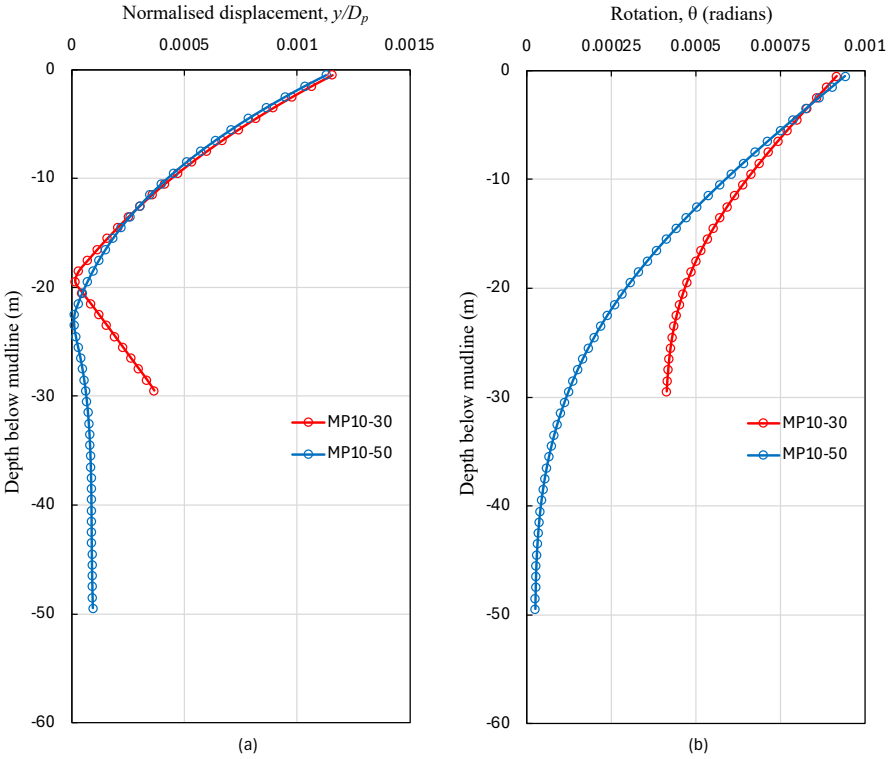


Figure 6.58: deformation profiles with depth for monopiles MP10-30 and MP10-50: (a) y/D_p; (b) θ

Although analysing the damping profile of ξ_y is important, the presence of a transient zone around the point of rotation limits the clarity of the results. Therefore, it is more effective to investigate the effect of L_p on the distributed foundation damping using the ξ_θ profiles. Figure 6.57b shows that

close to the mudline, where the rotations (θ) of the two monopiles MP10-30 and MP10-50 are approximately the same, the values of ξ_θ are nearly equal to each other. However, at greater depths along the monopiles, the MP10-30 monopile generates significantly higher ξ_θ than MP10-50 monopile. The reason for this can be explained by Figure 6.58b, which shows that at greater depth the rotations experienced by MP10-30 monopile are much larger than those of MP10-50 monopile, and hence the larger of values of ξ_θ at the deeper sections generated by MP10-30 monopile. Furthermore, it is worth mentioning that the behaviour of MP10-50 monopile is almost fully slender (i.e., long pile), as indicated by the very small displacements and rotations close to the pile tip in Figure 6.58.

To gain a deeper understanding, the effect of L_p on the hysteretic damping ratios at discrete depths along the monopile must be examined. Therefore, two depths are selected: one at a shallow depth of 5.5 m below the mudline, and the other at a greater depth of 12.5 m below the mudline. Comparisons of the relationships between ξ_y and y/D_p, and between ξ_θ and θ, for monopiles MP10-30 and MP10-50 are shown in Figure 6.59 and Figure 6.60, for pile sections located 5.5 m and 12.5 m below the mudline.

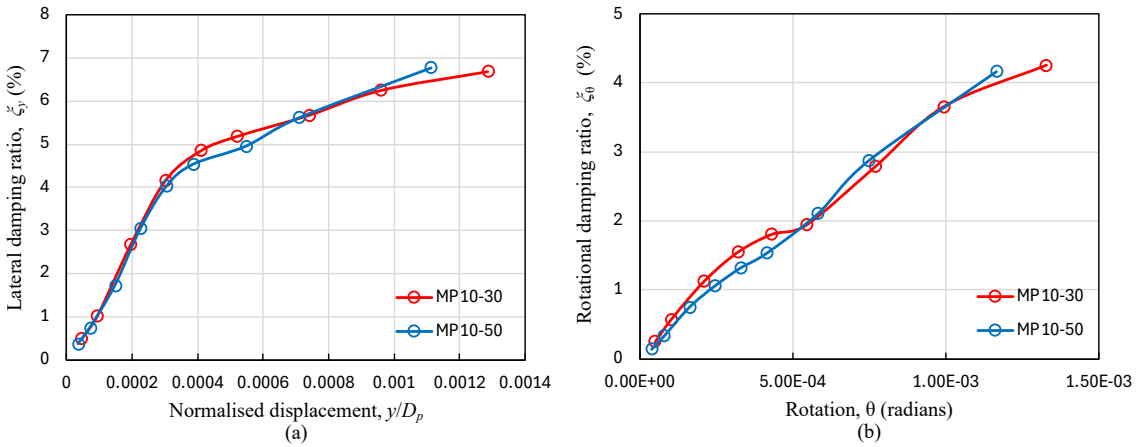


Figure 6.59: Effect of L_p on a pile section 5.5 m below the mudline: (a) ξ_y-y/D_p; (b) ξ_θ-θ

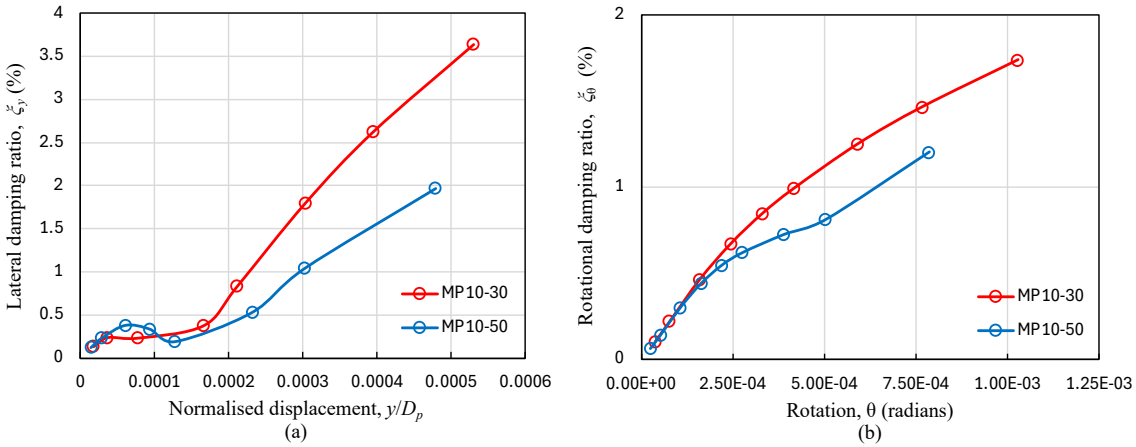


Figure 6.60: Effect of L_p on a pile section 12.5 m below the mudline: (a) ξ_y-y/D_p; (b) ξ_θ-θ

The results in Figure 6.59 and Figure 6.60 present contradicting trends. On the one hand, Figure 6.59 shows that for a given y/D_p and θ at a shallow depth of 5.5 m below the mudline, both monopiles MP10-30 and MP10-50 produce approximately the same damping ratios (ξ_y and ξ_θ). However, at a greater depth of 12.5 m below the mudline, the damping ratios generated by the shorter monopile (MP10-30) are larger than those generated by the longer monopile (MP10-50) across the investigated range of normalised displacements and rotations, as demonstrated in Figure 6.60. This observation is significant, as the effect of L_p on damping ratios at discrete depths has not been previously studied. Understanding the discrepancy between the trends in Figure 6.59 and Figure 6.60 is essential for accurately incorporating foundation damping in OWTs. However, further analyses are required to fully understand the influence of L_p on distributed foundation damping ratios, and to explain why the damping ratios are similar at shallow depths but diverge at greater depths.

6.5.2.4 Effect of monopile diameter (D_p)

Similar to the investigations conducted on the effect of L_p on foundation damping, this section examines the influence of D_p on the variation of distributed foundation damping ratios with depth. Furthermore, the influence of D_p is evaluated in relation to the relationships between foundation damping ratios and their corresponding deformations at various discrete depths. To achieve these aims, comparisons are made between monopiles MP10-30 and MP10-12, which have the same embedment depth (L_p) of 30 m and diameters (D_p) of 10 m and 12 m, respectively. Figure 6.61a presents the profiles of ξ_θ for both monopiles, while Figure 6.61b shows the variation of rotation with depth for the same two monopiles.

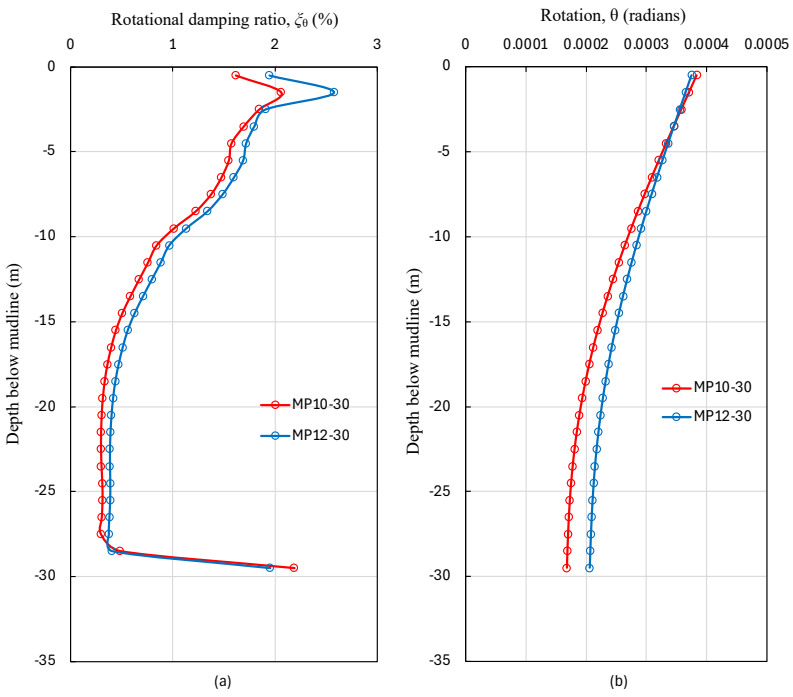


Figure 6.61: Effect of D_p on the profiles of: (a) ξ_θ with depth; (b) θ with depth

Figure 6.61a reveals that rotational damping ratios (ξ_θ) generated by the larger diameter monopile (MP12-30) are slightly higher than those produced by the smaller diameter monopile (MP10-30) across the same embedded depth of 30 m. Furthermore, Figure 6.61b clearly demonstrates that, for approximately the same mudline rotation (θ_g), the MP12-30 monopile exhibits more rigid behaviour than MP10-30, as indicated by its larger distributed rotations (θ) along the pile. Although analysing the effect of D_p on the ξ_y profile with depth is important, it was excluded from this analysis in the same manner as in the previous section. This exclusion is due to the large ξ_y values in the transition zone around the point of rotation, which prevent drawing reliable conclusions regarding the effect of D_p.

Investigating the effect of D_p on the relationships between ξ_y and y/D_p, and between ξ_θ and θ, is important as it enables the accurate incorporation of foundation damping using the Winkler modelling approach. Figure 6.62 and Figure 6.63 compare the local discrete foundation damping ratios and their relationships with the corresponding deformations for monopiles MP10-30 and MP12-30 at depths of 5.5 m and 12.5 m below the mudline, respectively.

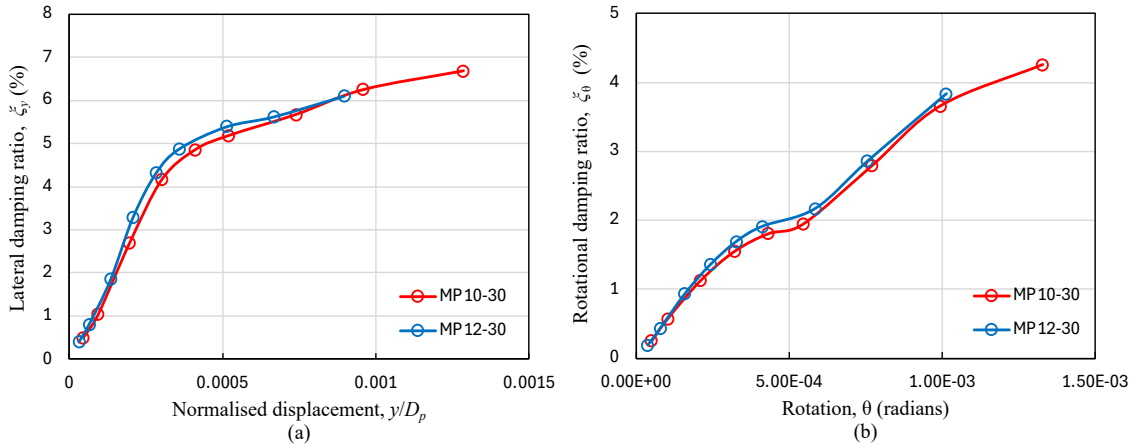


Figure 6.62: Effect of D_p on a pile section 5.5 m below the mudline: (a) ξ_y-y/D_p; (b) ξ_θ-θ

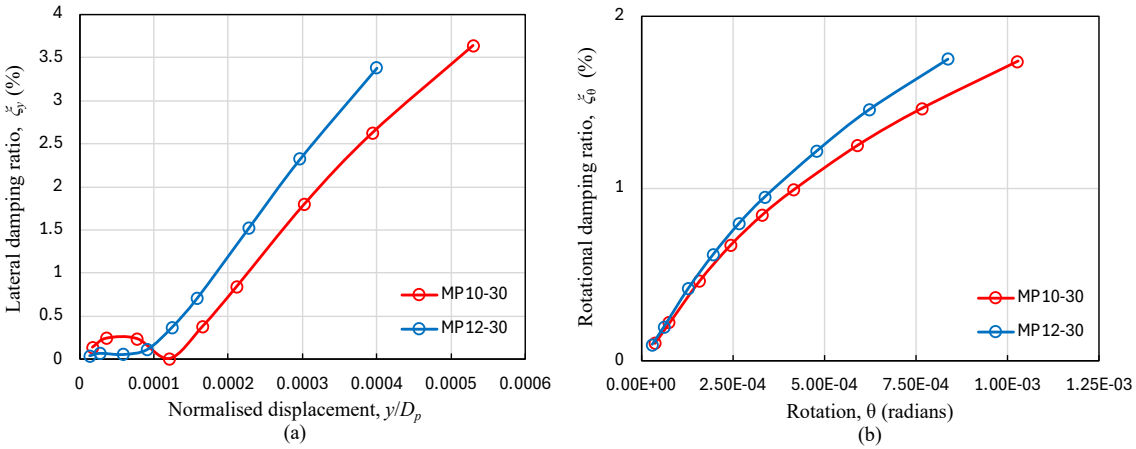


Figure 6.63: Effect of D_p on a pile section 12.5 m below the mudline: (a) ξ_y-y/D_p; (b) ξ_θ-θ

Figure 6.62 shows the same conclusion as observed for the effect of L_p on foundation damping ratios at shallow depths, indicating that at the same y/D_p and θ, ξ_y and ξ_θ are not influenced by the monopile diameter (D_p). However, at greater depths below the mudline, as demonstrated by the results in Figure 6.63, the local damping ratios at the same y/D_p and θ increase as the monopile diameter (D_p) becomes larger. This observation is contrary to the effect of embedment depth (L_p), which causes ξ_y and ξ_θ for a given pile section to decrease as L_p increases. Based on the analysis results presented in Sections 6.5.2.3 and 6.5.2.4, it is more meaningful to draw conclusions about the variation patterns of ξ_y and ξ_θ at any given depth in terms of the slenderness ratio (L_p/D_p). At very shallow depths below the mudline, the monopile dimensions and slenderness ratio do not appear to influence the relationships between the local hysteretic damping ratios and their corresponding pile section deformations. However, at greater depths, for a given y/D_p and θ, the local damping ratios decrease as the slenderness ratio (L_p/D_p) increases whether due to decreasing the monopile diameter (D_p) or increasing the embedment depth (L_p).

6.6 Summary

This chapter presented a detailed account of the 3D FE analysis results based on simulations carried out using the HSsmall and SANISAND-MS constitutive models. The findings highlighted key trends in the variation of foundation damping, particularly in relation to the influence of monopile geometry and the in-situ relative density of the soil profile. Two types of FE analyses were performed:

i. Free-decay simulations: These were conducted to determine the global foundation damping ratios (ζ_f).
ii. Cyclic push-over simulations: These were carried out to evaluate the local hysteretic foundation damping ratios (ξ_y and ξ_θ), determined at the mudline level and along the depth of the monopile.

From these analyses, detailed trends were derived. Regarding the effects of soil relative density and monopile dimensions on ζ_f, the following trends were observed:

i. ζ_f decreases with increasing the monopile embedment depth (L_p). However, this effect diminishes once L_p exceeds the critical pile embedment depth.
ii. ζ_f decreases as the monopile diameter (D_p) increases.
iii. ζ_f is lower in monopiles installed in soil profiles with higher relative density.

Regarding local damping ratios (ξ_y and ξ_θ), obtained from load–deformation hysteresis loops at the mudline, the following observations were made:

i. Local damping ratios (ξ_y and ξ_θ) at the mudline level follow a decreasing trend with increasing pile embedment (L_p).
ii. ξ_y and ξ_θ increase as the monopile diameter (D_p) becomes larger.
iii. For the same monopile dimensions, ξ_y and ξ_θ are lower in soil profiles with higher relative density.

The primary mechanism driving these trends in local damping ratios is monopile slenderness. A monopile with greater embedment depth or one installed in a denser soil profile tends to exhibit a more slender deformation pattern below the mudline, characterised by increased bending rather than rigid body rotation. This results in reduced hysteretic soil response around the monopile at a given depth, thereby lowering the associated damping ratios.

Although, this chapter also covered the local damping ratios (ξ_y and ξ_θ) and provided some important observations, certain discrepancies were noted. For example, monopile dimensions appeared to have little influence on ξ_y-y/D_p and ξ_θ-θ near the mudline, whereas a dependency was observed at greater depths along the embedded length of the monopile. Therefore, to advance the understanding of foundation damping and soil-structure interaction of monopile-supported OWTs, further numerical investigations focusing specifically on damping ratios derived from distributed soil reactions are strongly recommended.

Chapter 7

Conclusions

This research investigated foundation damping for monopile-supported OWTs using 3D FE numerical analyses that incorporated soil constitutive models carefully calibrated through extensive laboratory triaxial test results. It represents a combined experimental and numerical modelling effort to account for the hysteretic behaviour of soil in the soil-structure interaction of OWTs. Half of the research focused on conducting triaxial experiments to understand soil behaviour under varying stress and relative density conditions, while the other half was dedicated to calibrating appropriate constitutive soil models and developing detailed 3D FE models that integrated the soil domain, the monopile, and the OWT structure. The findings of this research provide new insights into how foundation damping varies with different monopile dimensions and ground conditions, ultimately contributing to the design of more efficient monopiles. The primary novelty of this work lies in leveraging state-of-the-art laboratory experiments and constitutive soil models to achieve a more comprehensive understanding of hysteretic foundation damping for OWTs. Furthermore, the database generated from the 3D FE analysis results offers immense value in verifying the development of future advanced soil-structure interaction models. The three main contributions of this thesis are:

i. A new database for dynamic soil parameters are provided.
ii. A new set of calibrated parameters for HSsmall and SANISAND-MS constitutive models.
iii. Detailed investigation of foundation damping through dynamic and cyclic push-over 3D FE simulations.

The first contribution of this research is the development of an extensive database of soil damping ratio and shear modulus reduction curves, derived from cyclic tests conducted using the state-of-the-art DYNTTS triaxial apparatus. The study investigated the variation of these parameters with respect to relative density, mean effective stress, drainage conditions, and the number of cycles. The study found that the damping ratio increases as the mean effective stress reduces, aligning with the behaviour observed from numerous research studies. In terms of the effect of relative density, both drained and undrained cyclic tests revealed that the effect of relative density is insignificant for small cyclic shear strain levels below 0.1%. However, undrained tests demonstrated that as soil dilatancy becomes more pronounced, the damping ratios of contractive loose samples exceed those of dilative dense samples. In terms of the normalised shear modulus ratio, the drained tests

confirmed the findings of previous studies, showing that at a given shear strain, the normalised shear modulus ratio increases with mean effective stress and is largely unaffected by relative density. The experimental study also placed significant emphasis on the impact of the number of cycles on the damping ratio, given that large number of cycles is the key feature of the dynamic loads imposed on OWTs. The results showed that the damping ratio decreases as the number of cycles increases, regardless of the initial relative density. However, the rate of this decay was found to be minimal, with the damping ratio fully stabilising by 1000 cycles. Notably, the effect of the number of cycles may vary between different soils, as some studies have found its impact to be negligible, while others found it to be significant. A novel aspect of this research is the comparison of damping ratios obtained from both drained and undrained tests, revealing that the damping ratios from the drained tests were higher than those from the undrained tests. The higher damping observed in the drained test results could be attributed to the presence of volumetric hysteretic behaviour, which occurs when drainage is permitted. In contrast, undrained tests lack this contribution and only exhibit deviatoric hysteretic behaviour. However, further tests on different soil materials are required to fully validate this finding. In addition to identifying the trends in the variations of damping ratio and shear modulus reduction, the dynamic parameters were curve-fitted using empirical functions. These empirical functions can provide representative damping ratio and shear modulus reduction curves when laboratory test results are unavailable during the early stages of design. Extensive monotonic tests were also conducted on Blessington sand to evaluate its softening and hardening behaviour under varying mean effective stresses and relative densities. The results of these monotonic tests were instrumental in calibrating the HSsmall and SANISAND-MS model parameters, ensuring that the models replicate the observed monotonic behaviour with reasonable accuracy.

The results and trends obtained from the triaxial testing campaign were used to calibrate the parameter values of both the HSsmall model and the advanced SANISAND-MS constitutive model, which has been recently incorporated into Plaxis 3D. Parameters for each model were derived from monotonic and cyclic triaxial tests conducted on Blessington sand. These calibrated models offer a reliable framework for realistically capturing the mechanical behaviour of sand, thereby enabling accurate analysis of soil-structure interaction for monopile-supported OWTs. Calibrating two distinct constitutive models, each governed by different hardening laws and mechanical evolution mechanisms and subject to specific limitations, provides greater confidence in the findings and observed trends related to the soil-structure interaction of large-scale OWT systems. Finally, in addition to parameter calibration, this study also highlighted the limitations of the HSsmall and SANISAND-MS models in representing certain aspects of the monotonic and cyclic behaviour of soil.

The 3D FE analyses extensively covered the effects of monopile dimensions and soil relative density (i.e., ground conditions) on foundation damping and provided interpretations and

underlying mechanisms of the trends observed from the numerical analysis results. The monopile dimensions were selected to fall within the range commonly used for large OWTs, such as the reference IEA 15 MW wind turbine. The ground conditions were modelled using two significantly different relative densities to provide a clear understanding of how soil profiles with varying densities can influence damping parameters for monopiles of the same size. Furthermore, the numerical analyses were conducted using two constitutive soil models (HSsmall and SANISAND-MS), which produced consistent patterns and thus validated the conclusions drawn from the simulations. The findings regarding the effects of the monopile dimensions and ground conditions were derived from two different types of numerical 3D FE analyses:

i. Dynamic free-decay simulations: These simulations were performed to evaluate the global foundation damping ratio (ζ_f). The value of ζ_f is governed by the total plastic energy dissipated by the soil continuum and the total elastic energy stored in the overall soil-OWT system.
ii. Cyclic push-over simulations: These simulations were used to evaluate local foundation damping ratios (ξ_y and ξ_θ) from hysteresis loops. Damping ratios were obtained from load-deformation loops at the mudline, representing overall foundation damping, and from soil reaction-deformation loops along the monopile depth, representing local damping at discrete depths.

Unlike previous studies, which focused solely on either global or local damping ratios, this research investigated both and examined the relationships between them. One important finding is that although changes in monopile dimensions can lead to higher local damping ratios, the global foundation damping ratio (ζ_f) may decrease. This occurs despite the increased local hysteresis at the foundation level, due to a rise in the total elastic energy stored in the overall soil-OWT system. As a result, this study provided a comprehensive understanding of the effects of the monopile geometry and ground conditions on foundation damping of OWTs.

The main outcome of the 3D FE numerical analyses is the determined values of the global and local foundation damping ratios. These can be adopted in integrated OWT dynamic analysis tools (such as OpenFAST and HAWC2) for modelling the response OWTs. However, field monitoring studies are necessary to validate whether the damping ratios derived from this research fall within the expected range for real-world OWTs. Furthermore, since the analyses were conducted under fully drained soil conditions, it would be worthwhile to extend the study to include undrained soil behaviour in order to examine the influence of drainage conditions on foundation damping.

Finally, the last sections of this chapter highlighted discrepancies in the effect of monopile geometry on the distributed foundation damping ratios at discrete depths along the monopile. While the monopile dimensions had no influence on the local damping ratios at shallow depths, they influenced the damping ratios at greater depths. This finding is important, and further studies

focusing specifically on distributed foundation damping ratios are needed to enable accurate incorporation of foundation damping using the Winkler approach.

References

Aasen, S., Page, A., Skau, K., & Nygaard, T. (2017). Effect of the Foundation Modelling on the Fatigue Lifetime of a Monopile-based Offshore Wind Turbine. *Wind Energy Science Discussions*, 361–376. https://doi.org/10.5194/wes-2016-37

Abadie, C. (2015). *Cyclic Lateral Loading of Monopile Foundations in Cohesionless Soils* [PhD thesis, University of Oxford]. https://ora.ox.ac.uk/objects/uuid:b3002ca4-742d-4b08-836f-1c15eafb7156

Abdellaziz, M., Karray, M., Chekired, M., Delisle, M.-C., Locat, P., Ledoux, C., & Mompin, R. (2023). New model of shear modulus degradation and damping ratio curves for sensitive Canadian clays. *Canadian Geotechnical Journal*, *60*(6), 784–801. https://doi.org/10.1139/cgj-2021-0475

Achmus, M., Kuo, Y.-S., & Abdel-Rahman, K. (2009). Behavior of monopile foundations under cyclic lateral load. *Computers and Geotechnics*, *36*(5), 725–735. https://doi.org/10.1016/j.compgeo.2008.12.003

Akeju, O. V., Senetakis, K., & Wang, Y. (2019). Bayesian Parameter Identification and Model Selection for Normalized Modulus Reduction Curves of Soils. *Journal of Earthquake Engineering*, *23*(2), 305–333. https://doi.org/10.1080/13632469.2017.1323051

Alderlieste, E., Dijkstra, J., & Tol, A. V. (2011). *Experimental Investigation Into Pile Diameter Effects of Laterally Loaded Mono-Piles*. https://api.semanticscholar.org/CorpusID:108508221

Anandavijayan, S., Mehmanparast, A., & Brennan, F. (2018). A numerical analysis of the effects of manufacturing processes on material pre-strain in offshore wind monopiles. *Procedia Structural Integrity*, *13*, 953–958. https://doi.org/10.1016/j.prostr.2018.12.178

Andersen, K. (2015, June). *Cyclic soil parameters for offshore foundation design. The 3rd McClelland Lecture.*

Andersen, K. H., Engin, H. K., D'Ignazio, M., & Yang, S. (2023). Determination of cyclic soil parameters for offshore foundation design from an existing data base. *Ocean Engineering*, *267*, 113180. https://doi.org/10.1016/j.oceaneng.2022.113180

API. (2010). *RP 2A-WSD - Recommended Practice for Planning, Designing and Constructing Fixed O shore Platforms*.

Arulnathan, R., Boulanger, R., & Riemer, M. (1998). Analysis of Bender Element Tests. *Geotechnical Testing Journal*, *21*(2), 120–131. https://doi.org/10.1520/GTJ10750J

Augustesen, A. H., Brødbæk, K. T., Møller, M., Sørensen, S. P. H., Ibsen, L. B., Pedersen, T. Ø., & Andersen, L. V. (2009). *Numerical Modelling of Large-Diameter Steel Piles at Horns Rev*. https://api.semanticscholar.org/CorpusID:113456992

Bakri, H. (2021). *Experimental and numerical study of soil-structure interaction subjected to cyclic-dynamic loading: Application to o shore wind turbine monopile foundation* [PhD thesis]. Ecole des Ponts ParisTech.

Been, K., & Jefferies, M. (1985). A state parameter for sands. *Geotechnique*, *35*, 99–112. https://doi.org/10.1680/geot.1985.35.2.99

Been, K., Jefferies, M., & Hachey, J. (1991). The critical state of sand. *Geotechnique*, *41*, 365–381. https://doi.org/10.1680/geot.1991.41.3.365

Benz, T. (2007). *Citation-268592022.bib* [PhD thesis]. universität stuttgart.

Beuckelaers, W. (2017). *Numerical Modelling of Laterally Loaded Piles for Offshore Wind Turbines* [PhD thesis, University of Oxford]. https://ora.ox.ac.uk/objects/uuid:9feba16c-fc8e-464e-8928-3ca3a7a9fb73

Bhattacharya, S., Nikitas, N., Garnsey, J., Alexander, N. A., Cox, J., Lombardi, D., Wood, D. M., & Nash, D. F. T. (2013). Observed dynamic soil–structure interaction in scale testing of offshore wind turbine foundations. *Soil Dynamics and Earthquake Engineering*, *54*, 47–60. https://doi.org/10.1016/j.soildyn.2013.07.012

Bishop, A. W., & Henkel, D. J. (1962). *The Measurement of Soil Properties in the Triaxial Test*. Edward Arnold. https://books.google.ie/books?id=-Ra2tAEACAAJ

Blaker, Ø., & Andersen, K. H. (2019). Cyclic properties of dense to very dense silica sand. *Soils and Foundations*, *59*(4), 982–1000. https://doi.org/10.1016/j.sandf.2019.04.002

Brinkgreve, R., Engin, E., & Engin, H. K. (2010, June). *Validation of empirical formulas to derive model parameters for sands*. https://doi.org/10.1201/b10551-25

Brinkgreve, R., Kappert, M., & Bonnier, P. (2007). *Hysteretic damping in a small-strain stiffness model*. https://doi.org/10.1201/NOE0415440271.ch106

Burd, H. J., Beuckelaers, W. J. A. P., Byrne, B. W., Gavin, K. G., Houlsby, G. T., Igoe, D. J. P., Jardine, R. J., Martin, C. M., McAdam, R. A., Muir Wood, A., Potts, D. M., Skov Gretlund, J., Taborda, D. M. G., & Zdravković, L. (2020). New data analysis methods for instrumented medium-scale monopile field tests. *Géotechnique*, *70*(11), 961–969. https://doi.org/10.1680/jgeot.18.PISA.002

Burd, H. J., Taborda, D. M. G., Zdravković, L., Abadie, C. N., Byrne, B. W., Houlsby, G. T., Gavin, K. G., Igoe, D. J. P., Jardine, R. J., Martin, C. M., McAdam, R. A., Pedro, A. M. G., & Potts, D. M. (2020). PISA design model for monopiles for offshore wind turbines: Application to a marine sand. *Géotechnique*, *70*(11), 1048–1066. https://doi.org/10.1680/jgeot.18.P.277

Burland, J. (1989). Ninth Laurits Bjerrum Memorial Lecture. 'Small is beautiful'. The stiffness of soils at small strains. *Canadian Geotechnical Journal - CAN GEOTECH J*, *26*, 499–516. https://doi.org/10.1139/t89-064

Byrne, B., Mcadam, R., Burd, H., Houlsby, G., Martin, C., Gavin, K., Doherty, P., Igoe, D., Taborda, D. M. G., Potts, D., Jardine, R., Sideri, M., Schroeder, F., Muir-Wood, A., Kallehave, D., & Skov-Gretlund, J. (2015, September). *Field testing of large diameter piles under lateral loading for offshore wind applications*.

Byrne, B., Mcadam, R., Burd, H., Houlsby, G., Martin, C., Zdravkovic, L., Taborda, D. M. G., Potts, D., Jardine, R., Sideri, M., Schroeder, F., Gavin, K., Doherty, P., Igoe, D., Wood, A., Kallehave, D., & Gretlund, J. (2015, June). *New design methods for large diameter piles under lateral loading for offshore wind applications*. https://doi.org/10.1201/b18442-96

Carswell, W., Arwade, S. R., Johansson, J., & DeGroot, D. J. (2022). Influence of foundation damping on offshore wind turbine monopile design loads. *Marine Structures*, *83*, 103154. https://doi.org/10.1016/j.marstruc.2021.103154

Carswell, W., Johansson, J., Løvholt, F., Arwade, S. R., Madshus, C., DeGroot, D. J., & Myers, A. T. (2015). Foundation damping and the dynamics of offshore wind turbine monopiles. *Renewable Energy*, *80*, 724–736. https://doi.org/10.1016/j.renene.2015.02.058

Casagrande, A. (1976). *Liquefaction and Cyclic Deformation of Sands: A Critical Review*. Harvard University. https://books.google.ie/books?id=SK86nQEACAAJ

Cerfontaine, B. (2014). *The cyclic behaviour of sand, from the Prevost model to offshore geotechnics* [PhD thesis]. University of Liège.

Chu, J. (1995). An experimental examination of the critical state and other similar concepts for granular soils. *Canadian Geotechnical Journal*, *32*(6), 1065–1075. https://doi.org/10.1139/t95-104

Ciancimino, A. (2021). *Performance of caisson foundations subjected to flood-induced scour* [PhD thesis]. Politecnico di Torino.

Ciancimino, A., Lanzo, G., Alleanza, G., Amoroso, S., Bardotti, R., Biondi, G., Cascone, E., Castelli, F., Di Giulio, A., d'ONOFRIO, A., Foti, S., Lentini, V., Madiai, C., & Vessia, G. (2020). Dynamic characterization of fine-grained soils in Central Italy by laboratory testing. *Bulletin of Earthquake Engineering*, *18*. https://doi.org/10.1007/s10518-019-00611-6

Clayton, C., & Khatrush, S. (1986). A new device for measuring local axial strains on triaxial specimens. *Geotechnique*, *36*, 593–597. https://doi.org/10.1680/geot.1986.36.4.593

Clayton, C., Khatrush, S., Bica, A., & Siddique, A. (1989). Use of hall effect semiconductors in geotechnical instrumentation. *Geotechnical Testing Journal*, *12*, 69–76. https://doi.org/10.1520/GTJ10676J

CLAYTON, C. R. I. (2011). Stiffness at small strain: Research and practice. *Géotechnique*, *61*(1), 5–37. https://doi.org/10.1680/geot.2011.61.1.5

Corciulo, S., Zanoli, O., & Pisanò, F. (2017). Transient response of offshore wind turbines on monopiles in sand: Role of cyclic hydro–mechanical soil behaviour. *Computers and Geotechnics*, *83*, 221–238. https://doi.org/10.1016/j.compgeo.2016.11.010

Cox, W. R., Reese, L. C., & Grubbs, B. R. (1974). *Field Testing of Laterally Loaded Piles In Sand: Vol. All Days*. https://doi.org/10.4043/2079-MS

Cuccovillo, T., & Coop, M. R. (1997). THE MEASUREMENT OF LOCAL AXIAL STRAINS IN TRIAXIAL TESTS USING LVDTS. *Geotechnique*, *47*, 167–171.

Cuéllar, P., Baeßler, M., & Rücker, W. (2009). Ratcheting convective cells of sand grains around offshore piles under cyclic lateral loads. *Granular Matter*, *11*, 379–390. https://doi.org/10.1007/s10035-009-0153-3

Dafalias, Y. F., & Popov, E. P. (1975). A model of nonlinearly hardening materials for complex loading. *Acta Mechanica*, *21*, 173–192.

Dafalias, Y., & Manzari, M. (2004). Simple Plasticity Sand Model Accounting for Fabric Change Effects. *Journal of Engineering Mechanics-Asce - J ENG MECH-ASCE*, *130*. https://doi.org/10.1061/(ASCE)0733-9399(2004)130:6(622)

Damgaard, M. (2014). *Dynamic Properties of Offshore Wind Turbine Foundations* [PhD thesis]. Aalborg University.

Damgaard, M., Andersen, J., Ibsen, L., & Andersen, L. (2012). Natural frequency and damping estimation of an offshore wind turbine structure. *Proceedings of the International Offshore and Polar Engineering Conference*, 300–307.

Damgaard, M., Ibsen, L., Andersen, L., & Andersen, J. (2013a, January). Time-varying dynamic properties of offshore wind turbines evaluated by modal testing. *Proceedings of the 18th International Conference on Soil Mechanics and Geotechnical Engineering*.

Damgaard, M., Ibsen, L. B., Andersen, L. V., & Andersen, J. K. F. (2013b). Cross-wind modal properties of offshore wind turbines identified by full scale testing. *Journal of Wind Engineering and Industrial Aerodynamics*, *116*, 94–108. https://doi.org/10.1016/j.jweia.2013.03.003

Damgaard, M., Zania, V., Andersen, L. V., & Ibsen, L. B. (2014). Effects of soil–structure interaction on real time dynamic response of offshore wind turbines on monopiles. *Engineering Structures*, *75*, 388–401. https://doi.org/10.1016/j.engstruct.2014.06.006

Darendeli, M. (2001). *DEVELOPMENT OF A NEW FAMILY OF NORMALIZED MODULUS REDUCTION AND MATERIAL DAMPING CURVES* [PhD thesis]. University of Texas at Austin.

Devriendt, C., Jordaens, P. J., De Sitter, G., & Guillaume, P. (2013). Damping estimation of an offshore wind turbine on a monopile foundation. *Renewable Power Generation, IET*, *7*, 401–412. https://doi.org/10.1049/iet-rpg.2012.0276

Diambra, A. (2010). *Fibre reinforced sands: Experiments and constitutive modelling* [PhD thesis]. University of Bristol.

DNV. (2014). *Offshore Standard—Design of Offshore Wind Turbine Structures (DNVOS- J101)*.

Dobry, R., Ladd, R. S., Yokel, F. Y., Chung, R. M., & Powell, D. J. (1982). *Prediction of pore water pressure buildup and liquefaction of sands during earthquakes by the cyclic strain method*. https://api.semanticscholar.org/CorpusID:127267410

Doherty, P., & Gavin, K. (2012). Laterally loaded monopile design for offshore wind farms. *Proceedings of the Institution of Civil Engineers - Energy*, *165*(1), 7–17. https://doi.org/10.1680/ener.11.00003

ESCRIBANO, D. (2014). *EVOLUTION OF STIFFNESS AND DEFORMATION OF HOSTUN SAND UNDER DRAINED CYCLIC LOADING* [PhD thesis]. University of Bristol.

Fam, M. A., Cascante, G., & Dusseault, M. B. (2002). Large and Small Strain Properties of Sands Subjected to Local Void Increase. *Journal of Geotechnical and Geoenvironmental Engineering*, *128*(12), 1018–1025. https://doi.org/10.1061/(ASCE)1090-0241(2002)128:12(1018)

Fam, M., & Santamarina, C. (1995). Study of Geoprocesses with Complementary Mechanical and Electromagnetic Wave Measurements in an Oedometer. *Geotechnical Testing Journal*, *18*(3), 307–314. https://doi.org/10.1520/GTJ10999J

Fioravante, V. (2000). Anisotropy of Small Strain Stiffness of Ticino and Kenya Sands from Seismic Wave Propagation Measured in Triaxial Testing. *Soils and Foundations*, *40*(4), 129–142. https://doi.org/10.3208/sandf.40.4_129

Fuentes, W., & Triantafyllidis, T. (2015). ISA model: A constitutive model for soils with yield surface in the intergranular strain space. *International Journal for Numerical and Analytical Methods in Geomechanics*, *39*, 1235–1254.

Gaertner, E., Rinker, J., Sethuraman, L., Zahle, B. A., & et al. (2020). *Definition of the IEA 15-megawatt offshore reference wind turbine*.

Gajo, A., & Wood, M. (1999). Severn–Trent sand: A kinematic-hardening constitutive model: The q–p formulation. *Géotechnique*, *49*(5), 595–614. https://doi.org/10.1680/geot.1999.49.5.595

Germanischer Lloyd. (2005). *Overall damping for piled offshore support structures'. Guideline for the Certification of OffshoreWind Turbines, WindEnergie*.

Ghionna, V. N., & Porcino, D. (2006). Liquefaction Resistance of Undisturbed and Reconstituted Samples of a Natural Coarse Sand from Undrained Cyclic Triaxial Tests. *Journal of Geotechnical and Geoenvironmental Engineering*, *132*(2), 194–202. https://doi.org/10.1061/(ASCE)1090-0241(2006)132:2(194)

Goto, S., Tatsuoka, F., Shibuya, S., Kim, Y.-S., & Sato, T. (1991). A Simple Gauge for Local Small Strain Measurements in the Laboratory. *Soils and Foundations*, *31*(1), 169–180. https://doi.org/10.3208/sandf1972.31.169

GWEC. (2024a). *GLOBAL OFFSHORE WIND REPORT 2024*.

Hardin, B., & Drnevich, V. (1972a). Shear modulus and damping in soil: Measurement and parameter effects. *Journal of the Soil Mechanics and Foundation Engineering ASCE*, *98*, 603–624. https://doi.org/10.1061/JSFEAQ.0001756

Hardin, B., & Drnevich, V. (1972b). Shear Modulus and Damping in Soils: Design Equations and Curves. *J. Soil Mech. Found. Div.*, *98*. https://doi.org/10.1061/JSFEAQ.0001760

Hardin, B., & Kalinski, M. (2005). Estimating the Shear Modulus of Gravelly Soils. *Journal of Geotechnical and Geoenvironmental Engineering - J GEOTECH GEOENVIRON ENG*, *131*. https://doi.org/10.1061/(ASCE)1090-0241(2005)131:7(867)

Hardin, B. O., & Black, W. L. (1966). Sand Stiffness Under Various Triaxial Stresses. *Journal of the Soil Mechanics and Foundations Division*, *92*(2), 27–42. https://doi.org/10.1061/JSFEAQ.0000865

Henkel, D. J., & Gilbert, G. D. (1952). The Effect Measured of the Rubber Membrane on the Triaxial Compression Strength of Clay Samples. *Geotechnique*, *3*, 20–29.

Hird, C., & Yung, P. (1989). The Use of Proximity Transducers for Local Strain Measurements in Triaxial Tests. *Geotechnical Testing Journal*, *12*(4), 292–296. https://doi.org/10.1520/GTJ10987J

Hoque, E., Sato, T., & Tatsuoka, F. (1997). Performance Evaluation of LDTs for Use in Triaxial Tests. *Geotechnical Testing Journal*, *20*(2), 149–167. https://doi.org/10.1520/GTJ10735J

Houlsby, G., & Puzrin, A. (2007). Principles of Hyperplasticity, An Approach to Plasticity Theory Based on Thermodynamic Principles. *Principles of Hyperplasticity: An Approach to Plasticity Theory Based on Thermodynamic Principles*, 1–351. https://doi.org/10.1007/978-1-84628-240-9

IEA. (2019). *Offshore Wind Outlook 2019*.

Ishibashi, I., & Zhang, X. (1993). Unified Dynamic Shear Moduli and Damping Ratios of Sand and Clay. *Soils and Foundations*, *33*(1), 182–191. https://doi.org/10.3208/sandf1972.33.182

Ishihara, K. (1993). Liquefaction and flow failure during earthquakes. *Géotechnique*, *43*(3), 351–451. https://doi.org/10.1680/geot.1993.43.3.351

Ishihara, K. (1996). *Soil Behaviour in Earthquake Geotechnics*. Oxford University Press. https://doi.org/10.1093/oso/9780198562245.001.0001

Ishihara, K., Tatsuoka, F., & Yasuda, S. (1975). Undrained Deformation and Liquefaction of Sand Under Cyclic Stresses. *Soils and Foundations*, *15*(1), 29–44. https://doi.org/10.3208/sandf1972.15.29

Jaky, J. (1944). The coefficient of earth pressure at rest. *Journal of the Society of Hungarian Architects and Engineering*, 355–358.

Janbu, N. (1963). Soil compressibility as determined by oedometer and triaxial tests. *ECSMFE Wiesbaden*, 1, 19–25.

Jardine, R. J. (1992). Some Observations on the Kinematic Nature of Soil Stiffness. *Soils and Foundations*, *32*(2), 111–124. https://doi.org/10.3208/sandf1972.32.2_111

Jefferies, M., & Been, K. (2015). *Soil Liquefaction: A Critical State Approach, Second Edition*. CRC Press. https://books.google.ie/books?id=atiYCgAAQBAJ

Jindal, S., Rahmanli, U., Aleem, M., Cui, L., & Bhattacharya, S. (2024). Identification of soil damping for stiff piles based on experiments: Soil damping curves from physical model tests. *Ocean Engineering*, *310*, 118497. https://doi.org/10.1016/j.oceaneng.2024.118497

Kallehave, D., Byrne, B., Thilsted, C., & Mikkelsen, K. (2015). Optimization of monopiles for offshore wind turbines. *Philosophical Transactions. Series A, Mathematical, Physical, and Engineering Sciences*, *373*. https://doi.org/10.1098/rsta.2014.0100

Kallehave, D., Thilsted, C. L., & Liingaard, M. A. (2012). *Modification of the API P-y Formulation of Initial Stiffness of Sand: Vol. All Days*.

Kallioglou, P., Tika, T., & Pitilakis, K. (2008). Shear Modulus and Damping Ratio of Cohesive Soils. *Journal of Earthquake Engineering*, *12*, 879–913. https://doi.org/10.1080/13632460801888525

Kaynia, A., & Andersen, K. (2015). *Development of nonlinear foundation springs for dynamic analysis of platforms* (pp. 1067–1072). https://doi.org/10.1201/b18442-158

Kaynia, A. M. (2019). Seismic considerations in design of offshore wind turbines. *Soil Dynamics and Earthquake Engineering*, *124*, 399–407. https://doi.org/10.1016/j.soildyn.2018.04.038

Kementzetzidis, E., Corciulo, S., Versteijlen, W. G., & Pisanò, F. (2019). Geotechnical aspects of offshore wind turbine dynamics from 3D non-linear soil-structure simulations. *Soil Dynamics and Earthquake Engineering*, *120*, 181–199. https://doi.org/10.1016/j.soildyn.2019.01.037

Kirkpatrick, W. M., & Younger, J. S. (1970). Strain Conditions in Compression Cylinder. *Journal of the Soil Mechanics and Foundations Division*, *96*(5), 1683–1695. https://doi.org/10.1061/JSFEAQ.0001460

Kirwan, L. (2015). *Investigation into Ageing Mechanisms for Axially Loaded Piles Driven in Sand* [PhD thesis]. University College Dublin.

Klinkvort, R. (2012). *Centrifuge modelling of drained lateral pile-soil response* [PhD thesis]. DTU.

Klinkvort, R. T., & Hededal, O. (2013). Lateral response of monopile supporting an offshore wind turbine. *Proceedings of the ICE - Geotechnical Engineering*, *166*, 147–158. https://doi.org/10.1680/geng.12.00033

Klotz, E., & Coop, M. (2002). On the Identification of Critical State Lines for Sands. *Geotechnical Testing Journal*, *25*(3), 289–302. https://doi.org/10.1520/GTJ11090J

Kokusho, T. (1980). Cyclic Triaxial Test of Dynamic Soil Properties for Wide Strain Range. *Soils and Foundations*, *20*(2), 45–60. https://doi.org/10.3208/sandf1972.20.2_45

Koukoura, C., Natarajan, A., & Vesth, A. (2015). Identification of support structure damping of a full scale offshore wind turbine in normal operation. *Renewable Energy*, *81*, 882–895. https://doi.org/10.1016/j.renene.2015.03.079

Kowalczyk, P. (2020). *Validation and application of advanced soil constitutive models in numerical modelling of soil and soil-structure interaction under seismic loading* [PhD thesis]. University of Trento.

Kuerbis, R., & Vaid, Y. P. (1988). Sand Sample Preparation—The Slurry Deposition Method. *Soils and Foundations*, *28*(4), 107–118. https://doi.org/10.3208/sandf1972.28.4_107

Kuwano, R., Connolly, T., & Jardine, R. J. (2000). ANISOTROPIC STIFFNESS MEASUREMENTS IN A STRESS-PATH TRIAXIAL CELL. *Geotechnical Testing Journal*, *23*, 141–157.

Ladd, R. (1978). Preparing Test Specimens Using Undercompaction. *Geotechnical Testing Journal*, *1*(1), 16–23. https://doi.org/10.1520/GTJ10364J

Lade, P. (2005). Overview of Constitutive Models For Soils. *Geotechnical Special Publication*, 1–34. https://doi.org/10.1061/40771(169)1

Lade, P. (2016). *Triaxial Testing of Soils* (First Edition). John Wiley & Sons, Ltd.

Lade, P. V., & Ibsen, L. B. (1997). *A Study of the Phase Transformation and the Characteristic Lines of Sand Behaviour*. https://api.semanticscholar.org/CorpusID:132985194

Lanzo, G., Vucetic, M., & Doroudian, M. (1997). Reduction of Shear Modulus at Small Strains in Simple Shear. *Journal of Geotechnical and Geoenvironmental Engineering*, *123*(11), 1035–1042. https://doi.org/10.1061/(ASCE)1090-0241(1997)123:11(1035)

Leblanc, C., Byrne, B., & Houlsby, G. (2010). Response of stiff piles to long term cyclic loading. *Geotechnique*, *60*, 79–90. https://doi.org/10.1680/geot.7.00196

Leong, E., Yeo, S., & Rahardjo, H. (2005). Measuring Shear Wave Velocity Using Bender Elements. *Geotechnical Testing Journal*, *28*(5), 488–498. https://doi.org/10.1520/GTJ12196

Li, S., Zhang, Y., & Jostad, H. P. (2019). Drainage conditions around monopiles in sand. *Applied Ocean Research*, *86*, 111–116. https://doi.org/10.1016/j.apor.2019.01.024

Li, X.-S., Dafalias, Y. F., & Wang, Z.-L. (1999). State-dependant dilatancy in critical-state constitutive modelling of sand. *Canadian Geotechnical Journal*, *36*(4), 599–611. https://doi.org/10.1139/t99-029

Li, Z., Escoffier, S., & Kotronis, P. (2020). Study on the stiffness degradation and damping of pile foundations under dynamic loadings. *Engineering Structures*, *203*, 109850. https://doi.org/10.1016/j.engstruct.2019.109850

LIU, H. (2020). *Constitutive modelling of cyclic sand behaviour for offshore foundations* [PhD thesis]. Delft University of Technology.

Liu, H., & Kaynia, A. M. (2023). Characteristics of cyclic undrained model SANISAND-MSu and their effects on response of monopiles for offshore wind structures. *Géotechnique*, *73*(4), 294–309. https://doi.org/10.1680/jgeot.21.00068

Lo Presti, D., Pedroni, S., Cavallaro, A., Jamiolkowski, M., & Pallara, O. (1997). Shear modulus and damping of soils. *Geotechnique*, *47*, 603–617. https://doi.org/10.1680/geot.1997.47.3.603

Lombardi, D., Bhattacharya, S., & Muir Wood, D. (2013). Dynamic soil–structure interaction of monopile supported wind turbines in cohesive soil. *Soil Dynamics and Earthquake Engineering*, *49*, 165–180. https://doi.org/10.1016/j.soildyn.2013.01.015

Loukidis, D., & Salgado, R. (2009). Modeling sand response using two-surface plasticity. *Computers and Geotechnics*, *36*(1), 166–186. https://doi.org/10.1016/j.compgeo.2008.02.009

Løvholt, F., Madshus, C., & Andersen, K. (2020). Intrinsic Soil Damping from Cyclic Laboratory Tests with Average Strain Development. *Geotechnical Testing Journal*, *43*, 20170411. https://doi.org/10.1520/GTJ20170411

Lunne, T., Knudsen, S., Blaker, Ø., Vestgården, T., Powell, J., Wallace, C. F., Krogh, L., Thomsen, N. V., Yetginer, G., & Ghanekar, R. K. (2019). Methods used to determine maximum and minimum dry unit weights of sand: Is there a need for a new standard? *Canadian Geotechnical Journal*, *56*, 536–553. https://doi.org/10.1139/cgj-2017-0738

Luong, P. (1980). Stress strain aspects of cohesionless soils under cyclic and transient loading. Proceedings of the International Symposium on Soils under cyclic and transient loading. *Swansea*, 353–376.

Malekjafarian, A., Jalilvand, S., Doherty, P., & Igoe, D. (2021). Foundation damping for monopile supported offshore wind turbines: A review. *Marine Structures*, *77*, 102937. https://doi.org/10.1016/j.marstruc.2021.102937

Malekjafarian, A., Jalilvand, S., Igoe, D., & Doherty, P. (2019). On the estimation of foundation damping of mono pile-supported offshore wind turbines. *Vibroengineering PROCEDIA*, *23*, 7–12. https://doi.org/10.21595/vp.2019.20648

Manzari, M. T., & Dafalias, Y. F. (1997). A critical state two-surface plasticity model for sands. *Géotechnique*, *47*(2), 255–272. https://doi.org/10.1680/geot.1997.47.2.255

Masing, G. (1926). Eigenspannugen und Verfestigung beim Messing. *Proceedings of Second International Congress of Applied Mechanics*, 332–335.

Matlock, H. (1970). *Correlation for Design of Laterally Loaded Piles in Soft Clay*. https://api.semanticscholar.org/CorpusID:138662139

Menq. (2003). *Dynamic Properties of Sandy and Gravelly Soils* [PhD thesis]. University of Texas at Austin.

Mitchell, J. K., & Soga, Kenichi. (2005). Fundamentals of soil behavior. In *Fundamentals of soil behavior* (3rd ed). Wiley.

Miura, S., & Toki, S. (1982). A Sample Preparation Method and its Effect on Static and Cyclic Deformation-Strength Properties of Sand. *Soils and Foundations*, *22*(1), 61–77. https://doi.org/10.3208/sandf1972.22.61

Mortezaie, A., & Vucetic, M. (2016). Threshold Shear Strains for Cyclic Degradation and Cyclic Pore Water Pressure Generation in Two Clays. *Journal of Geotechnical and Geoenvironmental Engineering*, *142*, 04016007. https://doi.org/10.1061/(ASCE)GT.1943-5606.0001461

Mróz, Z. (1967). On the description of anisotropic workhardening. *Journal of the Mechanics and Physics of Solids*, *15*(3), 163–175. https://doi.org/10.1016/0022-5096(67)90030-0

Murphy, G., Igoe, D., Doherty, P., & Gavin, K. (2018). 3D FEM approach for laterally loaded monopile design. *Computers and Geotechnics*, *100*, 76–83. https://doi.org/10.1016/j.compgeo.2018.03.013

Newman, J. N. (2018). *Marine hydrodynamics*. The MIT press.

Nicholson, P. G., Seed, R. B., & Anwar, H. A. (1993). Elimination of membrane compliance in undrained triaxial testing. I. Measurement and evaluation. *Canadian Geotechnical Journal*, *30*(5), 727–738. https://doi.org/10.1139/t93-065

Niemunis, A., & Herle, I. (1997). Hypoplastic Model for Cohesionless Soils with Elastic Strain Range. *Mechanics of Cohesive-frictional Materials*, *2*, 279–299. https://doi.org/10.1002/(SICI)1099-1484(199710)2:4<279::AID-CFM29>3.0.CO;2-8

Niemunis, A., Wichtmann, T., & Triantafyllidis, T. (2005). A high-cycle accumulation model for sand. *Computers and Geotechnics*, 245–263. https://doi.org/10.1016/j.compgeo.2005.03.002

Nikitas, G., Vimalan, N. J., & Bhattacharya, S. (2016). An innovative cyclic loading device to study long term performance of offshore wind turbines. *Soil Dynamics and Earthquake Engineering*, *82*, 154–160. https://doi.org/10.1016/j.soildyn.2015.12.008

Oda, M., Koishikawa, I., & Higuchi, T. (1978). Experimental Study of Anisotropic Shear Strength of Sand by Plane Strain Test. *Soils and Foundations*, *18*(1), 25–38. https://doi.org/10.3208/sandf1972.18.25

O'neill, M. W., & Murchison, J. M. (1984). *Evaluation of p-y relationships in cohesionless soils*. https://api.semanticscholar.org/CorpusID:132084991

Oztoprak, S., & Bolton, M. D. (2013). Stiffness of sands through a laboratory test database. *Geotechnique*, *63*, 54–70.

Page, A. M., Grimstad, G., Eiksund, G. R., & Jostad, H. P. (2018). A macro-element pile foundation model for integrated analyses of monopile-based offshore wind turbines. *Ocean Engineering*, *167*, 23–35. https://doi.org/10.1016/j.oceaneng.2018.08.019

Page, A., Schafhirt, S., Eiksund, G., Skau, K., Jostad, H., & Sturm, H. (2016, June). *Alternative Numerical Pile Foundation Models for Integrated Analyses of Monopile-based Offshore Wind Turbines*.

Panagoulias, S., Brinkgreve, R., & Zampich, L. (2018). *PLAXIS MoDeTo manual 2018*. Plaxis bv.

Panagoulias, S., Nernheim, A., & Voges-Espelage, P. (2023, September). *Comparison of Soil Damping Methods for Offshore Wind Turbines*. https://doi.org/10.3723/SHDJ4954

Pennington, D. (1999). *The anisotropic small strain stiffness of Cambridge Gault clay* [PhD thesis]. University of Bristol.

Peralta, P. (2010). *Investigations on the Behavior of Large Diameter Piles under Long-Term Lateral Cyclic Loading in Cohesionless Soil* [PhD thesis]. Leibniz University.

Peralta, P., & Achmus, M. (2010). *An experimental investigation of piles in sand subjected to lateral cyclic loads*. https://api.semanticscholar.org/CorpusID:199109622

Pisanò, F., Del Brocco, I., Ho, H. M., & Brasile, S. (2024). 3D FE simulation of PISA monopile field tests at Dunkirk using SANISAND-MS. *Géotechnique Letters*, *14*(2), 35–45. https://doi.org/10.1680/jgele.23.00073

PLAXIS 3D Manual. (2023a). *PLAXIS 3D 2024.1 Material Models Manual*. Delft, Netherlands: Bentley Systems.

PLAXIS 3D Manual. (2023b). *PLAXIS 3D 2024.1 Reference Manual*. Delft, Netherlands: Bentley Systems.

PLAXIS 3D Manual. (2023c). *PLAXIS 3D 2024.1 Scientific Manual*. Delft, Netherlands: Bentley Systems.

Plaxis SANISAND-MS Manual. (2023). *SANISAND-MS UDSM*. Delft, Netherlands: Bentley Systems.

Ponce, V. M., & Bell, J. M. (1971). Shear Strength of Sand at Extremely Low Pressures. *Journal of the Soil Mechanics and Foundations Division*, *97*(4), 625–638. https://doi.org/10.1061/JSFEAQ.0001578

Poulos, H., & Hull, T. (1989). Role of analytical geomechanics in foundation engineering. *[No Source Information Available]*.

Poulos, S. J. (1981). The Steady State of Deformation. *Journal of the Geotechnical Engineering Division*, *107*(5), 553–562. https://doi.org/10.1061/AJGEB6.0001129

Prevost, J. H. (1985). A simple plasticity theory for frictional cohesionless soils. *International Journal of Soil Dynamics and Earthquake Engineering*, *4*(1), 9–17. https://doi.org/10.1016/0261-7277(85)90030-0

Rascol, E. (2009). *Cyclic Properties of Sand: Dynamic Behaviour for Seismic Applications* [PhD thesis]. ÉCOLE POLYTECHNIQUE FÉDÉRALE DE LAUSANNE.

Ratananikom, W., Likitlersuang, S., & Yimsiri, S. (2013). An investigation of anisotropic elastic parameters of Bangkok Clay from vertical and horizontal cut specimens. *Geomechanics and Geoengineering*, *8*, 15–27. https://doi.org/10.1080/17486025.2012.726746

Reese, L. C., Cox, W. R., & Koop, F. D. (1974). *Analysis of Laterally Loaded Piles in Sand*. https://api.semanticscholar.org/CorpusID:130401465

Richards, I. (2019). *Monopile foundations under complex cyclic lateral loading* [PhD thesis, University of Oxford]. https://ora.ox.ac.uk/objects/uuid:bc3fc931-1c15-4abf-a367-42b5b4971d2a

Rollins, K. M., Evans, M. D., Diehl, N. B., & III, W. D. D. (1998). Shear Modulus and Damping Relationships for Gravels. *Journal of Geotechnical and Geoenvironmental Engineering*, *124*(5), 396–405. https://doi.org/10.1061/(ASCE)1090-0241(1998)124:5(396)

Roscoe, K., Schofield, A., & Wroth, C. (1958). On The Yielding of Soils. *Geotechnique*, *8*, 22–53. https://doi.org/10.1680/geot.1958.8.1.22

Ryan, G. V., Adcock, T. A. A., & McAdam, R. A. (2025). Soil Masing Behaviour for Offshore Wind Turbines—Fatigue Design and a Simple Damping Model. *Wind Energy*, *28*(3), e2973. https://doi.org/10.1002/we.2973

Sadrekarimi, A., & Olson, S. (2012). Effect of Sample-Preparation Method on Critical-State Behavior of Sands. *Geotechnical Testing Journal*, *35*, 104317. https://doi.org/10.1520/GTJ104317

Santos, J., & Correia, A. (2001, January). *Reference threshold shear strain of soil. Its application to obtain an unique strain-dependent shear modulus curve for soil*.

Schofield, A., & Wroth, C. (1968). *Critical State Soil Mechanics*.

Scholey, G., Pincus, H. J., Frost, J. D., Presti, D. C. L., & Jamiolkowski, M. (1995). A review of instrumentation for measuring small strains during triaxial testing of soil specimens. *Geotechnical Testing Journal*, *18*, 137–156.

Seed, H., & Idriss, I. (1970). *Soil Moduli and Damping Factors for Dynamic Response Analyses*. https://ntrl.ntis.gov/NTRL/dashboard/searchResults/titleDetail/PB197869.xhtml

Seidel, M. (2014). Wave induced fatigue loads—Insights from frequency domain calculations. *Stahlbau*, *83*. https://doi.org/10.1002/stab.201410184

Sheil, B., & McCabe, B. (2016). Biaxial Loading of Offshore Monopiles: Numerical Modeling. *International Journal of Geomechanics*, 04016050. https://doi.org/10.1061/(ASCE)GM.1943-5622.0000709

Shibuya, S., Park, C., Tatsuoka, F., Abe, F., Teachavorasinskun, S., Kohata, Y., & Sato, T. (1994). The significance of local lateral-strain measurement of soil specimens for a wide range of strain. *Soils and Foundations*, *34(2)*, 95–105.

Shirley, D. J., & Hampton, L. D. (1978). Shear-wave measurements in laboratory sediments. *Journal of the Acoustical Society of America*, *63*, 607–613.

Shirzadeh, R., Devriendt, C., Bidakhvidi, M. A., & Guillaume, P. (2013). Experimental and computational damping estimation of an offshore wind turbine on a monopile foundation. *Journal of Wind Engineering and Industrial Aerodynamics*, *120*, 96–106. https://doi.org/10.1016/j.jweia.2013.07.004

Shirzoi, A. G., Ma, Z., Zhang, B., Dai, S., & and, H. B. (2025). Investigation of soil damping for offshore wind turbine monopile-soil system in stiff clay on elastoplastic-damage model. *Marine Georesources & Geotechnology*, *43*(6), 949–964. https://doi.org/10.1080/1064119X.2024.2372816

Skempton, A. W. (1954). The Pore-Pressure Coefficients A and B. *Géotechnique*, *4*(4), 143–147. https://doi.org/10.1680/geot.1954.4.4.143

Sladen, J. A., D'Hollander, R. D., & Krahn, J. (1985). The liquefaction of sands, a collapse surface approach. *Canadian Geotechnical Journal*, *22*(4), 564–578. https://doi.org/10.1139/t85-076

Souto, A., Hartikainen, J., & Özüdoˇgru, K. (1994). Measurement of dynamic parameters of road pavement materials by the bender element and resonant column tests. *Géotechnique*, *44*(3), 519–526. https://doi.org/10.1680/geot.1994.44.3.519

Stokoe, K. H., Hwang, S. K., Lee, J.-K., & Andrus, R. (1995). *EFFECTS OF VARIOUS PARAMETERS ON THE STIFFNESS AND DAMPING OF SOILS AT SMALL TO MEDIUM STRAINS*. https://api.semanticscholar.org/CorpusID:126502728

Taborda, D. M. G., Zdravković, L., Kontoe, S., & Potts, D. M. (2014). Computational study on the modification of a bounding surface plasticity model for sands. *Computers and Geotechnics*, *59*, 145–160. https://doi.org/10.1016/j.compgeo.2014.03.005

Taborda, D. M. G., Zdravković, L., Potts, D. M., Burd, H. J., Byrne, B. W., Gavin, K. G., Houlsby, G. T., Jardine, R. J., Liu, T., Martin, C. M., & McAdam, R. A. (2019). Finite-element modelling of laterally loaded piles in a dense marine sand at Dunkirk. *Géotechnique*, *70*(11), 1014–1029. https://doi.org/10.1680/jgeot.18.PISA.006

Takahashi, A., Omura, N., Kobayashi, T., Kamata, Y., & Inagaki, S. (2022). Centrifuge model tests on large-diameter monopiles in dense sand subjected to two-way lateral cyclic loading in short-term. *Soils and Foundations*, *62*(3), 101148. https://doi.org/10.1016/j.sandf.2022.101148

Tarp-Johansen, N. J., Mørch, C. S., Andersen, L. V., Christensen, E. D., & Frandsen, S. T. (2009). *Comparing Sources of Damping of Cross-Wind Motion*. https://api.semanticscholar.org/CorpusID:126234204

Tatsuoka, F. (1988). *State-of-the-Art Paper: Some Recent Developments in Triaxial Testing Systems for Cohesionless Soils*. https://api.semanticscholar.org/CorpusID:260460261

Tatsuoka, F., Ochi, K., Fujii, S., & Okamoto, M. (1986). Cyclic Undrained Triaxial and Torsional Shear Strength of Sands for Different Sample Preparation Methods. *Soils and Foundations*, *26*(3), 23–41. https://doi.org/10.3208/sandf1972.26.3_23

Vaid, Y., Sivathayalan, S., & Stedman, D. (1999). Influence of Specimen-Reconstituting Method on the Undrained Response of Sand. *Geotechnical Testing Journal*, *22*(3), 187–195. https://doi.org/10.1520/GTJ11110J

Verdugo, R., & Ishihara, K. (1996). The Steady State of Sandy Soils. *Soils and Foundations*, *36*(2), 81–91. https://doi.org/10.3208/sandf.36.2_81

Versteijlen, W. G., Metrikine, A., Hoving, J., Smidt, E., & de Vries, W. (2011). Estimation of the vibration decrement of an offshore wind turbine support structure caused by its interaction with soil. *Knowledge, Technology & Policy*.

Viggiani, G., & Atkinson, J. H. (1995). Interpretation of bender element tests. *Géotechnique*, *45*(1), 149–154. https://doi.org/10.1680/geot.1995.45.1.149

Vo, L. (2022). *Natural Frequency and Soil Damping Analyses for Monopile Foundation Supporting Shared Anchoring of Offshore Wind Turbines and Wave Energy Systems* [PhD thesis]. North Carolina State University.

Von Soos, P. (1990). *Properties of soil and rock*. Grundbautaschenbuch, Berlin.

Vucetic, M. (1994). Cyclic Threshold Shear Strains in Soils. *Journal of Geotechnical Engineering*, *120*, 2208–2228.

Vucetic, M., & Dobry, R. (1991). Effect of Soil Plasticity on Cyclic Response. *Journal of Geotechnical Engineering*, *117*(1), 89–107. https://doi.org/10.1061/(ASCE)0733-9410(1991)117:1(89)

Vucetic, M., Lanzo, G., & Doroudian, M. (1998). Damping at Small Strains in Cyclic Simple Shear Test. *Journal of Geotechnical and Geoenvironmental Engineering*, *124*(7), 585–594. https://doi.org/10.1061/(ASCE)1090-0241(1998)124:7(585)

Weijtjens, W., Shirzadeh, R., De Sitter, G., & Devriendt, C. (2014, March). Classifying resonant frequencies and damping values of an offshore wind turbine on a monopile foundation for different operational conditions. *European Wind Energy Association Conference and Exhibition 2014, EWEA 2014*.

White, J. (2020). *A LABORATORY INVESTIGATION INTO THE BEHAVIOUR OF SAND AT LOW CONFINING STRESSES* [PhD thesis]. University of Oxford.

Wichtmann, T. (2005). *Explicit accumulation model for non-cohesive soils under cyclic loading* [PhD thesis]. Ruhr-Universit at Bochum.

Wichtmann, T., Fuentes, W., & Triantafyllidis, T. (2019). Inspection of three sophisticated constitutive models based on monotonic and cyclic tests on fine sand: Hypoplasticity vs.

Sanisand vs. ISA. *Soil Dynamics and Earthquake Engineering*, *124*, 172–183. https://doi.org/10.1016/j.soildyn.2019.05.001

Wichtmann, T., Niemunis, A., & Triantafyllidis, T. (2008, November). *Prediction of long-term deformations for monopile foundations of offshore wind power plants*.

Wichtmann, T., & Triantafyllidis, T. (2013). Effect of Uniformity Coefficient on G/Gmax and Damping Ratio of Uniform to Well-Graded Quartz Sands. *Journal of Geotechnical and Geoenvironmental Engineering*, *139*(1), 59–72. https://doi.org/10.1061/(ASCE)GT.1943-5606.0000735

Wind Europe. (2024b). *2023 Statistics and the outlook for 2024-2030*.

Yimsiri, S., Ratananikom, W., & Likitlersuang, S. (2009, October). *Investigation of some anisotropic characteristics of Bangkok Clay*.

Yimsiri, S., & Soga, K. (2002). A review of local strain measurement systems for triaxial testing of soils. *Geotechnical Engineering, SEAGS*, *33*, 42–52.

Zeng, X., & Grolewski, B. (2005). Measurement of Gmax and Estimation of K of Saturated Clay Using Bender Elements in an Oedometer. *Geotechnical Testing Journal*, *28*(3), 264–274. https://doi.org/10.1520/GTJ11318

Zhang, J., Andrus, R., & Juang, C. H. (2005). Normalized Shear Modulus and Material Damping Ratio Relationships. *Journal of Geotechnical and Geoenvironmental Engineering - J GEOTECH GEOENVIRON ENG*, *131*. https://doi.org/10.1061/(ASCE)1090-0241(2005)131:4(453)

Zhang, Y., Aamodt, K. K., & Kaynia, A. M. (2021). Hysteretic damping model for laterally loaded piles. *Marine Structures*, *76*, 102896. https://doi.org/10.1016/j.marstruc.2020.102896

Zhang, Y., & Andersen, K. H. (2019). Soil reaction curves for monopiles in clay. *Marine Structures*, *65*, 94–113. https://doi.org/10.1016/j.marstruc.2018.12.009

Ziegler, H. (1977). *An Introduction to Thermomechanics*. North-Holland Publishing Company. https://books.google.ie/books?id=6I5sPwAACAAJ

Appendix A

Location	Height [m]	diameter [m]	Thickness [mm]	Mass Density [kg/m]
Mud line	0	10	55.341	13572.39304
	0.001	10	55.341	13572.39304
	5	10	55.341	13572.39304
	5.001	10	53.449	13110.87351
	10	10	53.449	13110.87351
	10.001	10	51.509	12637.4619
	15	10	51.509	12637.4619
	15.001	10	49.527	12153.60948
	20	10	49.527	12153.60948
	20.001	10	47.517	11662.72371
	25	10	47.517	11662.72371
	25.001	10	45.517	11174.08238
Water line	30	10	45.517	11174.08238
	30.001	10	43.527	10687.68844
	35	10	43.527	10687.68844
	35.001	10	42.242	10373.50616
	40	10	42.242	10373.50616
	40.001	10	41.058	10083.94627
Tower start	45	10	41.058	10083.94627
	45.001	10	39.496	9701.836644
	58	10	39.496	9701.836644
	58.001	10	36.456	8957.821168
	71	9.926	36.456	8891.290748
	71.001	9.926	33.779	8240.624558
	84	9.443	33.779	7838.26581
	84.001	9.443	32.192	7471.269485
	97	8.833	32.192	6986.988604
	97.001	8.833	30.708	6666.023383
	110	8.151	30.708	6149.541091
	110.001	8.151	29.101	5828.878824
	123	7.39	29.101	5282.728621
	123.001	7.39	27.213	4941.26548
	136	6.909	27.213	4618.459905
	136.001	6.909	24.009	4076.589466
	149	6.748	24.009	3981.261687
	149.001	6.748	20.826	3455.079577
	162	6.572	20.826	3364.685898
	162.001	6.572	23.998	3875.282631
Tower top	174.582	6.5	23.998	3832.671106

Appendix B

The appendix here provides the script for running the ID FE model

```
import numpy as np

import pandas as pd

import matplotlib.pyplot as plt

import math as math

#Importing Youngs Modulus, Second moment of area, length, and distributed mass

df = pd.read_csv('Beams_Input.csv')

E = np.array(df['E'].dropna())

I = np.array(df['I'].dropna())

L = np.array(df['L'].dropna())

m = np.array(df['m'].dropna())

# Generating the global stiffness and mass matrix

K = np.zeros([len(L)*2 + 2, len(L)*2 + 2])

M = np.zeros([len(L)*2 + 2, len(L)*2 + 2])

# Functions for returning the local mass and stiffness matrices

def Stiffness(E, I, L):

    return (E*I/(L**3))*np.array([[12, 6*L, -12, 6*L], [6*L, 4*L**2, -6*L, 2*L**2], [-12, -6*L, 12, -6*L], [6*L, 2*L**2, -6*L, 4*L**2]])

def Mass(m, L):

    return (m*L/420)*np.array([[156, 22*L, 54, -13*L], [22*L, 4*L**2, 13*L, -3*L**2], [54, 13*L, 156, -22*L], [-13*L, -3*L**2, -22*L, 4*L**2]])

# Superimposing the local matrices to obtain the global matrix

for i in range(0, len(L), 1):

    if i == 0:

        K[0:4, 0:4] = K[0:4, 0:4] + Stiffness(E[i], I[i], L[i])

        M[0:4, 0:4] = M[0:4, 0:4] + Mass(m[i], L[i])
```

```
    else:
        K[i*2: i*2 + 4, i*2: i*2 + 4] = K[i*2: i*2 + 4, i*2: i*2 + 4] + Stiffness(E[i], I[i], L[i])
        M[i*2: i*2 + 4, i*2: i*2 + 4] = M[i*2: i*2 + 4, i*2: i*2 + 4] + Mass(m[i], L[i])
# Soil stiffness and Damping Matrix
K_soil = np.zeros([len(L)*2 + 2, len(L)*2 + 2])
Kxx =
Ktheta =
K_soil[0:2, 0:2] = np.array([[Kxx, 0], [0, Ktheta]])
K = K + K_soil
C = np.zeros([len(L)*2 + 2, len(L)*2 + 2])
C_soil = np.zeros([len(L)*2 + 2, len(L)*2 + 2])
Cxx =
Ctheta =
C_soil[0:2, 0:2] = np.array([[Cxx, 0], [0, Ctheta]])
C = C + C_soil
# Determination of eigen values
M_Inv = np.linalg.inv(M)
KM = np.dot(M_Inv, K)
w,v = np.linalg.eig(KM)
print(0.5*np.sqrt(w)/math.pi)
# Time domain analysis
df = pd.read_csv('Time_Stepping_Method.csv')
dt = 0.005
Time = np.array(df['Time'].dropna())
Force_Matrix = np.zeros([len(K), len(Time)])
Force_Matrix[len(K) - 2] = np.array(df['Force'].dropna())    # Horizontal load at RNA level
K_Hat_Matrix = K + (4/(dt**2))*M + (2/dt)*C
```

```
d_P = np.zeros((len(K), len(Time)-1))

for i in range(0, len(Time)-1, 1):

    d_P[len(K) - 2,i] = Force_Matrix[len(K) - 2,i+1] - Force_Matrix[len(K) - 2,i]

    d_P_Hat = np.zeros((len(Force_Matrix), len(Time)-1))

X = np.zeros((len(K), len(Time)))

V = np.zeros((len(K), len(Time)))

A = np.zeros((len(K), len(Time)))

for i in range(0, len(Time)-1, 1):

    d_P_Hat[:,i] = d_P[:,i] + np.dot(M, ((4/dt)*V[:,i] + 2*A[:,i])) + np.dot(C, 2*V[:,i])

    dx = np.dot(np.linalg.inv(K_Hat_Matrix), d_P_Hat[:,i])

    dv = (2/dt)*dx - 2*V[:,i]

    X[:,i+1] = X[:,i] + dx

    V[:,i+1] = V[:,i] + dv

    A[:,i+1] = np.dot(np.linalg.inv(M),(Force_Matrix[:,i+1] - np.dot(C,V[:,i+1]) - np.dot(K,X[:,i+1])))
```